INFORMATION TO USERS

This manuscript has been reproduced from the microfilm master. UMI films the text directly from the original or copy submitted. Thus, some thesis and dissertation copies are in typewriter face, while others may be from any type of computer printer.

The quality of this reproduction is dependent upon the quality of the copy submitted. Broken or indistinct print, colored or poor quality illustrations and photographs, print bleedthrough, substandard margins, and improper alignment can adversely affect reproduction.

In the unlikely event that the author did not send UMI a complete manuscript and there are missing pages, these will be noted. Also, if unauthorized copyright material had to be removed, a note will indicate the deletion.

Oversize materials (e.g., maps, drawings, charts) are reproduced by sectioning the original, beginning at the upper left-hand corner and continuing from left to right in equal sections with small overlaps.

Photographs included in the original manuscript have been reproduced xerographically in this copy. Higher quality 6" x 9" black and white photographic prints are available for any photographs or illustrations appearing in this copy for an additional charge. Contact UMI directly to order.

Bell & Howell Information and Learning
300 North Zeeb Road, Ann Arbor, MI 48106-1346 USA
800-521-0600

Multinuclear Solid-State and Hyperpolarized Xenon-129 NMR Studies of Organic Surfaces

by

Lucy Dickinson

A thesis submitted to the Faculty of Graduate Studies and Research

in partial fulfillment of the requirements for the degree of

Doctor of Philosophy

Department of Chemistry
McGill University
Montreal, Quebec
Canada

August 1998

Abstract

While solid state NMR spectroscopy represents a versatile and widely applicable probe of molecular structure and behavior, the highly desirable goal of utilizing it to study surfaces of both bulk materials and thin films has, until recently, been limited by the insensitivity inherent to the procedure. This work examines and seeks to combine two approaches with which to overcome the problems arising from the physical restrictions of the Boltzmann distribution, which governs the NMR experiment. In the first part the bonding and dynamic properties of the highly popular self-assembled monolayers (SAMs) are examined by multinuclear cross polarization magic angle spinning (CPMAS) NMR, as well as a variety of more complex two dimensional experiments. In the past, many investigations of the three most widely studied SAMs (alkylsilanes on silica, alkylphosphonates on metal oxides and alkanethiols on gold) have been carried out on monolayers synthesized on planar substrates. While such systems have been extensively examined by vibrational spectroscopy, ellipsometry and electron scanning techniques, many fundamental issues have remained unresolved. The use of higher surface area metal oxide particles and gold colloids as substrates for the same self-assembled layers allows the use of NMR, which is shown to be a very good tool with which to gain molecular level information. This section addresses the validity of comparing SAMs on planar and particulate surfaces and expounds upon the wide range of experiments made possible by this methodology.

The NMR study of surfaces of bulk materials such as polymers is precluded by the difficulty of distinguishing between bulk and surface nuclei as well as the relatively low concentration of surface species compared with bulk nuclei. The probe nucleus ^{129}Xe has previously proved useful in the study of high surface area porous structures. Xenon is a large inert nucleus, which exhibits a wide chemical shift range on interaction with surfaces, allowing even weak Van der Waal forces to be observed. Its use has been restricted to porous materials and amorphous polymers and has typically required long acquisition times and high pressures of gas (a factor which complicates sample preparation). Recent advances have coupled the process of optical pumping of xenon via

rubidium with the NMR experiment, leading to production of hyperpolarized xenon, which in turn yields a huge signal enhancement. In the second part the practical details of this experiment are presented. Initial work on bulk polypropylene and some polyalkyl-methacrylates is described, the spectra above and below the glass transition temperatures are discussed in terms of chain dynamics. Finally the ^{129}Xe probe is applied to a variety of SAM systems as well as a polymer coating. The potential utility of the experiment as a complimentary tool for examining chain behavior is assessed along with the drawbacks and possible limitations of the current experimental set-up.

Résumé

Alors que la RMN de l'état solide représente une sonde polyvalente et largement applicable à l'étude de la structure et du comportement moléculaire, le but hautement souhaitable d'utiliser la RMN pour l'étude de surface de matériel en bloc et de films minces a, jusqu'à récemment, été limité par le manque de sensibilité inhérent à cette procédure. Ce travail examine et cherche à combiner deux approches pour surmonter les problèmes provenant des restrictions physiques de la distribution de Boltzmann, qui gouverne la RMN. Dans la première partie, les liaisons et les propriétées dynamiques des très populaires mono-couches auto-assemblées (SAMs - self-assembled monolayers) sont examinées de façon multinucléaire par RMN en utilisant l'expérience de polarization croisée de rotation à l'angle magique (CPMAS), ainsi qu'une variété d'expériences plus complexes à deux dimensions. Dans le passé, plusieurs recherches sur les trois "SAMs" les plus étudiés (silanes d'alkyles sur silice, phosphonates d'alkyles sur oxide de métal, et alkanethiols sur de l'or) ont été accomplies sur une mono-couche synthétisée sur un substrat plat. Alors que de tels systèmes ont été examinés avec beaucoup de détails par spectroscopie de vibration, ellipsométrie et des techniques d'exploration électronique (electron scan), plusieurs aspects fondammentaux sont demeurés non-résolus. L'utilisation de surface de plus grande dimension pour les particules d'oxyde de métal et de colloïde d'or comme substrat pour les mêmes couches auto-assemblées permet l'utilisation de la RMN, qui est reconnue comme étant un très bon outil avec lequel on peut obtenir des informations au niveau moléculaire. Cette section discute de la validité de la comparaison de "SAMs" sur surface plate ou particulaire et expose un large évantail d'expériences rendues possibles par cette technique.

L'étude de surface de matériel en bloc comme les polymères est exclue par la difficultée de distinguer entre les noyaux du bloc et ceux en surface ainsi que par la relativement faible concentration d'espèces en surface comparée avec les noyaux de l'ensemble. La sonde nucléaire ^{129}Xe a été utilisée avec succès dans le passé dans une étude de structures poreuses de grande surface. Le xénon est un gros noyau inerte, caractérisé par un large intervalle de déplacements chimiques lorsqu'il interagit avec une

surface, permettant même l'observation de faibles forces de Van der Waal. Son utilisation a été restreinte aux matériaux poreux et aux polymères amorphes, et a requis typiquement de long temps d'acquisition et des hautes pressions de gaz (un facteur qui complique la préparation de l'échantillon. De récentes études ont couplé le processus de pompage optique du xénon par le rubidium avec l'expérience de RMN, conduisant à la production de xénon hyper-polarisé, qui à son tour produit un énorme accroissement du signal. Dans la seconde partie, les détails pratiques de cette expérience sont présentés. Le travail initial sur le polypropylene en bloc et quelques polyalkyls métacrylates est décrit, les spectres au-dessus et en dessous de la température de transition de verre sont discutés en termes de dynamiques de chaînes. Finallement la sonde ^{129}Xe est appliquée à une variété de systèmes SAMs aussi bien qu'à un enrobage de polymère. L'utilitée potentielle de l'expérience à titre d'outil complémentaire pour examiner le comportement de la chaîne est évalué avec les inconvénients et les limitations possibles du montage expérimental courant.

Foreword

In accordance with guideline 7 of the "Guidelines Concerning Thesis Preparation" (Faculty of Graduate Studies and Research), the following text is cited:

> "Candidates have the option of including, as part of the thesis, the text of one or more papers submitted or to be submitted for publication, or the clearly-duplicated text of one or more published papers. These texts must be bound as an integral part of the thesis.
>
> If this option is chosen, connecting texts that provide logical bridges between the different papers are mandatory. The thesis must be written in such a way that it is more than a mere collection of manuscripts; in other words, results of a series of papers must be integrated.
>
> The thesis must still conform to all the other requirements of the "Guidelines for Thesis Preparation". The thesis must include: A Table of Contents, an abstract in English and French, an introduction which clearly states the rationale and objectives of the study, a review of the literature, a final conclusion and summary, and a thorough bibliography or reference list.
>
> Additional material must be provided where appropriate (e.g. in appendices) and in sufficient detail to allow a clear and precise judgement to be made of the importance and originality of the research reported in the thesis.
>
> In the case of manuscripts co-authored by the candidate and others, the candidate is required to make an explicit statement in the thesis as to who contributed to such work and to what extent. Supervisors must attest to the accuracy of such statements at the doctoral oral defense. Since the task of the examiners is made more difficult in these cases, it is in the candidates interest to make perfectly clear the responsibilities of all the authors of the co-authored papers."

In accordance with university regulations, the first part of this thesis is made up in part of five papers, whose titles and publication details are listed below. Copyright clearance has been obtained from all the co-authors, whose contributions will now be outlined. In the interests of clarity, and to avoid repetition of the theoretical and experimental details of the solid state NMR experiments, the relevant sections of the papers have been amalgamated and expanded to provide the introductory Chapter. All the CPMAS and multidimensional NMR experiments were carried out by myself under the supervision of Dr. Linda Reven, and with the help of Dr. Fred Morin. The inclusion of a number of "test-case" spectra in Chapter One is intended to illustrate the functions of the various pulse sequences.

Chapter Two consists of a literature survey undertaken prior to the study of the self-assembled monolayers of octadecyltrichlorosilane on silica followed by presentation of experimental data and a comparison of this monolayer system with the bulk OTS polymers. Part of this work is described in paper one ("NMR Spectroscopy of Self-Assembled Monolayers"). The synthesis was carried out by Wei Gao, all other work in this chapter is my own, carried out under the supervision of Dr. Reven.

Chapter Three is made up of the results included in the two papers "Self-Assembled monolayers of Alkylphosphonic Acids on Metal Oxides" and "Order-Disorder Transitions in Self-Assembled Monolayers: A ^{13}C Solid-State NMR Study". The synthesis of these samples was carried out by Wei Gao, with the help of an undergraduate honors student, Christina Grozinger. They also ran some of the infrared spectroscopy reported here. All of the solid-state NMR spectra shown were acquired by myself, under the supervision of Dr Reven, except for that of the ZrO_2-ODPA sample at –100°C, which was provided by Dr Fred Morin. His name is also included on these papers in recognition of his assistance and expertise in solid-state NMR.

The results presented in Chapter Four were obtained as part of a collaboration with the group of Dr Bruce Lennox at McGill University. The synthesis of the gold nanoparticle systems was carried out in his laboratory by Dr. Antonella Badia, with the help of two undergraduate students, Linette Demers and Helene Schmitt. They also acquired all of the liquid phase NMR data presented. The solid state NMR experiments presented were carried out by myself under the supervision of Dr. Linda Reven. These

results have been published in the form of two papers: "Gold-Sulfur Interactions in Alkylthiol Self-Assembled Monolayers Formed on Gold Nanoparticles Studied by Solid-State NMR" and "The Effect of Terminal Hydrogen Bonding on the Structure and Dynamics of Nanoparticle Self-Assemble Monolayers (SAMs): An NMR Dynamics Study".

The optically polarized ^{129}Xe spectroscopy studies presented in Part Two of the thesis are all my own work, carried out under the guidance of Dr. Reven. Some of this work has been published in a Conference Proceedings: "Optically Polarized ^{129}Xe NMR Spectroscopy of Polymers and Thin Films". The monolayer samples were provided by Wei Gao (as noted in the text), and the zirconia-PEG system was synthesized by Shane Pawsey.

Acknowledgements

I should like to offer my sincere thanks to my supervisor, Professor Linda Reven for the opportunity to work in her laboratory and for her help during the writing up of this thesis. I am also grateful to all of my coworkers, especially Wei Gao and Shane Pawsey for their work on the synthesis of the systems described in this thesis. The collaboration on the alkanethiol systems developed by Antonella Badia and Professor Bruce Lennox is also gratefully acknowledged. I would like to thank Dr Francoise Sauriol for translation of the abstract.

I am grateful to the Commonwealth Agency for funding my Ph.D. program, and for their help and efficiency over the last five years.

Finally I should like to thank Lana, Ross and David for their friendship during my time in Montreal. I am especially indebted to Dr. Fred Morin, both for his NMR expertise and emotional support. I dedicate this thesis to my parents for their love and encouragement, without which this would not have been possible.

Table of Contents

Chapter Two: Experimental

Chapter Three: Optically Polarized ^{129}Xe NMR of Bulk Polymers

Chapter Four: Polarized ^{129}Xe NMR of Self Assembled Monolayers and Polymer Coated Metal Oxides

List of Frequently Used Symbols and Abbreviations

SAM:	Self assembled monolayer
NMR:	Nuclear magnetic resonance
CPMAS:	Cross polarisation magic angle spinning
DSC:	Differential scanning calorimetry
FTIR:	Fourier transform infrared
CSA:	Chemical shift anisotropy
RF:	Radio frequency
T_1:	Longitudinal or spin-lattice relaxation time
T_2:	Transverse or spin-spin relaxation time
BMS:	Bulk magnetic susceptibility
FID:	Free induction decay
OTS:	Octadecyltrichlorosilane
ODPA:	Octadecylphosphonic acid
OPA:	Octylphosphonic acid
WISE:	Wideline separation

Part One

Part Two

List of Tables

Part One

Part Two

Part One

Chapter One- General Introduction

1.1 Self assembled monolayers

The synthesis and characterization of self-assembled monolayers (SAMs) have become of great interest due to the wide ranging potential uses of these systems. Possible applications discussed in the literature include: optoelectronics and modified electrodes (where the use of ordered organic components allows for control of order at a molecular level), catalysis, creation of biomimetic and biocompatible structures with capabilities such as biochemical sensing, development of coatings designed for corrosion prevention and wear protection.[1,2,3] More importantly these systems provide a general model for the study of behavior in two dimensional systems,[4] so that such research is of fundamental importance in achieving an understanding of the chemistry and physics which occur at surfaces and interfaces. In particular one would like to be able to connect macroscopic behavior with precise microscopic structures, a correlation which remains difficult to elucidate. Comprehension of complex interfacial properties requires extensive interdisciplinary approaches, specifically the integration of theory, synthetic techniques and molecular characterization.[5] Both the Langmuir-Blodgett[6] and self-assembly techniques permit assembly of molecules into ordered architectures into which functional groups can be incorporated and in which thermal stability can be controlled by adjustment of the intra- and inter-molecular covalent bonding.

A variety of SAM systems exists, and their properties can be modified by changing either the substrate and/or the organic film. In the case of self-assembled monolayer structures, a seemingly diverse group of assemblies have in common the strength of their thin film-substrate interactions which arise from the apparent formation of chemical bonds at the interface. The most widely investigated examples include:

a. organosilicon compounds on hydroxylated surfaces (e.g. silica or alumina)

b. alkanethiols and dialkylsulfides on coinage metals

c. alkyl phosphonates on metal oxides

d. n-alkanoic acids on metal oxides

In addition these surface coatings often display high stability (including water resistance and thermal stability) due to the effects of interchain Van der Waals forces. The optimization of these two properties (both by changing the components of the systems as well as modifying synthesis conditions) necessitates thorough characterization.

1.2 Characterization techniques

If the capacity of these systems for molecular level control is to be fully understood, and tailoring of thin films for specific applications is to be realized it will be necessary to characterize films at a molecular level.[7] Early work in this field used planar substrates such as silicon wafers to give samples which could be studied by contact angle measurements, ellipsometry, infrared and Raman spectroscopy and atomic force and scanning tunnel microscopy.[5] Ellipsometry and contact angle measurement give a rough estimate of monolayer quality. Vibrational spectroscopy is useful for determining the conformation and orientation of the organic groups, but the strong bands in the substrate region often preclude observation of bands due to substrate-film bonds. Scanning probe microscopies can detect the formation of domains and the registry of the organic groups with the underlying substrate but do not yield any chemical information.

The use of solid state NMR to study surfaces of any type has been restricted by sensitivity problems inherent to the NMR experiment. Nuclei at the surfaces of organic materials such as polymers can not readily be distinguished from those of the bulk. High surface area inorganic materials such as zeolites and silica gels are frequently studied by solid state NMR,[8] and by extension of this approach, studies have been carried out on organic species adsorbed or grafted onto high surface area substrates. Investigations of chemically modified silica gels[9] or polymers adsorbed onto metal oxides[10] have confirmed that NMR studies offer a wealth of information which is difficult to obtain by other techniques, specifically details about surface bonding,[11] the role played by the

substrate in altering chain mobility of adsorbed polymers[10] or the dynamic properties of alkylsilyl-modified silica in the presence of different solvents.[12]

There have been attempts to reproduce these self assembled monolayers on non-porous high surface area materials such as colloidal or fumed metal or metal oxide substrates. These substrates open up the opportunity of using bulk characterization techniques such as differential scanning calorimetry (DSC), transmission infrared spectroscopy (FTIR) and elemental analysis. The rest of this chapter describes the various characterization techniques used, in particular the range of solid-state NMR techniques available. In chapters 2-4, three different types of SAMs are discussed; alkylsiloxanes on silica, alkylphosphonates on metal oxides, and organothiols on gold nanoparticles. The wide range of information gained by solid state NMR is presented along with suggestions about how this data compares with other methods of characterization. Finally the relative strengths and weaknesses of these three types of assemblies are compared and contrasted.

1.3 Basic high resolution solid state NMR techniques

NMR spectroscopy has many potential benefits, being a non-destructive technique capable of yielding information about both chemical structure and dynamic behavior. The following sections will present the theory behind the solid state NMR techniques that will be applied to the SAM systems, along with examples of their applications to well known systems.

For a spin 1/2 nucleus, the NMR spectrum is determined by the Hamiltonian;

$$H = Hz + H_{DD} + H_{CS} \qquad \textbf{Equation 1.1}$$

where H_Z is the Zeeman interaction, H_{DD} is the dipole-dipole interaction and H_{CS} is the chemical shift. These interactions will be examined independently in order to outline their effects on a solid state NMR experiment. The scalar coupling interaction, which is common in solution state NMR, is small enough in the cases in which we are interested that it can be neglected.

The Zeeman interaction

The Zeeman interaction describes the interaction of the nuclear spin with the applied field, B_0. It is defined by equation 1.2:

$$Hz = -\gamma hB_0\bar{I}_z/2\pi \qquad \textbf{Equation 1.2}$$

where γ is the magnetogyric ratio of the nucleus, h is Planck's constant, B_0 is the magnetic field strength and $\bar{I}_z$ is the z component of the spin angular momentum operator. This interaction produces two spin states, the lower and upper states being denoted by α and β respectively. If all the nuclei placed in the magnetic field were equivalent, this interaction would give rise to a single transition and a single observed peak. Transitions between these states occurs upon irradiation in the radiofrequency (RF) range. The Zeeman interaction is the largest interaction seen in NMR spectroscopy, having a magnitude on the order of Megahertz. As shown in equation 1.1, the spin Hamiltonians for spin 1/2 nuclei contain additional terms, all of which are much smaller than H_z. For the sake of the following discussion, consider the interactions between an isolated ^1H and ^{13}C pair.

Dipolar interaction

Each nuclear spin generates its own local magnetic field shown by the field lines in Figure 1.1. These have a component in the z direction and can be aligned with or against B_0 depending on whether the spin is in its α and β energy state. This component is denoted as B_z in Figure 1.1. The Hamiltonian which describes this local field is given by equation 1.3:

$$H_{DD} = \frac{\left(3\cos^2\theta - 1\right)}{r_{CH}^3}\gamma_C\gamma_H\vec{I}_H\vec{I}_C \qquad \textbf{Equation 1.3}$$

where $\bar{I}_H$ and $\bar{I}_C$ are the spin angular momentum operators of the proton and carbon nuclei respectively.

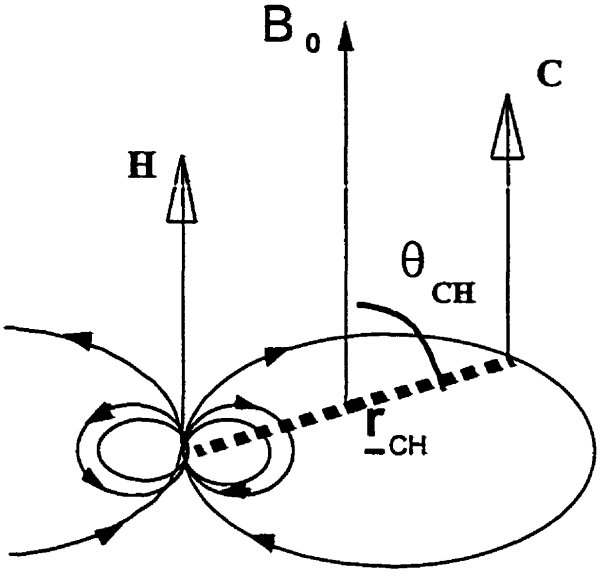

Figure 1.1 Schematic depicting the heteronuclear dipolar coupling interaction between a ^{13}C nucleus and a proton; r_{CH} is the internuclear vector and θ is the angle between the internuclear vector and the applied field.

Since the proton can be in either the α or β state, the effect of its local field at the carbon nucleus is either to add to or subtract from the applied field. The carbon nucleus therefore experiences two different effective fields, resulting in two possible transitions split by $\frac{\gamma_C \gamma_H h}{2\pi r^3_{CH}}(3\cos^2\theta - 1)$.

However this outcome assumes a single orientation between internuclear vector, r_{CH} of an isolated pair of dipolar coupled nuclei and the applied field direction. In reality, for solid samples all possible orientations are present. Summing over all possible angles θ leads to a so-called Pake doublet.[13] Presence of further dipolar couplings to multiple abundant proton spins broadens the line to give a Gaussian shaped resonance. The cumulative effects of the Zeeman and dipolar interactions are shown in Figure 1.2.

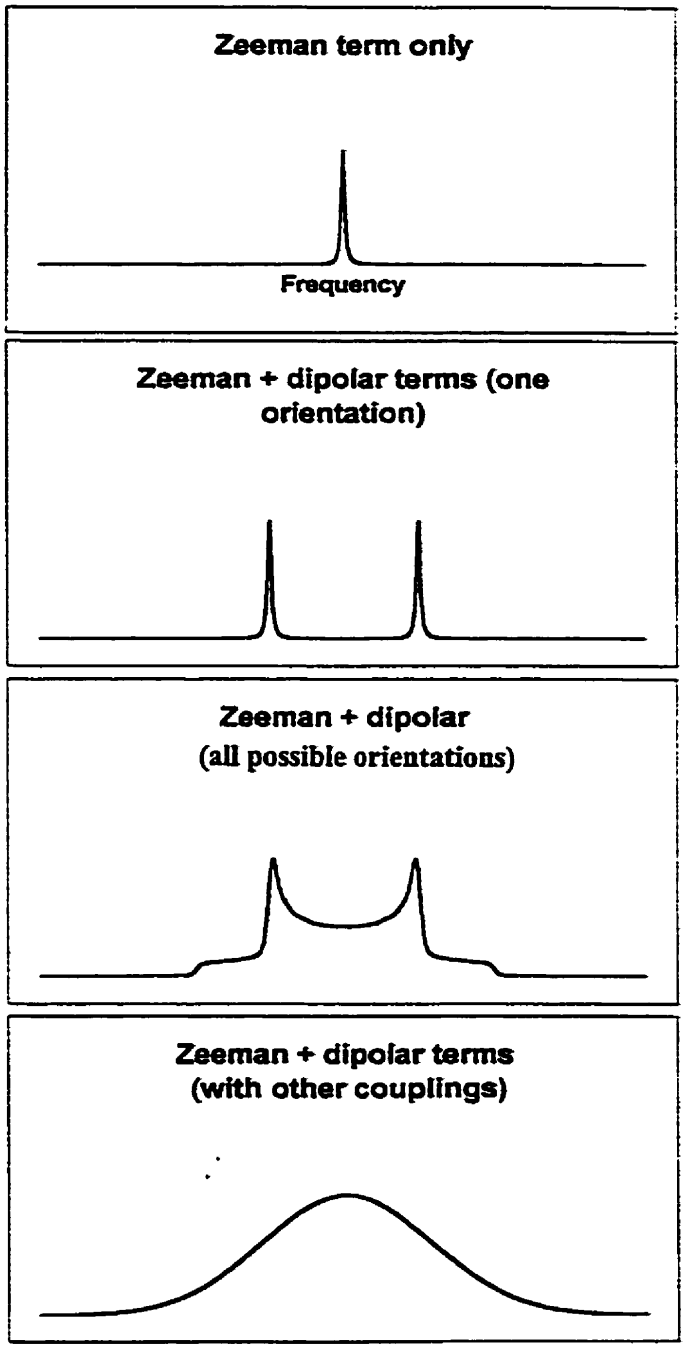

Figure 1.2 Depiction of the effects of the Zeeman and heteronuclear dipolar interactions on lineshape.

The dipolar coupling constant is defined in general as $D = \gamma_I\gamma_S\, h^2/(4\pi^2 r^3)$. The width of a dipolar broadened proton line is typically ~ 60-70 kHz. For the heteronuclear ^{13}C-^{1}H interaction (assuming a bond length of 0.11 nm) the dipolar coupling is about 15 kHz, since γ_C is approximately four times smaller than γ_H. In order to remove the heteronuclear dipolar interaction, the abundant spin nuclei are strongly irradiated by application of an RF field. This causes the ^{1}H nuclei to undergo rapid transitions between the α and β states, averaging the dipolar interaction to zero. Efficient decoupling of dipolar interactions requires that the strength of the RF irradiation (in frequency units) be greater than the width of the broadened line. Experimentally this usually equates to application of an RF field of ~60 kHz. Use of a decoupling field also eliminates broadening caused by the smaller scalar coupling (a through-bond, non-orientational coupling which is observed in solution state NMR). From equation 1.3 it is evident that the dipolar interaction is independent of external field strength, B_0.

Molecular motion serves to average the dipolar interaction. Large amplitude motions with frequencies greater than the width of the resonance will reduce the dipolar coupling. In the extreme of the solution state, D is zero.

Homonuclear dipolar couplings are only significant in solid state ^{1}H or ^{19}F spectra, being negligible in cases involving the observation of dilute spins. This fortuitous effect is due to the larger internuclear distances involved as well as the much smaller magnetic moments of nuclei other than ^{1}H or ^{19}F. In the case of ^{13}C and ^{29}Si, the internuclear distances are large due to the low isotopic abundance of these nuclei (1.1 % and 4.7 % respectively). In the ^{31}P studies, dilution is due to the lower concentration within the systems of interest.

Owing to the fact that the proton spins in a system are strongly coupled by homonuclear dipolar coupling, a process called spin diffusion occurs in which energy conserving flip-flops of coupled spins results in rapid diffusion of the state of spins throughout the sample. This results in an equilibration of the ^{1}H spin reservoir to a single spin temperature, i.e. the ^{1}H spins can be considered as a uniform bath of spins. It should be noted that molecular motion will reduce the spin diffusion rate through a reduction in the dipolar couplings as mentioned above. The spin diffusion process is depicted in Figure 1.3.

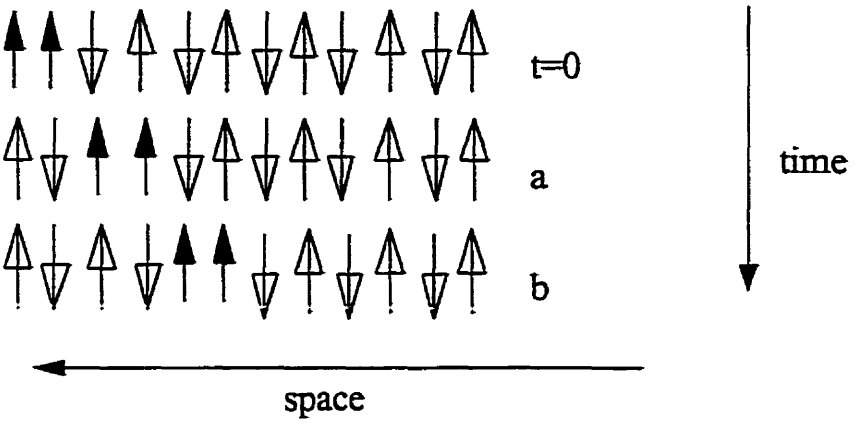

Figure 1.3 A depiction of spin diffusion, the spatial migration of magnetization via energy conserving flip-flops.

Chemical shift

For dilute spins such as ^{13}C, the next largest interaction affecting the nuclear spin is the chemical shift. The description in the preceding section assumed an isolated carbon atom with a spherical electronic distribution. In reality the electronic distribution is determined by the chemical bonding between nuclei which serves to remove electron density from the atoms and place it into the bonds. In effect each nucleus is shielded from the applied field by an amount determined by the surrounding electron density. Classically electrons placed within a magnetic field will circulate in such a way as to create a field which opposes that of the external field. The magnitude of this induced field depends on the electronic environment of the observed nucleus (specifically the electron density in the plane perpendicular to the applied field) and results in the well known isotropic chemical shift observed in solution. In solution molecules tumble rapidly and all orientations with respect to B_0 are sampled.

The study of solid state samples is more complex, since these will contain molecules of fixed orientations with respect to B_0. Thus in addition to the isotropic chemical shifts arising from chemical environment observed in all samples, for solids there will also be orientation dependence to the chemical shift. This orientation

dependence is called chemical shift anisotropy. Consider a sample of solid benzene placed in a magnetic field.[14] Some molecules will reside with the plane of the molecule perpendicular to the magnetic field. Since the plane contains no π electron density, only σ electron density, these molecules will resonate in the region of the NMR spectrum typical of aliphatic carbons. Some molecules will reside with B_0 along the C-H bond. Since the plane perpendicular to B_0 contains π electron density, the molecules will resonate in the aromatic region of the ^{13}C spectral range. It is easy to see that a powder sample will contain all possible orientations and therefore produce a spectrum consisting of the overlap of a very large number of individual resonances.

The Hamiltonian describing the chemical shift is given by equation 4:

$$H_{CS} = \frac{h}{2\pi}\gamma \bar{I}.\hat{\sigma}\bar{B} \qquad \textbf{Equation 1.4}$$

Since the distribution of the electronic density is a three dimensional property, the chemical shift is described by a tensor $\hat{\sigma}$, for which a principle axis system can be chosen such that the tensor is diagonal with three principle values, i.e:

$$\begin{vmatrix} \sigma_{XX} & \sigma_{XY} & \sigma_{XZ} \\ \sigma_{YX} & \sigma_{YY} & \sigma_{YZ} \\ \sigma_{ZX} & \sigma_{ZY} & \sigma_{ZZ} \end{vmatrix} \xrightarrow{\text{diagonalize}} \begin{vmatrix} \sigma_{11} & 0 & 0 \\ 0 & \sigma_{22} & 0 \\ 0 & 0 & \sigma_{33} \end{vmatrix}$$

The sum and average of the diagonal elements are constant. The average, or isotropic shift, which is what is observed in solution is described by equation 1.5:

$$\delta_{ISO} = \frac{1}{3}(\sigma_{11} + \sigma_{22} + \sigma_{33}) \qquad \textbf{Equation 1.5}$$

The chemical shift anisotropy resulting from the orientational dependence of the shifts observed in solids leads to a lineshape defined by:

$$\Delta\sigma = \sigma_{33} - \frac{1}{2}(\sigma_{11} + \sigma_{22}) \qquad \textbf{Equation 1.6}$$

An additional parameter which characterizes the chemical shift anisotropy tensor is the asymmetry factor, η:

$$\eta = \left|\frac{\sigma_{22} - \sigma_{11}}{\sigma_{33} - \delta iso}\right| \qquad \textbf{Equation 1.7}$$

This parameter takes on values between 0 and 1, where 0 is a result of axial symmetry, i.e. $\sigma_{11} = \sigma_{22} \neq \sigma_{33}$. This is the case for molecules of cylindrical symmetry such as CO_2.

The elements of the diagonalized tensor, along with the isotropic shift, are depicted in Figure 1.4.

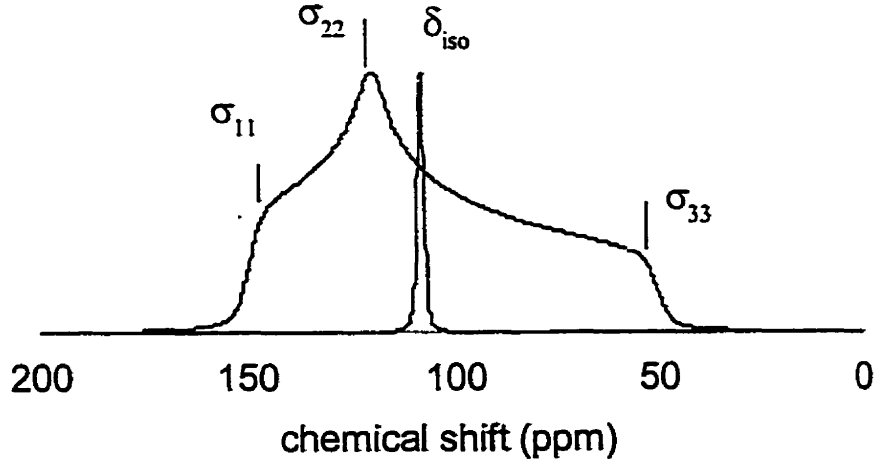

Figure 1.4 Diagram showing a typical CSA powder pattern along with the corresponding isotropic shift.

The shape of the CSA pattern gives information about the electronic distribution for a given site. Aliphatic carbons tend to possess a small CSA, the presence of an electron withdrawing group will increase the anisotropy. The largest CSAs are generally exhibited by aromatic and carbonyl carbons. Although the CSA pattern can give useful information, the presence of several overlapping powder patterns for chemically distinct nuclei will obviously produce a featureless broad spectrum. This problem is circumvented by the development of magic angle spinning (MAS) techniques as described below.

Magic angle spinning

MAS was invented by E.R Andrew in 1954[15] as a method of eliminating the dipolar interaction. However it was subsequently discovered that MAS was also effective in collapsing the CSA pattern to give the isotropic shift. It can be shown that under conditions of sample spinning, the chemical shift Hamiltonian can be split into time independent and time dependent parts.[16] Rotation at a frequency ω_r about an angle θ with respect to B_0 leads to the following equations for the time independent and time dependent Hamiltonians:

$$H_{\sigma}^{ind} = \frac{\gamma h}{2\pi} B_0 I_z \left[\frac{1}{2} \sin^2\theta \left(\sum_{i=1}^{3} \sigma_{ii} \right) + \frac{1}{2} \left(3\cos^2\theta - 1 \right) \sum_{i=1}^{3} \sigma_{ii} \cos^2\beta_i \right]$$

Equation 1.8

$$H_{\sigma}(t) = \frac{\gamma h}{2\pi} B_0 I_z \left[\frac{1}{2} \sin 2\theta \left(\sum_{i=1}^{3} \sigma_i \sin 2\beta_i \cos(\omega_r t) \right) + \frac{1}{2} \sin^2\theta \sum_{i=1}^{3} \sigma_i \sin^2\beta \cos 2(\omega_r t) \right]$$

Equation 1.9

where β_i are the angles between B_0 and the principle axes of the CSA tensor.

If θ=54.7° then $\sin^2\theta$=2/3 and $(3\cos^2\theta-1)$=0 which simplifies the time independent chemical shift Hamiltonian to:

$$H_{CS}^{ind} = \frac{\gamma h}{2\pi} B_0 I_z \frac{1}{3}(\sum \sigma_{ii}) \qquad \textbf{Equation 1.10}$$

which is the Hamiltonian for the isotropic shift. This time averaging is depicted schematically for an axially symmetric sample (i.e. one where two of the principle axes are equivalent, so that $\sigma_{11}=\sigma_{22}$) in Figure 1.5:

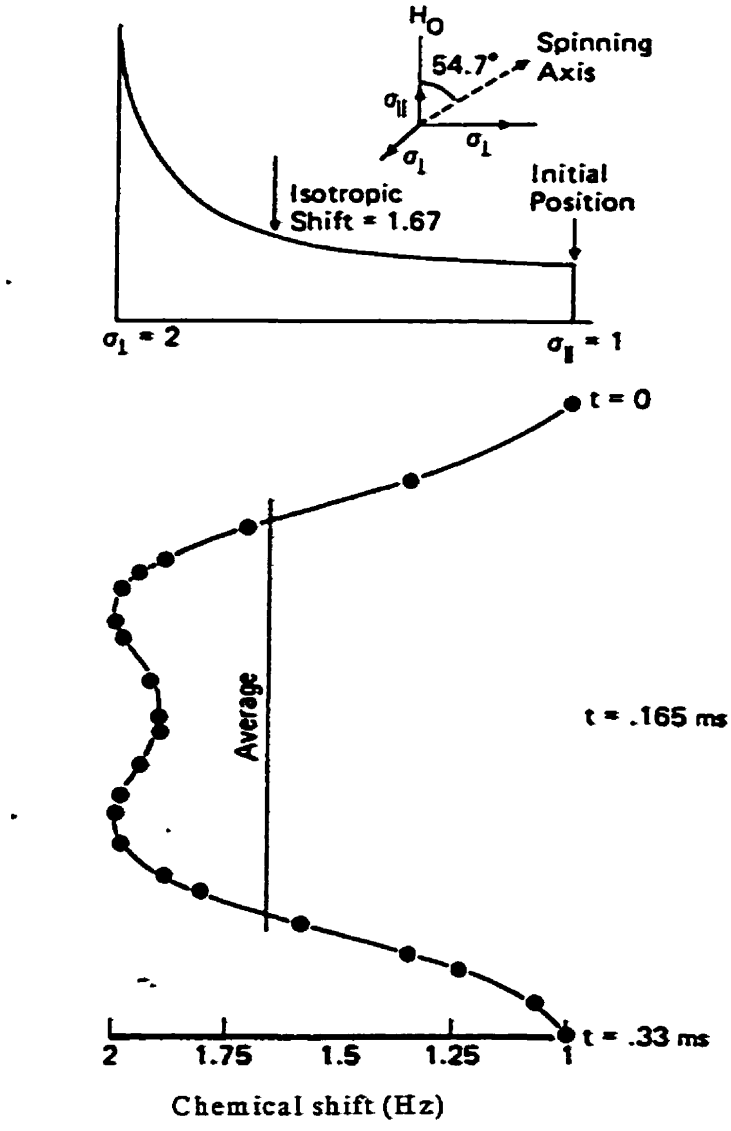

Figure 1.5 Schematic depicting the concept of time averaging of a CSA broadened line via magic angle spinning.[17]

On Fourier transformation to the frequency domain, the time dependent term, $H_{CS}(t)$, gives rise to sidebands at multiples of ω_r as shown in Figure 1.6. Since the powder pattern is an inhomogeneous lineshape (see section 1.4) spinning at even low speeds is successful in removing CSA. However, at spinning speeds less than the width of the shift anisotropy (in Hz units) the observed spectrum displays sidebands separated from the isotropic average peak by the spinning frequencies. Spinning at higher speeds will produce a spectrum consisting only of the isotropic peak. In some cases it can be helpful to run experiments at lower speeds and analyze the resulting sidebands in order to obtain the principle values of the shift tensors as described in work by Herzfeld and Berger.[18] The chemical shift anisotropy is linearly dependent on field, so that at higher fields the sample must be spun more rapidly in order to remove the anisotropy and reduce the spectrum to a single line.

Relaxation parameters

Spin-lattice relaxation time

As described above, when a sample is placed in a magnetic field, the nuclear spin states split. The population of the two states is governed by the Bolztmann distribution so that $n_- / n_+ = e^{-\Delta E/kT}$, where n_+ is the number of spins aligned with the field, and n_- is the number aligned against the field. The difference, $n_+ - n_-$ creates a net magnetization aligned with the field denoted M_0. Pulsed NMR involves the application of a radio frequency pulse designed to rotate M_0 from the B_0 direction into another plane. The system subsequently relaxes back to equilibrium. In the most simple case, the spin system is subjected to a 90° pulse which moves M_0 from the z axis into the xy plane (see Figure 1.7).

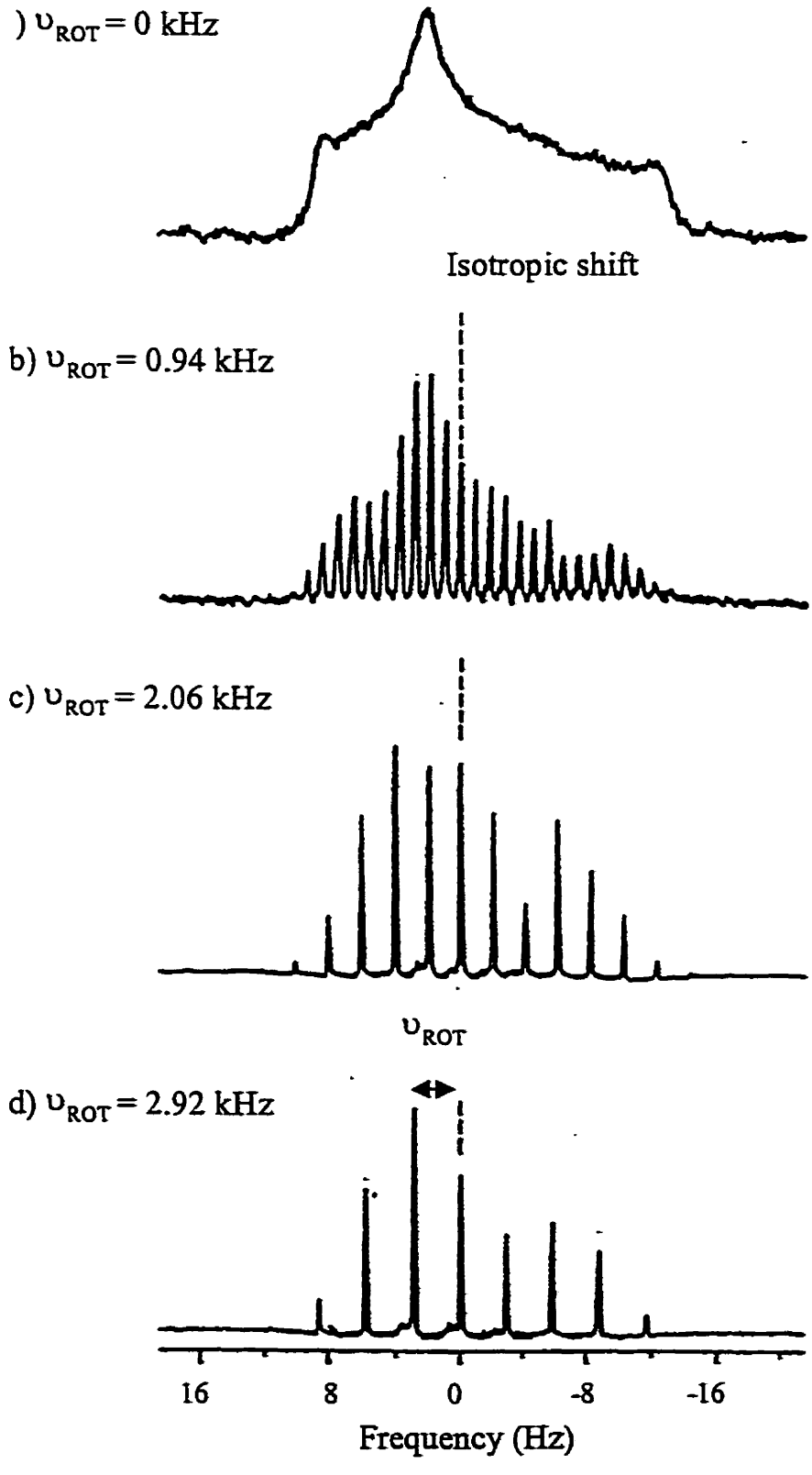

Figure 1.6 Static and spinning ^{31}P spectra of dipalmitoyl phoshatidylcholine.[20]

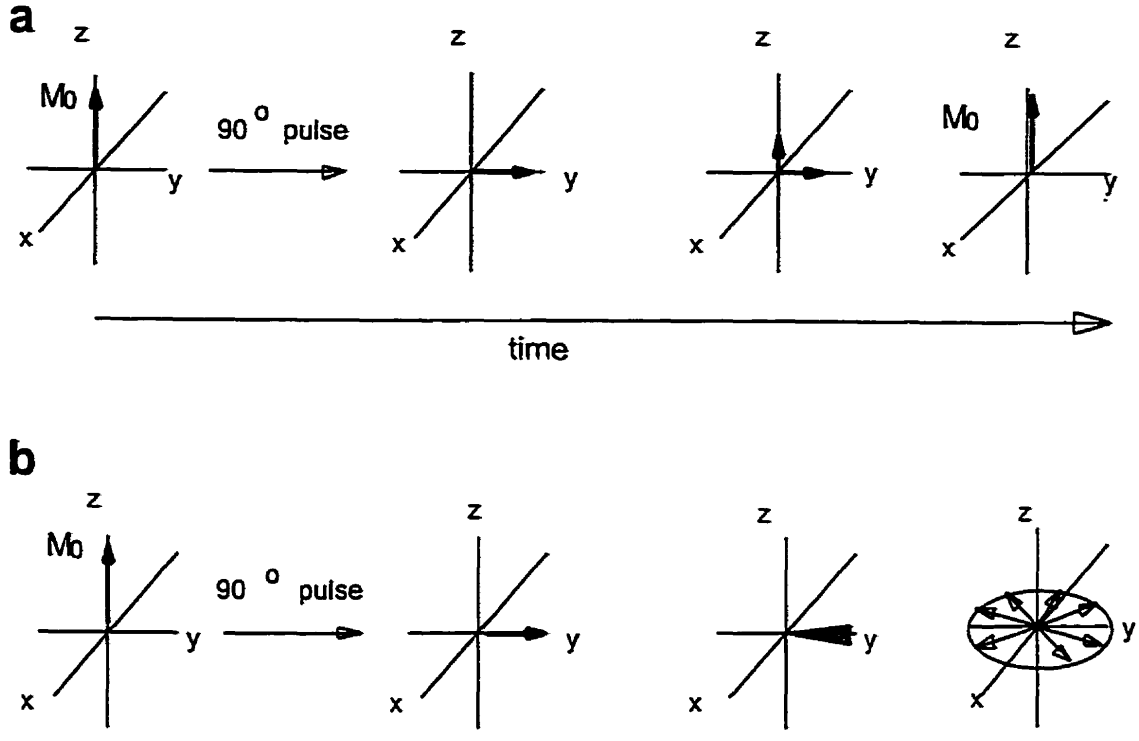

Figure 1.7 Schematic of T_1 and T_2 relaxation processes following a 90x pulse to move magnetization from the z axis to the y axis.

The rate constant which defines the return of the z component of M_0 to equilibrium is given by T_1 (the spin-lattice relaxation time), the rate constant for the return of the y component is T_2 (spin-spin relaxation time). Motions which affect T_1 occur near the Larmor frequency of the spins. Such rapid motion is often lacking in the solid state, so that the T_1 values of solids can be long. This has an effect on data acquisition, since the system must be permitted to relax at least partially to equilibrium after each FID is recorded. Experimentally this requires a delay of up to five times the T_1 value, which can greatly increase the overall experiment time. The relaxation of the nuclei is brought about by several mechanisms,[19] predominantly via modulation of the dipolar interactions through molecular motion. As such the measurement of relaxation times can be used to probe molecular motion and to obtain quantitative data on the energy barriers associated with motional processes. In general proton T_1 times in solids will be shorter than those of less abundant spins since each ^1H nucleus exhibits strong

dipolar coupling with the other ^{1}H spins in the system. Therefore if one ^{1}H site is undergoing rapid motion (e.g. in a methyl group) and relaxes rapidly, spin diffusion will cause all the protons to relax at the same rate. In contrast the relaxation of ^{13}C nuclei is often slower, and even where one ^{13}C site is undergoing rapid motion sufficient to shorten its T_1, this effect will not be transmitted to the other (immobile) ^{13}C spins because the ^{13}C-^{13}C couplings are small. Since there can be a difference in the relaxation time of individual ^{13}C nuclei depending on the mobility of the site, measurements can often be made of these individual ^{13}C T_1 values, and these offer a source of dynamic information.[20]

Spin-lattice relaxation in the rotating frame, $T_{1\rho}$

In order to fully understand the cross-polarization experiment to be described shortly, it is necessary to understand the process of spin-lattice relaxation in the rotating frame. The magnetization precesses around B_0 at the Larmor frequency of the particular nucleus. In order to remove this precession frequency one visualizes that the axis system is rotating at a frequency which is equal to the Larmor frequency and where M_0 appears stationary along the +z axis. This is called the rotating frame.

The experiment for measuring $T_{1\rho}$ is shown in Figure 1.8 as performed on a system of abundant spins (e.g. protons).

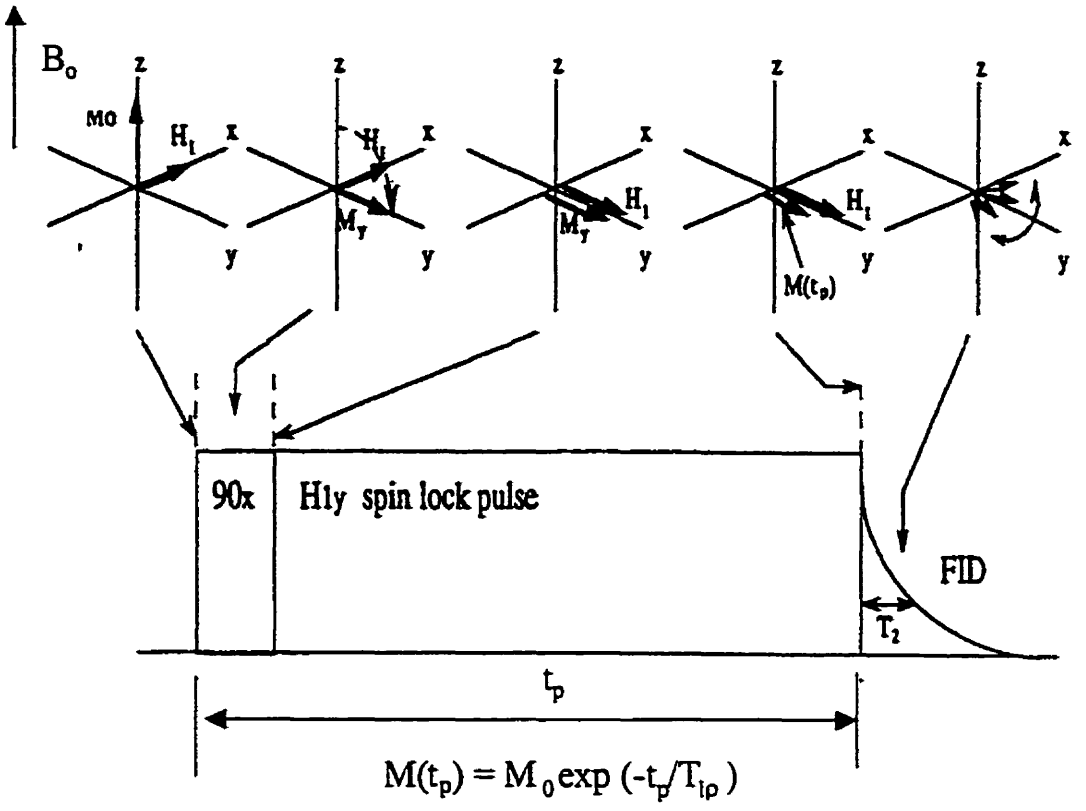

Figure 1.8 Pulse sequence used in the determination of $T_{1\rho}$, the spin lattice relaxation time in the rotating frame. Adapted from reference 21.

A 90°_{x} pulse rotates M_0 to the +y axis in the rotating frame, at which point the phase of the applied RF field is switched by 90° to the y axis as shown. At the outset of the experiment the population distribution is described as follows:

$$\frac{n_-}{n_+} = e^{-\gamma B_0 / kT_L} \qquad \textbf{Equation 1.11}$$

where n_- and n_+ are the populations of the upper and lower energy states and T_L is the spin temperature of the system at equilibrium, which is also the spin temperature of the lattice since at this point the system is in equilibrium with its surroundings. After application of the second pulse, the magnetization is locked along B_{1y} and the magnetization should be defined by a new spin temperature T_s:

$$\frac{n_-}{n_-} = e^{-\gamma B_1 / kT_s}$$ **Equation 1.12**

Since the magnitude of the magnetization is unchanged immediately after the phase shift, the right-hand sides of equations 1.11 and 1.12 must be equal. Since $B_1 \ll B_0$, this requires that $T_s \ll T_L$. As a result the proton spin system has effectively been cooled to a very low spin temperature, not by cooling the sample, but by lowering the effective field experienced by the spins from B_0 to B_1. The implications of this will be explored further in the section describing cross-polarization. It is sufficient to state at this point that the magnetization is no longer at equilibrium since it was generated along B_0 and now resides along B_1. Relaxation then takes place until it reaches the value determined by B_1. The relaxation along the y axis in the spin locking condition to equilibrium is called spin lattice relaxation in the rotating frame, $T_{1\rho}$. $T_{1\rho}$ is most often measured for protons. The equation governing the rate of spin lattice relaxation in the rotating frame contains a term which depends on $2\gamma B_1$.[21] Since γB_1 is about 60 kHz (for protons) this makes the measurement of $T_{1\rho H}$ very useful in the study of mechanical properties of polymer systems, which involve relatively slow motions. Measurement of ^{13}C $T_{1\rho}$ is complicated by the fact that the ^{13}C-^{13}C dipole-dipole couplings are small and the concept of spin temperature is not valid.

Cross polarization

Cross polarization takes advantage of the properties of the ^1H spins, specifically their high abundance and relatively short T_1 relaxation times to enhance the signals of more dilute spins.[22] The concept of spin temperature as outlined above is the basis for the cross polarization process. The process of cross polarization is most readily understood using a thermodynamic analogy. For the sake of the following argument consider the most popular case, that of ^1H-^{13}C cross polarization. The pulse sequence is shown in Figure 1.9.

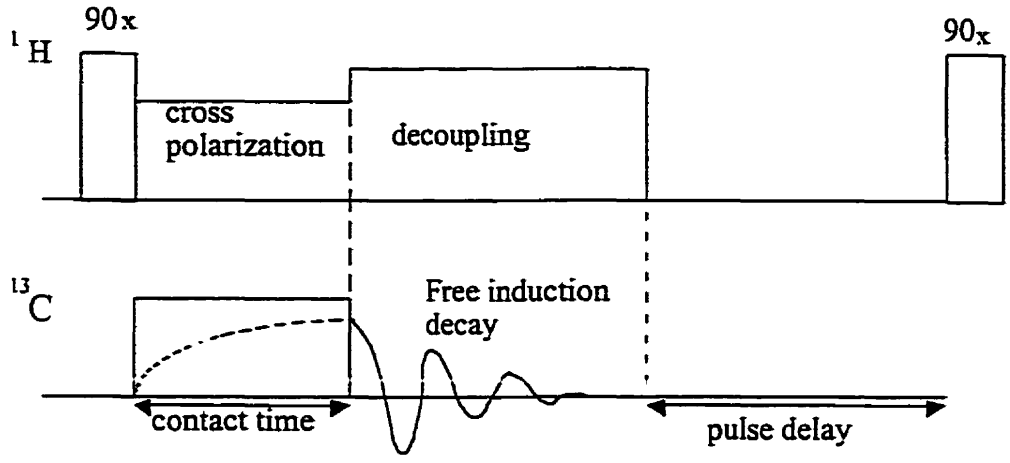

Figure 1.9 Cross polarization pulse sequence.

Figure 1.10 shows a schematic diagram of the ^{13}C and ^{1}H spin reservoirs in a typical organic solid, along with the relaxation parameters associated with the couplings between these reservoirs. Such a diagram is helpful in describing potential relaxation pathways available to the spin systems after application of specific RF pulse sequences.

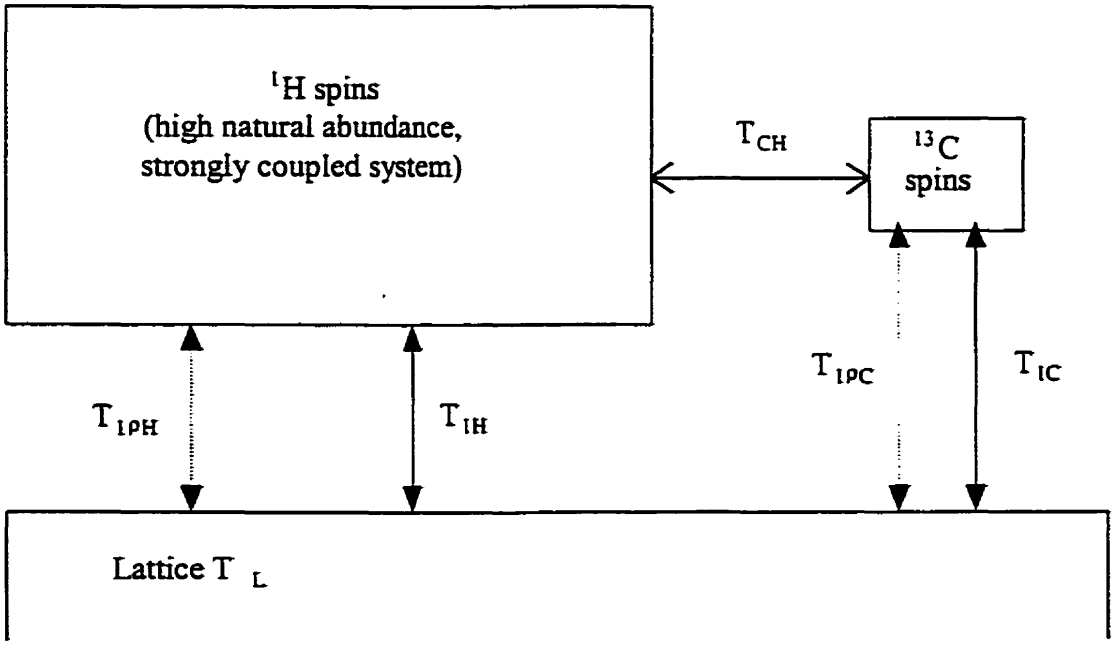

Figure 1.10 ^{13}C and ^{1}H spin reservoirs in an organic solid.

The ^{1}H spin reservoir is represented as being larger than the ^{13}C reservoir because of the higher natural abundance and larger magnetogyric ratio of protons. Both spin systems are in contact with the lattice through their respective T_1 and $T_{1\rho}$ relaxation pathways. As described in the section on spin-lattice relaxation in the rotating frame, the application of a 90° pulse followed by a 90° phase shift serves to cool the abundant proton spin system. This reservoir is brought into contact (the "contact time") with the smaller reservoir of rare ^{13}C spins allowing equilibration between the two spin systems. This cooling of the nuclei in the second pool is equivalent to increasing the magnetization of the ^{13}C spins (as shown in Equation 1.11). This equilibration is analogous to the thermal equilibration of two solid objects at different temperatures being brought into contact with one another.

The mechanism by which equilibration of the two spin reservoirs occurs is the heteronuclear dipolar coupling between protons and ^{13}C. The rate at which the equilibration occurs is determined by T_{CH}, the cross polarization rate constant, as shown in Figure 1.10. The coupling is strongest and the transfer of magnetization is most rapid for rigid methylene and methine groups where T_{CH} is typically less than 100μs.[22] Non-protonated carbons experience smaller dipolar couplings with protons because of the greater internuclear distance and therefore cross polarize at a slower rate. ^{13}C nuclei in mobile environments, including methyl groups, also cross polarize more slowly due to partial averaging of the dipole-dipole interaction.

In some instances it can be helpful to record a series of CPMAS spectra employing a range of cross polarization contact times. This allows selection of the optimal contact time value. For samples containing different carbon sites which cross polarize over a significant range of times, a more accurate picture of sample composition can be obtained. The intensity as a function of contact time is given by equation 1.13:

$$I \propto \left[\left(1-\exp\left(-t/T_{CH}\right)\right)\exp\left(-t/T_{1\rho H}\right)\right] \qquad \textbf{Equation 1.13}$$

where t is the contact time and T_{CH} and $T_{1\rho H}$ are the cross polarization and proton spin lattice relaxation in the rotating frame time constants respectively.

A specimen plot of peak intensity against contact time for a sample consisting of a mixture of crystalline and amorphous regions is shown in Figure 1.11. In the first part of each curve, the observed intensity is dominated by the build up effects of the cross polarization rate. Since mobility will reduce this rate through averaging of the ^{13}C-^{1}H dipolar couplings, it is clear that the amorphous region will give rise to a smaller peak, i.e. the cross polarization experiment is not quantitative. As the contact time is increased, the effects of $T_{1\rho H}$ will start to appear. Since the protons and ^{13}C nuclei are in contact, the relaxation of the protons will also cause relaxation of ^{13}C. Thus, although use of longer contact times will yield results which more accurately reflect the composition of the sample, they will also result in a decrease in overall intensity of the peaks. Selection of the most appropriate contact time for a given samples involves choosing a value long enough to allow the most efficient possible cross polarization of more mobile components, but without using a value so long that the signal-to-noise ratio is severely compromised.

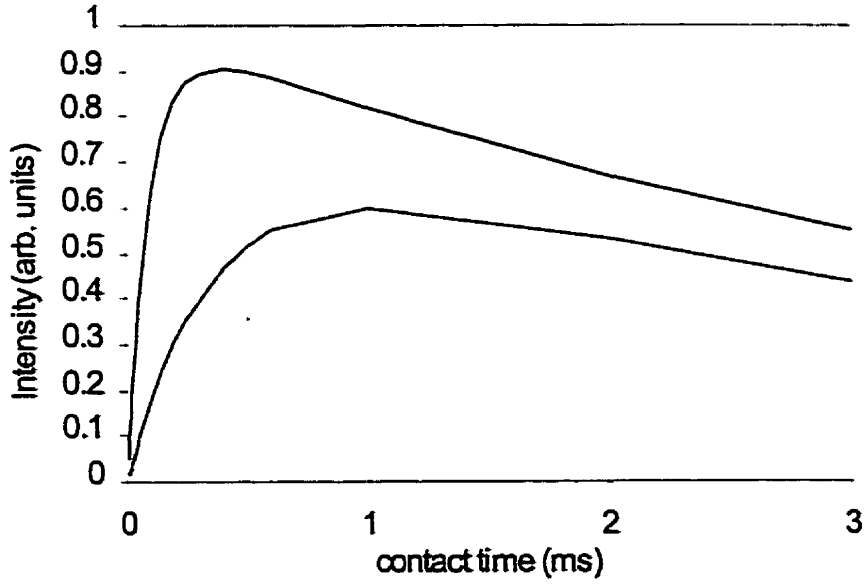

Figure 1.11 Graph of signal intensity against contact time for a mixture of rigid (above) and mobile (below) carbon chains. The T_{CH} for the rigid component was assumed to be 100 μs, for the amorphous component 400 μs, the $T_{1\rho H}$ was taken to be 5 ms.[23]

Plots such as the one shown in Figure 1.11 can be analyzed to extract T_{CH} and $T_{1\rho H}$ for a system. In a more general sense, variable contact time measurements offer an additional probe of mobility, this will be further addressed in Chapter 2.

In practice the cross polarization energy transfer is carried out by application of RF fields designed to cause the ^{1}H and ^{13}C nuclei to precess in the rotating frame at the same frequency, i.e. $\omega_1{}^H = \omega_1{}^C$, or equally $\gamma^H B_1{}^H = \gamma^C B_1{}^C$. Since $\gamma^H = 4\gamma^C$, fulfillment of this resonance condition, the so-called Hartmann-Hahn match requires that $B_1{}^C = 4B_1{}^H$. This is depicted by a vector diagram in Figure 1.12.

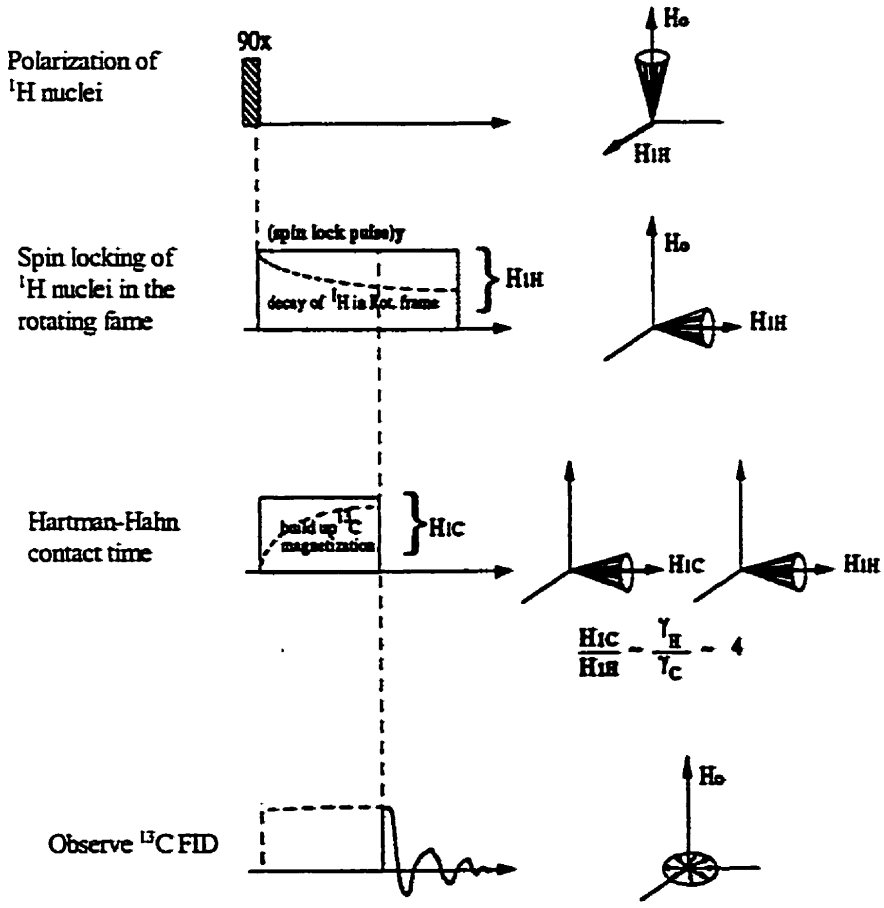

Figure 1.12 Diagram illustrating the development of nuclear spin vectors during the cross polarization experiment.[20] During the Hartmann-Hahn contact time the protons and ^{13}C precess around their B_1 fields at the same rate. This allows for energy conserving flip-flops which build up the ^{13}C signal.

1.4 Advanced Solid State NMR Experiments

The preceding description of the fundamental spin interactions and pulse sequences of solid-state NMR provided an introduction to the advanced solid state NMR experiments outlined in this section. These experiments were originally developed and applied to solid polymers[24] and the extension of their use to study the SAM systems represents the first application of such techniques to surfaces.

A simple 1D NMR experiment involves the acquisition of a free induction decay during a time t_2 which is then processed by a Fourier transformation. A general 2D experiment is shown in Figure 1.13. It consists of (1) a preparation period whereby transverse magnetization is created either by a 90° pulse or by cross-polarization; (2) an evolution period, t_1, during which the magnetization is allowed to evolve; (3) an optional fixed mixing time during which the magnetization is returned to the z axis in some experiments; (4) a detection period, t_2, in which the FID is measured.[25] In practice such experiments usually involve the recording of a series of FIDs with incremented evolution period. The result is a data set, $S(t_1,t_2)$ which is Fourier transformed twice to give a spectrum with two frequency dimension, $S(f_1,f_2)$.

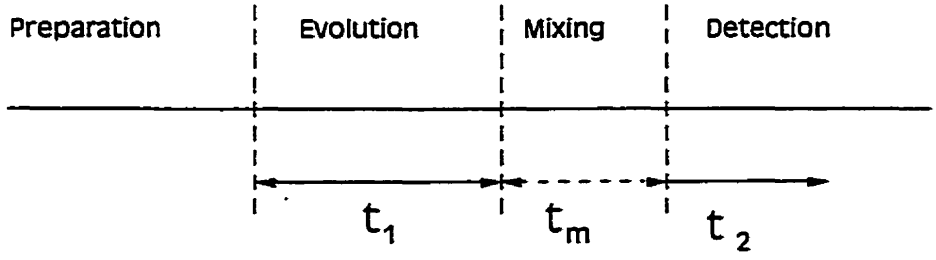

Figure 1.13 Generalized schematic of a 2D NMR experiment.

2D Wideline Separation NMR

The measurement of proton linewidths is complicated in solid state NMR by the broad nature of the lines, caused by the strength of the proton-proton dipolar coupling. This broadness introduces an instrumental problem, since broad lines arise from short

FIDs which are difficult to acquire due to the receiver deadtime (i.e. the time required to turn off the transmitter and turn on the receiver following an RF pulse). The deadtime problem is usually circumvented by the use of spin echoes for the acquisition of an undistorted broad line spectrum. The spin echo sequence consists of a 90° pulse followed by a time, τ, then a 180° pulse and a second waiting period, τ. The refocusing pulse creates an echo which appears after a period 2τ following the initial pulse. Thus the FID can be sampled at this point and since τ can be set to be much larger than the receiver deadtime, the broadline is samples without distortion. However, even when an undistorted proton FID is acquired using a spin echo, the resulting spectrum consists of overlapping broad resonances from all components of the sample. Solid-state proton resonances are typically on the order of ~10-70 kHz as a result of the strength of the ^{1}H-^{1}H dipolar interaction. Since the entire chemical shift range for protons is only a few kilohertz, resolution of individual peaks is almost impossible without using complex multipulse sequences which can only partially average these strong interactions.[26] Deconvolution of these overlapping wideline resonances is difficult or impossible in the case of many chemically distinct sites.

The 2D WISE experiment[27] uses the pulse sequence shown in Figure 1.14 in combination with MAS to yield a 2D spectrum consisting of the ^{13}C CPMAS spectrum in one dimension, while the second dimension contains the proton linewidth for each carbon site. Thus the 2D experiment separates the proton lineshape based on ^{13}C isotropic chemical shifts.

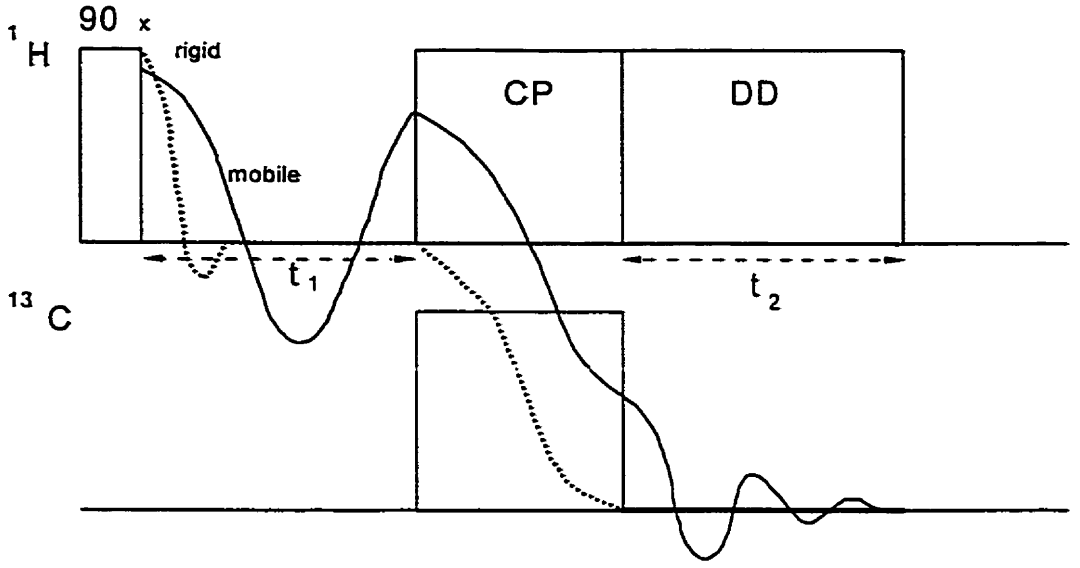

Figure 1.14 Pulse sequence for the 2D WISE experiment. Proton FIDs corresponding to rigid (fast decay) and mobile (slow decay) proton systems are shown during t_1, the proton evolution period of the pulse sequence.

During t_1, the incremented proton evolution period, the transverse ^1H magnetization created by the 90° pulse begins to decay due to dipolar interactions. The extent of this decay is monitored by cross polarizing to ^{13}C and acquiring the FID in t_2. As t_1 is incremented, the system will reach a point where the rigid component has decayed to zero and does not contribute to the observed FID. As an example the 2D WISE spectrum of a sample of low density polyethylene is shown in Figure 1.15 along with a ^{13}C CPMAS spectrum and the dipolar slices of the crystalline and amorphous regions.

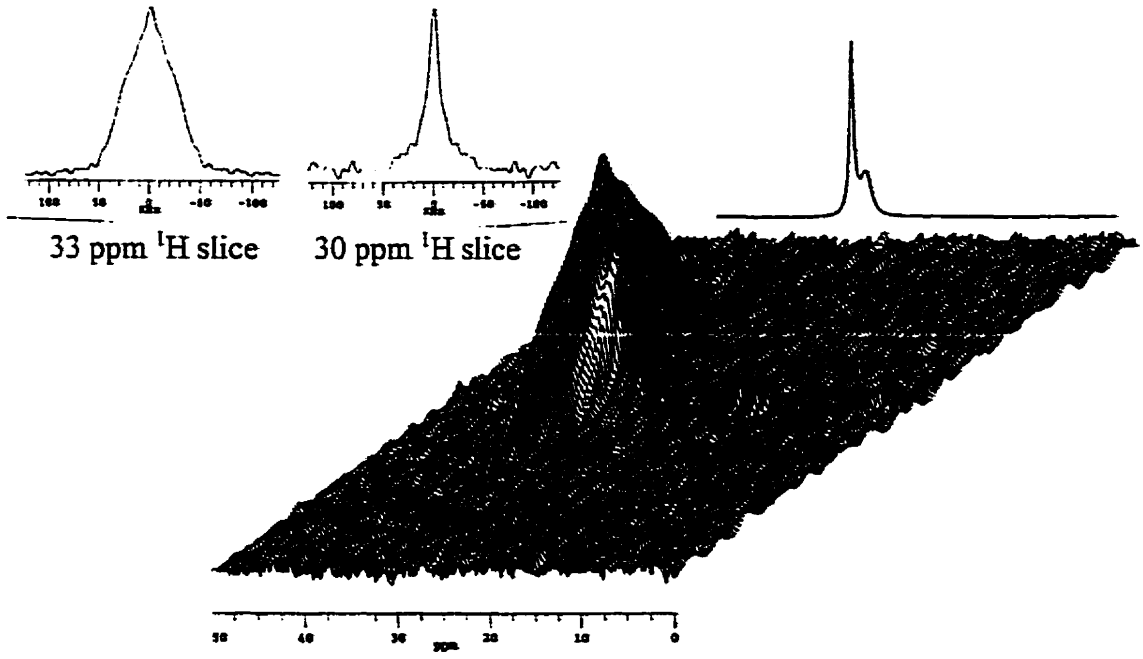

Figure 1.15 2D WISE of low density polyethylene. The 2D WISE spectrum was acquired with 12 scans, a contact time of 3 ms, recycle delay of 3 s. The proton evolution period consisted of 32 increments of 4μs.

The inset on the right hand side in Figure 1.15 is the simple ^{13}C CPMAS spectrum of the sample which consists of a peak at 33 ppm for the all-trans crystalline regions of the hydrocarbon chains and a peak at 30 ppm for the mobile amorphous material. The polymer chains in the mobile regions undergo trans-gauche jumps. The increase in population of the gauche state in the latter causes the well-known gauche upfield shift.[28] This is demonstrated in the Newman projections in Figure 1.16.

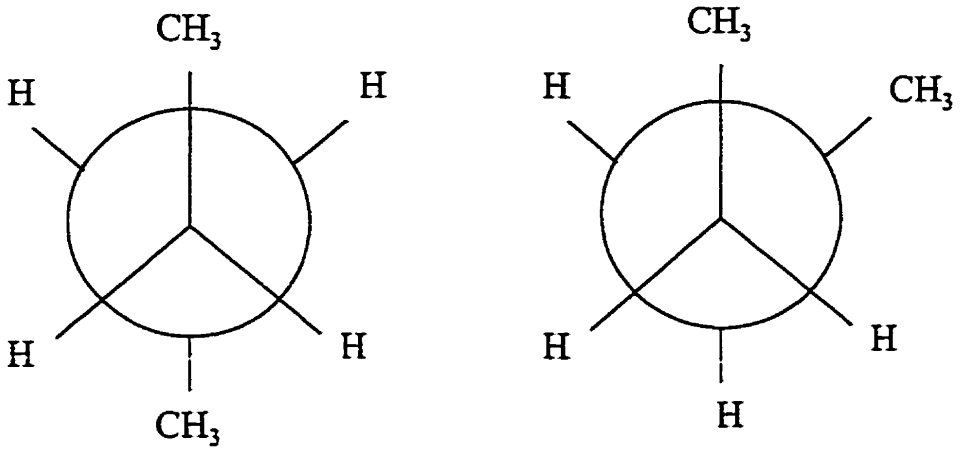

Figure 1.16 Newman projections of the trans and gauche conformers of butane. The closer steric relationship apparent between the two methyl groups in the gauche configuration leads to an increase in chemical shielding of ~6 ppm.[28]

The gauche effect is manifested as a shift of up to 4 ppm in the methylene resonance depending on the chain conformation. The 2D WISE experiment exploits the difference in shifts between the crystalline and amorphous regions allowing for the observation of separate proton lineshapes for each of these domains. The dipolar slices (shown on the left in Figure 1.15) corresponding to protons in the rigid all-trans crystalline region display a Gaussian linewidth with a peak width at half height (fwhh) of 50-70 kHz while the slice associated with the amorphous region at 30 ppm shows a motionally averaged lineshape with fwhh~ 10-20 kHz.

The proton linewidths offer a probe of mobility which has been exploited in a variety of other polymer systems. Reports in the literature include:

a) Studies of diblock copolymers such as polystyrene-co-poly(dimethyl siloxane)[24] in which evidence is given of a large difference in mobility of the two polymer segments (the PS being highly crystalline while the PDMS is highly mobile) in spite of the close spatial proximity (ca. 20nm) and significant chemical interactions between the two components.

b) A study of three polymers containing a stiff backbones with C_{16} aliphatic sidechains.[29] These polymers are highly relevant to consideration of the SAMs which are also essentially pinned alkyl chains. In these polymers, the mobilities of the sidechains

were shown to vary depending on the structure of the backbone. In the case where the backbone is a polyimide, the C_{16} sidechains exhibited well resolved broad (~70kHz) and narrow (<10kHz) proton slices corresponding to phase separated crystalline and amorphous regions. On a polyester backbone the sidechains displayed intermediate mobility, i.e. a proton linewidth of ~40kHz, indicative of a single phase of hydrocarbon chains undergoing highly ordered anisotropic motion. Finally C_{16} groups on a polyamide backbone gave rise to the superposition of an intermediate proton linewidth and a much narrower component. The authors described this system as having regions of extended and coiled chains in close spatial proximity.

These examples illustrate the strengths of the 2D WISE experiment in studying motional heterogeneity in polymers. In light of these studies it was proposed that this experiment could be used on the high surface area SAM-colloid systems, which owing to their relatively high surface areas produce 1D ^{13}C CPMAS spectra of sufficiently good signal-to noise to make 2D experiments a feasible option. The 2D WISE spectra of SAMs which will be presented and discussed in Chapters 2-4 represent the first applications of this experiment to monolayer systems. It should be noted that the motional information gathered by this approach is more qualitative in nature compared to the information which can be obtained on molecular reorientations by ^{2}H wideline NMR.[30] However ^{2}H NMR experiments have two major disadvantages compared to use of the 2D WISE experiment, namely the need to synthesize labeled samples, and the overlap which is observed in ^{2}H patterns. Use of this 2D approach separates the proton widelines according to the ^{13}C regions to which the protons cross polarize, and this separation of spectra makes interpretation more straightforward.

Dipolar filter experiment

The dipolar filter experiment exploits differences in mobility to study migration of magnetization via proton spin diffusion, giving an estimate of domain size.[31] The experiment utilizes proton multiple pulse decoupling, commonly used in CRAMPS experiments (Combined Rotation And Multiple Pulse Sequence).[32] CRAMPS is a

technique whereby one obtains "high resolution" proton spectra of solids. The rotation refers to MAS which removes chemical shift anisotropy; the multiple pulse refers to a train of closely spaced very short 90° pulses (typically ~1.5μs) which attempts to eliminate proton-proton dipolar couplings.

The effect of the 90° pulses is to place the proton magnetization on the x,y and z axes for equal periods of time. The net effect of this is to produce the same behavior as orienting the magnetization at the magic angle. since the diagonal of the cube formed by the three axes lies at the magic angle with respect to B_0 (the z axis). Thus the averaging takes place in spin space rather than in real space, i.e. involves the manipulation of the spins themselves rather than the sample, as is the case in MAS. If the CRAMPS experiment is set up correctly dipolar interactions are eliminated and transverse magnetization is retained rather than rapidly dephasing.

A similar process is used in setting up the dipolar filter experiment.[33] However in this case the pulse train consists of longer pulses (typically ~4.5μs) and longer interpulse spaces. The pulse sequence is shown in Figure 1.17. Magic angle spinning is employed.

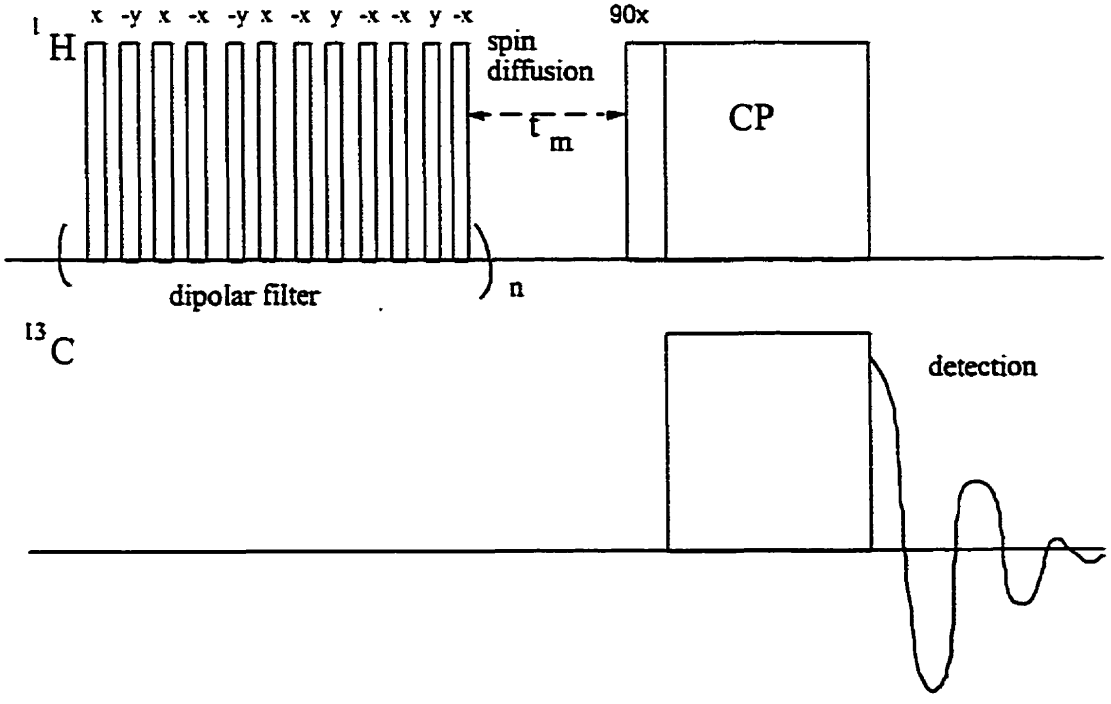

Figure 1.17 Dipolar filter pulse sequence.

In this case the pulse train tends to eliminate weak dipolar couplings but fails to remove the stronger dipolar interactions. Thus proton magnetization from mobile components is still present at the end of the filter cycle and can be cross polarized to ^{13}C. A test case consisting of a physically separated mixture of adamantane (a highly mobile species) and poly(β-hydroxybutyrate), PHB (a rigid polymer) yields the spectra shown in Figure 1.18. Clearly the use of the dipolar filter has successfully removed all peaks arising from the rigid component.

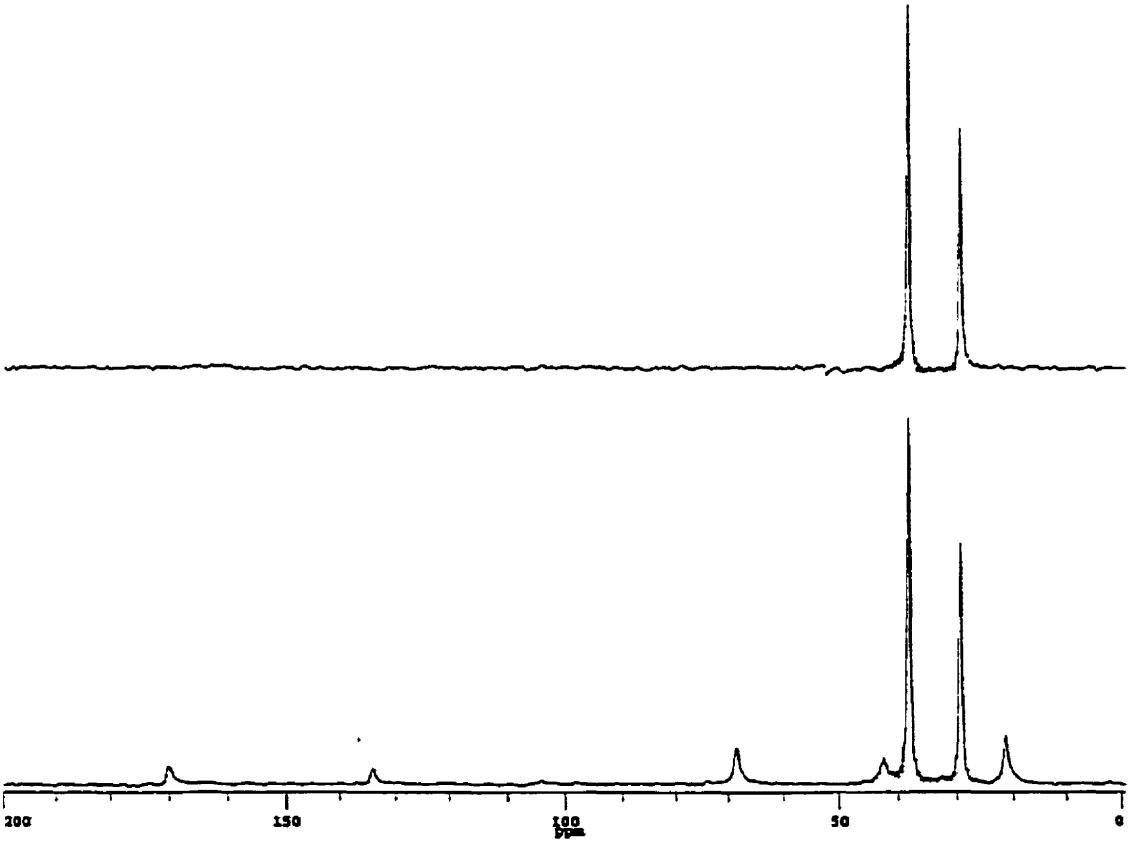

Figure 1.18 ^{13}C CPMAS spectrum (above) and dipolar filter spectrum (below) of a physical mixture of adamantane and PHB. The spectra were acquired via CP in 200 scans with a contact time of 1 ms and a recycle delay of 2 s. For the filter spectrum a filter pulse length of 4 μs, spacing of 15μs and a total of 10 filter cycles were used.

This method is employed in spin diffusion experiments in the following way. Conditions are optimized for a given sample in order to eliminate the rigid fraction (this is achieved by varying the pulse spacing). Once the amorphous component has been successfully selected, its magnetization is restored to the z axis. Spin diffusion (see Figure 1.3 in the previous section) is allowed to occur at this point for a period t_m, resulting in a redistribution of magnetization through a build up of the rigid component and concomitant decrease in the amorphous component. This is depicted in Figure 1.19, along with a schematic of the resultant NMR spectra for various mixing times.

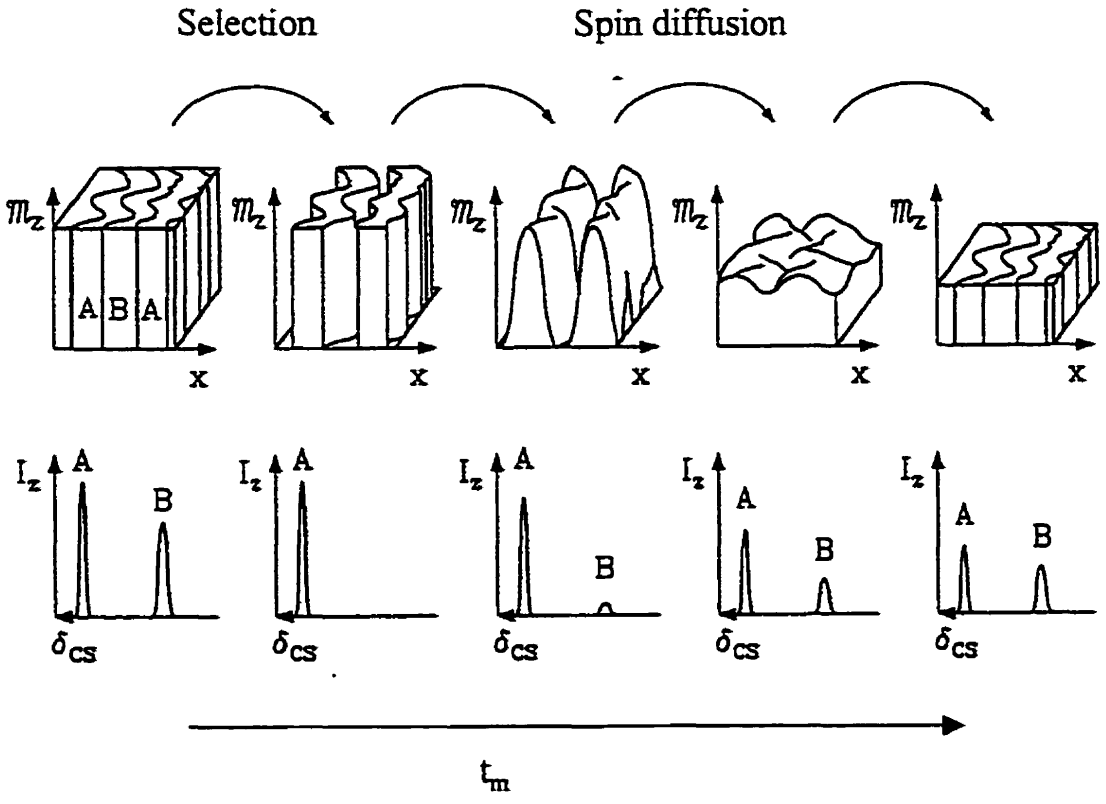

Figure 1.19 Schematic of the spin diffusion experiment and resulting NMR spectra. Adapted from reference 24.

Curves of the magnetization build up can be analyzed to extract domain sizes. However the sequence as provided fails to account for regrowth of magnetization during t_m due to T_1 relaxation rather than spin diffusion. In practice this was carried out in the

following way.[34] Firstly the application of a 180° phase correction during alternate acquisition cycles compensated for longitudinal relaxation for short mixing times. This modification also means that experiments carried out at long mixing times do not yield the CPMAS spectrum, but rather become dominated by T_1 effects so that the spectral intensities tend towards zero. In the final experiments this problem was overcome by acquiring a second set of spectra with the same mixing times, but without including the filter pulse sequence. In this way the contribution to the relaxation behavior of the system by spin-lattice behavior is ascertained, and the normalized intensity of the rigid peak of the filter experiment is divided by the corresponding intensity of the peak due to simple relaxation. This intensity is the parameter used in determining the domain size. The data arising from such experiments is analyzed according to the work by Spiess *et.al.*[27] as described in Chapter 2.

2D Exchange NMR

2D exchange NMR is an example of a 2D experiment also used to probe molecular mobility but which, in contrast to the 2D WISE experiment, contains a mixing time.[25] The pulse sequence is shown in Figure 1.20

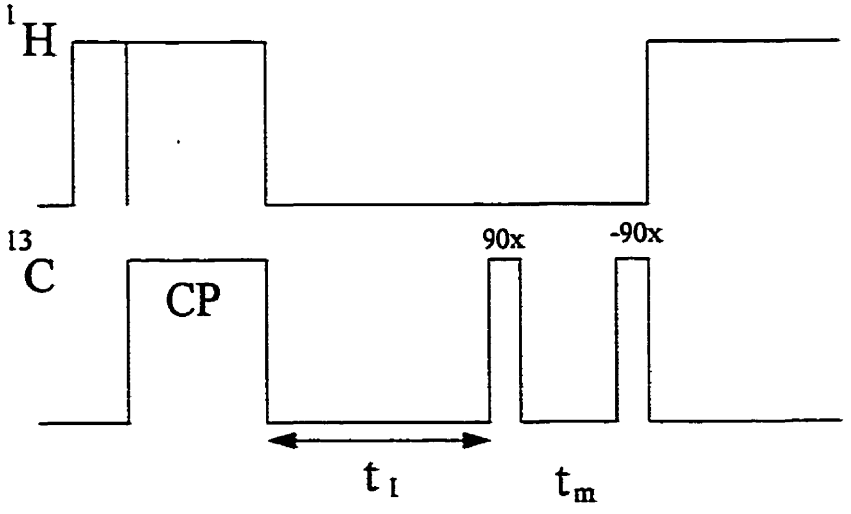

Figure 1.20 Pulse sequence for 2D exchange NMR.

The preparation period consists of cross polarization (or a simple 90° pulse); the transverse magnetization so created is permitted to precess during the evolution period at the end of which the magnetization is restored to the z axis for the mixing period. If chemical exchange occurs during the mixing time, the nuclei will find themselves in a different chemical environment which will alter their precessional frequency when another 90° pulse returns the magnetization to the transverse plane. If no exchange occurs within the mixing time, the two frequencies are equal and the 2D spectrum contains intensity only along the diagonal. If exchange does occur, the two frequencies will differ resulting in off-diagonal intensities. A useful example is provided by the case of dimethylsulfone which is known to undergo 180° flips.[35] Sample spectra are shown in Figure 1.21 for the mixing times indicated.

The nature of any off-diagonal intensities can be analyzed to give information about the type of exchange process which is occurring. 2D exchange experiments can be used to detect dynamic motion processes with correlation times in the range 10^{-5} to 10^{2} seconds[25] (the upper limit being determined by the spin lattice relaxation time). Thus slow dynamics are particularly amenable to detection by this technique.

Selective pulse excitation

As part of the investigation into the nature of the interaction between a gold nanoparticle surface and the sulfur headgroup of an alkanethiol it was necessary to find a method with which to distinguish between a homogeneous and inhomogeneous lineshape.[36] A homogeneous line is the sum of individual resonances which possess the same lifetime broadening ($1/T_2$) and which all have the same chemical shift. An example in the solid state would be that of a proton line where the spins in the sample are strongly coupled via dipolar interactions rendering the individual protons indistinguishable (see Figure 1.22 a). In contrast an inhomogeneous line consists of a superposition of non-overlapping individual resonances. As a result the linewidth is determined by a distribution of shifts. There is no coupling between individual resonances (see Figure 1.22 b).

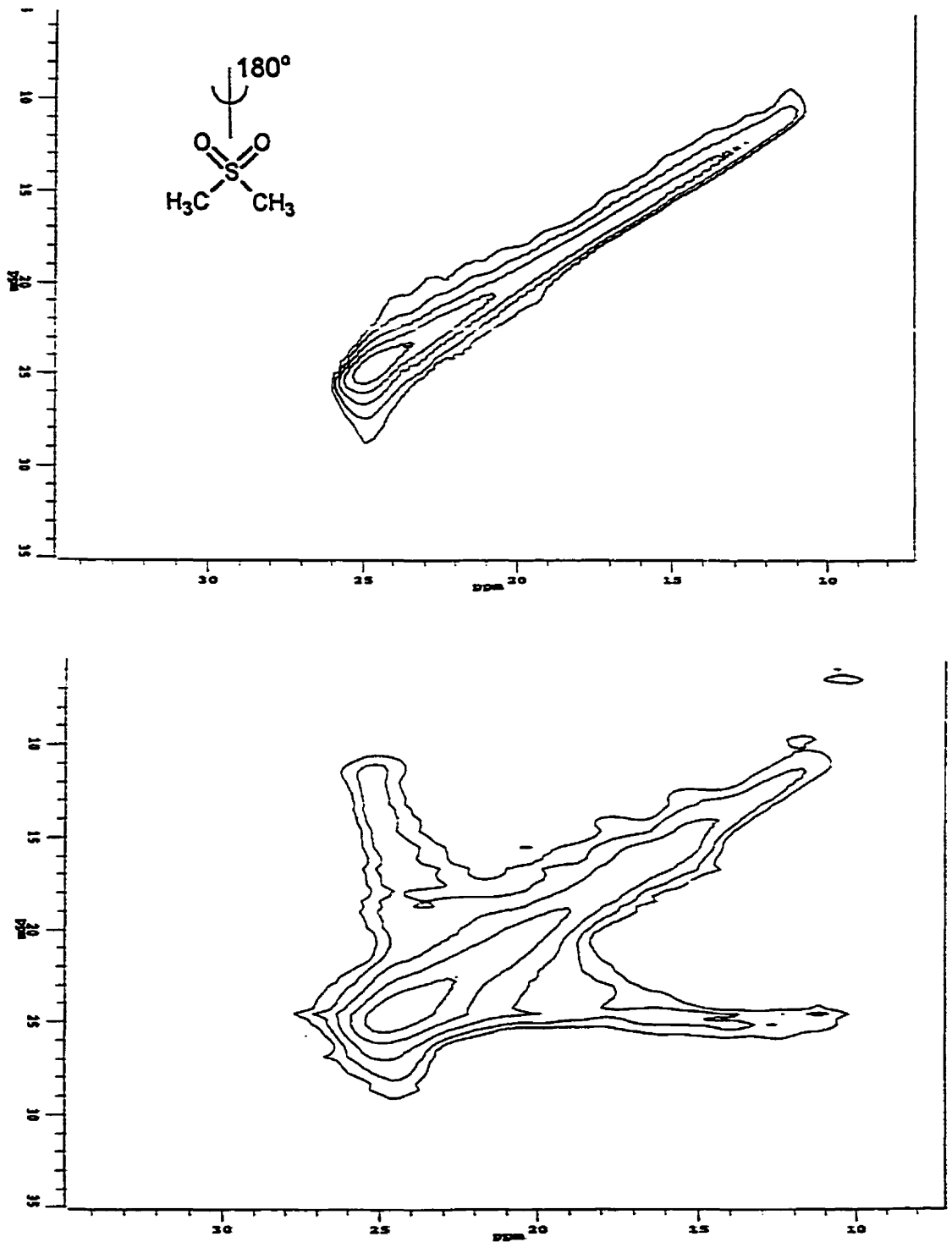

Figure 1.21 2D exchange spectra of dimethylsulfone with mixing times of 10ms (above) and 500ms (below). Spectra were acquired via CP preparation with a contact time of 3 ms, a recycle time of 3 s and 16 scans. The evolution period consisted of 64 increments of 50μs.

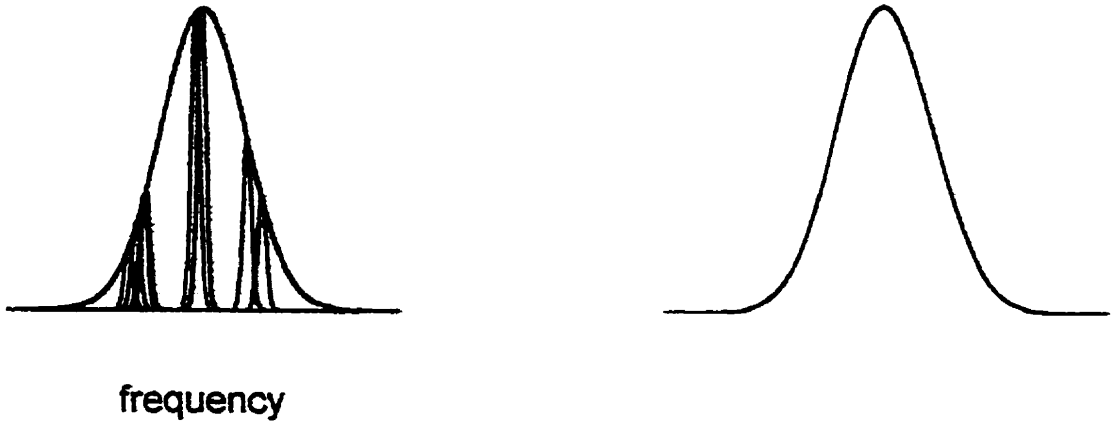

Figure 1.22 Depiction of (left) inhomogeneous and (right) homogeneous lineshapes. A representative example of the latter is a proton lineshape in the solid state (c.f. Figure 1.2d), a representative example of the former is a CSA powder pattern (c.f. Figure 1.4).

Application of a irradiating RF field at any single frequency within a homogeneous line will result in a decrease in intensity of the entire lineshape. In contrast irradiating a single frequency within an inhomogeneous lineshape will burn a hole in the lineshape. In practice there are two alternative methods for irradiation at a single frequency. The first is by application of a low power "soft pulse". If the pulse width is denoted by t_p, the range of frequencies that will be affected is $\pm 1/t_p$. This requires long pulses and instrument stability during the course of the pulse can be a problem. An alternative which uses a series of hard pulses, called the DANTE (Delays Alternating with Nutation for Tailored Excitation) sequence has been developed.[37] The pulse sequence is shown in Figure 1.23

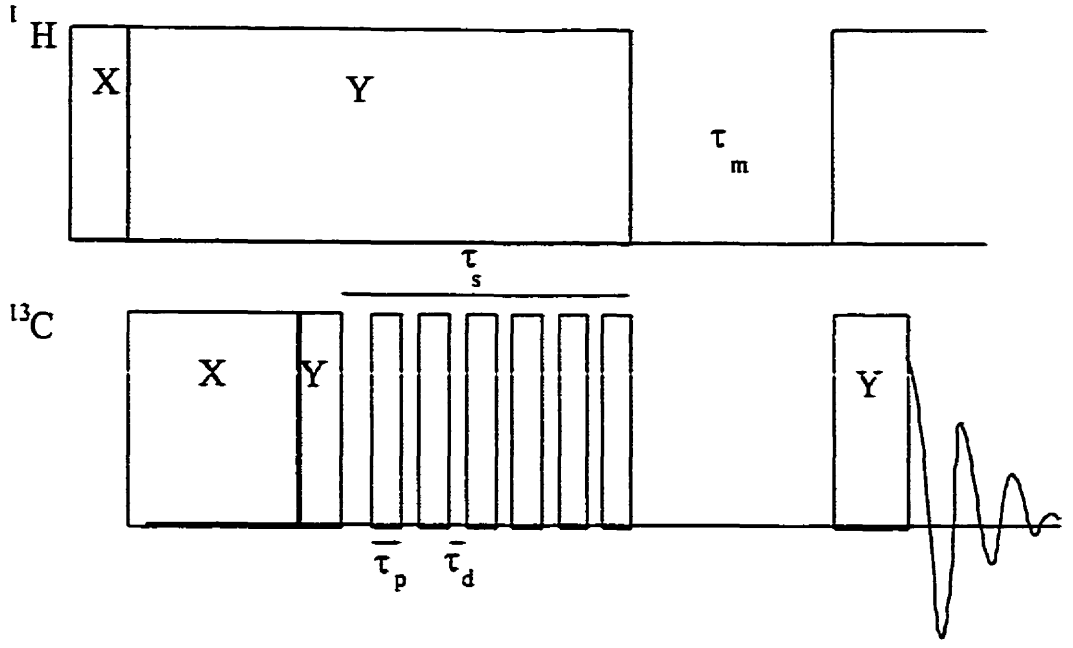

Figure 1.23 DANTE pulse sequence, t_p is the DANTE pulse width, and t_d is the pulse spacing. The pulse sequence may include a mixing time which can be used to observe the regrowth of intensity if exchange takes place.

The repetition of a number of pulses of identical phase (e.g. x) and small flip angle exerts a strong cumulative effect on those nuclei in resonance with the transmitter frequency. This is because, by definition, in the rotating frame the on-resonance nuclei do not precess during the spaces between pulses, but remain in the yz plane. Nuclei that are off-resonance will precess in the rotating frame during the interpulse periods. Thus all off-resonance magnetizations will precess away from the yz plane and consequently the successive pulses will be applied at ever changing phases of precession. As an illustrative example, consider the case of a nucleus which is off-resonance such that it precesses by 180° around the z axis after the initial pulse. On application of the second pulse, the magnetization will be rotated back onto the z axis. The net effect is to leave this nucleus unaffected by the pulses. In summary, at the end of the DANTE sequence, the on-resonance nuclei will lie along the +y axis and off-resonance nuclei will remain at or near the +z axis. The final read pulse rotates the off-resonance nuclei onto the +y axis and the

on-resonance nuclei to the -z axis. Subsequent acquisition of the FID will detect only the off-resonance nuclei. An example spectrum is shown in Figure 1.24.

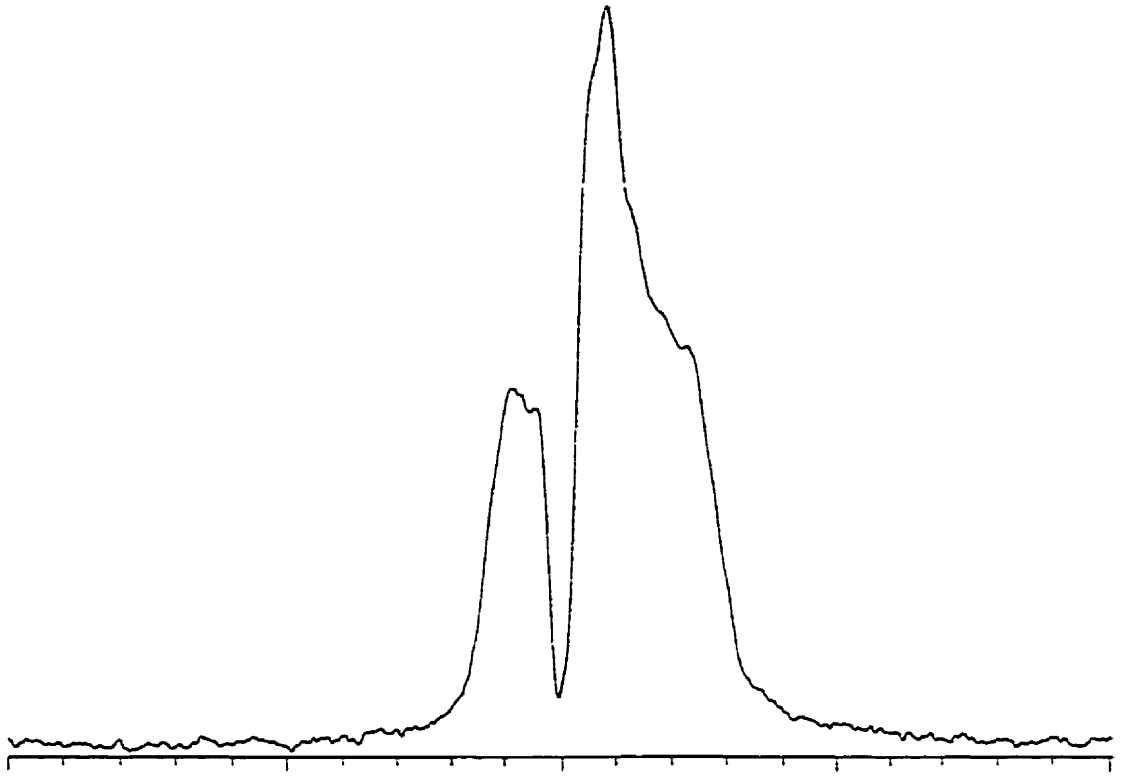

Figure 1.24 ^{31}P DANTE holeburning spectrum of a static sample of chirophos (bis(diphenylphosphinobutane). The spectrum was acquired via CP detection in 16 scans with a contact time of 2 ms and a pulse delay of 5 s. The selective DANTE pulse train consisted of pulses of 0.7 μs at a spacing of 10 kHz.

1.5 Infrared spectroscopy

The majority of work discussed here concerns the use of NMR techniques. However since previous literature on SAMs has made extensive use of vibrational spectroscopy, some infra-red experiments have been carried out and their results will be

discussed in conjunction with the NMR studies. Like ^{13}C solid state NMR, IR spectra in this region offer useful information about the conformation of methylene chains.[38]

Infrared spectroscopy involves the study of the characteristic stretching vibration frequencies of inter-atomic bonds. For the purpose of most of the systems to be investigated here the principle region of interest is the C-H stretching region around 3000 cm^{-1} due to the hydrocarbon chains of the SAMs. CH_2 groups in hydrocarbon chains exhibit two infrared bands corresponding to symmetric and asymmetric stretching vibrations of the C-H bonds.[39] The frequencies and band widths of these vibrations are higher for disordered, liquid-like chains. Representative values for crystalline (all-trans) and amorphous chains are given in Table 1.1. Clearly these can be used to study chain order in thin films, experimentally this approach is most popular for species deposited on planar substrates. The results presented for SAMs on particulate substrates are similar to those seen for planar SAMs. The limitations of infrared spectroscopy as a probe of mobility and defects in monolayers as compared with ^{13}C will be discussed in Chapters 2-4.

Chain environment	Symmetric stretching		Asymmetric stretching	
	Frequency (cm^{-1})	Width (cm^{-1})	Frequency (cm^{-1})	Width (cm^{-1})
Ordered solid	2849	10	2917	15
Disordered (liquid-like)	2856	18	2928	26

Table 1.1 Characteristic stretching frequencies for methylene C-H bonds in different environments.

Due to skeletal vibrations in the substrates, only a limited amount of information can be gathered from the region between 1000 and 1200 cm^{-1}, precluding observation of most of the headgroups of the SAMs and the effects of their interaction with the oxide

surfaces. Additional information about chain dynamics has been obtained in some instances by variable temperature infrared spectroscopy.

1.6 Experimental

1.6.1 Referencing of CPMAS and optimization of CP conditions

All CPMAS experiments were carried out on a Chemagnetics CMX-270 NMR spectrometer with a 7 mm double-tuned fast-MAS Doty probe. The probe was shimmed by observing the proton spectrum of acetone to minimize linewidth and give a symmetric signal. The 67.92-MHz ^{13}C spectra were referenced by a hexamethylbenzene sample, where the methyl peak is known to be resonant at 17.3 ppm. The same sample was used to optimize the ^{1}H-^{13}C cross-polarization by adjusting the power levels to achieve the Hartmann-Hahn match at 60 kHz and also to set the magic angle. 109-MHz ^{31}P spectra were referenced to chirophos: bis(diphenylphosphino)butane, where the upfield peak is set at -13.0 ppm. 53.66-MHz ^{29}Si spectra were referenced to the single silicon peak of the sodium salt of 3-(trimethylsilyl)-1-propane-sulfonic acid, which appears at 0 ppm. Proton 90° pulse widths were between 3.5 and 4.5 μs and unless otherwise stated, contact times of 3 ms were used. Samples were spun at 3.5-5 kHz. The pulse delay also depends on the relaxation times of the sample and must be chosen to be sufficient to allow return to equilibrium magnetization. Generally delays of several times the T_1 value are used. The dwell time is the time between the sample points of the FID and is equal to the inverse of the spectral width. These values depend on the T_2 of the sample (i.e. in a rapid decay points must be acquired more frequently in order to adequately characterize the FID) and must be chosen to give a wide enough spectral width to include all expected signals.

1.6.2 Variable temperature probe calibration

For the variable temperature CPMAS experiments the sample temperature was controlled to within +/- 2°C by a Chemagnetics temperature controller which heated the bearing air, and a variac which heated the drive air (and whose setting was monitored by

a resistance meter). Temperature calibration of the probe was carried out using a sample of ethylene glycol added to TTMSS (tetrakis(trimethylsilyl)silane) to allow MAS.[40] Ethylene glycol gives two proton signals whose separation is related to temperature as described in reference 36. A series of plots of actual temperature vs. thermocouple temperature for different levels of drive heating were produced allowing acquisition of CPMAS spectra between room temperature and 170°C. Temperatures were accurate to ±2°C.

1.6.3 Processing of 2D data (WISE and exchange experiments)

It is well known that 2D data sets are only amplitude modulated in t_1, and thus produce spectra which are phase twisted.[41] The phase problems are eliminated by processing in the following manner: a complex Fourier transform is applied to the data in t_2. The imaginary data is then zeroed and the data in the t_1 dimension is complex Fourier transformed. The effect of this processing is to symmeterize the proton lineshapes (or exchange spectra), however this approach is valid since the lineshapes are already symmetric.

1.6.4 Vibrational spectroscopy.

Samples for infrared analysis were prepared by dispersing the modified metal oxide into a KBr pellet. Data were collected on a Bruker IFS-48 Fourier transform spectrometer equipped with an A590 microscope and operated at 0.5 cm^{-1} nominal resolution.

References

[1] Ulman, A., *Chem.Rev.*, **1996**, *96*, 1533

[2] Bishop, A.R.; Nuzzo, R.G., *Curr.Opin.Colloid Interface Sci.*, **1996**, *1*, 127

[3] Ulman, A., *Introduction to Organic Thin Films*, **1991**, Acedemic Press.

[4] Ulman, A., *Adv.Mat*, **1991**, *3*, 298

[5] Swalen, J.D.; Allara, D.L.; Andrade, J.D.; Chandross, E.A.; Garoff, S.; Ishraelachvili, J.; McCarthy, T.J.; Pease, R.F.; Rabolt, J.F.; Wynne, K.J.; Yu, H., *Langmuir*, **1987**, *3*, 932

[6] Gaines, G.L.; *Insoluble monolayers Liquid-Gas Interfaces*, **1966** Interscience

[7] Reven, L.; Dickinson, L., *Thin Films*, **1998**, *24*, 149

[8] (a) Engelhart, G.; Michel, D., *High Resolution Solid-State NMR of Silicates and Zeolites*, **1987**, Wiley (b) Reven, L., *J.Mol.Catal.*, **1994**, *86*, 447

[9] Albert, K.; Bayer, E., *J.Chromatogr.*, **1991**, *544*, 345

[10] Blum, F.D., *Ann.Rep.Spectros.*, **1994**, *28*, 278

[11] Badia, A.; Demers, L.; Dickinson, L.; Morin, F.G.; Lennox, R.B.; Reven, L., *J.Am.Chem.Soc.*, **1997**, *119*, 11104

[12] McGovern, M.E.; Kallury, K.M.R., Thompson, M., *Langmuir*, **1994**, *10*, 3607

[13] Pake, G.E., *J.Chem.Phys.*, **1948**, *16*, 327

[14] Pines, A.; Gibby, M.G.; Waugh, J.S., *Chem.Phys.Lett.*, **1972**, *15*, 373

[15] Andrew, E.R.; Bradbury, A.; Eades, R.G., *Nature*, **1958**, *182*, 1659

[16] Stejskal, E.O.; Memory, J.D., *High Resolution NMR in the Solid State: Fundamentals of CP/MAS*, **1994**, Oxford University Press

[17] Reven, L., Solid-State NMR course 655, Class notes

[18] Herzfeld, J.;Berger, A.E., *J.Phys.Chem.*, **1980**, *73*, 6021

[19] Gerstien, B.C.; Dybowski, C.R., *Transient Techniques in NMR of Solids*, **1985**, Acedemic Press.

[20] Komoroski, R. A., *High Resolution NMR Spectroscopy of Synthetic Polymers in Bulk.*

[21] Cowan, B., *Nuclear Magnetic Resonance and Relaxation*, **1997**, Cambridge Univ. Press

[22] Hartmann, S.R.; Hahn, E.L., *Phys.Rev.*, **1962**, *128*, 2042

[23] Alemany, L.B.; Grant, D.M.; Pugmire, R.J.; Alger, T.D.; Zilm, K.W., *J.Am.Chem.Soc.*, **1983**, *105*, 2133

[24] Schmidt-Rohr, K.; Spiess, H.W., *Multidimensional Solid-State NMR and Polymers*, **1994**, Acedemic Press.

[25] Jeener, J.; Meier, B.H.; Bachmann, T.; Ernst, E., *J.Phys.Chem.*, **1979**, *71*, 4546

[26] Caravatti, P.; Neuenscwander, P.; Ernst, R.R., *Macromolecules*, **1985**, *18*, 119

[27] Schmidt-Rohr, K.; Clauss, J.; Spiess, H.W., *Macromolecules*, **1992**, *25*, 3273

[28] Earl, W.L; VanderHart, D.L., *Macromolecules*, **1979**, *12*, 762

[29] Clauss, J.; Schmidt-Rohr, K.; Adam, A.; Boeffel, C.; Spiess, H.W., *Macromolecules*, **1992**, *25*, 5208

[30] Chmelka, B.F.; Schmidt-Rohr, K.; Speiss, H.W., in *Nuclear Magnetic Resonance Probes of Molecular Dynamics*, **1996**, ed. Tycko, R: Kluwer Press

[31] Clauss, J.; Schmidt-Rohr, K.; Spiess, H.W., *Acta Polymer.*, **1993**, *44*, 1

[32] Clauss, J.; Schmidt-Rohr, K.; Bluemich, B.; Spiess, H.W., *Magn.Res.in Chem.*, **1990**, *28*, 3

[33] Clauss, J.; Schmidt-Rohr, K.; Bluemich, B.; Spiess, H.W., *Macromolecules*, **1992**, *25*, 172

[34] Landfester, K.; Boeffel, C.; Lambla, M.; Spiess, H.W., *Macromolecules*, **1996**, *29*, 5972

[35] Solum, M.; Zilm, K.W.; Michl, J.; Grant, D.M., *J.Phys.Chem.*, **1983**, *87*, 2940

[36] Fyfe, C.A., *Solid-State NMR For Chemists*, **1983**, C.F.C Press

[37] Caravatti, P; Levitt, M.H.; Ernst, R.R., *J.Magn.Reson.* **1986**, *68*, 323

[38] Tripp, C.P.; Hair, M.L., *Langmuir*, **1992**, *8*, 1120

[39] Snyder, R.G.; Strauss, H.L.; Elliger, C.A., *J.Phys.Chem.*, **1982**, *86*, 5145

[40] Raiford, D.S.; Fisk, C.L.; Becker, E.D., *Anal.Chem.*, **1979**, *51*, 2050

[41] Bax, A., *Two-Dimensional Nuclear Magnetic Resonance in Liquids*, **1984**, Delft Univ. Press

Chapter Two- Dynamic Properties and Crosslinking of Alkylsiloxane Monolayers Investigated by Solid State NMR

2.1 Introduction

Alkylsiloxane self-assembled monolayers (SAMs) are widely used to hydrophobicize and functionalize metal oxide surfaces[1] and for applications such as microcontact printing.[2] Despite the problems associated with reproducibility of high quality monolayers, alkylsiloxane SAMs remain popular due to their relatively high thermal stability compared with alkanethiol or long chain organic acid monolayers. As a consequence, numerous studies concerning the influence of water and temperature on structural properties have been carried out. Well ordered monolayers are produced below a chain length dependent threshold temperature due to an increasing surface coverage with decreasing temperature.[3] Several studies have shown that decoupling of the film from the substrate by surface hydration is required to minimize gauche defects.[3,4] Sufficient water to hydrate the silica surface is necessary, but excess water will lead to uncontrolled polymerization. Scanning probe microscopy shows that the alkylsiloxane monolayers have an island structure[5] and several groups have taken advantage of this morphology in order to synthesize phase separated mixed monolayers.[6] Whereas some studies assert that curing stabilizes the monolayer,[7] a recent scanning force microscopy study indicates that above a chain length dependent temperature (155°C for OTS-octadecyltrichlorosilane), the surface roughness irreversibly increases.[8] In this study, the authors proposed that the permanent structural changes in the monolayer, which is connected to the substrate by a limited number of Si-O-Si linkages, occurs through thermal hydrolysis of Si-O-Si bonds, allowing the monolayer to break up or fold back on itself. The chain length dependence of the structural transition temperature indicates that the rearrangement of the siloxane network may occur following or simultaneously with a loss of chain order.

The effects of solvent on monolayer quality have also been studied. It has been proposed that long chain hydrocarbons appear to intercalate into the OTS chains in a rod-

like manner, and are more easily replaced by subsequent OTS attachment to the substrate, so that longer chain solvents produce better ordered layers.[9] However, another study[10] indicated that the principle observed solvent effect involves the water extraction ability of the solvent. It is believed that the best results are obtained where the solvent extracts sufficient surface water from the substrate to hydrolyze the OTS in solution, promoting attachment to the silica surface. If the extraction is too great, this will cause polymerization in solution, lowering film density. In accordance with these literature findings, we have used toluene in production of our SAMs.

Based on the vibrational spectra, the long chain alkylsiloxane monolayers on silica have been generally described as crystalline although this technique probes only the conformational order and does not give direct information about the chain mobility. In actuality, very little is known about the dynamic properties of alkylsiloxane SAMs. As will be shown in Chapters 3 and 4, we used solid-state NMR spectroscopy to characterize the structural and dynamic properties of phosphonate[11,12] and alkanethiol[13] monolayers. For these two systems, we showed that the chains are not crystallized in the classical sense and the conformationally ordered, but motionally disordered, chains undergo chain length dependent, reversible order-disorder transitions. In the alkanethiol and phosphonate monolayers, the free volume available for thermal disordering is provided by the large size of the headgroup combined with the effects of surface roughness of the substrate. Head group size is known to affect hydrocarbon chain crystallinity in such samples. In the thiols, for example, the size of the sulfur atom is large enough to cause significant chain tilting.[13] A silicon atom head group is much smaller and a large mismatch is not predicted. Literature values[1b] suggest a Si-O-Si distance of around 4.4Å and no significant chain tilting. However it should also be noted that the alkylsiloxane monolayers are decoupled from the substrate and the final structure and dynamic properties of alkylsiloxane monolayers should depend more on the nature of the siloxane network rather than the underlying substrate. In spite of the importance of this structural feature, the actual degree of crosslinking in alkylsiloxane monolayers has not been directly characterized.

In a prior study by this laboratory, the ^{13}C NMR and infrared spectra of a partial OTS monolayers on fumed silica as well as bulk polymerized OTS were reported.[14] This study confirmed the island morphology of the monolayers as well as the temperature dependence of the film formation. In order to determine the extent of crosslinking, as well as investigate the chain dynamics, partial monolayers of OTS on nonporous silica monospheres with a high enough coverage for ^{29}Si and 2D solid state NMR experiments have been prepared. The ^{13}C solid state NMR spectra, detected by both direct and cross polarization, shows that this sample consists of domains of motionally restricted ordered chains and highly mobile disordered chains. Comparison of the dynamic behavior of monolayers of OTS on silica with that of the bulk polymerized OTS demonstrates that the room temperature chain dynamics of the ordered regions of the OTS monolayer are similar to the other types of self-assembled monolayers. Whereas a sharp transition due to chain melting is observed in the bulk polymerized OTS, the ordered regions in the monolayer disorder more gradually at higher temperatures. With regard to the degree of crosslinking, the ^{29}Si NMR spectra of the monolayer indicates that it contains mostly $RSiOH(OSi)_2$ linkages. This network is closer to that of the bulk polymerized OTS sample which was produced by rapid hydrolysis.

2.2 Synthesis

Silica R100 monospheres (Merck) were hydrated and calcined at 380 °C in air, degassed at 60 °C for 2 hours, mixed with toluene, sonicated and reacted with 1.5-2 ml OTS in a N_2 atmosphere. The reaction was carried out for 12 hours at 0 °C. From the elemental analysis the coverage is estimated to be 40%. Two samples of bulk OTS polymer were produced, one by slow hydrolysis by atmospheric water. The second sample was produced by rapid hydrolysis with excess water at 0 °C.

2.3 Results

2.3.1 Powder X-ray diffraction.

The poly(octadecylsesquisiloxane) produced by hydrolysis of OTS is believed to be a comb polymer with a lamellar structure.[15] The powder X-ray diffraction spectrum of the slowly hydrolyzed sample, shown in Figure 2.1, displays several even reflection lines in the low angle region ($2\theta < 15°$), typical of lamellar long-chain compounds.[16]

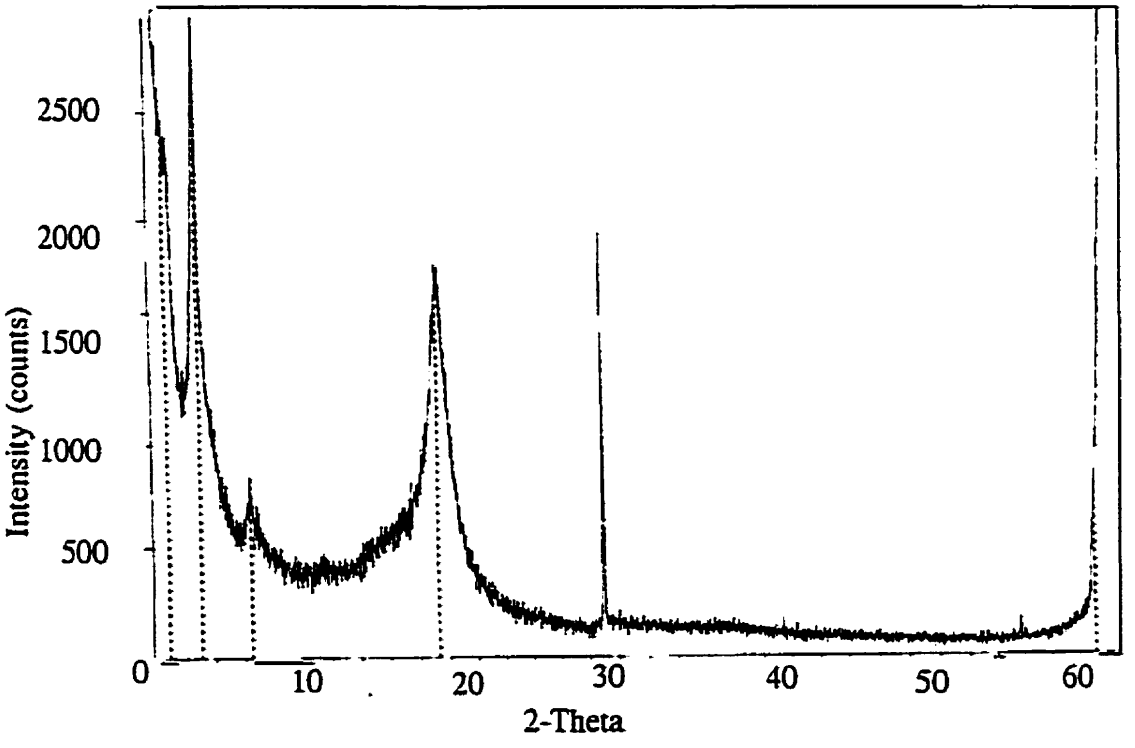

Figure 2.1 Powder X-ray diffraction pattern of slowly hydrolysed OTS polymer sample.

Analysis of the pattern, assumed to be due to the 0k0 progression, yielded a value of 52 Å for the interlayer distance. This value is close to that expected for extended all trans C_{18} chains, indicating that the chains are not interdigitated or greatly tilted. It

should be noted that in another study[17], in which a bulk polymer was produced by rapid hydrolysis of OTS at 5°C, followed by adjustment to neutral pH and vacuum drying, only a single peak was observed in the wide angle X-ray diffraction spectrum. This was fit to give a Bragg plane separation of 48.17Å, a value which is comparable with ours.

2.3.2 ^{29}Si Solid State NMR.

In Figure 2.2, the ^{29}Si CPMAS NMR spectra of the OTS monolayer and two polymer samples are shown.

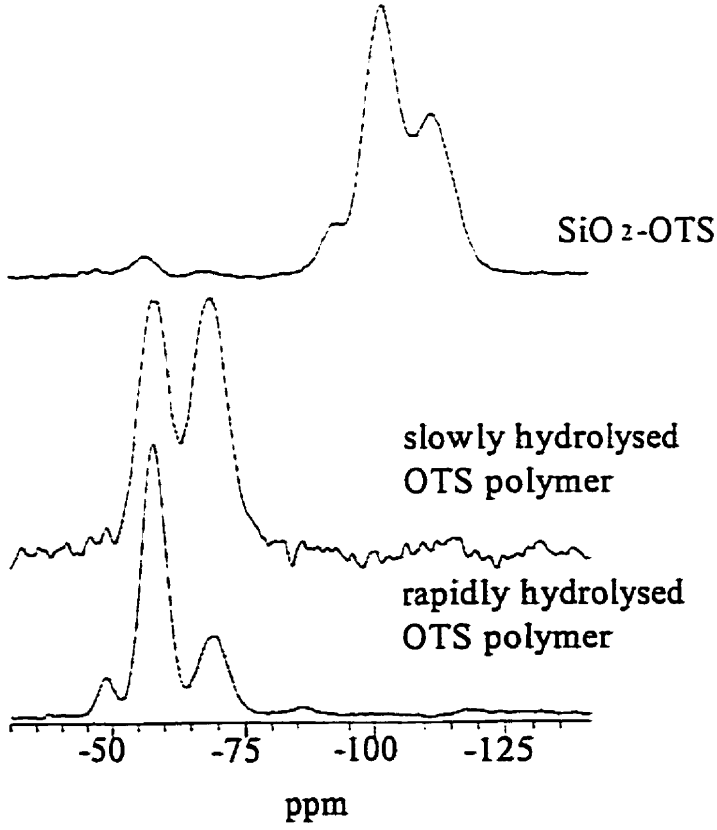

Figure 2.2 ^{29}Si CPMAS spectra of SiO_2-OTS monolayer and bulk OTS polymer samples as indicated. The spectrum of the monolayer was acquired in 10000 scans with a contact time of 4 ms and a recycle time of 5 s. The bulk polymer samples required 2000 scans with a contact time of 3 ms and recycle time of 3 s.

The monolayer sample has very strong peaks at -92 ppm, -102 ppm and -111 ppm corresponding to the geminal (Q_2), silanol (Q_3) and siloxane (Q_4) groups of the bulk silica substrate.[18] Only one peak arising from the silane is visible at ~ -56 ppm. This resonance, assigned to the R-Si(OH)(O-)$_2$ crosslinked species (T_2), also dominates the spectrum of the rapidly hydrolyzed polymer sample. The slowly hydrolyzed polymer sample displays an equally intense peak at -68.3 ppm assigned to the R-Si(O-)$_3$ species (T_3). Smaller peaks at -49 ppm for the R-Si(OH)$_2$(O-) species (T_1) and -68 ppm for R-Si(O-)$_3$ are also present at much lower intensity in the spectrum of the rapidly hydrolyzed polymer but are absent or are too weak to be visible in the spectrum of the OTS monolayer.

2.3.3 ^{13}C Variable Temperature CP MAS NMR.

The variable temperature ^{13}C CP and single pulse with proton decoupling MAS NMR spectra of the two polymer samples and the OTS monolayer are shown in Figures 2.3, 2.4 and 2.5. Although the extent of crosslinking differs, the cross polarized spectra of both OTS polymer samples exhibit a strong, narrow peak at 33.5 ppm for methylenes in an all trans conformation, suggesting a highly ordered packing environment. The monolayer sample also contains a significant component at 30.7 ppm corresponding to gauchoid chain segments. The cross polarization experiment selectively enhances the signal of the motionally restricted transoid chain segments in the monolayer sample. Variable contact measurements show that the 30.7 ppm component has a much longer cross polarization time requirement than the transoid chain signal at 33.5 ppm and is therefore revealed more clearly by the single pulse, proton decoupled spectrum. The single pulse sequence also reveals small disordered regions in both of the bulk polymer samples, although in the slowly hydrolyzed sample this component is quite small.

Both the cross polarization and single pulse sequences were used to monitor the changes of chain conformation with temperature. The bulk polymer samples undergo an abrupt chain melting which is manifested as a sudden deterioration in the CPMAS spectrum at ~ 70 °C as the chains become too mobile for efficient cross polarization. The

rapidly hydrolysed sample was also difficult to spin at high temperatures, so the spectra could only be recorded up to 80°C. Above 70 °C, the single pulse ^{13}C spectrum reveals a liquid like spectrum with the inner methylenes shifted to 30 ppm. This chain melting is also detected by differential scanning calorimetry (DSC), shown in Figure 2.6.

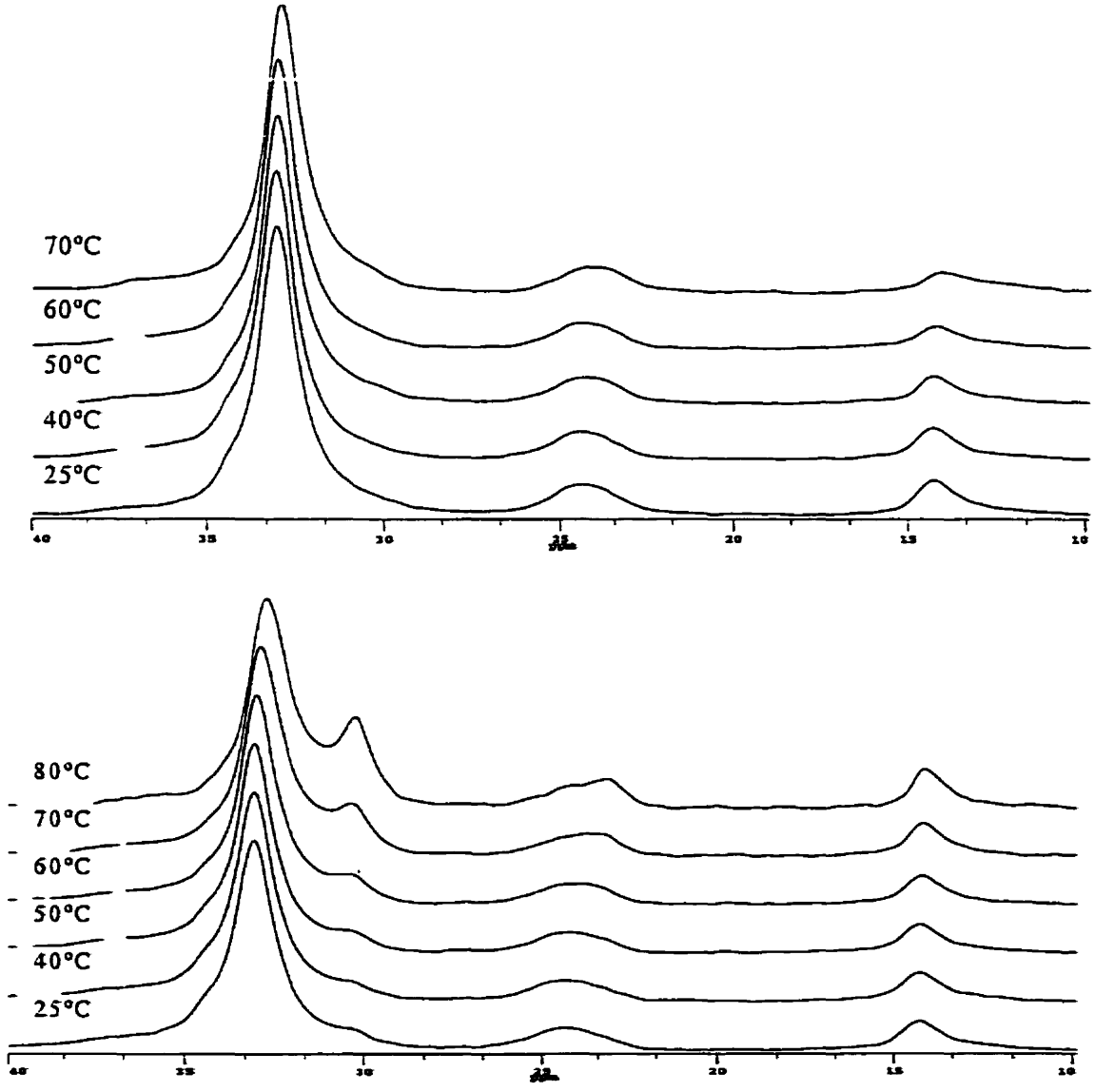

Figure 2.3 Variable temperature ^{13}C CPMAS (above) and single pulse (below) spectra of rapidly hydrolysed OTS at the temperatures indicated. CPMAS spectra were acquired in 40 scans where ct=3ms and pd=3s. Direct ^{13}C polarized spectra used a recycle time of 5 s and 200 scans.

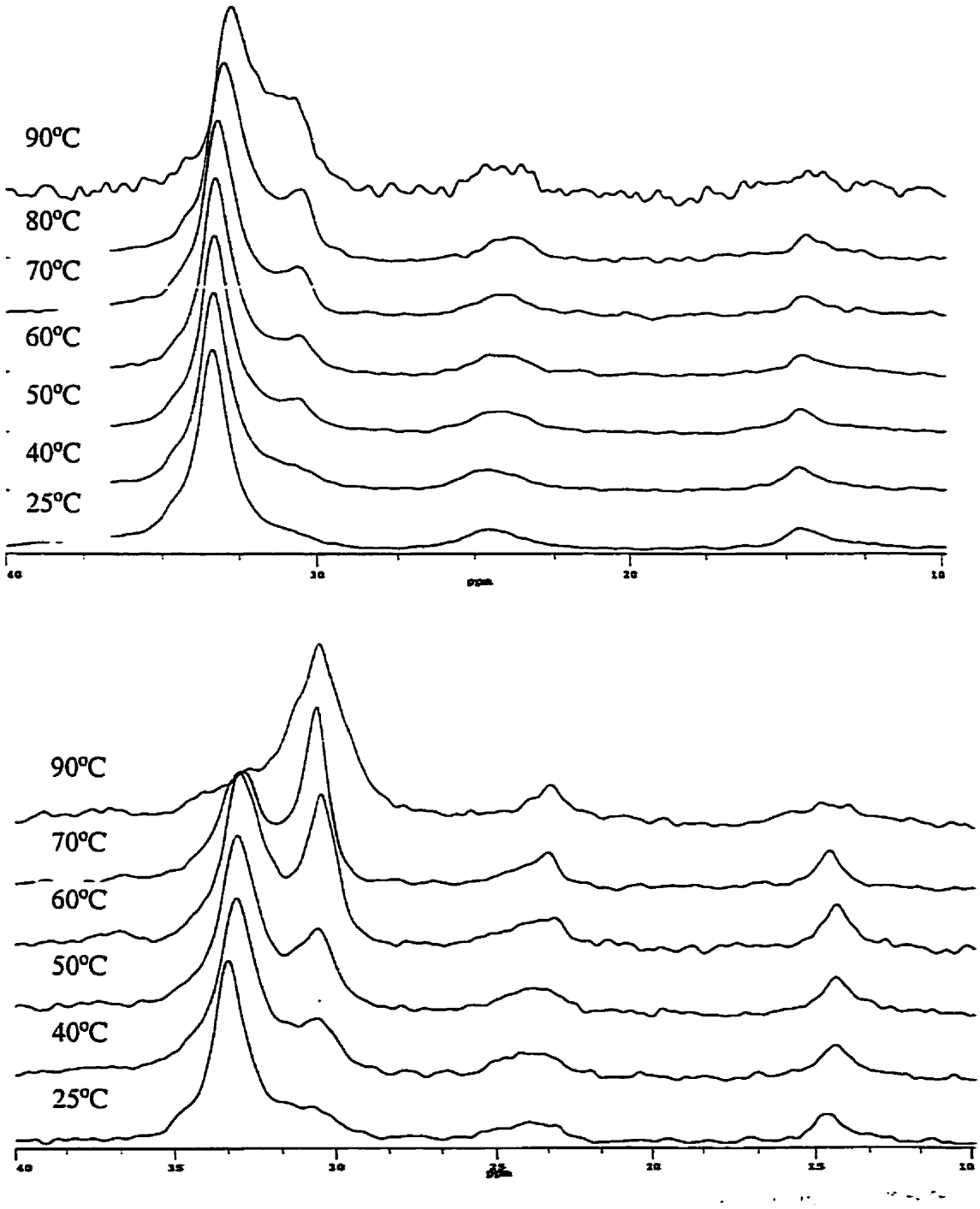

Figure 2.4 Variable temperature ^{13}C CPMAS (above) and single pulse (below) spectra of slowly hydrolysed OTS at the temperatures indicated. CPMAS spectra were acquired in 200 scans where ct=3ms and pd=3s. Direct ^{13}C polarized spectra used a recycle time of 5 s and 200 scans.

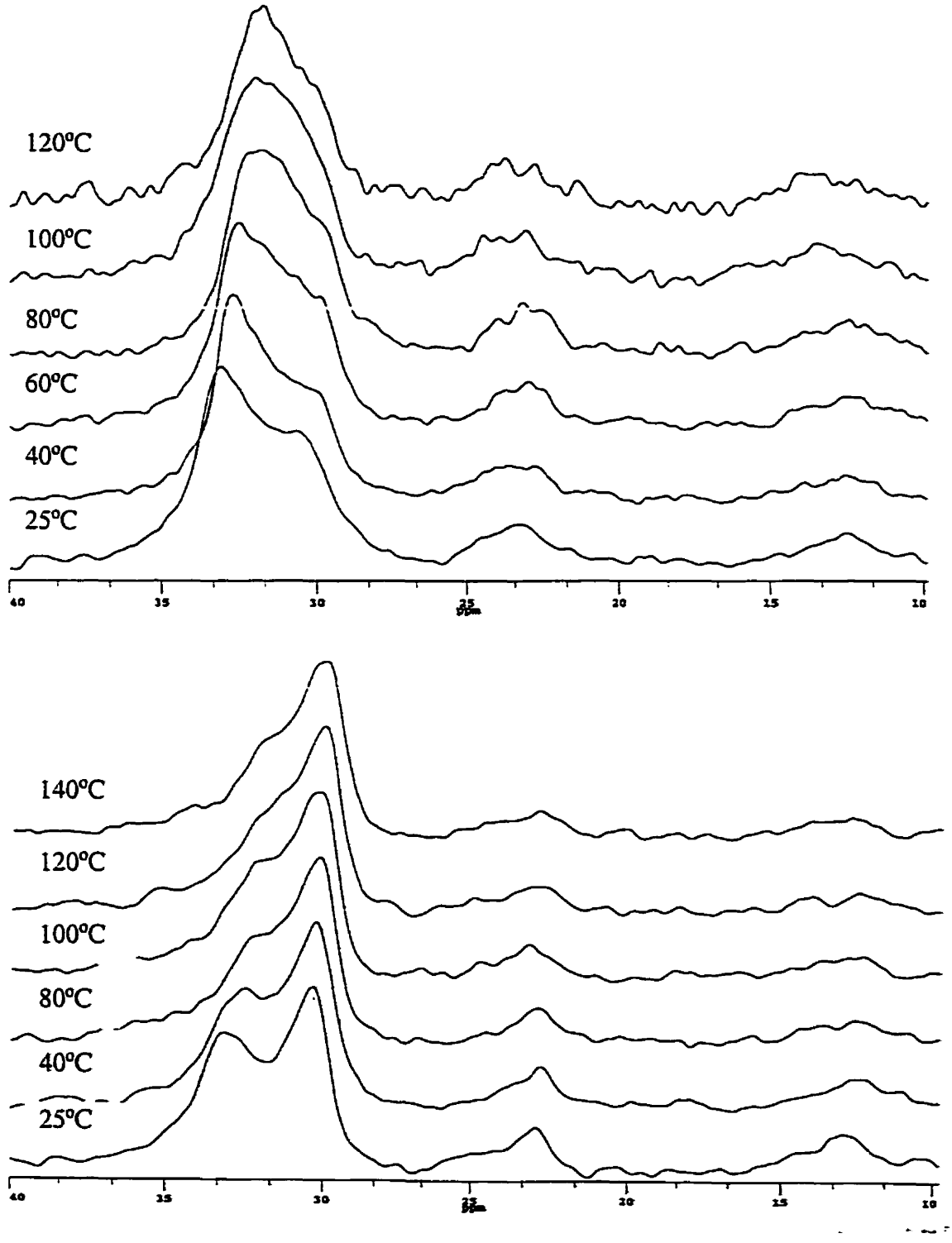

Figure 2.5 Variable temperature ^{13}C CPMAS (above) and single pulse (below) spectra of SiO_2-OTS at the temperatures indicated. CPMAS spectra were acquired in 1000 scans where ct=3ms and pd=3s. Direct ^{13}C polarized spectra used a recycle time of 3s and 1300 scans.

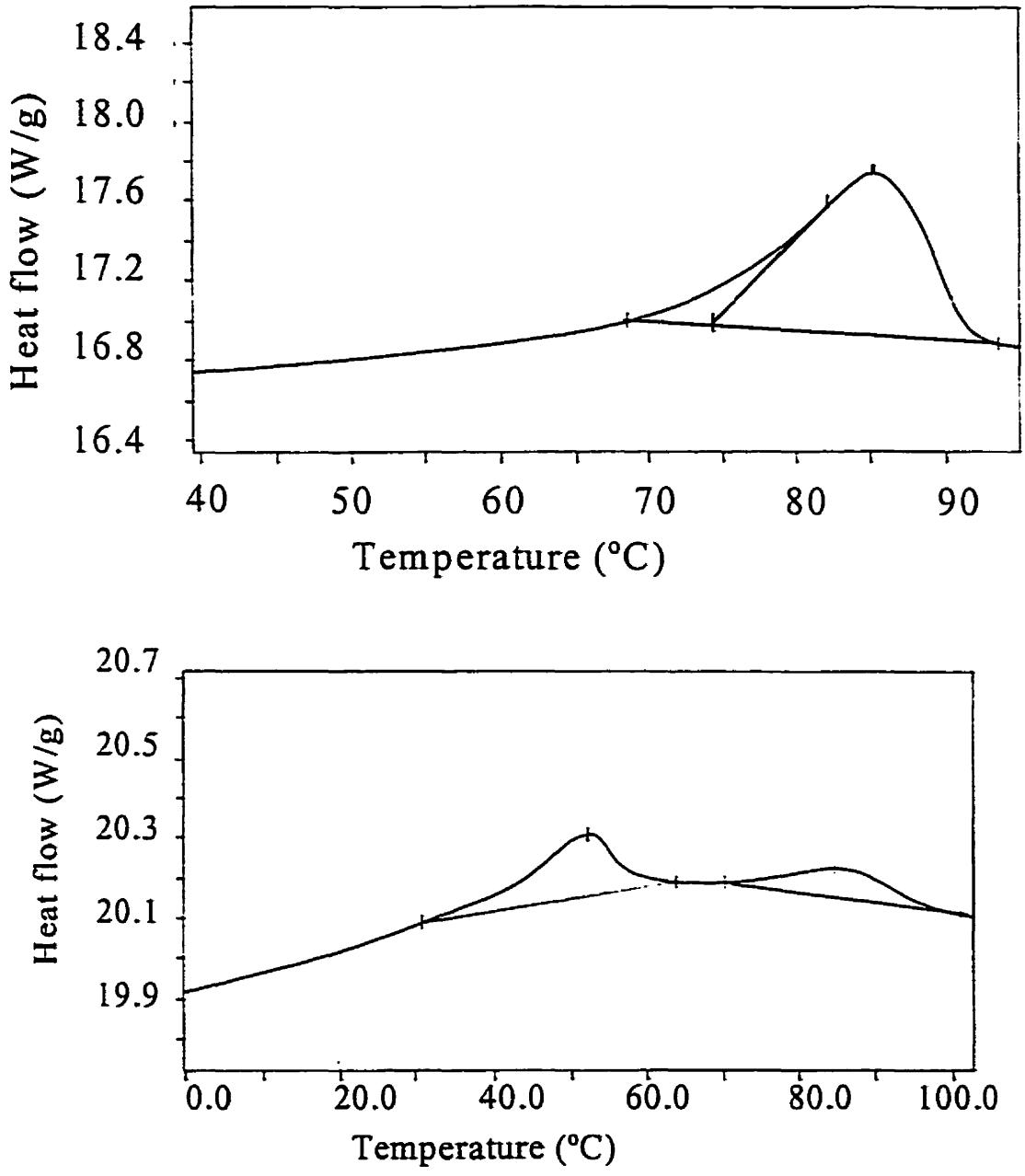

Figure 2.6 DSC endotherms for rapidly hydrolyzed OTS (above) and slowly hydrolyzed OTS (below).

For the rapidly hydrolyzed OTS, a broad endotherm centered at 85 °C with ΔH ~ 66 J/g is observed, indicative of a relatively heterogenous sample. The DSC endotherm of the highly crosslinked polymer is more complex with peaks at 55 °C and 85 °C and smaller enthalpies of 13 and 7 J/g.

As shown by the variable temperature ^{13}C CPMAS spectrum in Figure 2.4, the ordered domains of chains in the monolayer undergo a more gradual chain disordering. The peak assigned to transoid chain segments gradually shifts upfield from 33.3 ppm at 25 °C to 32 ppm at 120 °C. As reported here and previously for OTS monolayers on fumed silica,[14] this thermal disordering is completely reversible with the spectrum returning to its original state upon cooling back to room temperature.

2.3.4 2D WISE NMR.

The degree of chain mobility can be estimated from the proton linewidths as measured by two-dimensional wide line separation (WISE) NMR. Crystalline organic materials have proton linewidths up to 60 kHz due to strong dipolar interactions between the abundant proton spins.[19] The large ^{1}H linewidths are highly sensitive to the presence of molecular motion which will average the dipolar interaction. The use of this effect to investigate local dynamics is complicated by the small ^{1}H chemical shift range and the need to distinguish the proton signals arising from different chemical or dynamic environments. The 2D WISE experiment takes advantage of the much larger ^{13}C chemical shift range by providing a high-resolution ^{13}C CPMAS spectrum along one dimension and the proton linewidths associated with individual carbon sites along the second dimension. Thus the chain dynamics in crystalline and amorphous domains, which have different ^{13}C chemical shifts due to the γ effect, can be separately monitored.

The 2D WISE spectra of the rapidly hydrolyzed bulk polymer sample and the OTS monolayer are shown in Figures 2.7 and 2.8 along with the dipolar slices corresponding to methylene carbons in extended trans segments at ~33 ppm and mobile chain segments at ~30 ppm.

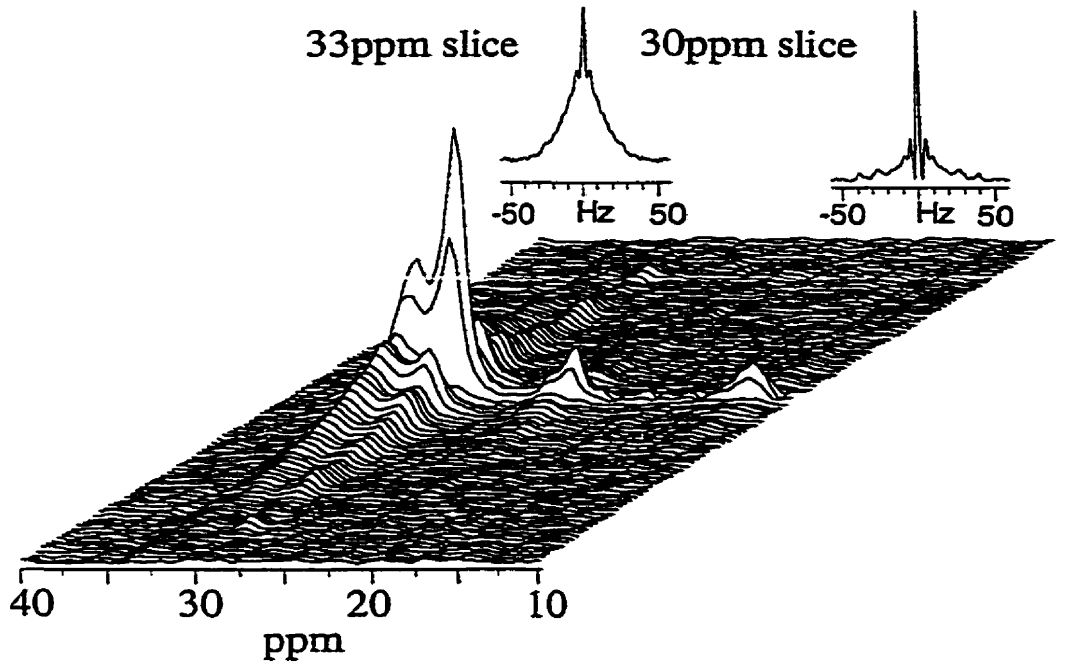

Figure 2.7 2D WISE spectrum of SiO_2-OTS; 500 scans, 3ms contact time, recycle delay 3s; proton evolution period of 120 increments of 4μs.

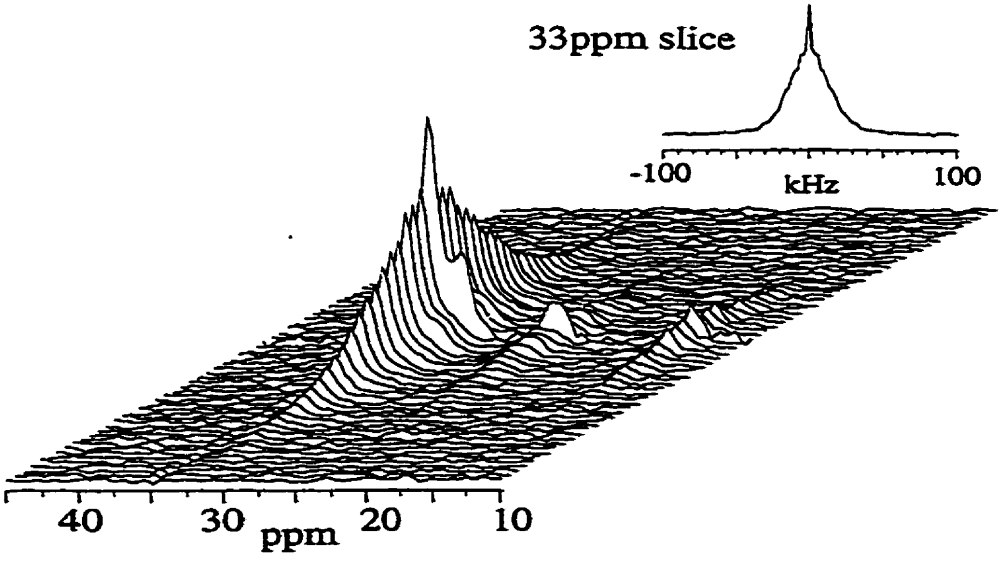

Figure 2.8 2D WISE spectrum of rapidly hydrolysed bulk OTS polymer; 200 scans, contact time 3ms, recycle delay 3s; proton evolution period of 120 increments of 4μs.

The inner methylenes of the rapidly hydrolyzed OTS samples display an intermediate linewidth, ca. 30 kHz. The dipolar slice of the ordered chains of the monolayer can be simulated by two components with intermediate and narrow linewidths of 30 and 5 kHz respectively. The disordered component at 30 ppm is quite mobile with a linewidth of ~1 kHz.

The 2D WISE technique involves indirect detection of the proton signal, and this allows deconvolution of proton lines associated with amorphous vs. crystalline regions. These broad peaks due to protons with large dipolar coupling are not visible in the 1 pulse ^{1}H MAS spectra shown in Figure 2.9.

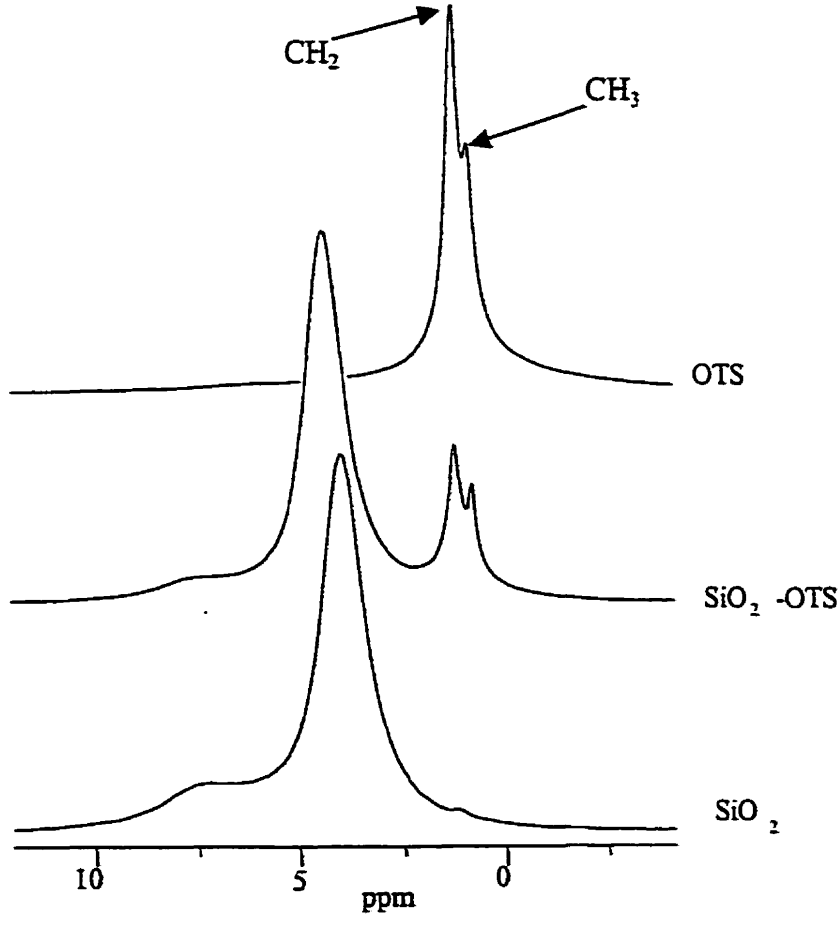

Figure 2.9 ^{1}H MAS spectra of OTS, SiO_2-OTS and SiO_2 as indicated. Spectra were acquired in 16 scans with a recycle delay of 3 s.

However the 1D proton spectra are interesting in that they confirm that very narrow components are present. Comparison of the spectra indicates that the peaks at 4-5 ppm (width ~300 Hz) and 7.7 ppm (width ~360 Hz) are due to surface silanol groups, since these are also seen (at slightly higher field) on the unreacted substrate surface. By comparison with literature values,[20] the broader more downfield peak is likely due to hydrogen bonded silanol groups and strongly H-bonded water, while the larger peak is due to physisorbed water. Silica contains internal silanol groups, and those on the surface are not consumed by the interaction with OTS since under these synthetic conditions (i.e. without heating or using a catalyst) the OTS monolayer is not extensively attached to the surface, but exists as a decoupled thin film.[7b,17] Hence the silanol peaks remain nearly unaltered by the addition of OTS. The OTS monolayer sample gives rise to at least two other peaks at 1.3 ppm (width 90 Hz) and 0.8 ppm (width 120 Hz), in the same positions as in the bulk polymer. These arise from the protons on the hydrocarbon chain (typical ^1H values for CH_3 and CH_2 groups are 0.9 ppm and 1.3 ppm respectively).[21] The narrow linewidths (compared with the expected 60 kHz width observed for dipolar coupling between protons in rigid systems) is due to substantial motion of the chains.

2.3.5 Spin diffusion NMR studies.

The use of ^1H spin diffusion experiments to determine domain sizes has been implemented in accordance with work on multi-component polymer systems as described in Chapter 1. Differences in mobility can be exploited to study migration of magnetization via dipolar coupling. Since the crystalline and amorphous regions are clearly visible in our monolayer system, we have applied the same principles to this sample. The set of spectra obtained for incremented mixing times following selection of the amorphous component by the dipolar filter is shown in Figure 2.10. The signal-to-noise is significantly worse than in the simple cross-polarization spectra, since the total magnetization in the system arises from the amorphous component only, which displays half the intensity of the rigid peak. This loss in signal has consequences for the quality of the data fit. However, a plot of intensity against the root of the mixing time as shown in

Figure 2.11 confirmed that spin diffusion occurs between the amorphous (mobile) and crystalline (rigid) regions, reaching a maximum at around t_m=100 ms, then decreasing as T_1 effects start to dominate.

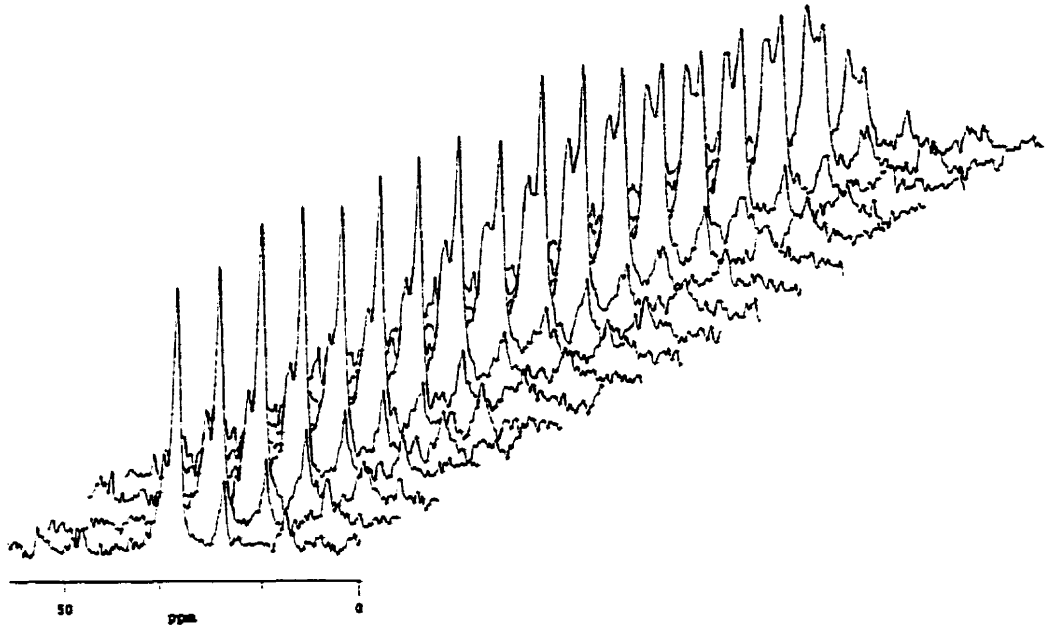

Figure 2.10 Spin diffusion experiment using ^{13}C detection and dipolar filter sequence of SiO_2-OTS. Spectra were acquired in 2000 scans with a contact time of 3 ms and recylcle delay of 3 s. The filter sequence consisted of 8 filter cycles and a pulse spacing of 15 ms. The mixing time was incremented from 0.2 to 500 μs.

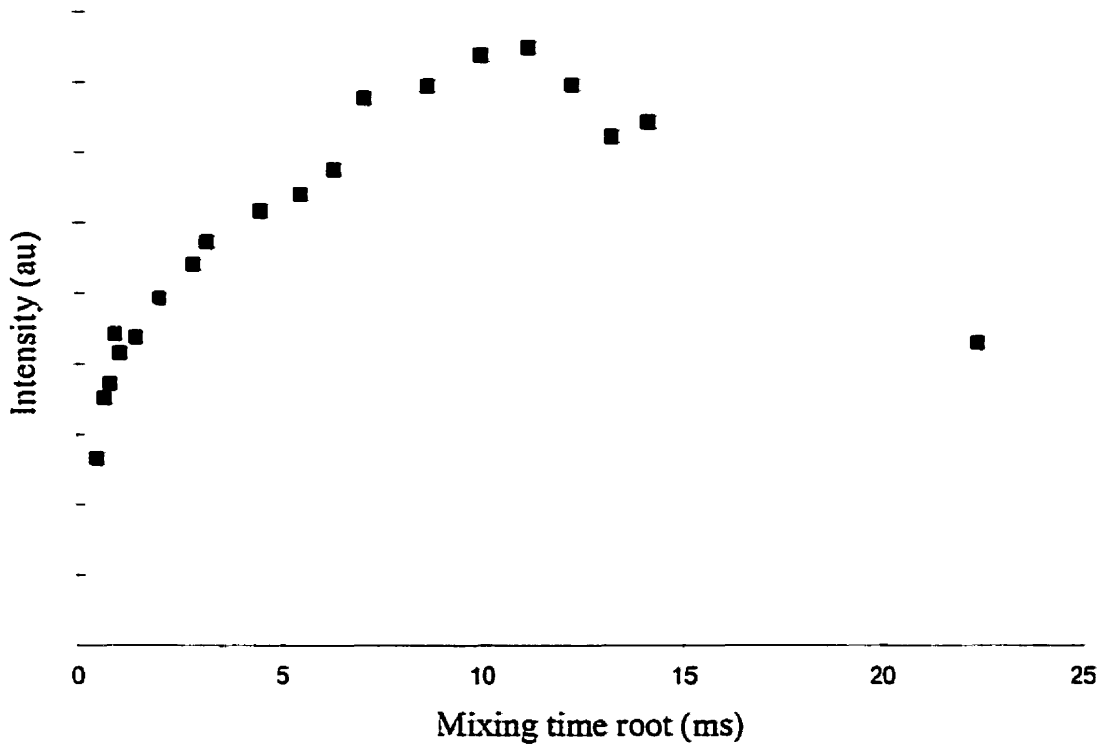

Figure 2.11 Plot of crystalline peak intensity against the root of the mixing time.

A second series of spectra were acquired with the same mixing times but without implementation of the filter pulse sequence. In this way the contribution to the relaxation behavior of the system by spin-lattice relaxation at each given mixing time is ascertained,[22] and the normalized intensity of the rigid peak of the filter experiment is divided by the corresponding intensity of the peak after simple relaxation. The domain size is proportional to the square root of the product of the spin diffusion constant and the time for spin diffusion to eliminate the initial polarization gradient.[23] This value can be obtained from a plot of the corrected intensity of the crystalline peak against the root of the mix time, this plot is shown in Figure 2.12.

mobility and sizes. In other words, there is likely a range of mobilities and domain sizes that is not a complication in the well defined morphologies of semicrystalline polymers. In light of this problem it was deemed inappropriate to attempt an exact fit of the data following the theories of Spiess et.al.[26] A simplified formula has been proposed to be adequate in estimating approximate domain sizes:

$$\langle |x| \rangle = \sqrt{D t_m^*} \qquad \textbf{Equation 2.1}$$

where $<|x|>$ is the average distance over which magnetization diffuses in a time t_m^*. t_m^* is estimated from the intersection of the two straight line sections of the graph, and D is the spin diffusion constant (not to be confused with the dipolar coupling constant D_{ij}) for the amorphous region. The rate of spin diffusion in the amorphous phase limits the overall rate of diffusion to the interface with the rigid component, from where it more rapidly diffuses into the rigid domains.

It is necessary to use an appropriate value for D. For rigid systems this is known to be ~0.8 nm^2/ms. If motion reduces the proton linewidth, D can be calculated by the relation: $D \sim \Delta\upsilon_{1/2} (r_{HH})^2$ where r_{HH} is the average interproton distance and $\Delta\upsilon_{1/2}$ is the proton linewidth. This formula is appropriate for linewidths down to 5 kHz.[27] Below this the formula predicts too low a value for D, suggesting that little or no spin diffusion should occur. However it has been established that even in cases where the proton linewidths have been motionally narrowed to 1kHz or less, spin diffusion is still possible.[23,28,29] This is more easily understood when we consider that such mobile material can still be cross-polarized to ^{13}C, a process which depends on the ^{13}C-^{1}H dipolar coupling. Since this is smaller than the ^{1}H-^{1}H dipolar coupling, this suggests that the latter is large enough to allow spin diffusion to occur. Using well defined polymer systems, others[24,28] have determined values for D of 0.05 to 0.09 nm^2/ms for proton linewidths of less than 1 kHz. Since an estimation of domain size requires that a reasonable value for D be assumed, we have taken D to be 0.09 nm^2/ms (at any rate the square root of D is employed in equation 2.1, and thus the estimate for $<|x|>$ is not so

sensitive to the exact value of D used in the calculation). From the plot of intensity against $t_m^{1/2}$, we obtain a $t_m^{1/2*}$ value of 14 ± 2 ms. These values indicate a domain size of around 4.2 ± 0.6 nm for the amorphous domains. The error analysis is not rigorous, however even studies using the more exact theoretical treatments quote uncertainties on the order of $\pm 20\%$.[23]

Additional attempts to confirm this data by use of alternative spin diffusion experiments were made. However implementation of the Goldman-Shen pulse sequence proved unsuccessful, selection of the amorphous peak over the crystalline peak being insufficient. An alternative method would be to run a series of 2D WISE spectra with increasing mixing times inserted into the pulse sequence. Again the selection of one peak over the other in the experiments was inadequate due to the overlap of resonance in the ^{13}C dimension. Alternate ways for producing a gradient in magnetization exist. If significant differences in either T_1 or $T_{1\rho}$ exist, these can be exploited for spin diffusion studies.[30] In the experiment which utilizes differences in $T_{1\rho}$, the protons are spin locked as described in section 1.3. A suitably long spin locking period is employed such that one of the components decays essentially to zero, at which point the remaining magnetization is restored to the z axis and spin diffusion is allowed to occur.

2.4 Discussion

Both the thermal behavior and the nature of the siloxane network of OTS monolayers deposited on silica can be usefully compared with the bulk polymerized OTS samples. The solid-state NMR, XRD and DSC analysis of the bulk polymerized OTS indicate that the siloxane units organize into a lamellar structure, driven by the van der Waals interactions between the long hydrocarbon chains. The slowly hydrolyzed sample is highly crosslinked, containing an equal proportion of $RSiOH(OSi)_2$ (T_2) and $RSi(OSi)_3$ (T_3) units. In alkylsesquioxanes, such as phenylsilsesquioxane and methylsilsesquioxane, the T_3 units can be arranged in random, ladder and cage structures depending on the initial reaction conditions used.[31] In the slowly hydrolyzed OTS, the chains or rings initially formed, gradually cross link to produce either ladder or cage units, allowing the

overall lamellar structure to be retained. The higher degree of order achieved by slow hydrolysis is reflected by the XRD spectra. Whereas the XRD spectrum of rapidly hydrolyzed OTS sample displays only one peak, several more peaks appear at small angles in the slowly hydrolyzed sample, indicating that more long range order is present. In contrast, the networks of both the rapidly hydrolyzed OTS and the OTS monolayer contains mostly $RSiOH(OSi)_2$ linkages, consistent with smaller oligomers, arranged into linear chains or rings.

The DSC scans combined with the variable temperature ^{13}C solid-state NMR spectra show that the slowly hydrolysed bulk OTS polymer undergoes a broad transition due to chain melting. Since the structure consists of a bilayer, some expansion must occur in the siloxane backbone in order to provide the additional free volume for chain disordering. The transition is much sharper in the rapidly hydrolyzed OTS, where, presumably, the smaller less cross-linked siloxane units can more easily accommodate chain disordering than a rigid, highly crosslinked network. Increasing the rigidity of the siloxane backbone inhibits this transition, as evident from the much smaller enthalpies measured for the slowly hydrolyzed polymer.

In a similar fashion, the gradual thermal disordering of the trans domains of the OTS monolayers, as compared to the discrete chain melting in the bulk analog, may be due to the immobilization of the siloxane network onto the silica surface. In addition, the substantial population of gauche defects indicates that much smaller domains of ordered chains are present in the OTS monolayer as compared to the bulk polymer, and the approximate size of these domains is estimated from spin diffusion measurements to be ~3.5 nm. Small domains of ordered chains or a range of domain sizes will broaden out a thermal transition. It would be useful to obtain an estimate of the size of any domains of greater mobility in the bulk polymer, in order to relate the domain size to the transition width. However since no significant disordered components are observed in either of the bulk polymer samples, the dipolar filter can not be used. It should be noted that, even in more complete and highly ordered monolayers, such those formed by the thiols and phosphonates, the order-disorder transitions are quite broad as compared to phase transitions in bulk materials.

As indicated by the proton linewidth measurements, sufficient free volume to accommodate chain motion exists at room temperature in both the monolayer and bulk polymer samples. Even in the case of the more highly crosslinked OTS polymer, the 2D WISE spectrum reflects the presence of substantial chain mobility below the order-disorder transition. The triangular lineshapes of the methylene protons are characteristic of an intermediate motional state in contrast to the broad 60 kHz Gaussian lines normally observed for crystalline organic materials. Like certain other stiff macromolecules with flexible aliphatic sidechains,[32] the chains in the polymerized OTS do not crystallize in the traditional sense, i.e. although there is significant ordering of the hydrocarbon chains, there is also substantial mobility, as in liquid crystals or membranes.[33]

The 2D WISE spectrum of the OTS monolayer exhibits an even greater degree of mobility and conformational disorder. The island structures formed by OTS, which have been observed by scanning force microscopy,[5a] consist of separate domains of ordered and disordered chains. This morphology is reflected in the 2D WISE spectrum of the monolayer. The disordered chains are highly mobile, exhibiting proton linewidths < 5 kHz; this greater mobility being due to the larger number of conformational defects as well as the fact that the chain motion will be less restricted in a monolayer as compared to a bilayer environment. The more motionally restricted chains in the ordered domains contain both narrow and broad components with the linewidth of the broad component being similar to that of the bulk polymerized OTS. The spin diffusion studies indicate a domain size of about 3.5 nm for the disordered regions. This value is clearly a reasonable estimate, each silica sphere having a surface area of around $3x10^4$ nm^2. However since this technique does not give any information about the size of the crystalline regions, there remains some concern as to whether vertical polymerization may occur, leading to patches of bulk polymer. This question will be addressed again by ^{129}Xe NMR in Part Two of this thesis, at this stage it is sufficient to note that the size of the disordered hydrocarbon chain domains is small compared to that of the substrate, suggestive of an adsorbed layer rather than bulk polymer.

The close packed chains of alkylsiloxane monolayers have been described as 2D crystals,[17] based on an estimated interchain distance of ~4.4Å and a measured chain tilt

angle of ~ 0 °. However, the interlayer distance in the bulk polymer is also consistent with fully extended chains, oriented perpendicular to the siloxane layers. Nevertheless, considerable chain motion is occurring even in the highly crosslinked OTS polymer. Based on these observations, we assert that even in a complete, highly ordered OTS monolayer, the chains are in a conformationally ordered but motionally disordered state. This type of dynamic behavior also occurs in thiol and phosphonate monolayers where the free volume for chain motion is provided by the large headgroup combined with surface roughness. Although the crosslinking in alkylsiloxane monolayers leads to a relatively small interchain distance, this does not lead to crystallization. The chain packing, determined by the underlying siloxane network, still provides sufficient free volume for motion about the chain axes. A literature discussion of the issue of structural properties of the octadecyl chains on the siloxane network points out that alkyl chains can be connected in two positions.[18a] The siloxane network can be described as sheets of interlocked Si-O trimers which have both axial and equatorial positions available for alkyl chain attachment as shown in Figure 2.10.

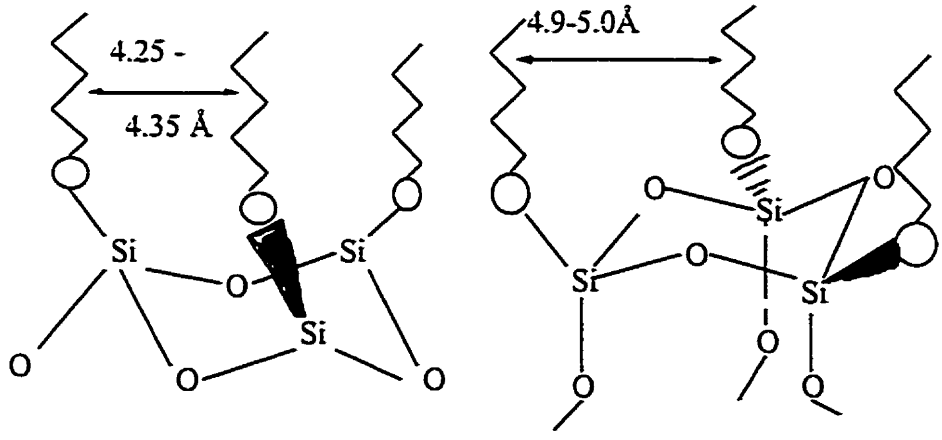

Figure 2.10 Schematic depicting the potential for axial (left) or equatorial (right) positioning of alkyl chains relative to the siloxane network produced on interaction with the silica surface.

The resulting difference in free chain volume is apparent. In addition, the axial isomer allows connection of exocyclic Si-O bonds to other polysiloxane units, or in the case of the monolayer system, to the silica surface, by equatorial Si-O bonds. This structure does not impose additional distortion on the siloxane backbone. Thus we can view the bulk OTS polymer as a comb-shaped polymer with a siloxane backbone and C_{18} hydrocarbon sidechains as described by Allara *et al* .[4] Chain melting will require an increase in free volume which may involve a change in configuration of the siloxane backbone to yield the less dense equatorial-alkyl based structure. However, attachment of the siloxane network to a silica substrate will clearly inhibit such a structural chance, so that the onset of chain melting is much higher than in the bulk polymer. There is significant motion observed in the hydrocarbon chains of both systems at room temperature, as indicated by the proton linewidth.

In summary, the crosslinking of the alkyl chains in alkylsiloxane SAMs results in an island structure with the coexistence of ordered and disordered domains but also imparts a greater thermal stability to these monolayers. However, this additional structural feature does not lead to rigid, crystalline chains. Instead , the degree of chain motion is similar to that seen in the thiol and phosphonate SAMs. The siloxane network of the OTS monolayers is only partially crosslinked, with a significant number of Si-OH groups remaining, similar to the network produced by rapid hydrolysis of OTS in the bulk phase. Future studies of OTS monolayers by ^{29}Si NMR spectroscopy will focus on determining whether annealing can induce further condensation of these silanol groups. The presence of regions of differing conformation is confirmed by ^{13}C NMR, the mobilities of these regions are probed by the 2D WISE experiment. Proton spin diffusion experiments were carried out via ^{13}C detection, these allowed an approximate estimate of domain size. This experiment should prove to be highly useful in systems where selection of the mobile region is more successfully accomplished, future samples could include mixed monolayers of two different chain lengths, and adsorbed polymer systems, where signal-to-noise would be improved.

References

[1] (a) Sagiv, J. *J. Am. Chem.Soc.* **1980**, *102*, 92. (b) Ulman, A. *Chem. Rev.* **1996**, *96*, 1533. and references therein.

[2] Mrksich M.; Whitesides G. M. *Ann. Rev. Biophys. Biomol. Struct.* **1996** *25*, 55.

[3] (a) Silberzan, P.; Léger, L.; Ausserré, D.; Benettar, J. J. *Langmuir*, **1991**, *7*, 1647. (b) Brzoska, J. B.; Azouz, I. B.; Rondelez, F. *Langmuir* **1994**, *10*, 4367. (c) Parikh, A. N.; Allara, D. L.; Azouz, I. B.; Rondelez, F. *J. Phys. Chem.* **1994**, *98*, 7577.

[4] Allara, D. L.; Parikh, A. N.; Rondelez, F. *Langmuir* **1995**, *11*. 235.

[5] a) Schwartz, D. K.; Steinberg, S.; Israelachvili, J.; Zasadzinski, *Phys. Rev. Let.* 1992, 69, 3354. b) Barrat, A.; Silberzan, P.; Bourdieu, L.; Chatenay, D., *Europhys. Lett.* **1992**, *20*, 633. c) Nakagawa, T.; Ogawa, K.; Kurumizawa, T. *Langmuir* **1994**, *10*, 525.

[6] (a) Matjauer, K: Frank, C. *Langmuir* **1993**, *9*, 3446. (b) Fang, Jiyu; Knobler, Charles M. *Langmuir* **1996**, *12*, 1368. (c) Takahara A.:Kojio K.: Ge SR. Kajiyama T. J. Vac. Sci. Tech. A **1996** *14*, 1747.

[7] (a) Angst, D. L.; Simmons, G. W. *Langmuir* **1991**, *7*, 2236. (b) Tripp, C. P.; Hair, M. L. *Langmuir* **1992**, *8*, 1120.

[8] Calistri-Yeh, M.; Kramer, E. J.; Sharma, R.; Zhao, W.; Rafailovich, M. H.; Sokolov, J.; Brock, J. D. *Langmuir* **1996**, *12*, 2747.

[9] Gun, J.; Sagiv, J., *J.Coll.Int.Sci.*, **1986**, *112*, 457

[10] McGovern, M.E.; Kallury, K.M.R.; Thompson, M. *Langmuir* **1994**, *10*, 3607

[11] Gao, W.; Dickinson, L.; Grozinger, C.; Morin, F. G.; Reven, L. *Langmuir* **1996**, *12*, 6429.

[12] Gao, W.; Dickinson, L.; Grozinger, C.; Morin, F. G.; Reven, L. *Langmuir* **1997**, *13*, 115.

[13] (a) Badia, A.; Gao, W.; Singh, S.; Demers, L.; Cuccia, L.; Reven, L. *Langmuir* **1996**, *12*, 1262. (b) Badia, A.; Dickinson, L.; Morin, F. G.; Demers, L.; Lennox, R. B.; Reven, L. *J. Am. Chem. Soc.* **1997**, *119*, 11104.

[14] Gao, W.; Reven, L. *Langmuir* **1995**, *11*, 1860.

[15] Gao, W.; Dickinson, L.; Morin, F.; Reven, L. *Chem.Mat.* **1997**, *9*, 1860.

[16] Cao,G.; Lee,H.; Lynch,V.M.; Mallouk,T.E. *Inorg.Chem.* **1988**, *27*, 2781.

[17] Parikh, A.N.; Schivley, M.A.; Koo, E.; Seshadri, K.; Aurentz, D.; Mueller, K.; Allara, D.L., *J.Am.Chem.Soc.*, **1997**, *119*, 3135

[18] (a) Loy,D.A.; Shea,K.J. *Chem.Rev.*. **1995**, *95*, 1431. (b) Engelhardt, G.; Michel, D. *High Resolution Solid-State NMR of Silicates and Zeolites*; John Wiley & Sons, 1987

[19] (a) Schmidt-Rohr, K.; Clauss, J.; Spiess, H.W. *Macromolecules* **1992**, *25*, 3273. (b) Clauss, J.; Schmidt-Rohr, K.; Adam,A.; Boeffel,C.; Spiess, H. W. *Macromolecules* **1992**,*25*. 5208.

[20] Maciel, G.E., from *Encyclopedia of Nuclear Magnetic Resonance*, **1996**, Ed. D.M.Grant and R.K.Harris.

[21] *The Sadtler Catalogue of Proton NMR Spectra*, **1978**, Philadelphia Press

[22] Landfester, K.; Boeffel, C.; Lambla, M.; Speiss, H.W., *Macromolecules*, **1996**, *29*, 5972

[23] Chin, Y.H.; Kaplan, S., *J.Mag.Res.*, **1994**,

[24] Cai, W.Z.; Schmidt-Rohr, K.; Egger, N.; Gerharz, B.; Speiss, H.W.; *Polymer*, **1993**, *34*, 267

[25] Bluemich, B., *Adv.Mat.*, **1991**, *3*, 237

[26] Egger, N.; Schmidt-Rorh, K.; Bluemich, B.; Domke, W. D.; Stapp, B., *J.App.Poly.Sci.*, **1992**, *44*, 289

[27] Clauss, J.; Schmidt-Rohr, K.; Spiess, H.W., *Acta Polymer.*, **1993**, *44*, 1

[28] Spiegel, S.; Schmidt-Rohr, K.; Boeffel, C.; Spiess, H.W., *Polym.Comm.*, **1993**, *34*, 4566

[29] Weigand, F.; Demco, D.E.; Bluemich, B.; Spiess, H.W.; *J.Magn.Reson.A.*, **1996**, *120*, 190

[30] Kimura, T.; Neki, K.; Tamura, N.; Horii, F.; Nakagawa, M.; Odani, H., *Polymer*, **1992**, *33*, 493

[31] Ulman, A. *Advanced Materials* **1990**, *2 (12)*, 573

[32] Clauss, J.; Schmidt-Rohr, K.; Adam, A.; Boeffel, C.; Spiess, H.W., *Macromolecules*, **1992**, *25*, 5208

[33] Opella, S.J., *Nature Structural Biology*, **1997**, *4*, 845

Chapter Three: Structure and Dynamics in Self-Assembled Monolayers of Alkylphosphonic Acids on Metal Oxides

3.1 Introduction

In a previous study from this laboratory, the possibility of synthesizing metal phosphonate monolayers on high surface area fumed silica was explored.[1] Zirconium octadecylphosphonate (ODPA) monolayers were deposited on Cab-O-Sil according to the procedure developed by Mallouk.[2] The resulting coverage was estimated by elemental analysis to be around 26%. This was shown to be sufficient for solid state NMR studies, and the ^{13}C spectrum indicated a predominantly trans conformation of the chains, but also identified a small population of gauche sites which was not visible by infrared spectroscopy. Zirconation of the fumed silica was found to provide a better surface for alkyphosphonate addition than initial phosphonate derivitization. In addition the ^{31}P shift confirmed that the majority of the phosphorus atoms had reacted with the surface, provoking a significant shift from 31.3 ppm to 7 ppm. These initial results confirmed that the self-assembly of dense, well ordered metal phosphonates was experimentally more straightforward than the synthesis of the silica-OTS systems, being less sensitive to reaction conditions. As indicated in the previous chapter, the formation of OTS monolayers involves a degree of polymerization which may limit the degree of coverage achieved, with vertical rather than horizontal polymerization of the siloxane headgroups occurring, and no evidence of surface Si-O bond formation. In contrast, the long chain alkylphosphonic acids self-assemble in an epitaxial fashion, and the nature of the interfacial region is more easily characterized. The use of ^{31}P NMR to characterize surface bonding has also been reported for hafnium α,ω-bis(phosphonate) multilayer films where it was successful in distinguishing between phosphonate ester and phosphonic acid moieties to confirm surface bonding in non-linear optical materials.[3]

Phosphonic acids have been shown to exhibit strong chelation properties which has led to their use in corrosion inhibition,[4] metal extraction[5] and calcification

prevention.[6] In addition they can be reacted with a variety of alkali and transition metals to produce bulk lamellar metal phosphonates used in ion exchange, selective sorption and catalysis.[7] These multilayer compounds can be deposited by self-assembly or Langmuir-Blodgett techniques onto a variety of substrates.[8] In related work, our group has reported on the interesting heat storage capabilities manifested by some of these systems.[9] There have been very few reports in the literature concerning the preparation of monolayers.[10] In the study on which this current work is based, the work of Mallouk and co-workers involving metalphosphonate multilayer synthesis was used as a basis for developing dense monolayers.[2] Mallouk's study used primer layers of either Zr^{4+} cations or PO_3H_2 functional groups attached to silica. As stated earlier, initial studies showed the zirconated silica to be a better substrate, film growth on a phosphonated surface being incapable of producing ordered monolayers owing to defects in the early stages of film formation and a mismatch between the organic and inorganic lattices. The degree of coverage in the zirconated silica phosphonate films was still limited owing to insufficient zirconation, and this synthetic approach also tended to produce some bulk zirconium phosphonate so the work to be reported here focused instead on the direct adsorption of the alkylphosphonic acids onto metal oxides.

The direct reaction of methyl- and phenylphosphonic acids with a silica surface has been confirmed by a solid state NMR study of these acids adsorbed onto silica gel.[11] The ^{29}Si and ^{31}P NMR shifts confirm the formation of a single covalent P-O-Si ester linkage. Unfortunately the longer chain phosphonic acids have higher pKa values and will not condense directly with the surface silanols, hence the need for a primer layer as mentioned above. However, in recent biotechnology studies,[12] TiO_2 and ZrO_2 powders were successfully modified with phosphoric acid and short chain alkylphosphonic acids to produce systems for use in liquid chromatography and to increase the hydrophobicity of membranes. The presence of the alkyl chain was found to promote formation of a permanent hydrophobic layer, which, unlike phosphonate ions, can not be removed from the oxide surfaces by water washing. The strength of the interaction with the phosphonic acid moiety is also great enough to allow modification of In_2O_3/SnO_2 electrodes by orientation of individual macromolecules between externally addressable contacts[13] as

well as anchoring of transition metal compounds through phosphonated polypyridyl ligands for use in photovoltaic devices.[14] The evidence of strong substrate-phosphonate bonding in these cases led us to investigate the possibility of synthesizing well ordered alkylphosphonate SAMs on metal oxides. While a contact angle study[15] of various long chain hydroxamic, carboxylic and phosphonic acids adsorbed onto native oxide surfaces suggested that the hydroxamic acid systems were the most stable for a majority of metal oxides (copper, silver, aluminium and zirconia) and the phosphonic acids were most stable on titania, the following work shows that absorption of octadecylphosphonate on both zirconia and titania produces high quality monolayers, with greater coverage than that observed for the silica-OTS system.

This chapter compares the conformational order and surface bonding of octadecyl phosphonic acid adsorbed onto Al_2O_3, TiO_2, ZrO_2 and zirconated silica as characterized by solid state NMR and vibrational spectroscopies. In addition the effects of chain length and temperature on the ordering of alkylphosphonates on zirconia (with which the strongest monolayer-substrate interaction is observed) is studied through the synthesis of a series of ZrO_2-alkylphosphonate systems with 8, 12, 14, 16 and 18 carbon atoms in the hydrocarbon chains and variable temperature NMR of the ZrO_2-ODPA system. The thermal stability of the ZrO_2-ODPA system is compared with bulk microcrystalline zirconium alkylphosphonate. Thermal stability is particularly important when considering the potential applications of these systems in technological applications.[16] As discussed in the previous chapter, the alkylsilanes produce monolayers with very high thermal disordering temperatures. The chain packing of alkanethiols on gold nanoparticles, as discussed in the next chapter is complicated by the small size of the gold colloids (~2.5 nm diameter) which leads to intercalation of chains on neighboring particles. In contrast, the metal oxide particles used in this study are larger (average size 30 nm) and hence a closer model for monolayers on planar substrates.

3.2 Synthesis

Commercial nonporous fumed silica, (Cab-O-Sil, BET surface area 100 m^2/g, Cabot Corp.), ZrO_2 (VP Zirconium Oxide, BET surface area 40 m^2/g, DeGussa AG), TiO_2 (Titanium Dioxide P25, BET surface area 50 m^2/g, DeGussa AG), and Al_2O_3 (Aluminum Oxide C, BET surface area 100 m^2/g, DeGussa AG) were used as received. The n-alkyl phosphonic acids were synthesized by the Michaelis-Arbuzov reaction[17] of the n-alkyl bromides and triethyl phosphite. The ODPA-Zr/SiO_2 was prepared as reported by Mallouk.[18] In a typical preparation of alkylphosphonate monolayers on the metal oxides, a 5-fold excess of alkylphosphonic acid relative to the moles estimated for a full surface coverage on the metal oxide was dissolved into 1000 ml of 3:1 methanol-water mixed solvent. A suspension of 2 g of metal oxide in 200 ml deionized water was added dropwise to the acid solution. The resulting suspension was held at 100 °C for three days with stirring. The solid was washed and centrifuged with 200 ml of methanol seven times to remove any physisorbed alkylphosphonic acid and then dried under vacuum at room temperature. A portion of the ODPA-Al_2O_3 sample was annealed for several hours at 100 °C under vacuum (10^{-5} torr). Microcrystalline $Zr(O_3PC_{18}H_{37})_2$ (ZrODPA) was prepared from a solution of 2.0 g octadecylphosphonic acid (ODPA) in 1000 mL ethanol and 1.2 g of $ZrOCl_2 \cdot 8H_2O$ in 200 mL water. The solutions were adjusted to pH 2 and filtered through 0.22 mm filter paper. The aqueous solution of $ZrOCl_2$ was added dropwise to the solution of ODPA with stirring. A fine white precipitate of poorly crystalline ZrODPA formed immediately. The solution was kept at 100 °C for two days, then held at 60 °C for a week to increase the crystallinity. The precipitate was washed repeatedly with ethanol and water and the dried under vacuum. Elemental analyses were carried out by Galbraith Laboratories, Knoxville, TN.

3.3 Results

3.3.1 Elemental analysis and calculated coverage of ODPA on metal oxides

The calculated coverages shown in Table 3.1 assume an area of 24 Å for each bound ODPA molecule,[7] and use surface areas for Cab-O-Sil as calculated from a N_2 BET isotherm, and for the other metal oxides as provided by the supplier (Degussa AG, Frankfurt, Germany, Technical bulletin No.56).

Metal Oxide	surface area (m^2/g)	% C	calculated (%) surface coverage
Zr/SiO_2	100	4.0	26
ZrO_2	40	3.99	73
TiO_2	50	4.10	61
Al_2O_3	100	28.05	230

Table 3.I Characterization by Elemental Analysis of ODPA Adsorbed onto Metal Oxides

The coverage of ODPA on zirconated silica is considerably less than a monolayer, while the coverage on titania and zirconia is substantially higher.[1] The quality of the initial zirconium primer layer on the Cab-O-Sil is vital in producing high quality coatings. Without any Zr layer the adsorption of ODPA is negligible. Previously this approach has been used[2] to synthesize multilayer films of metal phosphonates on silica, as discussed in the introduction to this chapter. In the assembly of multilayer films, a primer layer of phosphonic acid terminated silane appeared to produce a more uniform film. It has also been reported in an FTIR and polarized IR study that subsequent addition of further layers (i.e. sequential adsorption of alkylbisphosphonic acids and $ZrOCl_2$) can promote "self-annealing" of the film.[19] This is disputable as another group reports similar

average thicknesses for both forms of primer layer.[20] Similar results were observed for alkylbisphosphonates on hafnium treated gold films.[21] An AFM study of mono and multilayers of zirconium bis(phosphonate) on silica treated with a primer layer of PO_3H_2, then zirconated, indicates that the growth of the film occurs through island formation.[22]

The coverage achieved for the preparation of ODPA on zirconated silica seems to indicate that some of the initial Zr primer layer is lost during the steps of washing and centrifuging the sample to remove physisorbed species, and since no subsequent layers are added, no self-annealing can occur- hence the production of a patchy film on fumed silica. These synthetic problems were the impetus behind the search for a better substrate and coating route. Fortunately, as discussed previously, ODPA can be reacted directly with metal oxide surfaces, and the observed coverages on titania and zirconia are much higher. However they still do not appear to give full monolayer coverage, in contrast with the literature report of the reaction of phosphoric acid and short chain alkylphosphonic acids (with 1 to 4 carbon atoms) on ZrO_2 and TiO_2 powders prepared by a sol-gel process.[10b] Since the metal oxides used here consist of agglomerated particles, and the ODPA has a substantially longer chain, it is reasonable to assume that, as discussed in reference 16, not all of the BET surface area is available for ODPA absorption.

The reaction of ODPA with Al_2O_3 produces a sample with elemental analysis results indicative either of multilayer formation, or the formation of a bulk aluminophosphonate. The low angle region of the X-ray diffraction spectrum (not shown) displays a sharp series of peaks typical of the patterns observed for long chain lamellar alkylphosphonate metal salts.[23] The pattern can be analyzed (assuming it is based on the 0k0 progression) to give an interlayer spacing value of 45.2 Å, similar to that observed in Zr and Mn octadecylphosphonate multilayers.[24] The strength of the reflections in the high angle region seems to indicate the presence of more than two layers of the bulk compound, being stronger than the XRD reflections observed for multilayer Zr phosphonate films.[25] Bulk formation was also observed under milder reaction conditions, and the nature of this compound will be addressed later in the chapter, where its NMR spectra will provide a useful source of comparison in the study of the ZrO_2-ODPA and TiO_2-ODPA monolayer systems.

3.3.2 Vibrational spectroscopy

Many previous studies have used the methylene regions of the FTIR spectra to estimate the degree of alkyl chain ordering compared to bulk crystalline samples.[26] Although most of these studies involved coatings on planar substrates, the four samples examined here do produce sufficiently well resolved spectra to use this technique. The methylene stretching region is shown in Figure 3.1, and the frequencies and peak widths of the methylene asymmetric ($\nu_a(CH_2)$) and symmetric ($\nu_s(CH_2)$) modes are summarized in Table 3.2.

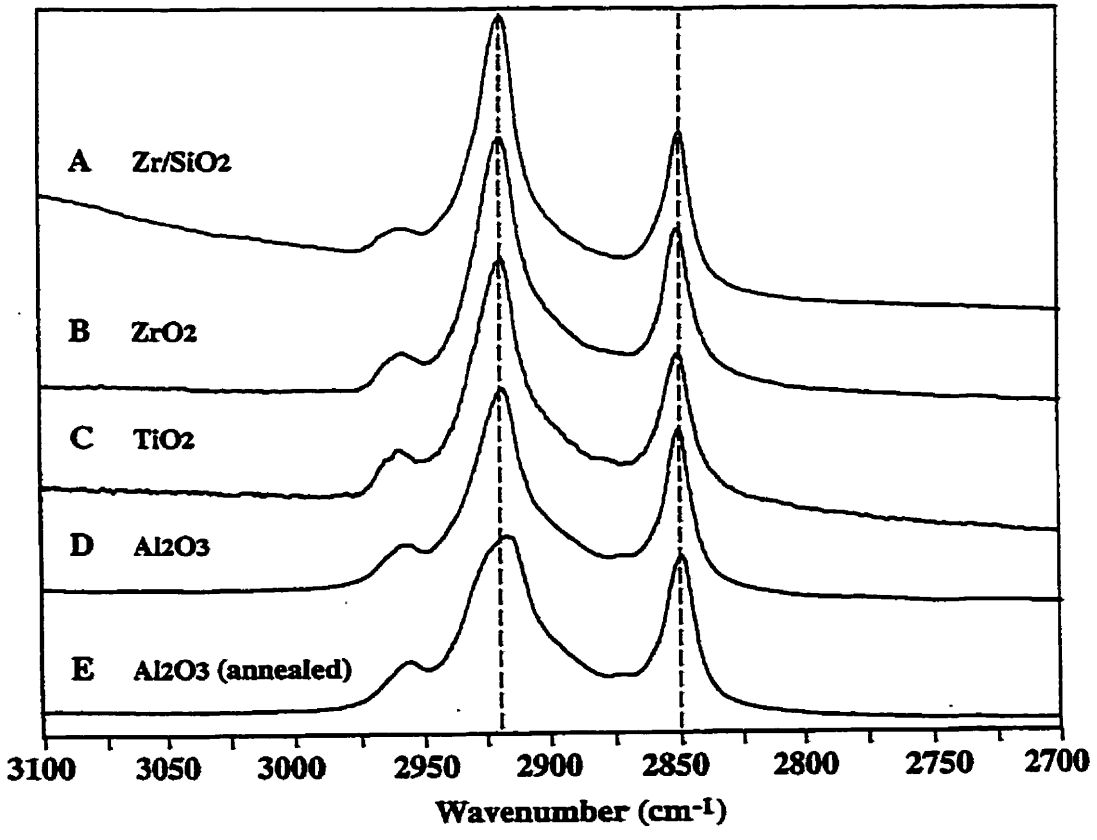

Figure 3.1 Infrared spectrum of ODPA on various metal oxides as indicated; Methylene stretching region.

Metal Oxide	$\nu_a(CH_2)$ (cm^{-1})	fwhh (cm^{-1})	$\nu_s(CH_2)$ (cm^{-1})	fwhh (cm^{-1})
Zr/SiO_2	2918.6	17.4	2849.3	9.9
ZrO_2	2918.8	18.4	2850.6	10.4
TiO_2	2918.2	19.9	2850.4	12.0
Al_2O_3	2918.8	19.3	2850.2	10.2
Al_2O_3 (annealed)	2915.0	30	2848.0	12.0

Table 3.2: Peak Positions and Line Widths for the Methylene Stretching Region

All of the samples studied have very similar methylene frequencies (2918 cm^{-1} and 2850 cm^{-1} for the asymmetric and symmetric stretches respectively). The linewidths provide additional information, with the zirconated silica based system displaying the narrowest band (fwhh=17cm^{-1}) and the titania-ODPA the broadest (fwhh=20cm^{-1}). Lower frequencies and narrower bands are generally indicative of more ordered chains, as observed for the octadecylsilane system, for which frequencies as low as 2917cm^{-1} (fwhh=15cm^{-1}) have been reported. Annealing of the ODPA-Al_2O_3 sample leads to line broadening and a more asymmetric line shape for ($\nu_a(CH_2)$), but the low frequency edge does move to lower wave number, indicating an increase in crystallinity in part of the sample. In general the values obtained for these systems seem to be consistent with those reported for ODPA on a silicon wafer.[8c] Such values are typically taken as evidence of a high degree of conformational order suggestive of a crystalline region as compared with the higher frequencies ($\nu_a(CH_2)$ = 2925cm^{-1}) and broader lines (fwhh>35cm^{-1}) observed in more disordered "liquid-like" films. However, our work shows that such characterization presents an incomplete picture, and in addition, solid state NMR provides a description of the dynamic nature of the hydrocarbon chains.

Another disadvantage inherent to the infrared studies of these systems is the difficulty encountered in determining the nature of the interfacial layer. In the case of the silica, alumina and titania substrates, the oxides themselves give rise to large adsorption bands which mask any information in the phosphorus stretching region. However ZrO_2 does not have a strong adsorption band in this region of the infrared spectrum, so the P-O stretching region can be observed for the ZrO_2-ODPA system, and is shown in Figure 3.2.

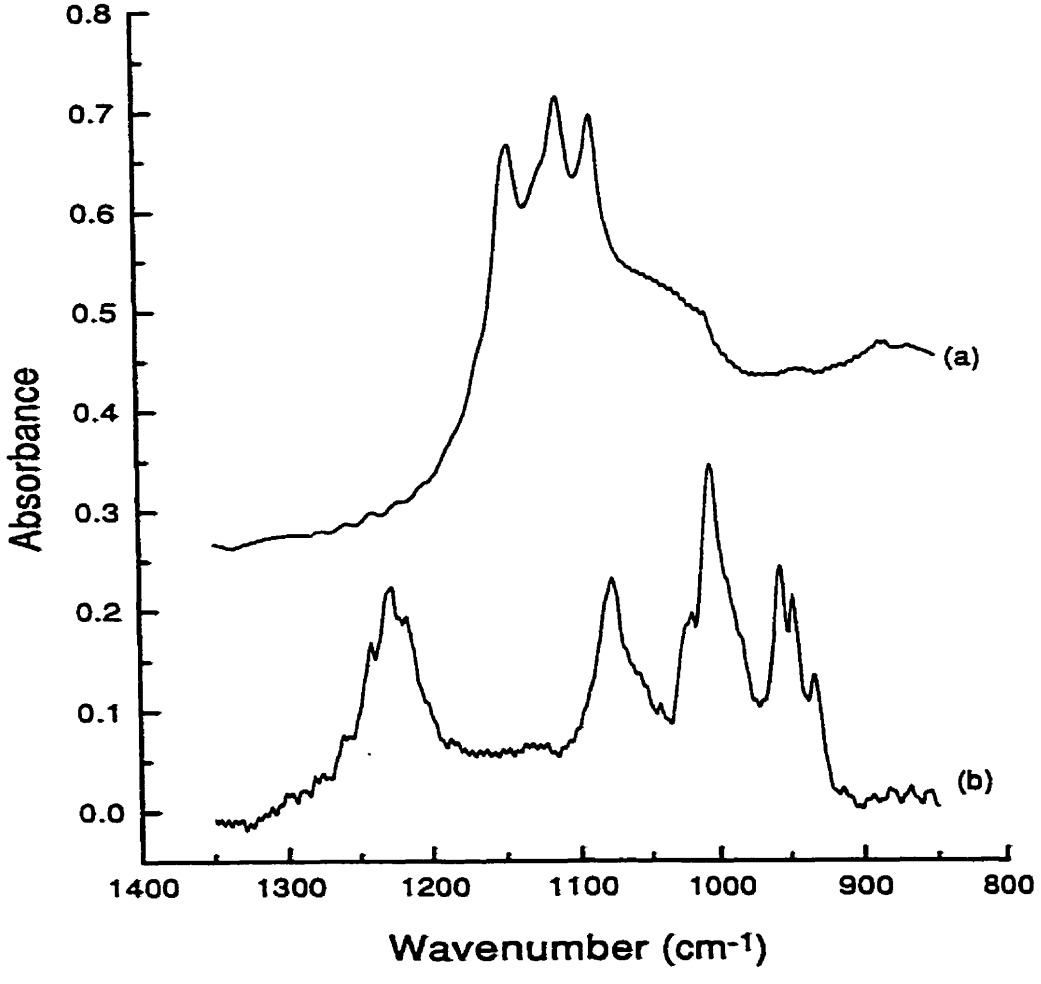

Figure 3.2 Infrared spectrum of (a) ODPA on zirconia and (b) bulk ODPA; P-O stretching region.

This region of the spectrum is complex, but the substantial changes on bonding to ZrO_2 indicate a strong interaction between the substrate and the alkylphosphonate. P-O bands at 1228 and 950cm^{-1} disappear following adsorption, and the PO_3 stretching bands at 1077 and 1006cm^{-1} are broadened and shifted. The three bands observed in the bound ODPA can be assigned by comparison with a study on LB films and bulk samples of cadmium octadecyl-phosphonate,[26] the upper of these frequencies is likely due to the asymmetric PO_3^{2-} stretch, while the lower bands are the symmetric PO_3^{2-} stretches, which are split due to the local symmetry of the phosphonate headgroups (less than C_{3v}). The disappearance of peaks at around 1200 and 950cm^{-1} is also reported for phenylphosphonic acid on ZrO_2,[10b] where the authors attributed these bands to the P=O and P-O-H groups respectively, and interpreted their disappearance as evidence of a tridentate bonding mode. In our spectrum the bands are broad and overlapped, so that the suggested spectral assignments may be inaccurate. Fortunately this is another area where NMR is helpful, the ^{31}P shifts being more revealing.

3.3.3 ^{31}P Solid-State NMR

The nature of the interaction between the phosphonic acid headgroup and the various substrates can be more fully characterized by the ^{31}P solid state NMR spectra shown in Figure 3.3.

In bulk metal alkylphosphonate salts the ^{31}P chemical shifts decrease with increasing valency and electronegativity of the cation, ranging from 26 to 0 ppm.[1,27] Bulk zirconium octadecylphosphonate has one peak at 7 ppm while pure ODPA displays one peak at 31.5 ppm. These spectra are also shown in Figure 3.3 for comparison.

The similarities between the spectra of ODPA on zirconated silica and the bulk metal compound confirm the earlier suspicions that this synthetic route tends to produce mainly bulk compound (a small additional broad peak at ~16 ppm remains unassigned but may be due to partially coordinated PO_3^{2-} groups). The formation of small amounts of bulk material is also observed in the TiO_2-ODPA and ZrO_2-ODPA samples prepared under prolonged reaction times.

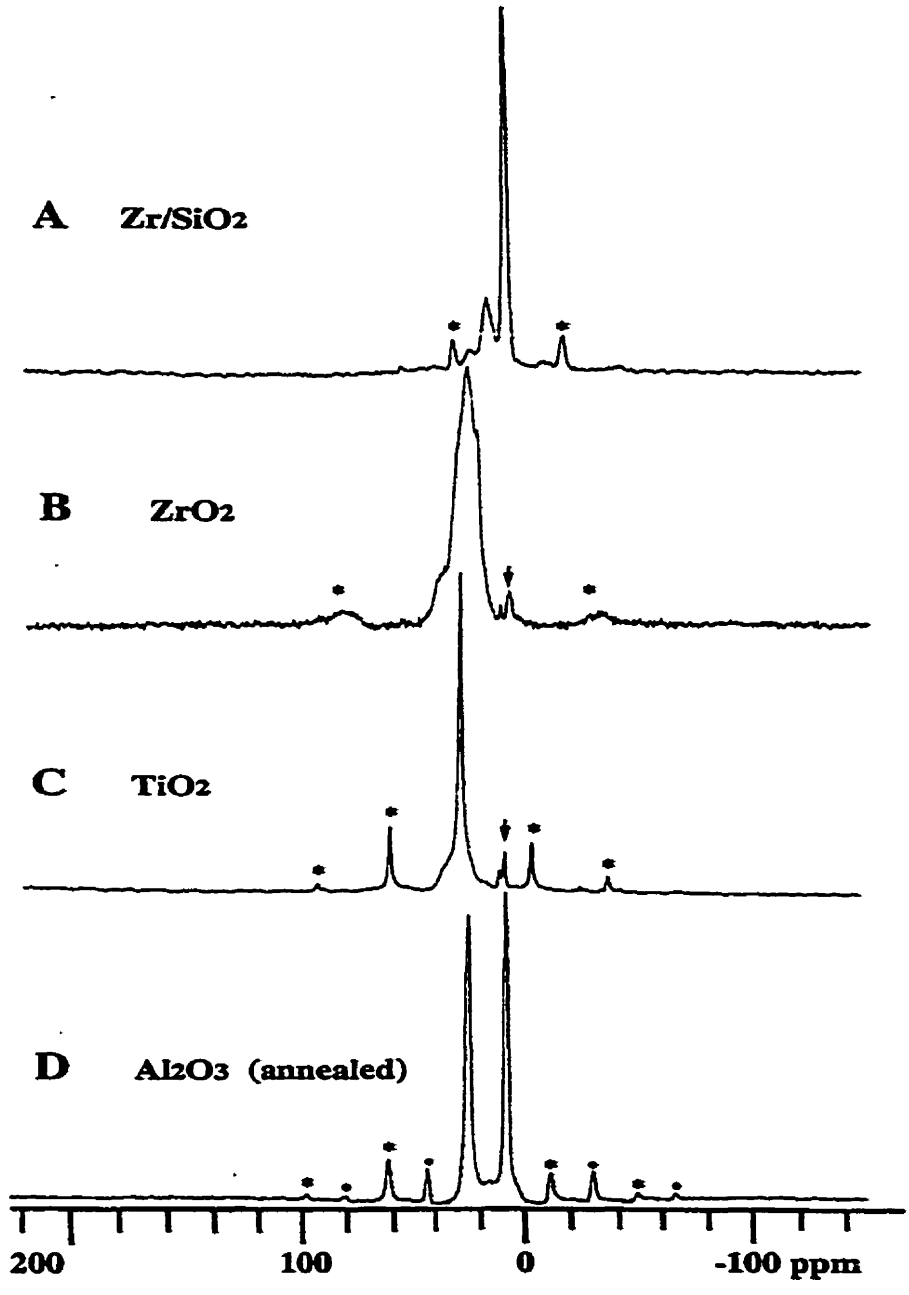

Figure 3.3 ^{31}P CPMAS spectra of metal oxide-octadecylphosphonic acids as indicated. Spectra were acquired in 100 scans, with a contact time of 2 ms and recycle delay of 5 s, except for the bulk zirconium octadecylphosphonate which required 1000 scans. Spinning sidebands are indicated by *, the arrows indicate peaks due to the presence of bulk metal phosphonate in the monolayer samples.

For the TiO_2 and ZrO_2 systems, the extent of interaction with the phosphonic acid headgroup can be assessed by the magnitude of the upfield shift from the unbound ODPA. In the TiO_2-ODPA sample the ^{31}P shift is only slightly upfield at 28 ppm compared to 31.5 ppm, indicating a relatively weak interaction with the substrate and possibly incomplete deprotonation of the phosphonic acid headgroup. The change observed on bonding to ZrO_2 is much greater, not only does the ^{31}P peak move to 25 ppm, but the line is inhomogeneously broadened. Broad phosphorus signals in MAS spectra are quite common, the ^{31}P shift is very sensitive to environment, varies with the O-P-O bond angle and/or the number and electronegativity of nearest neighbor atoms. The distribution of chemical shifts observed here is due to the presence of different types of surface bonds and/or bonding sites on the ZrO_2 surface.

The surface of ZrO_2 is known to be very complex, having two types of surface hydroxyls which can be protonated or deprotonated in addition to some coordinatively unsaturated zirconium(IV) ion sites which act as strong Lewis acid centers.[23] These different sites are depicted in Figure 3.4.

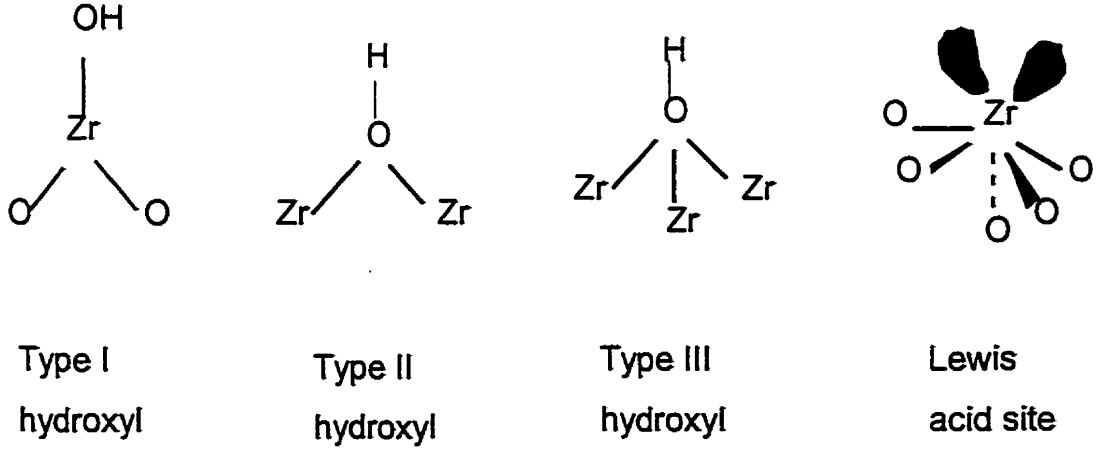

Figure 3.4 Depiction of different types of surface groups on zirconia. Adapted from reference 28.

In accordance with the shifts observed in the study of porous ZrO_2 modified with phosphoric acid,[10a] it is proposed that the binding of ODPA occurs principally through esterification with the surface hydroxyls. In a study of methylphosphonic acid reacted onto silica,[9] the ^{31}P chemical shifts expected for mono-, bi- and tri-dentate ester linkages were estimated by comparisons with model silyl compounds. The methylphosphonic acid shifted upfield by 5 ppm on absorption with silica, as consistent with formation of a single ester linkage. A system with two ester linkages would be expected to show an upfield shift of 14 ppm, giving a chemical shift of around 17 ppm. The bulk ZrODPA with coordination through all three phosphonate oxygen atoms to Zr cations displays the largest upfield shift moving 24 ppm to 7 ppm. Assuming a similar trend for ODPA bound to ZrO_2 rather than silica, mono- and bidentate species would appear around 26 and 17 ppm respectively. The bidentate mode may be the origin of the additional peak observed at ~16 ppm in the ODPA-zirconated silica sample, which would mean that although this technique produced mostly bulk zirconium octadecylphosphonate, and any monolayer formed was of low coverage. The bidentate bonding mode can also be inferred for shorter chain phosphonic acids ($C_nH_{2n+1}PO_3H_2$ where n=1,2,8,12) adsorbed on alumina, all of which display ^{31}P peaks around 13-16 ppm (with the exception of the octylphosphonic acid, OPA, on alumina which produces a bulk metal phosphonate with spectra similar to those described for ODPA- Al_2O_3 below). The average upfield shift of 6.5 ppm from the free acid for the ZrO_2-ODPA is taken as proof that the primary mode of attachment is monodentate rather than tridentate, in contrast to the conclusions drawn from the P-O region of the IR data.[10b] The broadening of the phosphorus peak may also arise from adsorption of some ODPA species to the strong Lewis acid sites. A study of phosphoric acid adsorption on zirconia[10a] found that initial adsorption occurred primarily at the coordinatively unbound Zr^{4+} sites, with esterification of the acid with the surface hydroxyls requiring longer reaction times. Unfortunately stronger reaction conditions here (low pH, high acid concentration, high temperature and longer reaction times) were found to promote dissolution of the bulk ZrO_2 matrix, increasing the amount of bulk zirconium phosphonates formed. The advantage of using ^{31}P NMR is that these species can be easily identified by the peak at ~7 ppm (see Figure 3.3). While this is seen in

samples prepared at long reaction times and low pH (<2), in samples obtained under milder conditions this reaction seems to be suppressed, while equally high coverages are still achieved. ZrO_2 was also reacted with shorter chain alkylphosphonic acids for an investigation of alkyl chain order dependence on chain length to be discussed below. The ^{31}P spectra of these systems also exhibited single broad peaks around 26 ppm, indicative of similar bonding to the substrate and thus validating the comparison between these systems.

Reaction of ODPA or OPA with alumina produces a sample which displays a complex ^{31}P spectrum, as shown in Figure 3.5, apparently owing to the partial formation of a bulk aluminophosphonate.

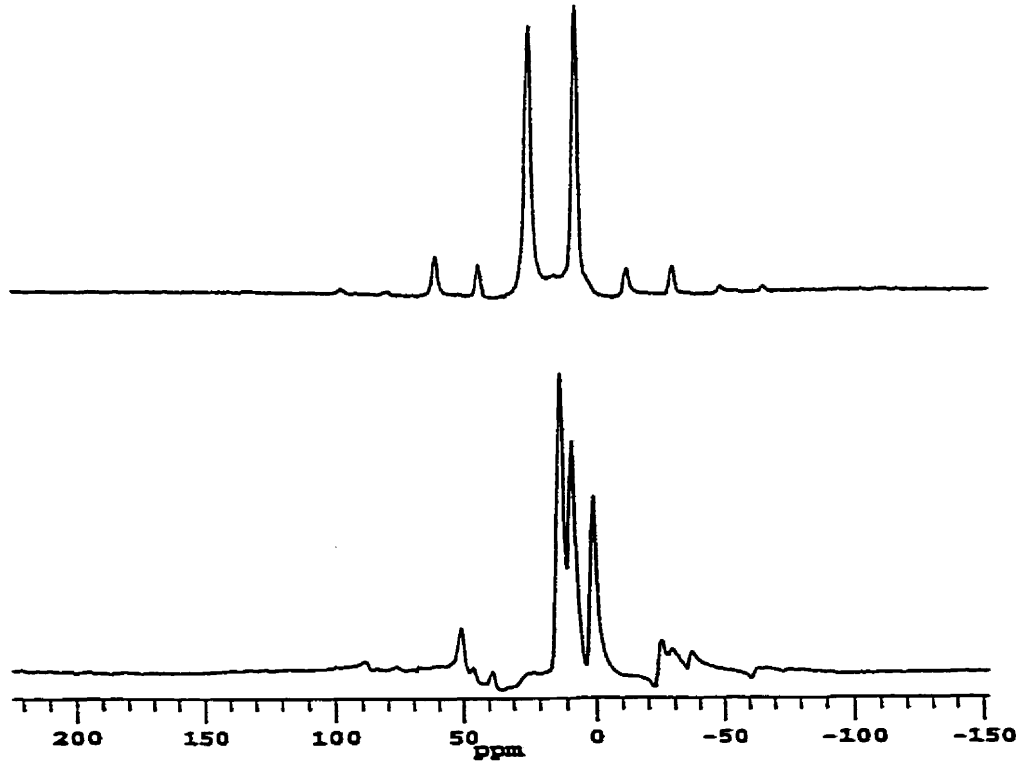

Figure 3.5 ^{31}P CPMAS spectra of annealed (above) and non-annealed (below) Al_2O_3-ODPA sample; spectra were acquired in 100 scans with a contact time of 3 ms and a recycle delay of 3 s.

Annealing of the sample at 100°C led to a simplification of the spectrum to give two isotropic peaks at 25 ppm and 8 ppm as shown. The synthesis of a microporous bulk (aluminomethyl)phosphonate by reaction of methylphosphonic acid with Al_2O_3 in water under extreme conditions of high temperature and pressure has been reported in the literature.[29] The longer chain phosphonic acids presumably undergo similar reactions to form lamellar compounds similiar to those reported for other metals.[21] The simplification of the ^{31}P spectrum on heating is assumed to be due to some rearrangement of the aluminophosphonate network.

3.3.4 ^{13}C Solid-state NMR

While the ^{31}P CPMAS spectra provide insights into the bonding to the surface, they reveal nothing about the nature of chain packing. For that we turn to ^{13}C CPMAS NMR. As stated in section 3.3.2, the methylene stretching frequencies of the four systems under investigation all appear to be very similar, and based on previous work would seem to indicate that the hydrocarbon chains are in an ordered environment. The ^{13}C CPMAS NMR spectra shown in Figure 3.6 confirm this and provide additional information.

Regions of ordered and disordered chains can be resolved as described for the silica-OTS system in Chapter 2. The differing shifts of the all-trans and partially gauche conformations (resonant at 33 ppm and 30 ppm respectively)[30] of the interior methylene populations are clearly seen in the TiO_2-ODPA, indicating both ordered regions and a significant population of disordered chains on this substrate. In contrast the ODPA on ZrO_2, zirconated silica and Al_2O_3 exhibit intense peaks at 33 ppm, but no evidence of substantial disordering in the form of separately resolvable peaks at 30 ppm. However, the greater linewidth of all the monolayer trans peaks compared to the bulk aluminophosphonate is also suggestive of greater disorder in the SAM systems. The ^{13}C spectrum of the Al_2O_3-ODPA before annealing clearly shows a larger disordered signal at 30 ppm along with multiple splitting of the chain end peaks around 12 ppm. This suggests that the presumed rearrangement on annealing also increases the crystallinity of the chains.

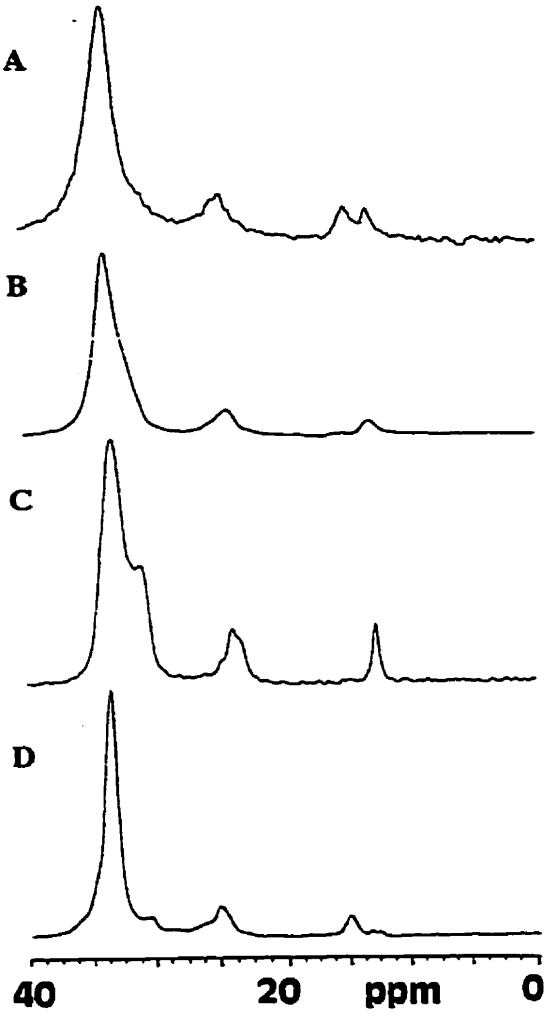

Figure 3.6 ^{13}C CPMAS spectra of ODPA on A) zirconated silica, B) zirconia, C) titania and D) alumina. Spectra were acquired in 2000 scans with a contact time of 3 ms and a recycle delay of 3 s.

The terminal methyl groups appear at around 12.5-13.0 ppm in all the spectra. Single peaks are observed for the two monolayer samples on TiO_2 and ZrO_2, while the Zr/SiO_2 and annealed Al_2O_3 samples give rise to two methyl peaks at 12.5-13.0 ppm and 14-15 ppm. The higher field shifts are again indicative of conformational disorder, in this case due to the situation of the methyl peaks at the chain termini. Methyls in a bulk crystalline or bilayer environment will be less disordered and appear further downfield, e.g. the bulk aluminophosphonates. The bilayer situation is demonstrated for

octadecanethiol-capped gold, where the small size of the gold colloids leads to intercalation of chains on neighboring particles, and the chain termini are resonant at 15.0 ppm.[31] In some instances the presence of ordered and disordered components is sufficient to provide different chain termini environments, as seen for alkylsilanes on silica.[32] The origin of the two methyl peaks in the spectrum of ODPA on Zr-SiO_2 must be considered in conjunction with the earlier conclusions. If this splitting were due to regions of ordered and mobile chains, these would be visible in the methylene region at 33 and 30 ppm respectively. Furthermore raising the sample temperature should lead to coalescence of the peaks as all the chains become disordered. The ^{13}C spectrum at 120°C is shown in Figure 3.7.

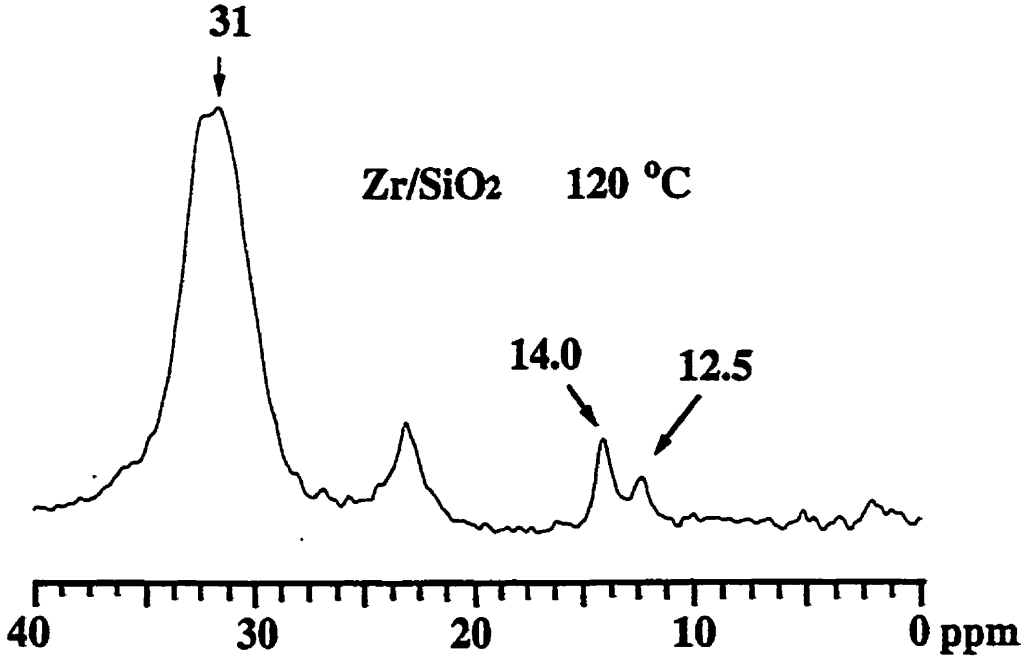

Figure 3.7 Direct polarization ^{13}C MAS spectrum of Zr/SiO_2-ODPA at 120°C. Spectrum was acquired in 20,000 scans with a recycle delay of 3 s.

Direct polarization was used in the acquisition of this spectrum since the chain mobility was substantial enough to make cross polarization inefficient. Although the chains have become completely mobile, as reflected in the shift of the interior methylene

peak to 31 ppm, the two terminal methyl peaks remain well resolved. A similar splitting is also seen in the Al_2O_3 -ODPA sample in which multilayer formation is confirmed, thus the two peaks are assigned to methyl end groups in the bulk and monolayer environments.

These assignments were confirmed by studying an octylphosphonic acid (OPA)-ZrO_2 sample treated by zirconating with a $ZrOCl_2$ solution. Spectra before and after treatment are shown in Figure 3.8.

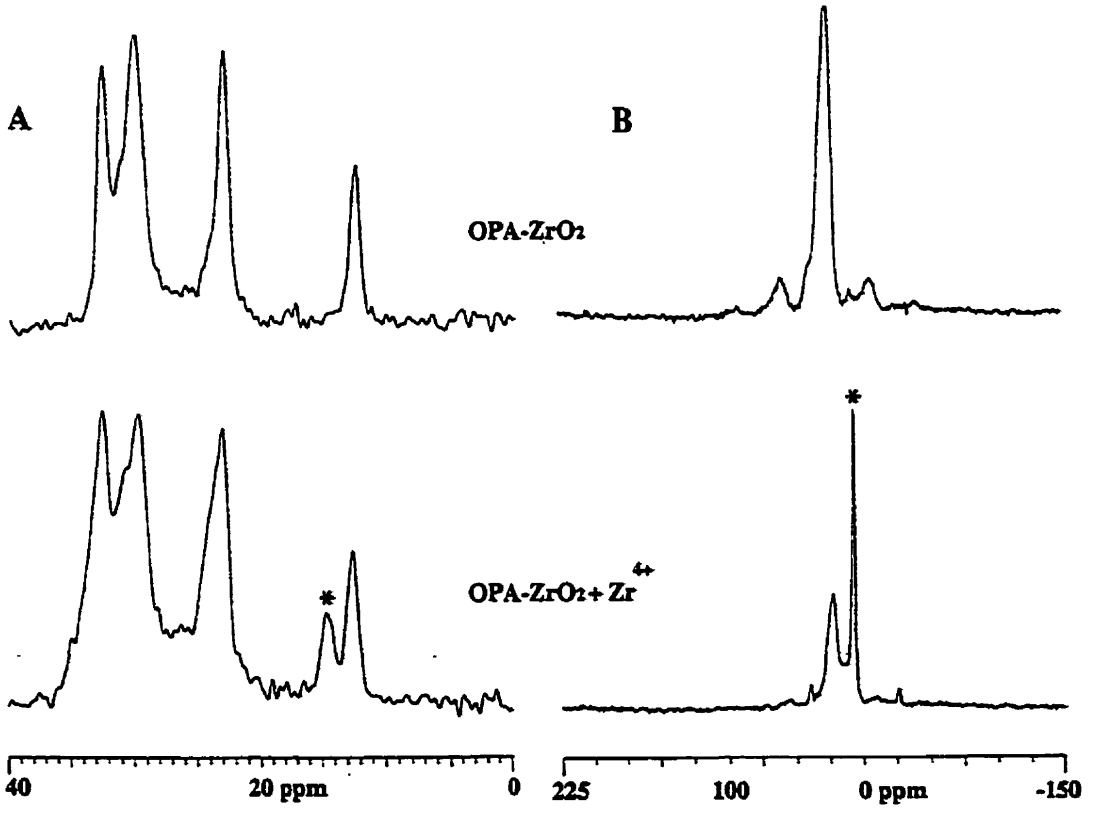

Figure 3.8 ^{13}C CPMAS spectra (left) and ^{31}P CPMAS spectra (right) of ZrO_2-OPA with and without added Zr^{4+} as indicated. Spectra were acquired in 2000 scans, with contact times of 3 ms and recycle delays of 3 s. * indicates peaks due to bulk ZrOPA.

The methylene groups in the chain centers resonate at 30 ppm, indicating that this shorter phosphonic acid is conformationally disordered at room temperature, and the end methyl group is at 12.5 ppm. The surface bound phosphonate headgroup gives rise to a

broad ^{31}P peak at 25 ppm as described previously. The zirconation leads to addition of a new peak in the ^{31}P spectrum at 7 ppm; the result of Zr^{4+} reacting with weakly bound OPA molecules to produce some bulk ZrOPA. The ^{13}C spectrum now displays two methyl peaks, confirming the assignment of the peak at 14-15 ppm as the methyl in a bulk hydrocarbon environment and the upfield peak at 12.5-13 ppm as methyls at the hydrocarbon/air interface. In a complete monolayer environment, chain termini are expected to remain very disordered at room temperature. For highly ordered systems such as alkanethiol SAMs on planar gold, evidence of disorder at the chain ends has been observed for temperatures as low as 100K.[33] The metal oxide particles used here have rough surfaces and exhibit various types of surface bonding both of which may be expected to lead to a lack of order and high population of the gauche conformations at the chain ends.

3.3.4.1 Dependence of SAM conformational order on chain length

The γ-gauche effect, which was used to study the relative degrees of chain order of ODPA on a variety of substrates, has also been used to study the effect of chain length by examination of the ^{13}C solid state NMR spectra of a series of alkylphosphonic acids absorbed on zirconia. This substrate was chosen because the reaction with ODPA was strongest, and the monolayer coverage was highest. The series of acids (C_nH_{2n-1})-PO_3H_2 (with n=8,12,14,16,18) all gave similar ^{31}P spectra on reaction with zirconia, with the broad peak at ~26 ppm being assigned to monodentate bonding through the phosphonate headgroup. The ^{13}C spectra of these systems are shown in Figure 3.9.

As shown previously ODPA-ZrO_2 displays a predominantly ordered environment, with a small disordered shoulder at ~31 ppm arising from some gauchoid segments. Decreasing chain length is accompanied by an upfield shift of the interior methylene resonances, with the spectrum of the octylphosphonic acid system showing a resolvable peak for the C6 carbon at 33 ppm and shifting of the inner methylenes (C4 and C5) to 30 ppm. The chains with less than 16 carbon atoms are disordered at room temperature. This same cut-off length was observed for gold alkanethiols.[26] The gold alkanethiol systems undergo distinct chain length dependent phase transitions observable by DSC. The peak maxima of the DSC thermograms occur at 22, 41 and 51°C for C_{14}, C_{16} and C_{18} respectively, so that gold alkanethiol monolayers with 16 or more carbon atoms are ordered at room temperature.[26]

3.3.4.2 Thermal disordering of ZrO_2-ODPA, SiO_2/Zr-ODPA and bulk $Zr(O_3PC_{18}H_{37})_2$

On heating, the hydrocarbon chains in the ZrO_2-ODPA system undergo thermal disordering, causing a gradual upfield shift of the carbon signal originating from the inner methylene group, as shown in Figure 3.10a.

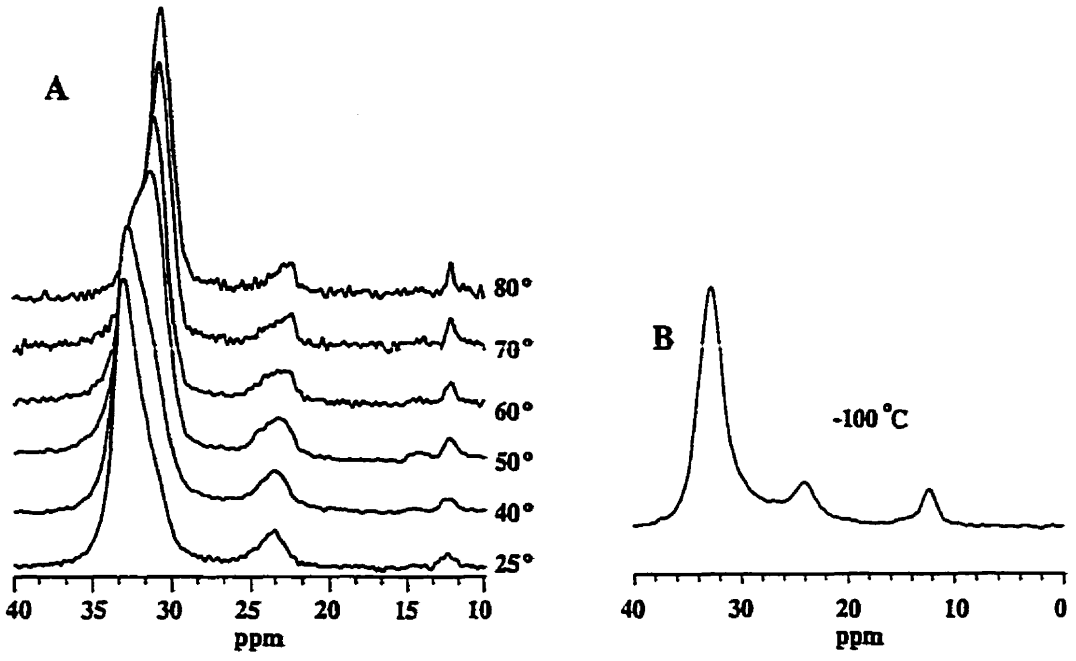

Figure 3.10: (a) The spectra displayed for temperatures above 60°C were acquired by a single pulse experiment, since the chain mobility decreases the cross-polarization efficiency, and this lowers the signal-to-noise ratio. The cross-polarization spectra which were also taken for comparison, confirmed the data, but had a significantly poorer S/N ratio. By 50°C the chain peak intensity has shifted to 31 ppm, indicating that the chains are predominantly disordered, and above 60°C little change is seen. The thermal disordering is fully reversible, the spectrum returning to its original appearance on cooling. Spectra were acquired in 2000 scans with a contact time of 3 ms (CPMAS experiments) and a recycle delay of 5 s. (b) ^{13}C CPMAS spectrum at –100°C.

The low temperature spectra are also interesting, the peak arising from the mobile chain termini at 13 ppm, as discussed in section 3.3.4, remains at the same shift in the spectrum acquired at -100°C (shown in figure 3.10b). However the shoulder for gauche chain populations at 31 ppm is not present at this temperature. Since the 13 ppm peak was assigned to chain end gauche defects, it is apparent that these ends remain dynamically disordered at low temperature, as seen in the alkanethiol SAMs on planar gold substrates.[28]

The ^{31}P spectra were also acquired at each temperature, and remained unchanged throughout the chain melting process, indicating that the integrity of the substrate-phosphonate headgroup bond is maintained. The TiO_2-ODPA system also undergoes reversible chain melting over a similar temperature range.

In section 3.3.4, the spectrum of ODPA deposited on zirconated silica was shown at 120°C, in order to prove that the two end methyl peaks observed arose from bulk and monolayer chain ends. The methylene peak at this temperature indicates that only partial disordering has occurred, the chains showing a broad resonance at 31 ppm. The formation of bulk material also occurs for shorter alkyl chains, as evidenced by the presence of two methyl peaks in the spectrum. Figure 3.12 shows ^{13}C CPMAS spectra of (C_nH_{2n+1})-PO_3H_2, n=12,14,18 on zirconated silica. No chain length dependence is observed, with all the systems showing methylene carbon shifts of 33.5 ppm due to chains in an all-trans conformation. This is further evidence of bulk rather than monolayer formation.

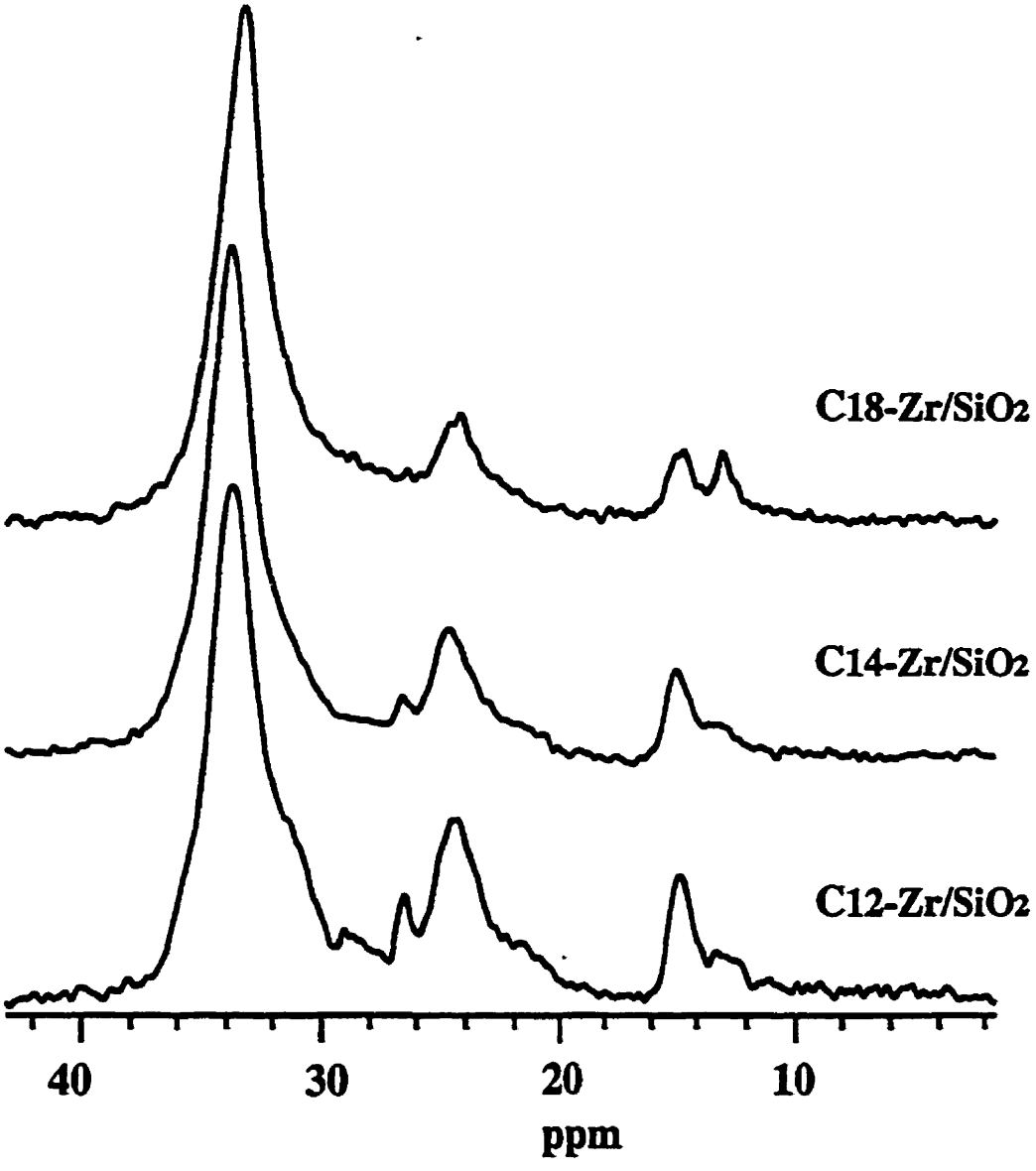

Figure 3.11 ^{13}C CPMAS spectra of zirconated silica-alkylphosphonic acids (chain lengths as indicated). Spectra were acquired in 10,000 scans with a contact time of 2 ms and a recycle delay of 3 s.

A sample of semicrystalline $Zr(O_3PC_{18}H_{37})$ was also studied by variable temperature ^{13}C CPMAS, shown in Figure 3.12. Chain disordering is not complete until above 110°C, confirming the higher thermal stability of the bulk crystalline material.

3.3.5 2D WISE

A further probe of chain mobility in the different regions of these samples was provided by the 2D WISE experiment described in section 1.4. This technique allows the indirect determination of proton linewidths, which are broad in crystalline solids, and narrowed by molecular motion.[34] The 2D WISE spectra acquired for the two monolayer samples; ZrO_2-ODPA and TiO_2-ODPA, and the spectrum of the bulk Al_2O_3 -ODPA are shown in Figures 3.13, 3.14 and 3.15 respectively together with the slices in the proton dimension for the hydrocarbon chain carbons in the extended trans segments (δ~33 ppm) and the gauchoid segments (δ~30 ppm).

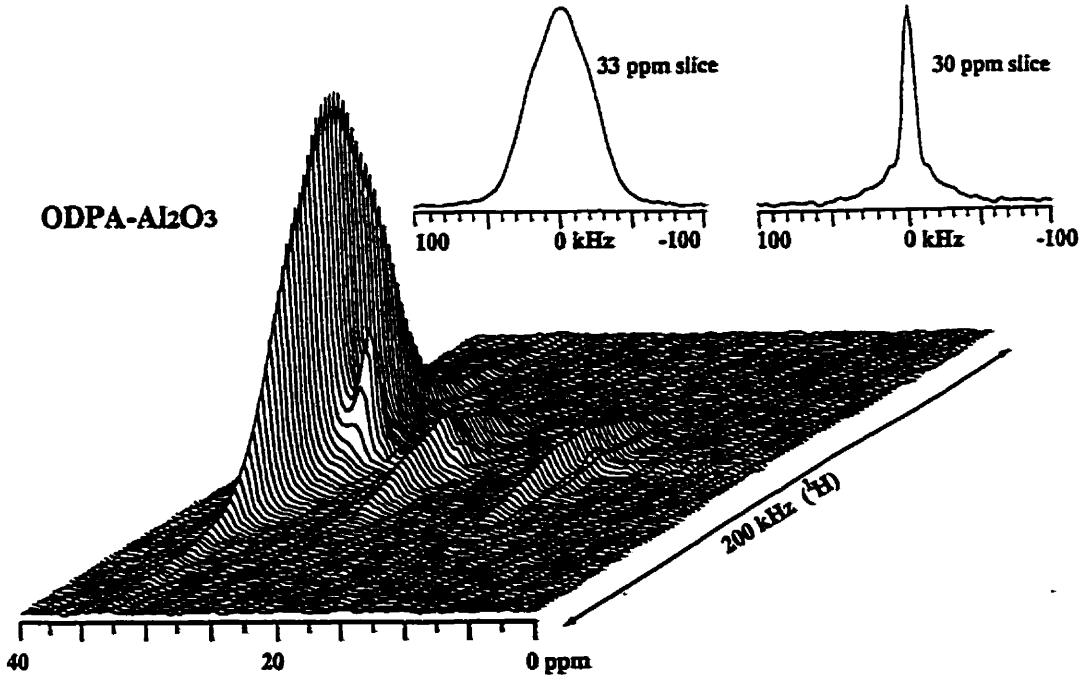

Figure 3.13 2D WISE spectrum of Al_2O_3-ODPA; spectrum was acquired in 142 scans with a contact time of 3 ms and a recycle delay of 3 s. The proton evolution period consisted of 128 increments with a dwell time of 1 μs.

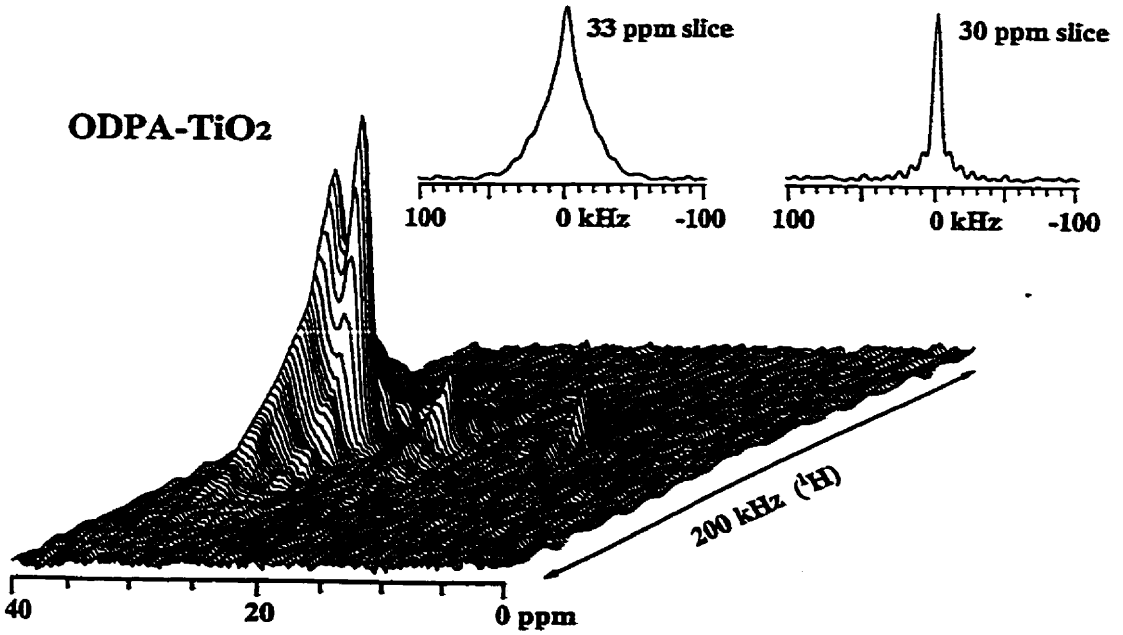

Figure 3.14 2D WISE spectrum of TiO_2-ODPA; spectrum was acquired in 500 scans with a contact time of 5 ms and a recycle delay of 1 s. The proton evolution period consisted of 64 increments with a dwell time of 2 μs.

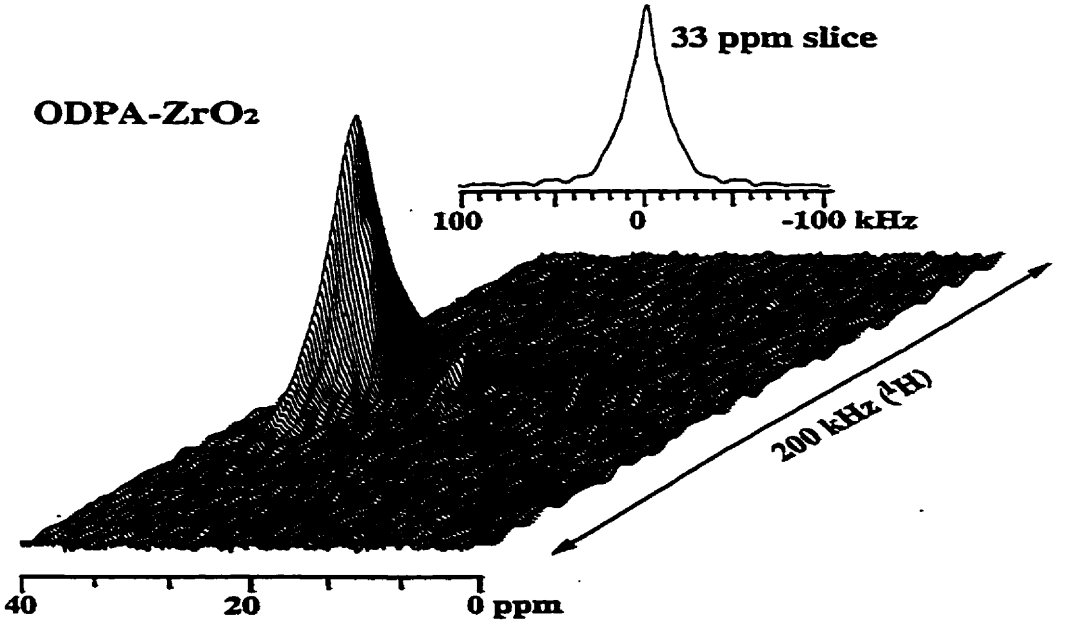

Figure 3.15 2D WISE spectrum of ZrO_2-ODPA; spectrum was acquired in 148 scans with a contact time of 3 ms and a recycle delay of 2 s. The proton evolution period consisted of 128 increments with a dwell time of 1 μs.

The bulk Al_2O_3-ODPA sample exhibits two domains with very different proton linewidths. The 30 ppm carbon peak has an associated ^1H linewidth of only ~7 kHz, typical of a highly mobile chain. The trans carbon peak at 33 ppm has a corresponding ^1H linewidth of $\Delta\upsilon_{1/2}$=52 kHz, comparable to those seen in crystalline polymers. By contrast, the TiO_2-ODPA monolayer sample, which also has so-called trans and gauche regions yields corresponding ^1H linewidths of ~20 and ~7 kHz respectively. The narrow width of the proton line associated with the so-called trans region reflects a less rigid packing of the all-trans chains compared with the packing seen in a bulk crystalline structure. A similar linewidth is also observed for the proton line associated with the single resolvable methylene carbon peak of the ZrO_2-ODPA ($\Delta\upsilon_{1/2}$ =23kHz). Comparable reductions in proton linewidths of the trans chains are evident for both the silica-OTS system and octadecanethiol-capped gold colloids. In the former case, the substantial motion of the chains was thought to be allowed for by the underlying siloxane network. In the gold alkanethiol sample the headgroup size along with the small particle size is thought to provide the additional volume needed for chain motion. The ZrO_2 particles have a much larger particle size, so that any intercalation is thought to be negligible, and chain packing should be similar to that observed on planar substrates. The loose packing of the chains must therefore be due to headgroup size and defects in surface bonding.

3.3.6 Spin diffusion

A number of attempts were made to carry out spin diffusion experiments on the TiO_2-ODPA system, where separate domains of ordered and disordered chains can be seen by ^{13}C CPMAS NMR. The dipolar filter and Goldman-Shen pulse sequences were unable to preferentially remove the rigid component. A series of 2D WISE spectra with incremented spin diffusion times also failed to isolate any appreciable spin diffusion. These pulse sequences succeed when the differential in dipolar couplings is large (i.e. the rigid and mobile regions have significantly different ^1H linewidths). Here the differential is relatively small (20 and 7 kHz), so it is impossible to discriminate against the more ordered component. In light of the small domain sizes calculated for the SiO_2-OTS

system (see Chapter 2), it is also possible that the different phases in this sample are not sufficiently separated.

3.3.8 2D Exchange

^{31}P 2D exchange spectra were carried out on non-spinning samples of TiO_2-ODPA and ZrO_2-ODPA in order to determine whether the proposed rotational motion of the hydrocarbon chains along their axes involves concomitant motion of the phosphonic acid head group. Spectra are shown in Figures 3.16 and 3.17 for ZrO_2-ODPA at room temperature with mixing times of 10 ms and 500 ms respectively. The slight growth in off diagonal intensity on increasing the mixing time suggests some slow motion of the phosphorus atom. This motion is likely random reorientation on the surface. Since we propose a monodentate binding, this motion could involve very slow small angle reorientations about the -P(O_2)–O-Zr surface linkage. Given the lack of substantial well defined off-diagonal patterns such as those seen in dimethylsulphone, a two site exchange is unlikely. Further interpretation of this data requires the use of simulation programs. These spectra will be repeated at higher and lower temperatures to confirm that a dynamic process is occurring.

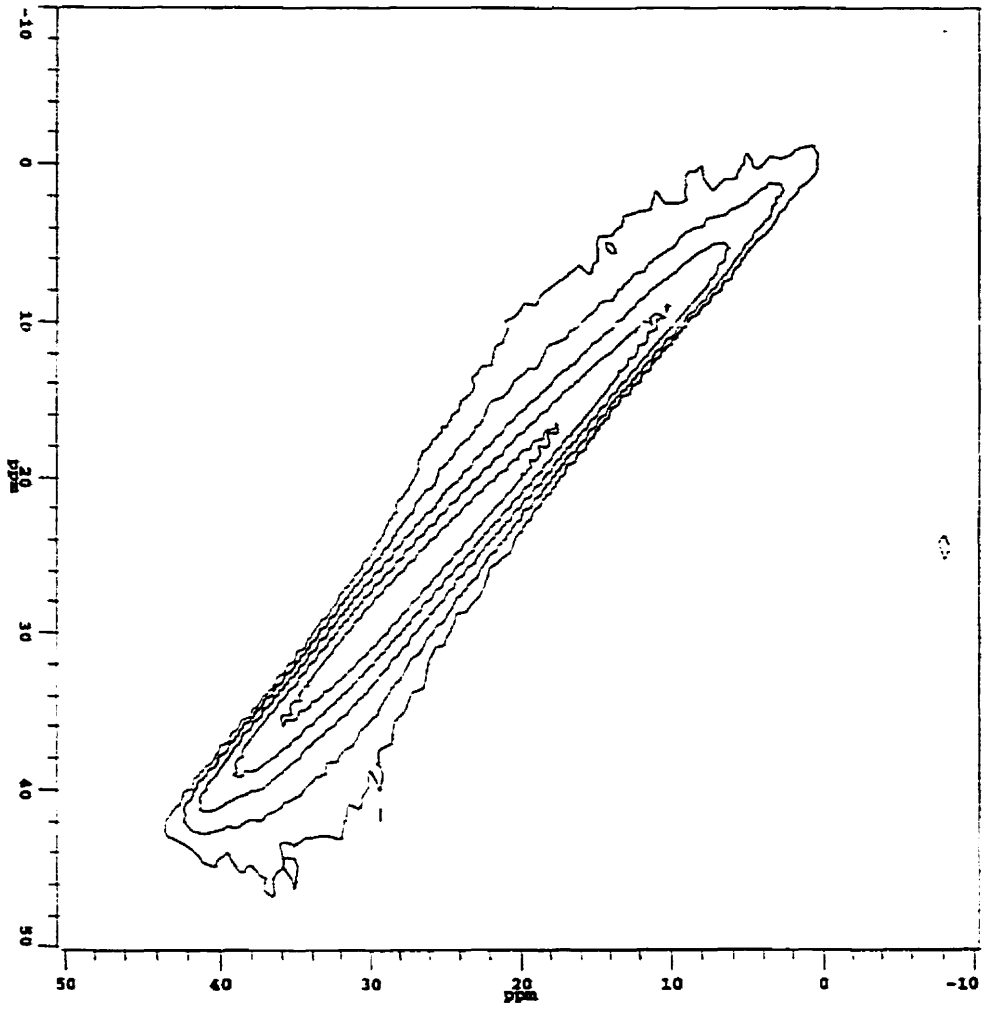

Figure 3.16 ^{31}P 2D exchange spectrum of ZrO_2-ODPA (static) with a mixing time of 10 ms. Spectrum was acquired in 660 scans with a contact time of 3 ms and a recycle delay of 1 s. The evolution period consisted of 128 increments with a dwell time of 20 μs.

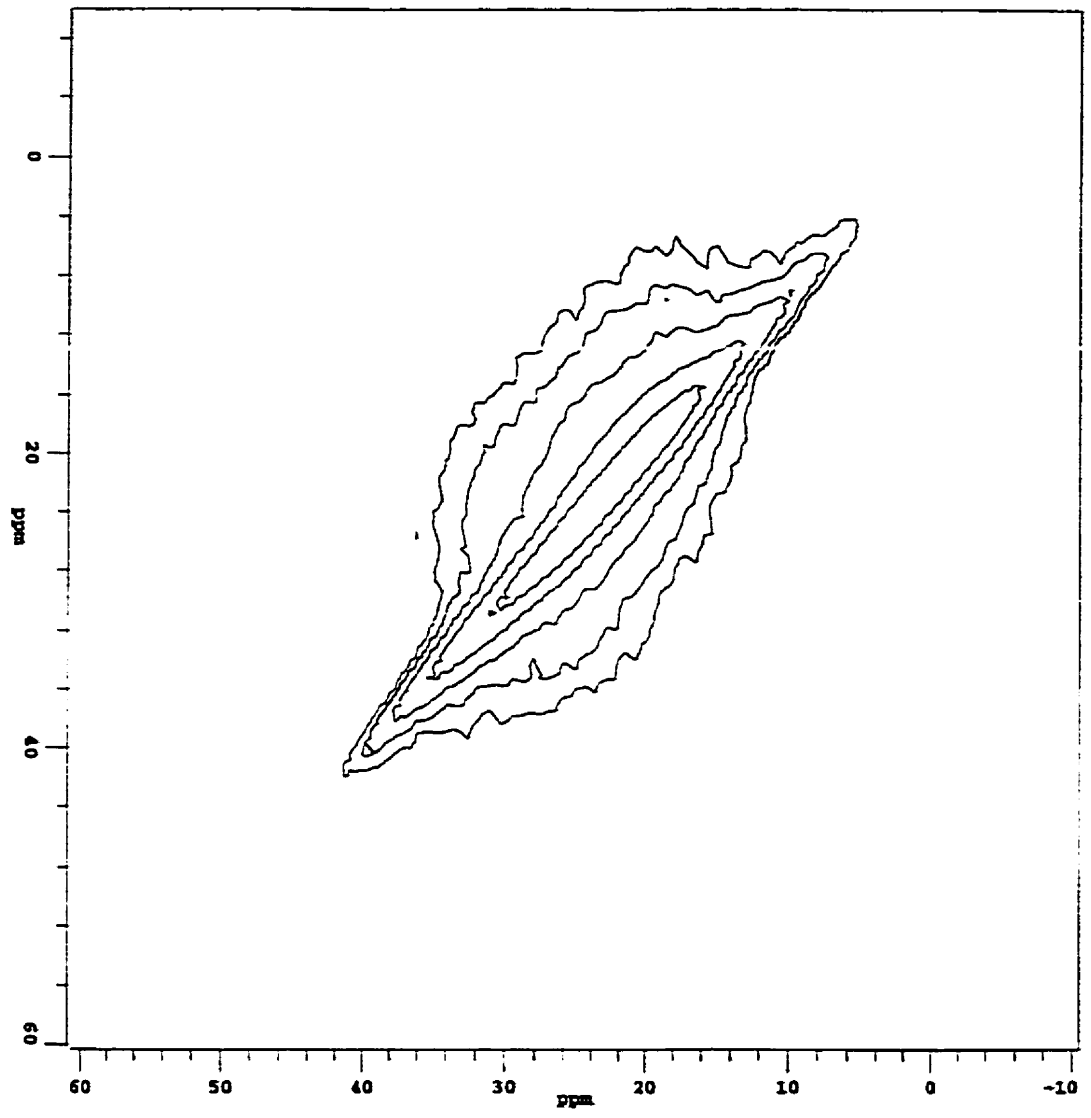

Figure 3.17 ^{31}P 2D exchange spectrum of ZrO_2-ODPA (static) with a mixing time of 500 ms. Spectrum was acquired in 660 scans with a contact time of 3 ms and a recycle delay of 1 s. The evolution period consisted of 128 increments with a dwell time of 20 μs.

3.4 Discussion

Of the four substrates used in this study, ZrO_2 produces the most ordered monolayers. Once again the potential of ^{13}C CPMAS NMR in assessing chain conformation has been demonstrated. In addition this system has also benefited from the use of ^{31}P CPMAS NMR. In spite of the heterogeneity of the ZrO_2 surface, and the large

size of the phosphonic acid headgroup, the bonding between SAM and substrate is strong, and the resulting monolayers have a high degree of conformational order, although with significant motional freedom around an axis parallel to the chain axis. TiO_2 provides a less satisfactory substrate, with a higher fraction of disordered chains, lower coverage and a weaker interaction between the phosphonate group and the oxide surface (as indicated by the smaller ^{31}P shift). Subsequent work has produced more highly ordered monolayers on titania, and optimization of preparation conditions is ongoing in our laboratory. Reaction with Al_2O_3 produces a bulk aluminoalkyl-phosphonate, rather than the desired monolayer structure. Literature from the supplier on this surface indicates that the Al_2O_3 is more susceptible to attack by acids than the titania and zirconia samples. The use of a silica substrate is also shown to be problematic due to the formation of a bulk complex when a Zr primer layer is employed. The other alternative primer layer, that of a phosphonic acid terminated silane is unfortunately prone to the problems commonly associated with the alkylsilane monolayers, namely vertical polymerization and lack of surface siloxane bonds.

The high conformational order and coverage displayed by the ZrO_2-ODPA system make it a good model for 2D SAMs on planar metal oxides. The relatively large average particle size as compared to the gold colloids produces monolayers without intercalation with chains on other particles, since extensive intercalation is only possible with very small particles (2-5 nm). The mobility within the hydrocarbon chains appears to be similar to that of the gold thiols, while the end methyl groups, which are at the hydrocarbon/air interface rather than a bilayer type environment, are more disordered in the ODPA monolayers. The principle importance of the NMR study lies in the more complete dynamic and structural picture offered by ^{13}C and ^{31}P CPMAS NMR, compared with earlier data from vibrational spectra. Like the alkylsilane system discussed in Chapter 3, the ZrO_2-ODPA and TiO_2-ODPA systems contain conformationally ordered, but motionally disordered chains. The presence of considerable motions about the chain axes make the dynamic state of these SAMs more closely resemble that of alkyl chains in stiff macromolecules with flexible side chains, or model bilayer systems.

The ^{31}P spectra allow more detailed analysis of interfacial bonding, which in the case of ZrO_2-alkylphosphonates is most probably due to monodentate surface-phosphonic acid ester linkages. These spectra also confirm the similarities in bonding to SAMs of different chain lengths, permitting the elucidation of the dependence of conformational order on chain length (chains with less than 16 carbon atoms are disordered at room temperature).

Variable temperature ^{13}C CPMAS spectra of both ZrO_2-ODPA and TiO_2-ODPA indicate a reversible gradual thermal disordering which is complete by 60°C. The presumed monodentate surface bonding mode would lessen the steric constraints on the rough surface of the metal oxide, while the large size of the phosphonate headgroup will increase the free volume available to the chains. Both these factors allow for more motion of the chains. In the bulk zirconium phosphonate salt the cross section of the chains is 25 Å (as estimated from X-ray diffraction studies of bulk zirconium phosphonates),[7] which is large compared to the cross section of 18 Å for the chains in crystalline polyethylene.[35] In the bulk structure the phosphonate headgroup is tridentate, with the oxygen atoms bound to three different Zr ions. Here the alkyl chains have large tilt angles of around 31°. The monolayer has less steric constraints and the larger available free volume is clearly manifested in the greater mobility of the chains at room temperature, and the relatively low temperature of the chain melting procedure (~60°C, compared with ~120°C in both the bulk zirconium phosphonate and the alkylsilane SAM). As evidenced by the broadness of the transition, the cooperative nature of the order/disorder transitions is restricted due to the attachment of the headgroup. The 2D exchange spectra indicate some very slow motion of the phosphonate group occurs. Further variable temperature studies will confirm that the observed patterns are motion related.

These results are helpful in considering the behavior of the thiol SAMs on gold (to be discussed in Chapter 4). The evidence suggests that order-disorder transitions are a general feature of self-assembled monolayers. The similarities observed between the alkylphosphonate systems and the alkane thiols, in spite of the differences in substrate size and surface type (i.e. spherical for the metal oxides compared with faceted surfaces on the gold colloids) shows that these transitions are inherent to self-assembled chains.

The alkylphosphonates are described as 2D SAMs, while the intercalation caused by the smaller size of the gold particles has led to their being described as 3D SAMs, yet the correspondence in the chainlength dependence of the order-disorder transition, along with clear evidence that the headgroups in both cases remain immobilized shows that the nature of the transitions is inherently similar in both cases.

References

[1] Gao, W.; Reven, L. *Langmuir* **1995**, *11*, 1860.

[2] Hong, H. G.; Sackett, D.D.; Mallouk, T. E. *Chem.Mater.* **1991**, *3*, 521.

[3] Neff, G. A.; Page, C. J.; Meintjes, E.; Tsuda, T.; Pilgrim, W. -C.; Roberts, N.; Warren, W. W. *Langmuir* **1996**, *12*, 238.

[4] Duprat, M.; Shiri, A.; Derbali, Y.; Pebere, N. *Electrochemical Methods in Corrosion Research. Materials in Corrrosion Research. Materials Science Forum:* Duprat, M., Ed.; Trans Tech: Aedermannsdorf, 1986; Vol 8, p.267.

[5] Aguilar, M.; Miralles, N.; Sastre, A.M. *Rev.Inorg.Chem.* **1989**, *10*, 93

[6] Francis, M. D.; Russell, R. G. G.; Fleisch, H. *Science* **1969**, *165*, 1264.

[7] Cao, G.; Hong, H.-G.; Mallouk, T. E. *Acc. Chem. Res.* **1992**, *25*, 420.

[8] (a) Katz, H. E. *Chem. Mater.* **1994**, *6*, 2227. (b) Byrd, H.; Pike, J. K.; Talham, D. R. *Chem.Mater.* **1993**, *5*, 709. (c) Byrd, H.; Whipps, S.; Pike, J. K.; Ma, J.; Nagler, S. E.; Talham, D. R. *J. Am. Chem. Soc.* **1994**, *116*, 295.

[9] Gao, W.;Dickinson, L.; Morin, F.G.; Reven, L. *Chem.Mater.* **1997**, *9*, 3113

[10] (a) Maoz, R.; Sagiv, J. *J. Colloid Inter. Sci.* **1984**, *100*, 465. (b) Schilling, M. L.; Katz, H. E.; Stein, S. M.; Shane, S. F.; Wilson, W. L.; Burarro, S.; Ungashe, S. B.; Taylor, G. N.; Putvinski, T. M.; Chidsey, C. E. D. *Langmuir* **1993**, *9*, 2156. (c) Woodward, J.T.; Ulman, A.; Schwartz, D.K. *Langmuir* **1996**, *12*, 3626

[11] Lukes, I.; Morbaruah, M.; Quin, L. D. *J. Am. Chem. Soc.* **1994**, *116*, 1737.

[12] (a) Schafer, W. A.; Carr, P. W.; Funkenbusch, E. F.; Parson, K. A. *J. Chromatography* **1991**, *587*, 137. (b) Randon, J.; Blanc, P.; Paterson, R. *J. Membrane Science* **1995**, *98*,

119. (c) Nawrocki, J.; Dunlap, C. J.; Carr, P. W.; Blackwell, J. A. *Biotechnol. Prog.* **1994**, *10*, 561.

[13] Gardner, T. J.; Frisbie, C.; Daniel; Wrighton, M. S. *J. Am. Chem. Soc.* **1995**, *117*, 6927.

[14] Péchy, P.; Rotzinger, F. P; Nazeeruddin, M. K.; Kohle, O.; Zakeeruddin, S. M.; Humphry-Baker, R.; Grätzel, M. *J. Chem. Soc., Chem. Commun.* **1995**, 65.

[15] Folkers, J. P.; Gorman, C. B.; Laibinis, P. E.; Buchholz, S.; Whitesides, G. M.; Nuzzo, R. G. *Langmuir* **1995**, *11*, 813.

[16] (a) Ulman, A. *Adv. Mater.* **1991**, *3*, 298. (b) Ulman, A. *Chem. Rev.* **1996**, *96*, 1533.

[17] Bhattacharya, A.K.; Thyagarajan, G. *Chem. Rev.* **1981**, *81*, 415.

[18] Hong, H.G.; Sackett,D.D.; Mallouk,T.E. *Chem.Mater.* **1991**, *3*, 521

[19] Frey, B. L.; Hanken, D. G.; Corn, R. M. *Langmuir* **1993**, *9*, 1815.

[20] Putvinski, T. M.; Schilling, M. L.; Katz, H. E.; Chidsey, C. E. D.; Mujsce, A. M.; Emerson, A. B. *Langmuir* **1990**, *6*, 1567.

[21] (a) O'Brien, J. T.; Zeppenfeld, A. C.; Richmond, G. L.; Page, C. J. *Langmuir* **1994**, *10*, 4657. (b) Zeppenfeld, A. C.; Fiddler, S. L.; Ham, W. K.; Klopfenstein, B. J.; Page, C. J. *J. Am. Chem. Soc.* **1994**, *116*, 9158.

[22] Byrd, H.; Snover, J. L.; Thompson, M. E. *Langmuir* **1995**, *11*, 4449.

[23] (a) Cao, G.; Lee, H.; Lynch, V.M; Mallouk, T.E. *Inorg.Chem.* **1988**, *27*, 2781. (b) Cao, G.; Lee, H.; Lynch, V.M; Mallouk, T.E. *Solid State Ionics* **1988**, *26*, 63

[24] Gao, W.; Dickinson, L.Morin, F.; Reven, L., *Chem.Mater.*, **1997**, *9*, 3113

[25] Cao, G.; Hong, H.-G.; Mallouk, T.E., *Acc.Chem.Res.*, **1992**, *25*, 420

[26] Seip, C.T.; Granroth, G.E.; Meisel, M.W.; Talham, D.R., *J.Am.Chem.Soc.*, **1997**, *119*, 7084

[27] (a) Harris, R. K.; Merwin, L. H.; Hägele, G. *Z. Naturforsch.* **1989**, *44b*, 1407. (b) Burwell, D.A.; Valentine,K.G.; Thompson, M.E. *J. Magn. Reson.* **1992**, *97*, 498. (c) Burwell, D.A.; Valentine, K.G.; Timmermans, J .H.; Thompson, M.E. *J. Am. Chem. Soc.* **1992**, *114*, 4144.

[28] Nawrocki,J.; Rigney, M.P.; McCormick, A.; Carr, P.W., *J.Chromatogr.*A, **1993**, *657*, 229

[29] Maeda, K.; Kiyozumi, Y.; Mizukami, F. *Angew. Chem. Int. Ed. Engl.* **1994**, *33*, 2335.

[30] (a) Earl, W. L.; VanderHart, D. L. *Macromolecules* **1979**, *12* , 762. (b) Tonelli, A. E.; Schilling, F. C. *Acc. Chem. Res.*, **1981**, 223.

[31] Badia, A.; Gao, W.; Singh, S.; Demers, L.; Cuccia, L, Reven, L. *Langmuir* **1996**, *12*, 1262.

[32] (a)Pursch, M.; Strohschein, S.; Händel, H.; Albert, K. *Anal. Chem.* **1996**, *68*, 386. (b) Albert, K.; Schmid, J.; Pfleider, B.; Bayer, E. *Chemically Modified Surfaces*; Elsevier Science Publishers: Amsterdam, 1992; Vol. 4, p. 105.

[33] Dubois, L. H.; Nuzzo, R. G. *Annu. Rev. Phys. Chem.* **1992**, *63*, 437.

[34] (a) Schmidt-Rohr, K.; Clauss, J.; Spiess, H. W. *Macromolecules* **1992**, *25*, 3237. (b) Clauss, J.; Schmidt-Rohr, K.; Adam, A.; Boeffel, C.; Spiess, H. W. *Macromolecules* **1992**, *25*, 5208.

[35] Bent, S. F.; Schilling, M. L.; Wilson, W. L.; Katz, H. E.; Harris, A. L. *Chem. Mater.* **1994**, *6*, 122.

Chapter Four: Surface bonding issues and the effect of terminal hydrogen bonding on the structure and dynamics of alkanethiol-capped gold particles.

4.1 Introduction

Many of the structural and dynamic properties of alkanethiol SAMs on gold colloids have already been studied using the solid state NMR techniques employed in the preceding chapters.[1] The synthesis of high surface area analogues of the ubiquitous planar gold-alkanethiol systems[2] proved helpful in resolving some of the questions concerning conformational order along the hydrocarbon chains.[3] In previous work,[1] the broadening of the ^{13}C spectra on absorption of both long (18 carbons) and shorter chain (7 carbons) alkanethiols onto colloidal gold, along with the complete disappearance of the carbon resonances of those nuclei closest to the sulfur headgroup has been cited as evidence of a strong interaction with the metal surface. In addition the γ-gauche effect observed in ^{13}C CPMAS NMR has been observed for the octadecylthiol-capped gold and the 2D WISE spectrum yields proton linewidths of ~20 kHz for the conformationally disordered shoulder at 31 ppm and ~35 kHz for the all-trans region. The similarities between these results and those obtained for the metal oxide-octadecylphosphonic acid systems was explored in Chapter 3. One important factor in considering the gold colloid substrates is the small size of the gold nanoparticle, which leads to significant intercalation between groups of chains on neighboring particles as shown by transmission electron microscopy. This will also affect the free volume available to the hydrocarbon chains. Chain length dependent order/disorder transitions were observed as a gradual increase in the component at 31 ppm and concomitant decrease in intensity of the 33 ppm peak. The overall degree of conformational order, along with the degree of thermal stability was found to be increased for a hydroxy terminated alkane thiol, $HO(CH_2)_{16}SH$ on gold, which underwent chain melting at around 70°C compared with 55°C for $Au\text{-}SC_{18}H_{37}$.

Synthesis of ^{13}C labeled gold-thiols was carried out in order to better determine the nature of the metal-thiol bond, which has been the source of much speculation in the literature.[4] Suggested bonding modes have included gold thiolates (RS^{-1}) and dialkyl disulfides (R-S-R). In the first part of this chapter, ^{13}C CPMAS NMR spectra of 1-^{13}C and 2-^{13}C labeled $CH_3(CH_2)_{12}CH_2S$/Au colloids and $[Au\{SC_{14}H_{29}\}]_n$ polymer complexes, along with their unlabeled shorter chain (4 carbons) analogues will be presented. It is believed that these spectra are indicative of the formation of a thiolate bond on chemisorption of the alkanethiols to gold, and that, in spite of the intercalation between hydrocarbon chains on adjacent colloids, the correspondence observed between the properties of the SAMs on colloidal and planar surfaces is good enough that this conclusion about the bonding mechanism can be extended to the planar SAMs.

Finally the effects of hydrogen bonding on chain conformation and stability have been further investigated through the solid-state NMR spectra of CO_2H terminated alkanethiols of intermediate chain length deposited on gold colloids. As discussed in Chapter 3, the simple alkanethiols are disordered for chain lengths under 16 carbon atoms. The presence of carboxylic acid moieties is shown to significantly improve thermal stability, offering a number of possibilities for future study.

4.2 Surface bonding characterization

Use of the gold-alkanethiol colloids in examining the nature of the surface bond depends on the viability of making a direct link between these nanoparticle systems and the planar systems. This connection has been proposed on the basis of three similarities:

a. an excellent correspondence between the chain-length dependent order/disorder phase transitions observed both by DSC and variable temperature FTIR spectroscopy studies on both systems.[5]

b. the fact that the colloids are actually highly faceted, with (111) and (100) single crystal faces, as shown by high resolution electron microscopy[6] (the 111 face is the one generally used in studies on planar gold samples).

c. the similarity in gauche hydrocarbon chain populations at room temperature as determined by FTIR studies.

Since the alkyl chain spacing, chain tilt and cooperative thermal behavior are largely controlled by the surface bonding, the assumption that both the planar and colloidal systems exhibit similar structural features seems reasonable. The similarities in the mode of alkylsulfur-gold bonding is confirmed by XPS data.[7]

The nature of the interfacial region can be investigated by solid state NMR, but unlike the alkylphosphonates and alkylsilanes, no information is available from the headgroup itself. This is because the ^{33}S nucleus is quadrupolar (it has spin 5/2) which make resonances too broad, and relaxation times too rapid for spectra to be observed. In addition the extensive line broadening of those signals for carbons close to the gold surface makes resolution of individual carbon sites difficult. For this reason the C_{14} thiol capped gold and its equivalent polymeric complex have been selectively ^{13}C labeled as close to the headgroup as possible. The solid state ^{13}C CPMAS NMR spectra of the C1 and C2 labeled nanoparticles and complex are shown in Figure 4.1, along with spectra of the unlabeled shorter 4-carbon thiol nanoparticle and complex. The chemical shifts are summarized in Tables 4.1 and 4.2, together with shifts for the free thiol, thiolate and disulfide salts. The selective peak enhancement provided by labeling indicates that in the 1-^{13}C and 2-^{13}C labeled $C_{14}S$/Au colloids, broad resonances are seen for C1 and C2 which are shifted downfield by 18 ppm and 12 ppm respectively from the unbound thiol shifts. Comparison of these shifts with the C1 and C2 shifts in the C14 thiolate salt, shifted downfield from the free thiol by 1.7 ppm (C1) and 5.2 ppm (C2) preclude the formation of a simple physisorbed thiolate salt, the shifts being much too large. Similarly other weakly associated organosulfur species can be eliminated from consideration; the ^{13}C chemical shift trend in the nanoparticles, where C2 is 4 ppm downfield from C1 is the reverse of the shifts observed in the disulfide or sulphonate where C2 appears upfield from C1 by 9.6 ppm and 22.9 ppm respectively. When attempting to assign the peaks and determine the most likely form of the gold species, it is therefore important to consider both the α and β carbons, since the C2 shifts are also known to be sensitive to substituents. Similarities in shift between only C1 or C2 and the model values may be

coincidental. By observing the trend of both the C1 and C2 shifts, it was concluded that the nanoparticles were most similar to the polymer, suggesting that the Au-S bonding is comparable in these two systems.

The inclusion of the shifts of the diamagnetic Au(I) alkylthiolates $[Au(I)\{SC_{14}H_{29}\}]_n$ in this study was aimed at ruling out a metallic contribution in the C1 shift of the thiol-capped colloids. Although ^{13}C Knight shifts have only previously been reported for carbons directly bound to metals,[8] it was considered that the Knight effect (a shift contribution from the conduction electrons of the gold core) may be operational here. Knight shifts for adsorbates on metals such as Pt and Pd are confirmed experimentally if the relaxation follows the Korringa law, i.e. a linear relationship is observed between T_1 and temperature. The contribution of the Knight shift leads to ^{13}C shifts which are much greater than the usual chemical shift range of diamagnetic organometallic species. The modified nanoparticles do not exhibit Korringa behavior, the spin-lattice relaxation time shows a temperature dependence which is typical of dipolar relaxation in the slow limit side of the correlation time vs. T_1 curve. However additional confirmation that a Knight shift is not responsible comes from both the C1 and C2 resonances in the $[Au(I)\{SC_{14}H_{29}\}]_n$ and the $[Au(I)\{SC_4H_9\}]_n$ complexes. In both cases,the C1 and C2 shifts are coincident, appearing at about 40 ppm, which is a downfield shift of ~16 ppm for C1 and ~4-5 ppm for C2 from the parent thiol. The majority of Au(I) thiolates are reportedly 2-coordinate with linear polymeric or ring structures.[9] The correspondence between the shifts of the complexes and the nanoparticles as indicated in Figure 4.1 suggest that the former can be used as a structural analogue in ruling out the contribution of a metallic Knight effect. This means that the large downfield shifts seen for those carbons closest to the headgroup much originate from interactions between the gold and the sulfur.

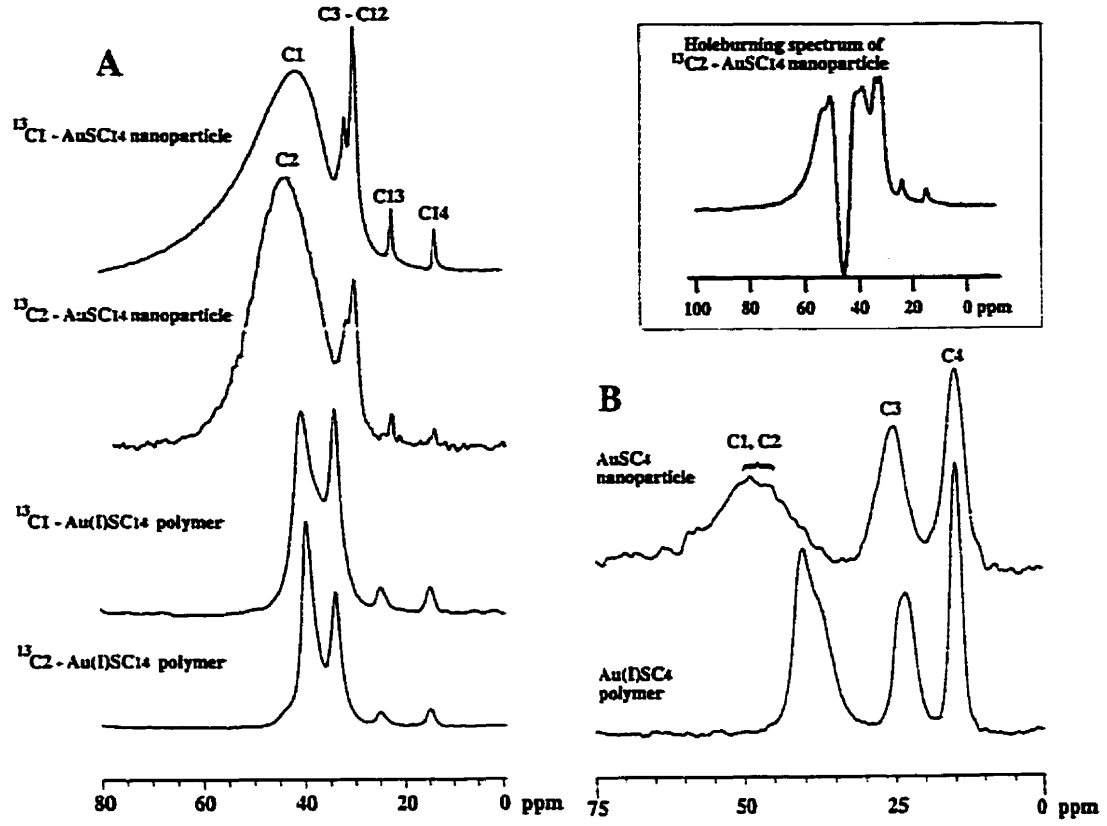

Figure 4.1 ^{13}C CPMAS spectra of various goldthiol compounds as indicated. For the nanoparticles between 10,000 and 25,000 scans were acquired, while the polymers were acquired with 100 to 1000 scans. Contact times were 2 ms, recycle delay was 3 s. The inset shows a DANTE experiment of the C2 labeled $AuSC_{14}$ nanoparticle. This spectrum was acquired in 100 scans, with a contact time of 2 ms and a recycle delay of 3 s. The DANTE sequence employed 12 pulses with a t_p of 0.7 μs and a t_d of 100μs.

C_4H_9	C_4H_9SH (thiol)[a]	C_4H_9SNa (thiolate)[a]	$(C_4H_9S)_2$ (disulfide)[b]	$Au(I)SC_4H_9$ (complex)[c]	Au/SC_4H_9 nanoparticles[c]	
					shift	width (kHz)
C1	24.1	24.1	38.9	40.1(sh 38)[d]	~46[e]	1115
C2	35.9	38.6	31.4	40.1[d]	~46[e]	1115
C3	21.3	21.6	21.7	23.4	25.2	285
C4	13.3	13.1	13.7	14.7	15.0	265

Table 4.1 Carbon-13 Chemical Shifts (δ (ppm)) for R = C_4H_9S. [a] Solution spectrum. [b] from reference 13. [c] Solid-state spectrum. [d] Deconvolution yields two peaks integrating at 3:1. [e] Integration yields two carbons.

$C_{14}H_{29}$	$C_{14}H_{29}SH$[a]	$C_{14}H_{29}SNa$[a]	$(C_{14}H_{29}S)_2$[a]	$C_{12}H_{25}SO_3Na$[a]	$Au(I)C_{14}H_{29}$[c]	$Au/SC_{14}H_{29}$[c]	
C1	24.5	26.2	39.2	52.74	40.1(sh 38)[f,g]	~42[g]	1300
C2	33.9	39.1	29.6	29.87	39.4[g]	~46[g]	1015

Table 4.2 Carbon-13 Chemical Shifts (δ (ppm)) for R = C_4H_9S. [a] Solution spectrum. [b] from reference . [c] Solid-state spectrum. [d] Deconvolution yields two peaks integrating at 3:1. [e] Integration yields two carbons. [f] Two peaks integrate as 1:1. [g] From ^{13}C labeled thiol.

Speculation in the literature in regards to the gold-sulfur interaction has suggested either a metal-thiolate or a metal-disulfide bond.[3] The C1 shifts in the Au(I) complexes (40 ppm) and Au/SC_{14} nanoparticles (42 ppm) are closest to those of the unbound dialkylsulfides (39 ppm). While this could be indicative of disulfide type bonding in both

the complex and, by extension, the thiol-capped colloid, there are examples in the literature of similar shifts for thiolate rather than disulfide structures. Fijolek *et al* studied a silver alkylthiol complex,[10] $AgS(CH_2)_3CH_3$, which was fully characterized by Raman spectroscopy, clearly indicating that the bridging organosulfur is a thiolate. ^{13}C NMR of the all trans form of this complex yielded peaks at 15.8, 226.4, 39.3 and 40.5 ppm. It therefore seems unlikely that the gold-sulfur bonding mechanism can be definitively assigned on the basis of correspondence with the shifts of the unbound dialkylsulfide. As stated previously, the trend in both C1 and C2 shifts must be considered, and for the present the relationship between the complex and the colloid system seems to support the assertion of a metal-thiolate bond. Finally this assertion is supported by the Raman spectra of the Au(I) thiolate complexes which are not consistent with a bridging disulfide.

In addition to the large shifts of the C1 and C2 carbons in the gold alkanethiol nanoparticles, the ^{13}C NMR spectra are notable for the extreme broadness of the C1 and C2 resonances. These linewidths vary linearly with field strength (the linewidth measured at 25MHz being one third of the linewidth acquired at 75MHz). This kind of field dependent broadening must arise from a distribution of isotropic chemical shifts, or similar shift-like interactions such as the Knight shift or bulk magnetic susceptibility (discussed below).

In order to confirm that a residual linewidth in the solid state which can not be narrowed via magic angle spinning is inhomogeneously broadened an experiment whereby strong irradiation at one frequency within the broad line produces a hole in the lineshape can be carried out. Strong irradiation at one frequency within a homogeneously broadened line will reduce the intensity of the whole lineshape uniformly.[11] A holeburning spectrum, acquired by the Dante pulse sequence described in sections 1.4 is also shown in Figure 4.1 and demonstrates that the line is indeed inhomogeneously broadened.

As discussed previously, the Knight shift has been ruled out as a possible cause of broadening. Inhomogeneous broadening via existence of a range of isotropic shifts probably arises from the presence of different chemisorption sites and/or non-spherical particle shapes. As described previously, the gold colloids are actually faceted, so that

thiolates can be adsorbed onto either the (111) or (100) faces of the small crystallites as well as on edge and corner sites. In diamagnetic substances materials tend to slightly exclude the magnetic lines of force, so that the internal field experience is somewhat lower than the applied field. This effect, known as bulk magnetic susceptibility[12] stems from the magnetic moments of the electrons, and causes a slight shift in all NMR signals. The effect is usually too small to be of concern. However in multifaceted particles, the BMS will vary for each type of face and it must therefore be considered a potential source of broadening. The linewidths of each carbon site in the short chain Au/SC_4 nanoparticle are also shown in Table 4.1, the fact that the line broadening drops off sharply along the chain is probably an indication that a chemical shift distribution is the major contributor (the BMS effect would have a more gradual decrease along the chain).

In summary, the similarity in ^{13}C chemical shifts of the Au/SR colloids and Au(I) alkylthiolates suggests that the chemisorbed species on the gold nanoparticle is probably a thiolate rather than a disulfide. The faceted nature of the particles give rise to broadened lines for the C1 and C2 positions. No evidence of a Knight shift contribution to the C1 shift is observed. The close correspondence observed thus far, between the properties of thiols absorbed on planar and colloidal surfaces indicates that any conclusions based on ^{13}C NMR studies of gold-sulfur interactions in the nanoparticle system can be legitimately transferred to the planar RS/Au SAMs.

4.3 The effects on chain stability, structure and dynamics of terminal hydrogen bonding in the gold-alkanethiol nanoparticle system.

4.3.1 Introduction

The effects of terminal group induced hydrogen bonding on the dynamics and thermal stability of the gold-alkanethiol system has been investigated for a wide variety of terminal groups.[13] Addition of terminal groups other than methyl entities has implications not only on structural properties of the SAMs themselves, but also opens up possibilities for further reactive steps, catalysis[14] and chemical sensor design.[15] Surface hydroxyl and carboxyl groups provide useful sites for chemical transformations, e.g. reactions with alkanoic acids or bases to give bilayer type structures stabilized by hydrogen bonds.[16] Characterization of these functionalized films, has been predominantly carried out on planar samples and using the usual methods popular in such studies, principally FTIR, ellipsometry, XPS and electrochemical investigations. Such work has ascertained that while intramonolayer hydrogen bonding can increase film stability,[17] it may also introduce conformational disorder through electrostatic repulsive interactions between polar terminal groups.[18] The extent to which this disorder penetrates along the hydrocarbon chain is also a relevant concern. Studies on planar systems have yielded a number of results, sometimes contradictory. Polar derivatives are prone to environmental contamination, such as moisture adsorption, so that long term stability may be low.[19] Certainly the hydroxy terminated monolayers seem to be problematic, with evidence for long-term reorganization, the rate of which depends on chain length and temperature.[20]

Fortunately the functionalized monolayers can also be incorporated into the colloidal gold-alkanethiol synthetic procedure. Results of solid state NMR of the hydroxy terminated alkanethiol-capped gold nanoparticles have been reported previously,[1] and will be presented here only as a basis of comparison for the carboxyl terminated systems. Like the unfunctionalized SAMs, a close correspondence is seen between results on the planar and colloidal systems, e.g thermal transitions are observed at 70°C for the HO-$(CH_2)_{16}$S-Au colloid as seen by variable temperature ^{13}C CPMAS and for the planar

system of the same thiol investigated by electrochemistry. Such similarities in behavior as seen by techniques with very different time scales and sensitivities is a good indication that the two dimensional and three dimensional systems are closely related.

4.3.2 Results and discussion

The presence of the carboxyl groups greatly enhances the conformational order seen in the SAMs. Due to this increased stabilization conferred on the assemblies by the intra particle hydrogen bonding, chains as short as eight carbons in length display ^{13}C spectra indicative of hydrocarbon environments with a predominantly trans chain structure, as shown in Figure 4.2.

In addition, this chain ordering persists to much higher temperatures, with the onset of chain melting occurring at 140°C, and a completely liquid-like spectrum only visible at 160°C. The FTIR spectra also reflect a high degree of order, but more informative is the position of the C=O stretching band, which appears at 1708cm^{-1}, a value typical for systems with extensive hydrogen bonding. No band is seen at 1740cm^{-1}, so that no non-hydrogen bonded carboxyl chain ends are present.

This increased thermal stability is not only significantly higher than that observed for hydroxy terminated thiols (where the transition temperature is only increased by about 20°C from the methyl terminated thiol), but is also accompanied by evidence of much greater dynamic stability under ambient conditions. The 2D WISE spectra of the Au-$S(CH_2)_{16}OH$ and Au-$S(CH_2)_7CO_2H$ samples, along with the proton slices of the 33 ppm ^{13}C peaks are shown in Figure 4.3. The acid terminated SAM displays a proton linewidth of 53 kHz, a value typical of rigid solids, indicative of a immobilized hydrocarbon chain structure.[21] By contrast the alcohol terminated monolayer has a reduced proton linewidth of around 30 kHz, and a triangular shape linewidth. This dipolar slice is similar to those seen for the alkylphosphonic acids and indicates that considerable motion occurs along the chain axis of the all-trans alkyl chains.[22]

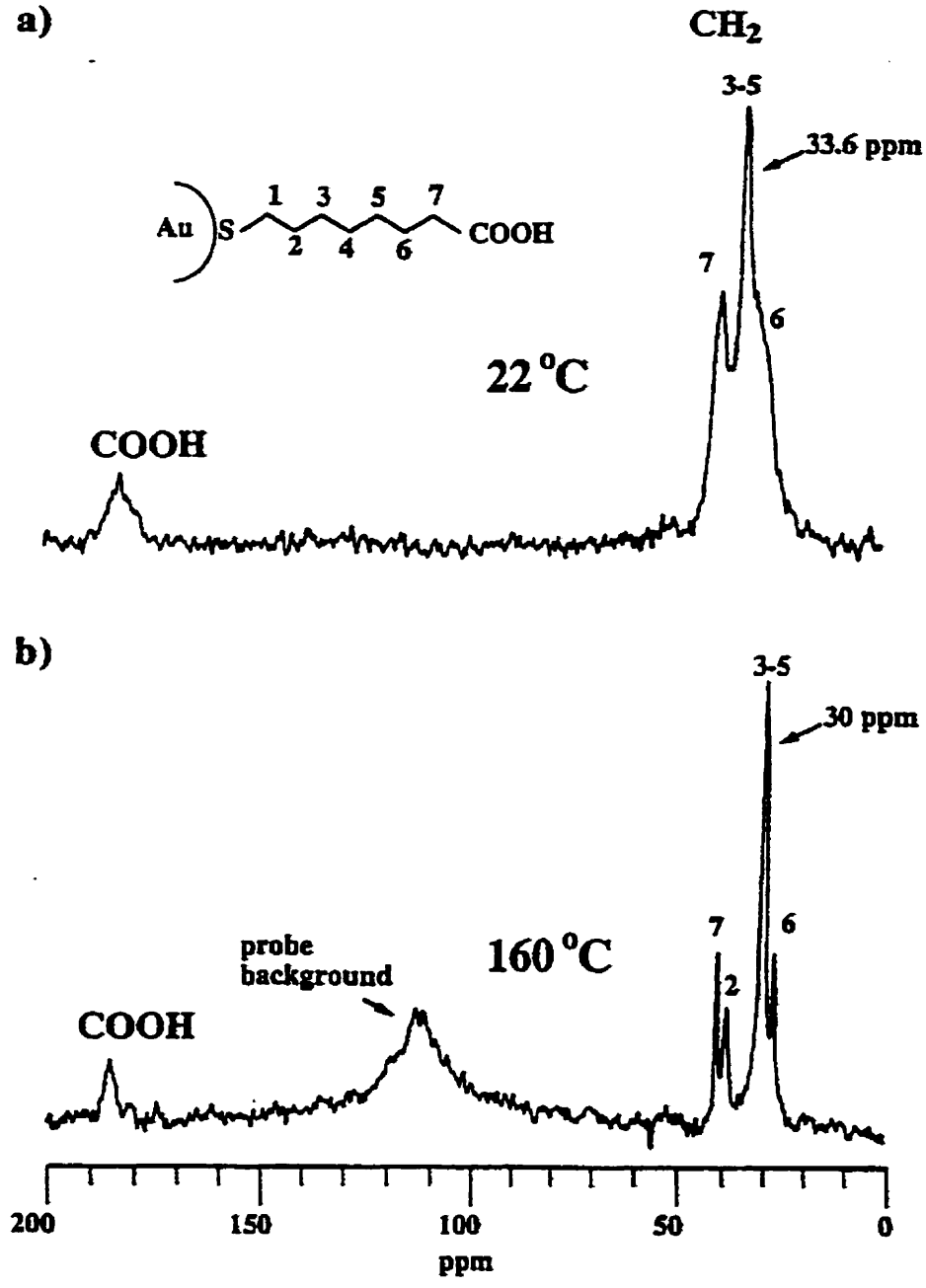

Figure 4.2 ^{13}C spectra of $HO_2C(CH_2)_7S$-Au nanoparticles at the temperatures indicated. At 20 °C the spectrum was acquired by CPMAS in 1000 scans with a contact time of 2 ms and a recycle delay of 2 s. At 160°C direct ^{13}C polarization was used with 200 scans and a recycle delay of 5 s.

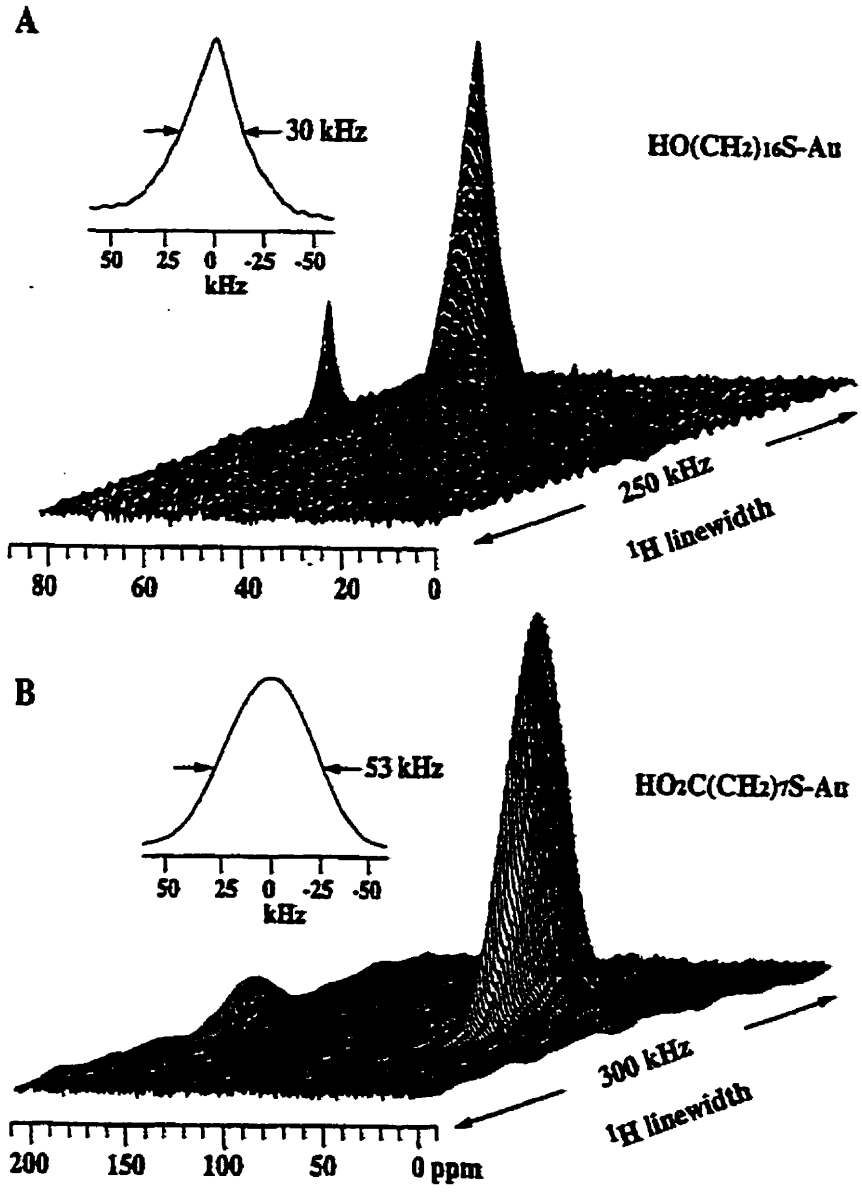

Figure 4.3 2D WISE spectra of (A) $HO(CH_2)_{16}S$-Au and (B) $HO_2C(CH_2)_7S$-Au nanoparticles. Spectra were acquired in 1000 scans with a contact time of 2 ms and a recycle delay of 1 s. The proton evolution period consisted of 32 increments of 2 μs.

An additional indication of static character is given by the carbon linewidths for particular sites or regions. The carboxyl chain termini of the Au-S$(CH_2)_7CO_2H$ system resonate at 182 ppm. This resonance is quite broad, $\Delta\upsilon_{1/2}$~ 325 Hz, consistent with a distribution of hydrogen bonded states at the monolayer/air interface. Comparing the three termini- methyl, hydroxy and carboxy- and their effects on the hydrocarbon chains, carbon linewidths of $\Delta\upsilon_{1/2}$~170Hz, ~205Hz and ~230Hz respectively are observed for the inner methylene (33 ppm) carbon peak. Thus both the terminal alcohol and the terminal carboxylic acid groups increase the population of gauche defects within the hydrocarbon chain region. However the disorder induced is similar, despite the much more extensive nature of the hydrogen bonding in the Au-S$(CH_2)_7CO_2H$ system.

An understanding of the nature of this bonding is desirable in assessing how the stabilization effect works. Since no solvent is present in the system, three possible mechanisms for hydrogen bonding exist:

a. interactions between acid groups on adjacent particle faces

b. interactions between acid groups on the same particle

c. interactions with surface bound water

The first two of these are depicted in Figure 4.4.

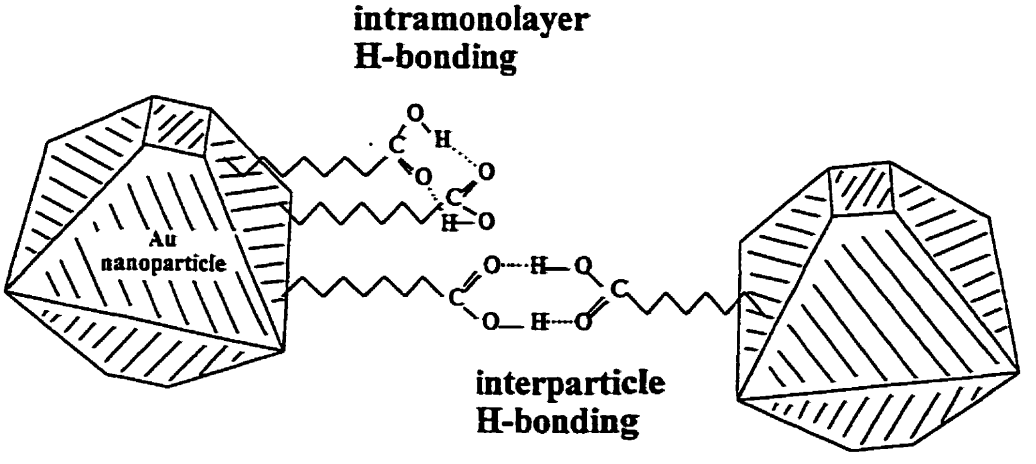

Figure 4.4 Figure depicting intramonolayer and interparticle hydrogen bonding.

A potential model for the formation of hydrogen bonding network is suggested by the thermal behavior of the system. As stated previously the chains do not melt until 160°C. On cooling the system recrystallises, but a small residual disordered component persists as evidenced by the shoulder at 31 ppm. A degree of hysteresis is also indicated by the narrower linewidth of the carboxyl resonance at 182 ppm, which narrows on heating, and remains narrowed ($\Delta\upsilon_{1/2}$~180 Hz) after the first heating cycle is complete.

Subsequent application of a second heating and cooling cycle leads to apparently permanent disordering of the assembly, so that on cooling the chain peak remains at 30 ppm, as shown in Figure 4.5. The 2D WISE spectrum at this stage is shown in Figure 4.6, and indicates a much higher chain mobility. This behavior seems to suggest that on initial heating and cooling, rearrangement of the hydrogen bonded network occurs, and a disordered chain component is trapped in the monolayer structure. If this hysteresis were related to complete chain desorption, the resulting high mobility of the free alkanethiol moeities would be seen in the 1 pulse (no cross polarization) experiment. In fact use of direct polarization does not give any evidence of untethered chains, and the signal-to-noise ratio of the ^{13}C CPMAS NMR experiment actually improves after the two heating cycles (this effect is most probably due to a coincidental change in the CP relaxation parameters).

Further study of the disordered system left by the second heating cycle showed that in fact very slow recrystallisation of the chains does occur. ^{13}C CPMAS and 2D WISE NMR spectra of the sample taken several weeks after the two heating cycles proved to be identical to the spectra of the virgin sample. Thus not only is the system highly stable, but the disorder incurred at very high temperatures takes place via some gradually reversible reorganization in the network. The proposed model is as follows:[23] constraint of the ω terminus through hydrogen bonded carboxylic acid groups alters the chain dynamics of the SAM through the strength of the hydrogen bonding, along with the interchain Van der Waals forces. The rigid crystalline carbon chain regions, and concomitantly higher thermal transition temperature depend on intra-monolayer hydrogen bonding between chains on the same face. This produces bundles which are bonded laterally, and therefore are more closely packed and motionally restrained.

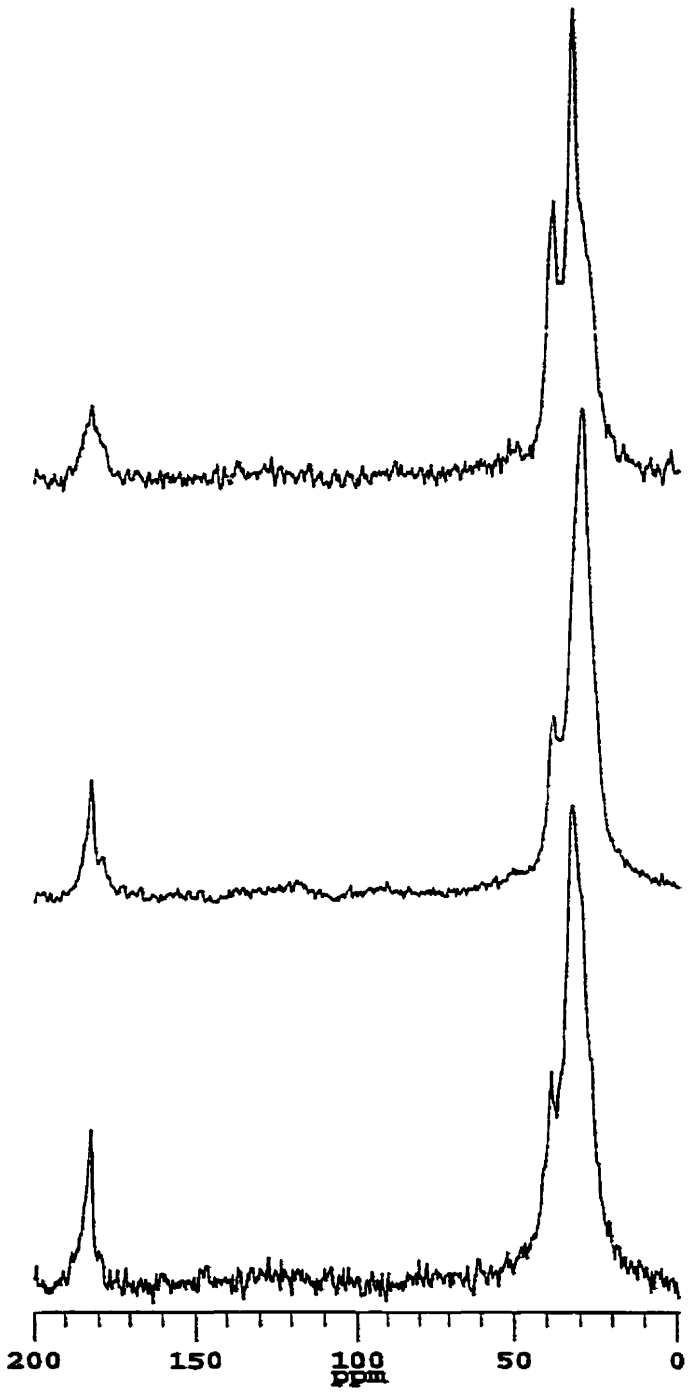

Figure 4.5 ^{13}C CPMAS spectrum of $AuS(CH_2)_7CO_2H$ at room temperature before (above) and after (middle) heating to 160°C twice as well as several weeks later (below). Spectrum was acquired in 1000 scans, contact time was 2ms, recycle delay 1s.

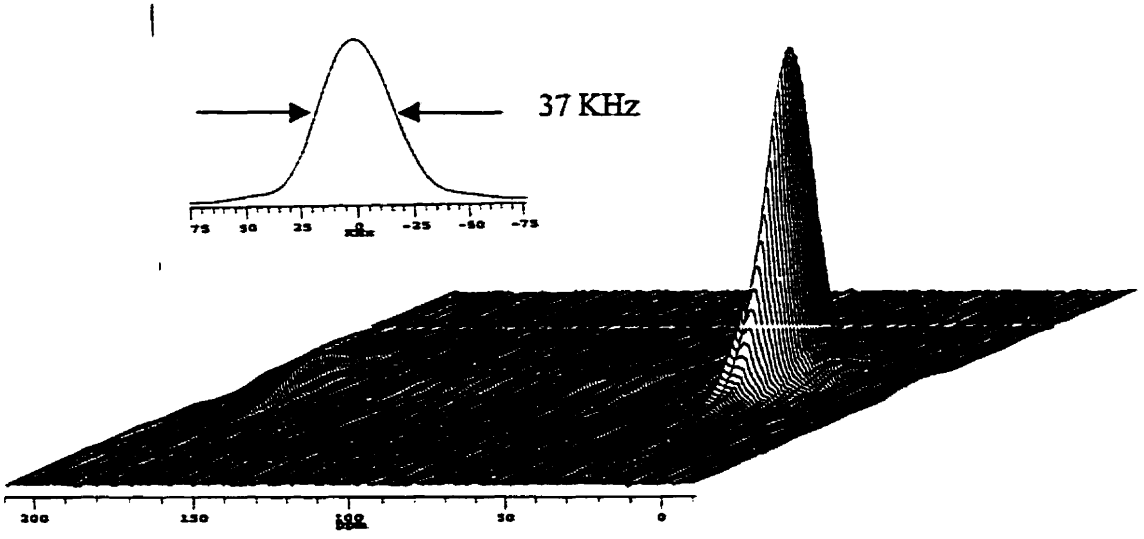

Figure 4.6 2D WISE spectrum of $AuS(CH_2)_7CO_2H$ at room temperature immediately after heating to 160°C twice. Spectrum was acquired in 1000 scans, contact time was 2ms, recycle delay 1s, proton evolution period 32 increments with a dwell of 2 μs.

The structural disorder following the first heating cycle would presumably be due to a change in the ratio of intra and interparticle hydrogen bonding as depicted in Figure 4.4. The persistence of the gauche defects on cooling would be aided by the hydrogen bonded network which would effectively lock the defects into place. Further annealing leads to total disordering, which may be due to dimerization of carboxyl groups on neighboring gold particles.

The FTIR carboxyl bands, as mentioned earlier, are a good measure of dimerization. In the planar systems two C=O stretching bands are seen at 1740cm^{-1} (non hydrogen bonded monomers) and 1718cm^{-1} (laterally hydrogen bonded acid dimers). The dimerization of carboxylic acid groups may be sterically hindered in a close-packed SAM, but the hydrogen-bond formation may energetically compensate for the barrier associated with rotation of the terminal C-C bond. While both free and bonded forms are seen on the planar substrate, as noted previously, the colloidal system does not display a band for unbound acid groups. The frequency of the carboxyl group, seen at 1708cm^{-1}, would be consistent with head-to head dimerized alkanoic acids. The change from intra to inter particle bonding can be seen as a change from a two dimensional to a three

dimensional type network, where the thermal treatment causes debundling of laterally bound chains on a single face and promotes interparticle bonding with associated loss of order.

This model will be tested by the preparation of systems with different hydrocarbon chain lengths and by variable temperature infrared studies. In addition a more extensive variable temperature ^{13}C NMR study of the hysteresis is planned. Through heating and cooling to different temperatures it is possible to obtain more detailed data on thermal transitions.[24] The kinetics involved could be compared with similar slow chain reorganization processes observed in some polymer systems.

In conclusion, the presence of strong hydrogen bonds between terminal carboxylic acid groups was found to induce order in intermediate chain length SAMs on gold colloids. Unlike the methyl and hydroxyl terminated chains of the same length, which are motionally isordered and exhibit reversible chain-length dependent order-disorder transitions, the all-trans chains of the $HO_2C(CH_2)_7S$-Au nanoparticles are in a thermally stable, motionally restricted state with a very high chain melting temperature. It is proposed that the strong thermal hysteresis observed may be due to a rearrangement of the hydrogen-bonding network from 2D (intraparticle)-like to 3D (interparticle)-like.

References

[1] Badia, A.; Gao, W.; Singh, S.; Demers, L.; Cuccia, L.; Reven, L. *Langmuir* **1996**, *12*, 1262. (b) A. Badia; Cuccia, L.; Demers, L.; Morin, F. G.; Lennox, R. B. *J. Am. Chem. Soc.* **1997**, *119*, 2682.

[2] (a) Brust, M.; Walker, M.; Bethell, D.; Schriffin, D. J.; Whyman, R. *J. Chem. Soc., Chem. Commun.* **1994**, 802 (b) Brust, M.; Fink, J.; Bethell, D.; Schiffrin, D.J.; Kiely, C. *J. Chem. Soc., Chem. Commun.* **1995**, 1655.

[3] (a) Badia, A.; Singh, S.; Demers, L. M.; Cuccia, L. A.; Brown, G. R.; Lennox, R. B. *Chem.-Eur. J.* **1996**, *96*, 2657. (b) A. Badia; Cuccia, L.; Demers, L.; Morin, F. G.; Lennox, R. B. *J. Am. Chem. Soc.* **1997**, *119*, 2682. (c) Terrill, R. H.; Postlethwaite, A.; Chen, C.-H.; Poon, C. -D.; Terzis, A.; Chen, A.; Hutchison, J. E.; Clark, M. R.; Wignall, G.; Londono, J.D.; Superfine, R.; Falvo, M.; Johnson Jr., C. S.; Samulski, E. T.; Murray, R. W. *J. Am. Chem. Soc.* **1995**, *117*, 12537. (d) Hostetler M.J.; Murray R. W. *Curr.Opin.Colloid & Interface Sci.* **1997**, *2*, 42. (e) Hostetler, M. J.;Stokes, J. J.; Murray, R. W. *Langmuir* **1996**, *12*, 3604.

[4] (a) Fenter, P.; Eberhardt, A.; Eisenberger, P. *Science* **1994**, *266*, 1216 (b) Gerdy, J. J.; Goddard, W. A. *J. Am. Chem. Soc.* **1996**, *118*, 3233 (c) Nishida N.; Hara M.; Sasabe H.; Knoll W. *Jpn. J. Appl. Phys. Pt. 1* **1996** *35*: 5866 (d) Nishida N.; Hara M.; Sasabe H.; Knoll W. *Jpn. J. Appl. Phys. Pt. 2* **1996** *35*: L799 (e) Schlenoff, J. B.; Li, M.; Ly, H. *J. Am. Chem. Soc.* **1995**, *117*, 12528. (f) Nuzzo, R. G.; Fusco, F. A.; Allara, D. L. *J. Am. Chem. Soc.* **1987**, *109*, 2358 (g) Strong, L.; Whitesides, G. M. *Langmuir* **1988**, *4*, 546 (h) Bain, C. D.; Biebuyck, H. A.; Whitesides, G. M. *Langmuir* **1989**, *5*, 723.

[5] Badia, A.; Back, R.; Lennox, R. B. *Angew. Chem. Int. Ed. Engl.* **1994**, *33*, 2332.

[6] (a) Whetten, R. L.; Khoury, J. T.; Alvarez, M. M.; Murphy, S.; Vezmar, I.; Wang, Z. L.; Stephens, P.W.; Cleveland, C.; Luedtke, W. D.; Landman, U. *Adv. Mater.* **1996** *8*, 428 (b) Luedtke, W. D.; Landeman, U. *J. Phys. Chem.* **1996**, *100*, 13323.

[7] (a) Johnson, S.R.; Evans, S.D.; Mahon, S.W.; Ulman, A., *Langmuir*, **1997**, *13*, 51 (b) Castner, D.G.; Hinds, K.; Grainger, D.W., *Langmuir*, **1996**, *12*, 5083.

[8] Ansermet, J. -Ph.; Slichter, C. P.; Sinfelt, J. H. *Progress in NMR Spectroscopy* **1990**, *22*, 401.

[9] (a) Brown, K.; Parish, R. V.; McAuliffe, C. A. *J. Am. Chem. Soc.* **1981**, *103*, 4943 (b) Al-Sa'ady, A. K. H.; Moss, K.; McAuliffe, C. A.; Parish, R. V. *J. Chem. Soc. Dalton Trans.* **1984**, 1609.

[10] Fijolek, H.G.; Grohal, J.R.; Sample, J.L.; Natan, M.J. *Inorg. Chem.* **1997**, *36*, 622.

[11] Caravatti, P.: Bodenhausen,G.; Ernst, R.R. *J.Mag.Res.* **1983**, 55,88.

[12] Freeman, R., *A Handbook of Nuclear Magnetic Resonance*, **1997**, Addison Wesley

[13] a) Nuzzo, R. G.; Dubois, L. H.; Allara, D. L. *J. Amer. Chem. Soc.* **1990**, *112*, 558.b) Chidsey, C. E. D.; Loiacono, D. N. *Langmuir* **1990**, *6*, 682.

[14] Ingram,R.S.; Hostetler, M. J.; Murray, R. W. *J. Am. Chem. Soc.* **1997**, *119*, 9175.

[15] Kepley, L. J.; Crooks, R. M.; Ricco, A. J. *Anal. Chem.* **1992**, *64*, 3191. b) Sun, L.; Crooks, R. M. *Langmuir* **1993**, *9*, 1775. d) Yang, H. C.; Dermody, D. L.; Xu, C.; Ricco, A. J.; Crooks, R. M. *Langmuir* **1996**, *12*, 726.

[16] Sun, L.; Kepley, L. J.; Crooks, R. M. *Langmuir* **1992**, *8*, 2101.

[17] a) Folkers, J. P.; Laibinis, P. E.; Whitesides, G. M. *Langmuir* **1992**, *8*, 1330. b) Atre, S. V.; Liedberg, B.; Allara, D. L. *Langmuir*, **1995**, *11*, 3882.

[18] Ulman, A., *Chem.Rev.*, 1996, *96*, 1533

[19] Ulman, A.; Evans, S. D.; Shnidman, Y.; Sharma, R.; Eilers, J. E.; Chang, J. C. *J. Am. Chem. Soc.* 1991, *113*, 1499.

[20] Evans, S. D.; Sharma, R.; Ulman, A. *Langmuir* 1991, *7*, 156.

[21] a) Schmidt-Rohr, K.; Clauss, J.; Spiess, H. W. *Macromolecules* 1992, *25*, 3237. b) Clauss, J.; Schmidt-Rohr, K.; Adam, A.; Boeffel, C.; Spiess, H. W. *Macromolecules* 1992, *25*, 5208.

[22] (a) Gao, W.; Dickinson, L.; Grozinger, C.; Morin, F.; Reven, L., *Langmuir*, 1996, *12*, 6429 (b) Antonietti, M.; Radloff, D.; Wiesner, U.; Spiess, H. W. *Macromol. Chem. Phys.* 1996, *197*, 2713.*6*, 122.

[23] Ulman, A., *Adv.Mat.*, 1991, *3*, 298

[24] Li., H.; Butler, I.S.; Gilson, D.F.R.; Harrod, J.F.; Morin, F., *J.Phys.Chem.*, 1995, *99*, 8490

Part One: Conclusions, contributions to original knowledge, ideas for continued research.

The synthesis of self assembled monolayers on small metal oxide particles and metal colloids has been shown to result in systems which are generally good model analogues for the two dimensional, planar systems. The increased surface area of these samples is particularly helpful because it allows the use of solid state NMR, a technique which suffers from sensitivity problems and can not be used on the two dimensional SAMs (e.g. those deposited on silicon wafers). The studies outlined in the previous chapters represent a breakthrough in the understanding of the structural and dynamic properties of monolayers, by providing a molecular level characterization method with which to investigate particular regions of the systems. Whereas planar substrate-monolayer samples could only be investigated on an atomic scale by FTIR, and other work obtained more general information about composition (e.g. by electron microscopies etc.), the nanoparticle based SAMs have been examined by ^{13}C and 2D NMR experiments, and where relevant by ^{31}P and ^{29}Si NMR. These experiments have shed much light on the principle areas of interest, namely the issue of the nature of surface bonding at the interfacial regions of the three different systems, as well as the chain order and dynamics of the monolayers themselves. The principle conclusions drawn from the NMR data are summarized below:

Surface bonding

- ^{29}Si NMR has been used to compare the siloxane network formed at the interface of the silica particles and the octadecylsilane monolayers. The network is similar to that seen in the polysesquisiloxane produced by rapid hydrolysis of OTS, and consists predominantly of $R\text{-}Si(OH)(O\text{-}Si)_2$ linkages.

- The modes of surface attachment seen in the SAMs of phosphonic acids vary greatly according to substrate. ^{31}P NMR has shown that the bond with TiO_2 is comparatively weak, while reaction with the ZrO_2 surface is stronger and probably occurs via a monodentate linkage. The synthesis of ODPA monolayers on Al_2O_3 and zirconated silica produced bulk metalalkylphosphonates.

- Alkanethiols are chemisorbed onto the gold colloids via a thiolate linkage: a covalent, two-coordinate bond similar to that observed in Au(I) thiolate complexes. Assuming that the two dimensional system has the same structure, this resolves a long-standing debate about the nature of the gold-sulfur bond.

Chain order, dynamic and thermal transitions

- The hydrocarbon chains containing 18 carbon atoms exhibit similar dynamic states in all three SAM systems. ^{13}C CPMAS can determine whether trans and/or gauche chain conformations are present. All the monolayers have large trans populations, the OTS-silica and ODPA-titania samples also show substantial gauche populations. The mobilities of the so-called trans chains in all the systems studies have been more fully characterized by the 2D WISE experiment. The proton linewidths of the conformationally ordered signals indicate that the chains are more loosely packed than conventional crystalline samples. The chains appear to undergo axial rotation about the chain axis and trans-gauche isomerizations, with a large mobility gradient along the chains.

- On the rough surfaces provided by the nanoparticles, alkylphosphonate and alkanethiol monolayers of chains with less than 16 carbon atoms are conformationally disordered.

- Chainlength dependent order-disorder transitions occur in both alkylphosphonate and alkanethiol SAMs, as followed by variable temperature ^{13}C CPMAS. The octadecylsilane SAMs also undergo reversible thermal disordering, but this occurs at

much higher temperatures due to the steric constraints imposed by the siloxane backbone. In none of these cases is chain melting accompanied by desorption of the SAM from the surface.

- In the case of the silica-OTS system, the differences in mobility between the crystalline and amorphous regions were used as the basis with which to carry out spin diffusion experiments via selection of the mobile component through the dipolar filter sequence. The resulting regrowth in intensity of the crystalline peak during an incremented mixing time was analyzed to give an approximate domain size of 3.5 nm, which was shown to be a reasonable result in light of the substrate size.

- The inclusion of terminal carboxylic acid groups on the alkanethiol monolayers greatly reduces the chain motion. This confers conformational order on chains much too short to be ordered by Van der Waals forces alone, and greatly increases the thermal stability of the chains.

Future research ideas

The experiments described here have concentrated mostly on the study of simple alkyl chains grafted to a variety of surfaces. The silica-OTS system is more difficult to synthesize than the metal-oxide phosphonate systems, but it would be useful to determine whether annealing of these samples would induce further condensation of the silanol groups, increasing the strength of the assembly. The alkylphosphonate and gold alkylthiol systems offer easily tailored SAMs which can be further exploited in fundamental studies including:

- <u>The influence of the substrate on the monolayer properties</u>

Evidence has shown that the gold colloids are not actually spherical, but consist of truncated octahedra with (111) and (100) single crystal faces. This has led to the assertion

that the gold particles offer planar surfaces for the attached alkyl chains which then exist in bundles on the crystal faces. It has proven difficult to synthesize larger gold colloids with which to explore this issue, but this approach would be helpful in resolving this question.

The metal oxides used in the deposition of alkylphosphonates are more readily available in a variety of sizes. Preliminary results of an ODPA SAM deposited on smaller 3 nm spherical ZrO_2 colloids indicates a completely disordered environment. The characterization of a number of different sizes of titania and zirconia colloids is being undertaken as a precursor to studying the effects of surface curvature on monolayer properties. ^2H lineshapes and ^{13}C chemical shifts will be used to determine a limiting radius of curvature of 2D behavior.

A number of alternative substrates are also being investigated as surfaces for the deposition of alkylphosphonate SAMs. Colloidal SnO_2 and α-Al_2O_3 are being investigated. In addition further work is underway to produce primed silica surfaces. Although use of a Zr^{4+} primer layer proved unsuccessful, it is possible to create a PO_3H_2 surface via silanization with an amine terminated silane. This reaction will be monitored by ^{13}C, ^{29}Si and ^{31}P NMR. These substrates exhibit an optical response based on the substrate type which makes the properties of monolayers deposited on such materials worthy of further study.

- <u>Molecular interactions in self-assembled monolayers.</u>

The influence of the presence of two adsorbing groups on the deposition of SAMs remains relatively unexplored. A study of α, ω- alkanedioic acid ($HO_2C(CH_2)_{30}CO_2H$ on silver[1] found that a monolayer of tightly folded molecules is formed. The alkanethiol system has been modified to incorperate dithiols which form networks of gold nanoparticles. In the study of alkylphosphonate multilayers, sequential adsorption is achieved by alternate addition of α, ω- organobis(phosphonic acids) and metal ions. Although structural studies indicate a linear increase in film thickness as layers are added, as yet there is no evidence to determine whether both acid groups of a molecule attach to

the surface to form a looped structure. This issue will be addressed by the synthesis of a series of amphibolic surfactants containing phosphonic acid functional groups at one end, and a second functional group (PO_3H_2, OH, CO_2H or NH_2) at the other. ^{31}P, ^{13}C and ^{1}H solid-state NMR will be used to investigate the extent of looping, hydrogen bonding between terminal groups and the effect of chain lengths (specifically whether a chain contains an even or odd number of carbon atoms). This will reveal the specificity of the phosphonic acid-substrate interaction and the role played by competition between different types of intermolecular forces on the self-assembly. Selective deuteration may also be useful in studying the mobility of such systems. The behavior of such bifunctional SAMs is important in the design of functionalized surfaces, as well as the assembly of multilayers.

As demonstrated in Chapter 4, the presence of terminal groups capable of forming hydrogen bonds has a dramatic effect on the stability and dynamics of SAMs. The 2D H-bonding network formed in thiol and phosphonate functionalized monolayers will be examined by ^{1}H CRAMPS, offering the opportunity to use proton isotropic shifts to determine H-bond length.[2] This information, which can not be obtained through X-ray diffraction for immobilized monolayers will be helpful in ascertaining the spacing and acid-base interactions of the terminal groups. This information has applications in the use of SAM-based templates for crystal growth and biosensors.

- Study of mixed monolayers.

The dipolar filter sequence used in Chapter 2 for the determination of domain sizes in the silica-OTS monolayer system offers a powerful tool for the study of mixed monolayer systems. The issue of phase segregation in such systems is difficult to study because very few techniques exist with which to study spatial distributions on the 1-100 nm scale. The preparation of mixed films is of interest for applications such as artificial receptor or molecular recognition sites in biomimetic systems. Previously the evidence for phase separation has come from scanning probe microscopy techniques, which are not sufficiently sensitive to fully characterize these systems. Mixed monolayers of thiols or

phosphonates would provide an interesting sample for ^{13}C detected proton spin diffusion measurements.

References

[1] Allara, D.L.; Atre, S.V.; Elliger, C.A.; Snyder, R.G., *J.Am.Chem.Soc.* **1991**, *113*, 1852

[2] Harris, R.K.; Jackson, P.; Merwin, L.H.; Say, B.J.; Haegele, G., *J.Chem.Soc.Faraday*, **1988**, *84*, 3649

Part Two

Chapter One

General Introduction

1.1 Conventional ^{129}Xe NMR as a probe of host structures

NMR studies of gases suffer from the same types of sensitivity problems as those encountered in the solid state. In addition to the limitations imposed by the Boltzmann distribution, a further restriction in the signal size is introduced by the lower density of nuclei in the gaseous state. Nevertheless, NMR of gas phase samples is used both directly on samples of interest, and as a probe, where it is particularly useful in studying high surface area substances, providing the degree of adsorption is large enough to produce an observable signal. Gaseous samples do offer some unique advantages including the significant reduction of intermolecular effects and in some cases the potential to extrapolate NMR variables to the limit of zero-density to give the molecular properties of an isolated molecule.[1] In general both temperature and pressure can be varied in a sample, and the variation in chemical shift can be modeled by a virial expansion:

$$\delta(T,\rho) = \delta_0 + \delta_1(T)\rho + \delta_2(T)\rho^2 + \ldots \qquad \textbf{Equation 1.1}$$

where δ_t are the chemical shift parameters, and ρ is the pressure. This expression can be modified to take into account whichever terms are appropriate for a given species and set of physical conditions. The quadratic and higher terms are due to collisions between more than two bodies and can be neglected for pressures less than 50 atm. Comparison with condensed phase data can give important information about solvent effects, while interpretation of chemical shift data of gases physisorbed onto surfaces, or trapped inside

pores, can be an additional resource in the study of solids. It is this second technique which will be explored in this part of the thesis.

Amongst the NMR active nuclei available for gas phase studies, ^{129}Xe is one of the most versatile and widely employed. The ^{129}Xe atom has no quadrupole moment, is large (free diameter = 4.4Å at room temperature) and chemically inert. Xenon is absorbed into samples often without greatly affecting the environment to be probed, since its principle interactions are via Van der Waals forces. The large number of electrons in the atom give rise to an extensive chemical shift range, as indicated in Figure 1.1, and small changes in the environment will have a significant effect on the chemical shift.

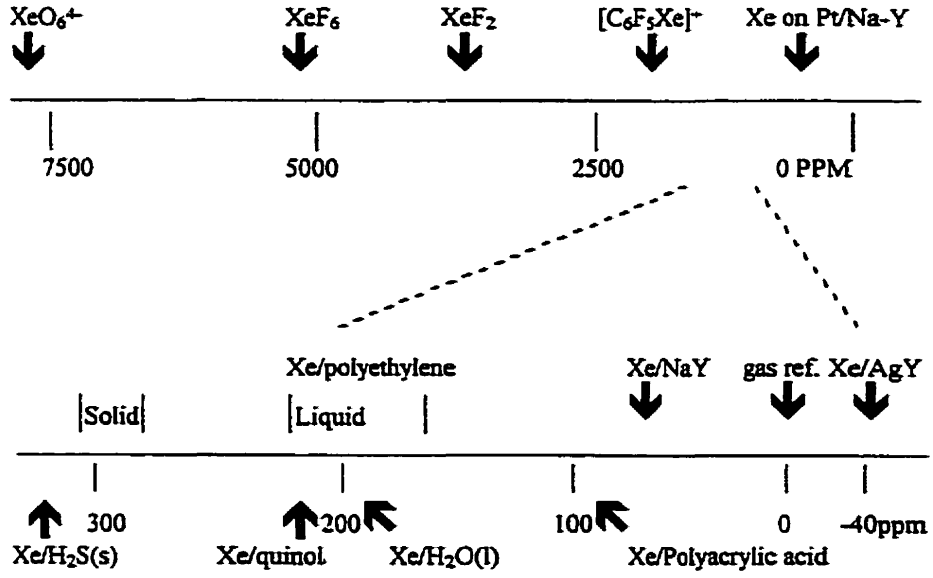

Figure 1.1 The chemical shift range observed for ^{129}Xe.

Two xenon isotopes are accessible to NMR studies. The ^{129}Xe nucleus has spin 1/2 and 26.44% natural abundance and comprises the basis of the majority of work in the literature. The ^{131}Xe nucleus has a quadrupolar nucleus (spin 3/2) and natural abundance of 21.18%. While the relaxation times of the ^{129}Xe nucleus can be very long in the pure gas form (up to an hour), the T_1 of xenon adsorbed inside solids is typically much

shorter, in the range of a 10 ms to a few seconds. This allows signal averaging to be carried out on sealed samples, to increase the signal to noise.

The sensitivity of ^{129}Xe to local environment has been exploited in many studies of zeolites, clathrates and porous materials. The gas is also moderately soluble in many liquids and the amorphous regions of solid polymers, and has been used to investigate a variety of systems ranging from proteins in solution to polymer blends. Many review articles have appeared on the use of xenon as a probe. The work on zeolites has been reviewed by its principle authors, Ito and Fraissard,[2] and an additional more comprehensive and critical paper has been produced by Barrie and Klinowski.[3] In the latter paper it was suggested that the net ^{129}Xe chemical shift in zeolites could be described, by analogy with the virial expansion expression of the chemical shift developed for pure gaseous samples, as a sum of terms resulting from the various interactions of the xenon with its environment:

$$\delta = \delta_o + \delta_s + \delta_{Xe\text{-}Xe}\cdot\rho_{Xe} + \delta_E\,(+\delta_M) \qquad \textbf{Equation 1.2}$$

where δ_o is the reference, δ_s is related to collisions between xenon and the surface of the adsorbate, $\delta_{Xe\text{-}Xe}\cdot\rho_{Xe}$ arises from xenon-xenon interactions (and for low pressures involving two-body collisions only will vary linearly with xenon density), δ_E is a term invoked by Fraissard to account for the observed dependence of chemical shift on exchangeable cations in the zeolite samples and δ_M is an extra term for use in situations involving paramagnetic species.

A variety of zeolites were studied, chemical shifts being recorded for dehydrated samples and quoted relative to a pure gas reference extrapolated to zero pressure. In the simplest case, that of zeolite Y, where only one possible adsorption zone is available, the predicted linear increase of chemical shift with xenon loading, arising from the $\delta_{Xe\text{-}Xe}\cdot\rho_{Xe}$ term was observed. However further experimental evidence disclosed little variation when other small cations were used, leading to the assertion that δ_E was equal to zero. Extension of the investigation to other zeolite structures also gave linear dependencies of

weak. Thus the van der Waals' terms are the only significant ones. Various approaches[1,2,3] have been proposed for the modeling of xenon shifts including statistical mechanical calculations in which a dispersive interaction between a pair of atoms or molecules is considered, and a continuum model which treats the solvent as a homogeneous medium.

The initial investigations of polymers by ^{129}Xe NMR are reviewed by Miller.[5] The morphology of homopolymers can be assessed by the chemical shift and breadth of the xenon resonance. Sefcik et al. studied poly (vinyl chloride)[6] which displayed a very broad resonance at 250 ppm (75 ppm wide) indicative of adsorption sites small compared to those in zeolites (chemical shifts typically around 60 ppm), and a heterogeneous environment. Similarly a conventional study of poly(ethyl methacrylate), PEMA, by Stengle and Williamson[7] found a downfield shift of 193 ppm from the free gas resonance at 85°C. A decrease in temperature was found to cause a further downfield shift due to the decrease in free volume caused as the polymer became more dense. The linewidth was sharper in this sample (~1 ppm), but the decrease in temperature caused linebroadening as the rapid diffusion between sites possible at higher temperatures became slower and the distribution of resonances due to heterogeneity became apparent. Studies of polyethylene[8,9] indicated shifts consistent with extrapolation of a plot of ^{129}Xe chemical shift vs. density for n-alkanes. This result corroborates the assertion that absorption occurs into the amorphous regions only. The temperature dependence and behavior of the ^{129}Xe resonances around the glass transition point will be further discussed in Chapter 3, where a series of polyalkyl(methacrylates) are investigated by optically polarized ^{129}Xe NMR to provide a bridge between the conventional studies and the hyperpolarized xenon experiments.

Regions of different heterogeneity, or separate regions within copolymers and polymer blends can often be distinguished by xenon NMR even in the presence of diffusion. In a study of uncrosslinked EDPM rubber,[10] four different amorphous regions were identified. On crosslinking the number of peaks decreased, and there was an overall downfield shift attributed to densification of the polymer.

Observation of multiple peaks in the spectra of polymer blends depends on the xenon diffusion time being long on the NMR experimental timescale. Multiple peaks have been observed in a variety of samples (including various blends of polychloroprene, polyisoprene and epoxidised polyisoprene),[11] and are unambiguously associated with a phase separated morphology. However, where a single line appears, this can not be taken as conclusive evidence of miscibility. The blend may also be separated into sufficiently small domains such that rapid diffusion averages the signal. Unlike the investigations of porous structures, the existence of multiple sites in the polymers can not be confirmed by cooling the temperature to slow down diffusion, since the xenon will be forced out of the interchain void spaces below the glass transition temperature (T_g). Temperature dependence studies of relative solubility and the chemical shift can be helpful in confirming miscibility. A study of a block copolymer of polystyrene and polyisoprene[12] found that while two resonances were observed, these were broader than in the pure materials and increased in breadth with decreasing block size, indicating that the xenon exchange between the two phases causes a lifetime broadening. An investigation of phase transitions in a blend of polyisoprene and polybutadiene found that variable temperature ^{129}Xe NMR was a more sensitive probe of morphology than calorimetry.[13] Heating of the blend led to a phase separation detected by the appearance of two separate peaks which subsequently recoalesced over time due to polymer interdiffusion to reestablish the original miscible blend structure.

Although such studies are mainly qualitative rather than quantitative in nature, various attempts have been made to better understand the physical processes involved. The temperature dependence of the chemical shift has been modeled by Cheung and Chu,[14] who proposed a free volume model which was tested on polypropylene and poly(4-methyl-1-pentene), PMP, and applied to the results of Stengle *et al.* on PEMA. Here a short range attractive potential between the xenon atom and the polymer was used. However the model worked best for the PMP, and was less successful for the other cases. An alternative approach was suggested by Miller et al.[15] who proposed a scheme based on an earlier model of gas diffusion in polymers. The van der Waals shift model assumes that the xenon atom creates a hole between the neighboring polymer chains, and the shift

is proportional to the work required to break the van der Waals' bonds between the chains, as calculated by a Lennard Jones potential. This model is more successful, predicting the temperature dependence of most polymers above T_g, as well as the magnitudes of the chemical shifts to an accuracy of +/-10%. Of course, the model did not hold for PEMA below its T_g, where the assumption of rapid exchange is most in error. In addition, since it involves a "smooth tube" approximation, it is not appropriate for polymers with bulky side-groups.

1.2 Optical Pumping- a brief history

The use of optically polarized xenon to enhance the NMR signal is a recent advance based on work done by physicists following the discovery of the laser. The xenon is not directly excited, instead the increase in nuclear spin polarization is created through spin exchange with optically excited rubidium atoms (^{87}Rb).[16] A full quantum mechanical theory has been developed to fully characterize the process,[17] here a more intuitative overview will be presented. Figure 1.2 shows how optical pumping with laser light of a particular wavelength, 795nm, creates a large polarization of the rubidium electron spins.[18]

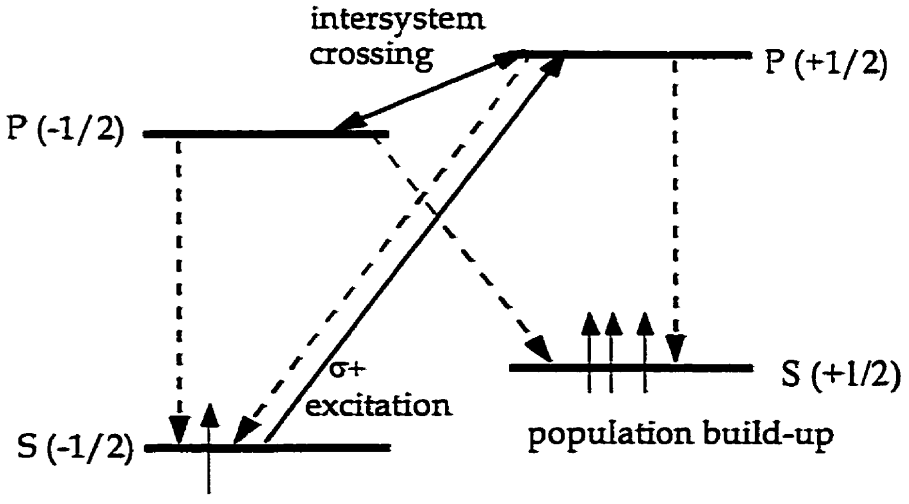

Figure 1.2 Schematic depicting the population buildup caused by circularly polarized light incident on alkali metal electons. Dashed lines represent relaxation processes.

In order to selectively excite electrons between the desired magnetic sublevels of the electronic states, circularly polarized light, denoted in the diagram by σ+, is used. Electrons in the $^2S_{1/2}(-1/2)$ sub-state will be excited according to the transition rule $\Delta m=+1$, giving a population increase in the $^2P_{1/2}(+1/2)$ state. From here, intersystem crossing will also populate the $^2P_{1/2}(-1/2)$ substate. Subsequent relaxation of the system can occur either to the original ground state, from which further excitation can occur, or to the $^2S_{1/2}(+1/2)$ substate. Thus optical pumping leads to a population inversion, i.e. a build up in the number of electrons in the rubidium $^2S_{1/2}(+1/2)$ sublevel. This effect has been observed in a variety of alkali metal atoms including rubidium, cesium, sodium and potassium, and the physics involved has been the subject of detailed investigation.[19] Subsequent experiments determined that angular momentum produced in the pumped ensemble of atoms could be transferred to other particles.[20] In the presence of certain noble gases, for example, the principle source of relaxation for the optically pumped rubidium was found to occur through the process of spin exchange, in which the electron spin polarization of the rubidium is transferred to the nuclear spins of gases such as ^{129}Xe.[21]

Comparisons between experimental evidence and theoretical calculations of spin rotation coupling constants determined that the energy transfer process takes place through the formation of short lived van der Waals molecules.[22] This situation is depicted schematically in Figure 1.3.

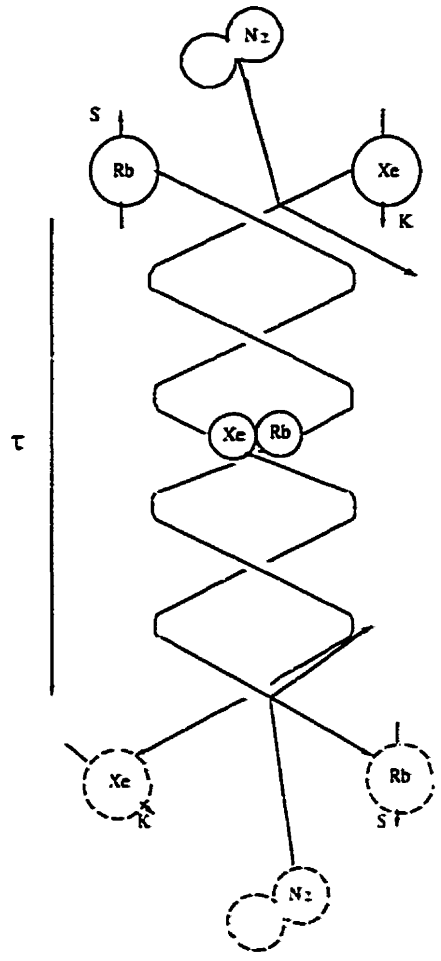

Figure 1.3 Schematic depicting the transfer of polarization between an electronically excited rubidium atom and a xenon nucleus.

The process involves a three-body collision, in which the lifetime of the Rb-Xe species is longer than that which would be the case in a simple binary collision. The spin exchange between the electrons and the nuclei is caused by the Fermi contact interaction. The Rb-Xe molecules are then broken up by further collisions with other atoms or molecules which dissipate the angular momentum of the combined species. The overall effect of this process is to alter the population of the nuclear spin states, producing a large non-equilibrium nuclear magnetization of the ^{129}Xe gas. Clearly this has ramifications for the NMR process, the combination of optical pumping with NMR offering a novel method of increasing sensitivity.

1.3 Hyperpolarized ^{129}Xe NMR

Conventional xenon NMR is carried out by evacuating a sample, then freezing a known pressure of xenon into the tube and either sealing the glass or using a high pressure valve.[23] Because of the low sensitivity, high pressures of gas (i.e. several atmospheres) are often needed, and the resulting samples may require long acquisition times. When combined with the NMR experiment, optical pumping leads to an optimum signal enhancement factor of ~10^4. This approach was first reported in 1991,[24] when polarized ^{129}Xe NMR was used to detect the signal arising from the interaction of xenon with the surface of benzanthracene (surface area ~0.5 m^2/g) and a low surface area carbon black (surface area ~10 m^2/g). The low surface areas and the long relaxation times of xenon adsorbed on organic materials would have prevented observation of these surface signals by conventional ^{129}Xe NMR. A subsequent study of a polymer surface, polyacrylic acid, further demonstrated the potential of this technique.[25] The contribution to the chemical shift from the xenon-surface interaction and an approximate diffusion coefficient were estimated by combining the variable temperature and pressure chemical shift data with xenon isotherms. In order to probe only the surface, these measurements were carried out on a semicrystalline polymer far below the glass transition temperature to avoid any diffusion of xenon into the polymer. We have extended this experiment to thin organic films and polymers in the vicinity of T_g where a signal for polarized xenon dissolved into the polymer can be detected. This will be discussed in the following chapters.

Other areas have also been investigated by optically polarized ^{129}Xe NMR. Some preliminary reports in the literature include; a study of semiconductor nanocrystals of CdS, to investigate the surface distribution of the organic capping species[26]; a study of the influence of thermal treatments on the surface of a porous silicon (after annealing the sample at 400°C, the number of dangling bonds increases which shortens the T_1 of xenon but leaves the chemical shift dependence on temperature unchanged.[27]); $^{13}CO_2$ has been

frozen into polarized xenon and cross-polarization created enhancement of the ^{13}C resonance[28]; polarization of the surface proton spins of a polymer, poly(triarylcarbinol) via a double resonance ^{129}Xe to ^{1}H cross polarization experiment[29]; a double resonance technique was also extended to enhancement of the surface proton signals of a fumed silica sample.[30] Biological imaging experiments and solution state studies have also made use of enhancement through polarization of ^{129}Xe.[31,32,33]

This continues to be an active area of research, amongst the most recent developments are those based on a more complex experimental set-up which uses high-power diode lasers. This technique allows insertion of laser-polarized xenon into a spinning rotor under continuous flow conditions.[34,35] Previously, the magnetization of the polarized xenon had been transferred to the surface protons of a fumed silica under static conditions, an experiment described as spin polarized induced nuclear Overhauser effect (SPINOE). The ^{129}Xe spectrum of this sample at 173K exhibits narrow peaks at 0 ppm for the free gas and 302 ppm for solid ^{129}Xe, along with an additional resonance at about 150 ppm (with $\Delta\upsilon_{1/2}$ =70 ppm) for xenon adsorbed at the surface. It is this adsorbed xenon whose magnetization can be transferred to the surface protons. Spectra acquired with and without laser illumination confirm that the observed proton peak at around 1.5 ppm is due to spin polarization transfer, with the efficiency of the SPINOE process being temperature dependent, and giving a maximum intensity of 140% at 168K, where the adsorbed xenon peak is most intense.

What the above literature review indicates is that at this point polarized ^{129}Xe NMR remains a relatively unexplored technique. Successful application of the method is not automatic and is dependent on several factors. The experiment requires that xenon be rapidly adsorbed into the region of interest, and that equilibration of the gas with the surface occurs before relaxation of the polarized xenon precludes the observation of a signal. In the following chapters three areas of research will be described. Immediately following the set-up of the experiment in the laboratory, a number of studies were carried out on bulk polymers. These samples were chosen as a bridge from previous conventional xenon studies. Chapter Three describes this work, in particular the study of a series of

polyalkylmethacrylates for which variable temperature polarized ^{129}Xe NMR spectra were acquired above and below the glass transition temperatures of the polymers. Chapter 4 describes the extension of this approach to study the surfaces of the metal oxide-SAM systems, and a number of metal oxide-polymer systems synthesized specifically for this project. The aim was to use ^{129}Xe NMR as a probe to examine the changes in mobility observed in the monolayer and polymer chains anchored to a surface. The possibilities and problems associated with this methodology will be examined.

References

[1] Jameson, C.J. *Chem Rev.*, **1991**, *91*, 1375

[2] Fraissard, J., Ito, T. *Zeolites*, **1988**, *8*. 350

[3] Barrie, P. J., Kinowski, J. *Prog. Nucl.Magn.Reson.Spectrosc.*, **1992**, *24*, 91

[4] Walton, J.H., *Polym.and Polym.Composites* **1994**, *2(1)*, 35

[5] Miller, J.B., *Rubber Chem.and Techn.* **1994**, *66*, 455

[6] Sefcik, M.D., Schaefer, J., Desa' J.A.E., Yelon, W.B., *Polym.Preprints*, **1983**, *24*, 85

[7] Stengle, T. R., Williamson, K. L., *Macromolecules*, **1987**, *20*, 1428

[8] Kentgens, A.P.M., van Boxtel, H.A., Verweel, R.-J., Veeman, W.S., *Macromolecules*, **1991**, *24(12)*, 3712

[9] Ferrero, M.A., Webb, S.W., Conner, W.C., Bondardet, J.L., Fraissard, J., *Langmuir*, **1992**, *8(9)*, 2269

[10] Kennedy, G.J., *Polymer Bulletin*, **1990**, *23*, 605

[11] Walton, J. H., Miller, J. B., Roland, C. M., *J. Poly. Sci. B:Poly. Phys.*, **1992**, *30*, 527

[12] Brownstein, J. E., Roovers, J. E. L., Worsfold, D.J., *Magn.Reson.Chem.*, **1988**, *26*, 392

[13] Walton, J. H., Miller, J. B., Roland, C. M., Nagode, J.B., *Macromolecules*, **1993**, *26*, 4052

[14] Cheung, T.T.P., Chu, P.J., *J.Phys.Chem.*, **1992**, *96*, 9551

[15] Miller, J. B., Walton, J. H., Roland, C. M. *Macromolecules*, **1993**, *26*, 5602

[16] Happer, W. *Annales de Physique*, **1986**, *6*, 645

[17] Walker, T.G., Happer, W., *Rev.Mod.Phys.*, **1997**, *69*, 629

[18] Bender, P. L., Beaty, E. C., Chi, A. R., *Phys. Rev. Lett.*, **1958**, *1*, 311

[19] Happer, W., *Rev.Mod.Phys.*, **1972**, *44*, 169

[20] Carver, T.R., *Science*, **1963**, *141*, 599

[21] Bhaskar, N.D. *et.al.*, *Phys.Rev.Lett.*, **1982**, *49*, 25

[22] Happer, W., Miron, E., Schaefer, S., Schreiber, D., van Wijngaarden, W. A., Zeng, X., *Phys. Rev. A.*, **1984**, *29*, 3092

[23] Raftery, D., Chmelka, B.F., *NMR Basic Principles and Progress*, **1994**, *30*, 111

[24] Raftery, D., Long, H. W., Meersmann, T., Grandinetti, P. J., Reven, L., Pines, A., *Phys. Rev. Lett.*, **1991**, *66*, 584

[25] Raftery, D., Reven, L., Long, H. W., Pines, A., Tang, P., and Reimer, J. A., *J. Phys. Chem.*, **1993**, *97*, 1649

[26] Bowers, C. R., Pietrass, T., Barash, E., Pines, A., Grubbs, R. K., and Alivisatos, A. P., *J. Phys. Chem.*, **1994**, *98*, 9400

[27] Pietrass, T., Bifone, A., Pines, A., *Surface Science*, **1995**, *334*, L730

[28] Bowers, C.R., Long, H.W., Pietrass, T., Gaede, H. G., and Pines, A. *Chem. Phys. Lett.*, **1995**, *205*, 168

[29] Long, H. W., Gaede, H. G., Shore, J., Reven, L., Bowers, C. R., Kritzenberger, J., Pietrass, T., Pines, A., *J. Am. Chem. Soc.*, **1993**, *115*, 8491

[30] Gaede, H. G., Song, Y. Q., Taylor, R. E., Munson, E. J., Reimer. J. A., and Pines, A., *Appl.Magn.Reson.*, **1995**, *8*, 373

[31] Albert, M. S., Cates, G. D. Driehuys, B., Happer, W. Saam, B., Springer, C. S., Wishnia, A., *Nature*, **1994**, *370*, 199

[32] Navon, G., Song, Y. Q., Room, T. Appelt, S., Taylor, R. E., and Pines, A., *Science*, **1996**, *271*, 1848

[33] Song, Y.Q., Goodson, B.M., Taylor, R.E., Laws, D.D., Navon, G., Pines, A., *Angew.Chem. Int.Ed.Engl.*, **1997**, *36(21)*, 2368

[34] Brunner, E., Seydoux, R.,Haake, M., Pines, A., Reimer,J.A., *J.Mag.Res.*, **1998**, *130*, 145

[35] Raftery,D., MacNamara, E., Fisher, G., Rice, C.V., Smith, J., *J.Am.Chem.Soc.*, **1997**, *119*, 8746

Chapter Two

Experimental

2.1 Instrumental

74.71-MHz ^{129}Xe single pulse Bloch decay spectra were acquired on a Chemagnetics CMX-270 NMR instrument using a variable temperature static probe with a coil diameter of 9mm internal diameter. The probe can be heated or cooled using a dewared stack which delivers gas directly into the sample region. Above room temperature, dry heated air is used while lower temperatures are achieved by cooling incoming nitrogen gas by passing through a coil in a liquid nitrogen dewar. In this way the temperature of the sample can be controlled to within +/-1°C. Temperature calibration is carried out by acquiring a series of spectra of sealed samples of methanol and ethylene glycol and using the techniques outlined in reference 1.[1] The ^{129}Xe spectra were referenced to a sealed sample of pure xenon containing approximately 2 atmospheres of gas. The single free gas peak was referenced to 0 ppm. This sample was also used to determine the ^{129}Xe 90° pulse widths, which were between 3.5 and 5 μs. An average of 400-50000 scans were acquired for the sealed samples, while the optically pumped spectra were acquired in 1 scan after 30 minutes of laser pumping.

The laser beam for optical pumping of the rubidium-xenon mixture was produced by a Ti-sapphire tunable-CW laser (Schwartz Electro-optics) in the single frequency ring configuration. This laser was pumped by a water cooled argon laser (Spectra physics model 2030). A pumping power of 10 watts typically gave a 1.5 Watt beam at 794.9 nm.

The experimental setup used to combine optical pumping with NMR is shown in Figure 2.1. The glassware is coated with Surfrasil, a siliconizing agent which reduces the rate of wall-induced relaxation of the pumped ^{129}Xe.[2] The cell contains a film of rubidium which is heated to between 80 and 120°C. The temperature required to vaporize the metal varies depending on the amount of rubidium suboxides dissolved in the metal film.[3] It

2.2 Sample preparation

Prior to the acquisition of optically pumped ^{129}Xe spectra, samples were evacuated at 90°C to remove physisorbed water (except for bulk polymer samples of low melting points which were evacuated at room temperature). Sealed samples were made by evacuation, addition of xenon and subsequent sealing while the xenon was frozen into the sample region.

2.2.1 Bulk polymers

In general bulk polymers were used as received from Scientific Polymer (New York). Where samples were not available in powdered form, polymers were powdered by cooling in liquid nitrogen and grinding in a wiggle bug, followed by sieving through a 100 mesh brass sieve.

2.2.2 Zirconia coated with polyethylene glycol

The high surface area zirconia (Degussa) was the same substrate used for the deposition of self-assembled alkyl-phosphonate monolayers in Part One. It has an average particle size of about 30nm and a specific surface of around $40m^2/g$. Polyethylene glycol samples of two different molecular weights (Mw=400 and Mw=10,000) were purchased from Aldrich. Adsorption was carried out by addition of the oxide powder to 250ml of 1mM NaCl solution.[4] A solution of the polymer was added to this suspension, reaction was carried out for 48 hours under nitrogen and with pH adjustment to maintain pH=3. The resulting samples were washed and centrifuged with toluene, dichloromethane and acetone. Preliminary characterization of the coated samples was by elemental analysis and solid state ^{13}C CPMAS NMR procedures similar to those described in Part One. Elemental analysis indicated a high amount of organic material present in the samples; 8.4% carbon for the high molecular weight (10,000) PEG on zirconia, and 6.9% for the

low molecular weight (400) PEG-ZrO_2 assembly. The self assembled monolayer samples are the same ones used in the conventional solid state NMR studies in Part One.

2.3 BET isotherms

Xenon isotherms were carried out on a number of the bare oxide and thin-film samples in order to measure the surface area and adsorption energies of xenon on the surfaces. In general the BET (Brunauer, Emmet, Teller) isotherm[5] gave an excellent fit to the data. The treatment of isotherm data will be described as it arises in the text. The apparatus used for these experiments is a standard volumetric isotherm rack, provided with both xenon and helium reservoirs. Helium is used to carry out dead volume measurements for each temperature at which an isotherm is obtained. The samples are put into a bulb with a narrow bore capillary attachment blocked with glass wool. These are then sealed and inverted for attachment to the rack. The samples are heated at 100°C under a diffusion pump vacuum of 10^{-6} torr for 12 hours prior to isotherm measurements. The pressure is read with an Edwards pressure gauge accurate to +/- 0.1 torr. Cold baths of liquid nitrogen and linear alkanes are used and the temperature monitored to +/-1°C.

References

[1] Raiford, D.S., Fisk, C.L.; Becker, E.D., *Anal.Chem.*, **1979**, *51*, 2050

[2] Raftery, D., Long, H.W.; Meersman, T.; Grandinetti, P.J.; Reven, L.; Pines, A., *Phys.Rev.Lett.*, **1991**, *66*, 584

[3] Rheingold, H. from *Homoatomic Rings, Chains and Macromolecules of Main Group Elements* **1977** Elsvier

[4] Veluda, R.R., Spencer, H.G.,*Colloids and Surfaces*, **1991**, *58*, 99

[5] Brunauer, S., from *Physical Adsorption* **1945** Princeton University Press

Chapter Three

Optically Polarized ^{129}Xe NMR of Bulk Polymers

One of our principle aims in this work has been to develop the use of polarized ^{129}Xe as a permeate of polymers in order to study both chain mobility and the diffusion of gases into polymer systems. To this end we decided to compare semicrystalline and amorphous polymers. In general, xenon diffuses exclusively into the amorphous domains of semicrystalline polymers where chain motion creates free volume in which the xenon can reside.[1] In conventional ^{129}Xe studies using sealed samples, adsorbed ^{129}Xe signals in both semicrystalline[2] and amorphous[3] polymers are still observed below the glass transition. However, a break in the dependence of chemical shift on temperature is observed around T_g, and the xenon permeates more easily above T_g.

The rate of diffusion of xenon into polymers is a function of temperature, pressure, surface area, and chain mobility. Xenon diffusion coefficients range between 0.1×10^{-7} to 10×10^{-7} (cm^2/sec) for amorphous polymers above their glass transitions.[4] Thus on the time scale of the polarized xenon experiment, we are probing several micrometers into the polymer, keeping in mind that the diffusion will be slower at the low xenon pressures (< 1 atm) typically used. As discussed below, this has implications for the ^{129}Xe peaks observed in semicrystalline polymers using the optical pumping rather than conventional sealed sample technique.

3.1 Polypropylene

Polypropylene samples were investigated by conventional and polarized xenon NMR. Differential scanning calorimetry (DSC) confirmed that the T_g values of these samples are in the range -23 to -28°C and the degree of crystallinity was ~ 37%. The ^{129}Xe NMR spectrum obtained with one scan using the optical pumping method is shown in Figure 3.1a. Conventional ^{129}Xe NMR spectra of a sealed sample were also acquired,

Figure 3.1b, in which the acquisition times were around 20 hours, as compared to a few seconds for the single acquisition used with the optically pumped gas. The signal at 0 ppm is due to gaseous xenon and the broad resonance centered at 216 ppm is due to xenon adsorbed in the amorphous regions of polypropylene.

The optically polarized ^{129}Xe shifts on polypropylene were studied as a function of temperature. Variable temperature spectra are shown in Figure 3.2. As the temperature is lowered the shift and linewidth of the adsorbed ^{129}Xe resonance gradually increase and at -20°C the resonance is no longer visible. The disappearance of the adsorbed peak is due to the decrease in mobility at the glass transition which greatly retards the diffusion of xenon into the amorphous domains of the polymer. The gradual increase in rigidity as the polymer is cooled also causes broadening of the ^{129}Xe resonance, as the mobility of the polymer affects the mobility of the gas. Slower xenon migration leads to observation of a wider range of isotropic shifts. It should be noted that a sealed sample study of polypropylene[2] observed peaks for xenon dissolved in the polymer below T_g (and a break in the temperature dependence of the ^{129}Xe chemical shift at T_g). This is likely due to the difference in timescales of the two experiments, where the use of optically polarized ^{129}Xe relies on rapid diffusion into the polymer chains. In conventional studies, the gas has much longer to permeate into the sample. This difference in the way in which the glass transition is manifested is not observed in the studies of amorphous polyalkyl methacrylates, for reasons to be discussed below.

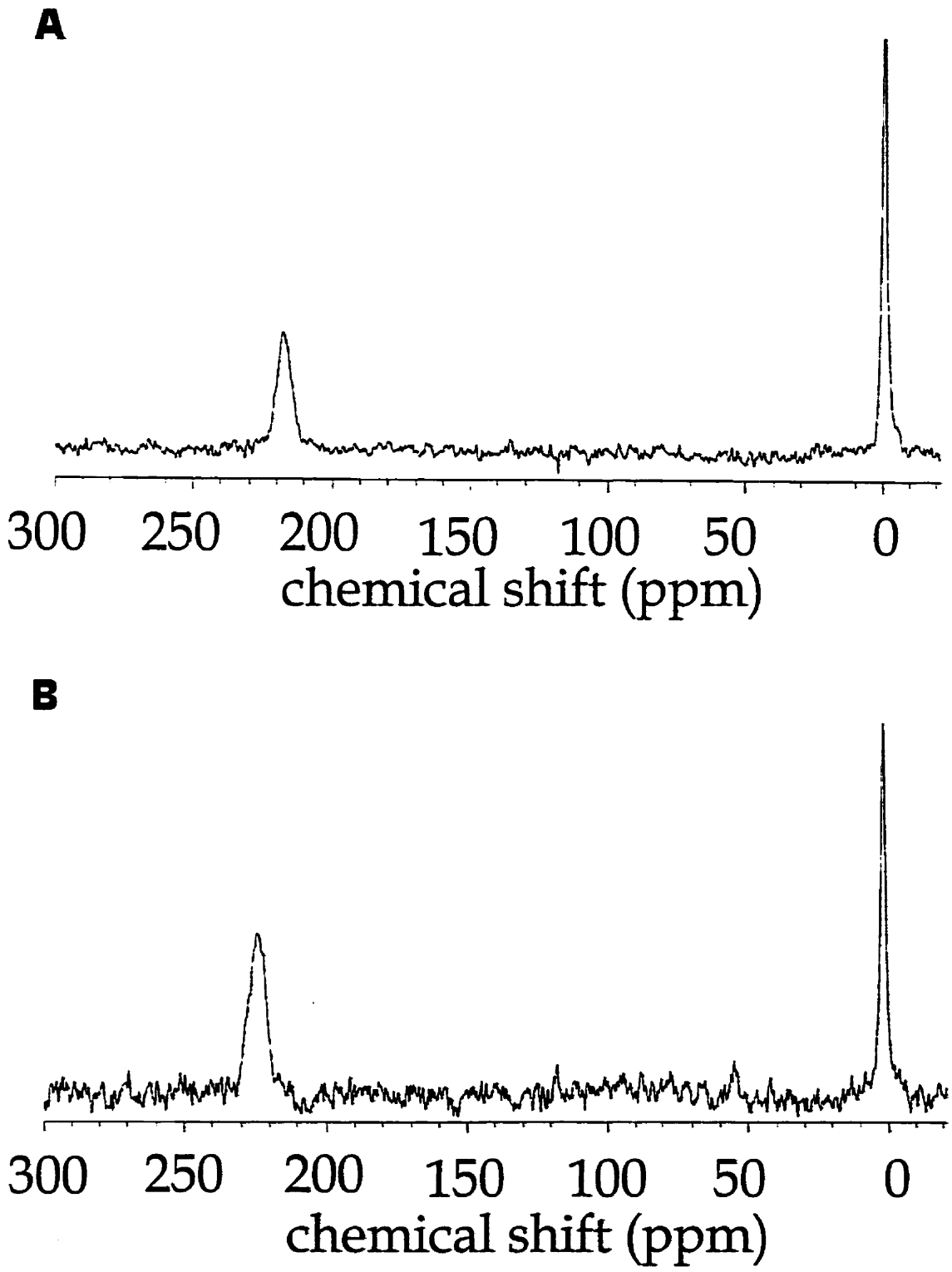

Figure 3.1 ^{129}Xe NMR spectra of xenon absorbed on polypropylene. A) Optically pumped xenon, 1 scan, acquisition time (including pumping) 30 minutes and B) conventional sealed xenon sample, 800 scans, acquisition time 10 hours.

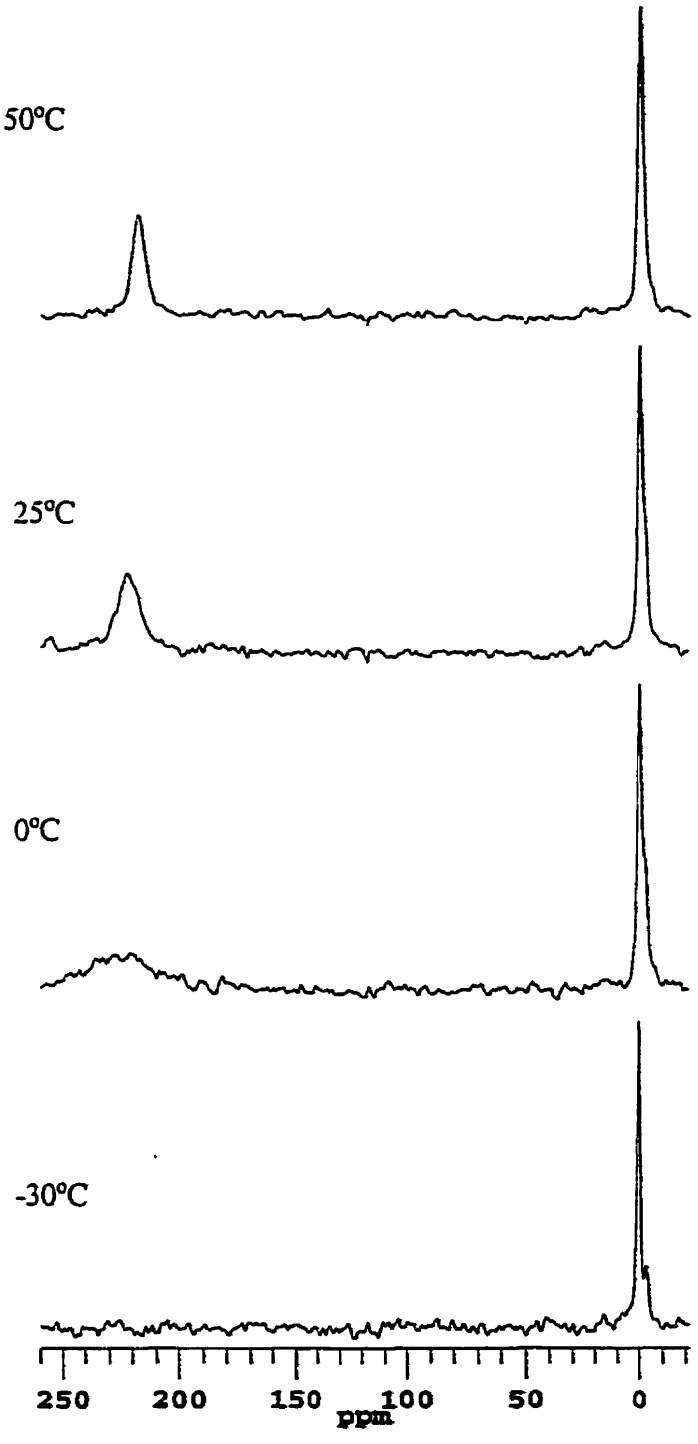

Figure 3.2 Variable temperature optically polarized ^{129}Xe NMR spectra of xenon dissolved in polypropylene at the temperatures indicated. Spectra were acquired after 30 minutes optical pumping.

3.2 Poly(n-alkyl)methacrylates: Amorphous Polymers

Optically polarized ^{129}Xe spectra of poly(n-butyl methacrylate) (left), poly(iso-butyl methacrylate) (center) and their copolymer (right) are shown in Figure 3.3. At room temperature the chemical shifts for the dissolved xenon peak are 199, 206 and 204 ppm respectively. The glass transition temperatures are at 29.9 °C for p(n-BMA), 56.6 °C for p(iso-BMA) and 35.2 °C for the copolymer. The spectra observed for the copolymer display only one adsorbed ^{129}Xe peak intermediate in shift to that of the two homopolymers. This suggests either a rapid exchange of the dissolved xenon between the different polymer sites, and/or intimate mixing of the copolymer constituents. There are reports of conventional xenon NMR in the literature in which two peaks are observed for block copolymers.[5] Miscible polymer blends are expected to show only one peak. Our sample is a random copolymer with two similar constituents, so the lack of phase segregation indicated by the single peak is expected. In some of the spectra a resonance near but separated from the free gas resonance is observed. This arises from gas residing in the interparticle spaces. This is also observed in other samples and will be discussed below.

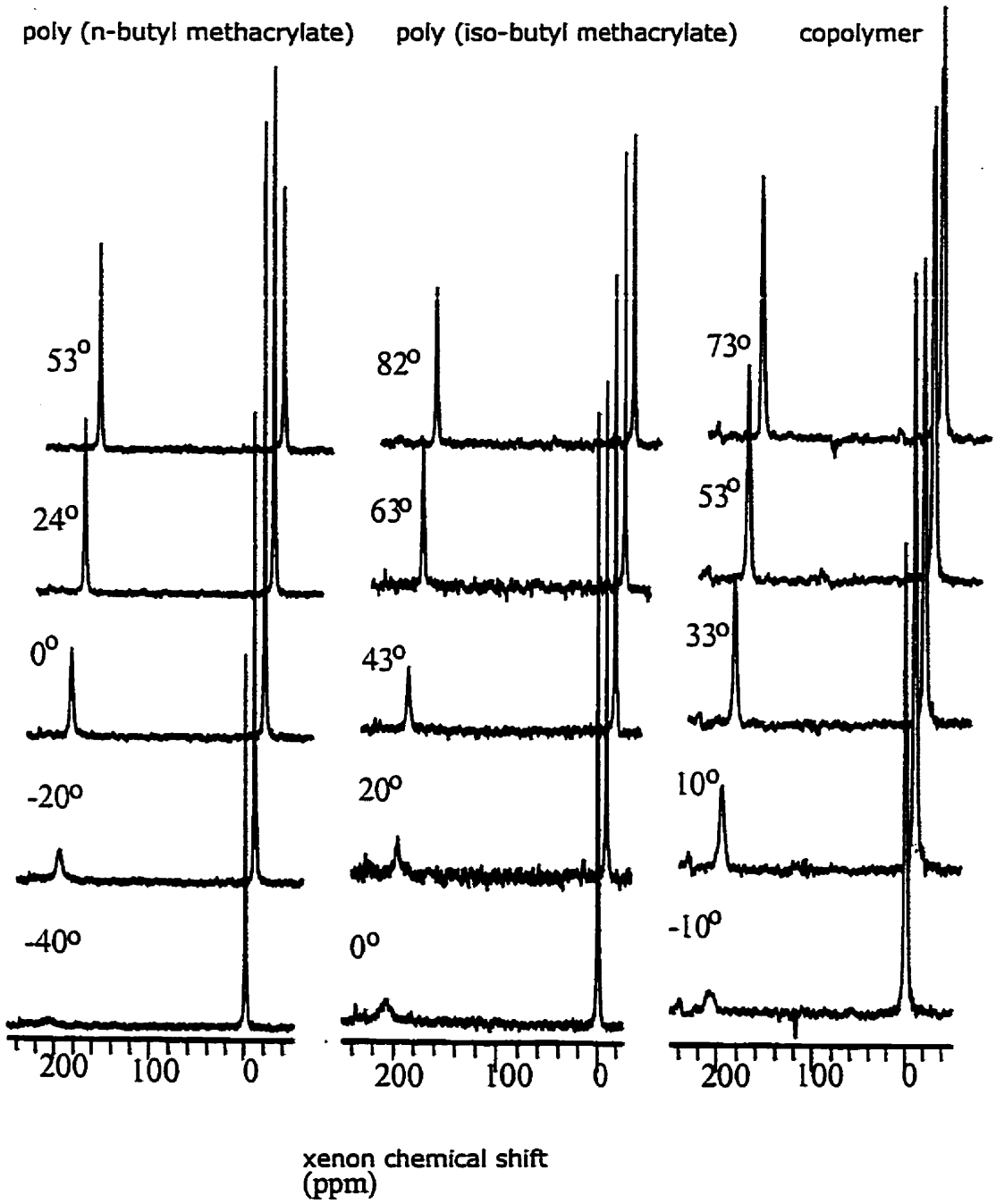

Figure 3.3 Variable temperature optically polarized ^{129}Xe spectra of xenon adsorbed in poly(n-butyl methacrylate), poly(iso-butyl methacrylate) and their copolymer. Temperatures are shown in degrees celsius.

In contrast to the polarized ^{129}Xe spectra observed for xenon adsorbed in the unbranched polypropylene, signals for ^{129}Xe adsorbed in polyalkyl methacrylates are observed at much lower temperatures, up to 60°C below their T_g values. Results for poly(n-butyl methacrylate) show that xenon rapidly dissolves into the polymer at -30°C (60 degrees below T_g), whereas in poly(methyl methacrylate) the adsorbed peak does not appear until the polymer is heated to 100°C (5 degrees below T_g). The molecular motions of the poly(alkyl methacrylates) have been studied by conventional NMR.[6] The main α relaxation (or slow chain motion) stops at T_g, while the localized side chain motions, or β processes persists into the glassy state.

The free surface is known to affect the glass transition of polymers, where a depression in T_g is observed at the surface because of the reduced chain density.[7] This effect can not be studied by solid state NMR as the concentration of surface nuclei is too low compared to the bulk. In addition conventional solid state NMR experiments study the glass transition indirectly via probing of chain dynamics. The chain motions associated with glass transitions are slow on the NMR timescale. As shown above, polarized ^{129}Xe NMR gives a direct observation of T_g. It was hoped to use this experiment to detect a separate surface glass transition, however the near surface region probed by the polarized xenon experiment (0.1 - 10 micrometers) is essentially bulk-like with no separate surface T_g being detected.

In the case of the poly(alkyl methacrylates), the degree to which the dissolved xenon peak persists below the glass transition is related to the length of the side chains. Since the bulkier butyl sidechains create a larger free volume for the xenon to occupy, the gas can readily permeate this polymer far below T_g. Presumably, as the side chain is lengthened, the ^{129}Xe signal will be observed until still lower temperatures. However, there is likely a limiting value for the side chain length above which crystallisation of the alkyl sidechains prevents any gas adsorption. In fact, ^{129}Xe spectra of poly (octadecyl methacrylate) did not display adsorbed xenon peaks at any temperature. These NMR experiments may thus be of use in the investigation of gas permeability in polymers.

Miller *et al.* have developed a van der Waals shift model which accurately predicts the dependence of the ^{129}Xe shift on temperature for a variety of polymers which

are approximated as smooth tubes.[8] Providing the xenon loading is sufficiently low to disregard xenon-xenon collisions (a condition more adequately fulfilled by the lower pressures used in the optical pumping experiment) and the xenon itself does not alter the polymer (also a better assumption at low xenon pressures), the Lennard Jones potential can be used to predict plots of chemical shift vs. temperature. However the presence of bulky side groups complicates analysis of the ^{129}Xe chemical shifts, since the polymer tube approximation is no longer valid.

A plot of ^{129}Xe chemical shift vs. temperature for all the polyalkylmethacrylates investigated is shown in Figure 3.4. As in the case of conventional ^{129}Xe NMR studies of polymers in sealed samples under high gas pressures, the plots of the chemical shift against temperature are linear above T_g. The discontinuity is due to the densification of the polymer at the glass transition since the xenon shift is inversely proportional to the available free volume. A study by Stengle and Williamson[3] of poly(ethyl methacrylate) using sealed xenon samples also shows a break in the slope of chemical shift vs temperature at T_g. In fact the break is only small, and the authors point out that the discontinuity in this case is better highlighted in the plot of linewidth vs. temperature. Our extension to a wider range of alkyl methacrylates confirms this observation. In all the poly (alkylmethacrylates) where the dissolved xenon signal persists below the glass transition, we see a break both in the dependence of chemical shift on temperature (Figure 3.4) as well as in linewidth (Figure 3.5).

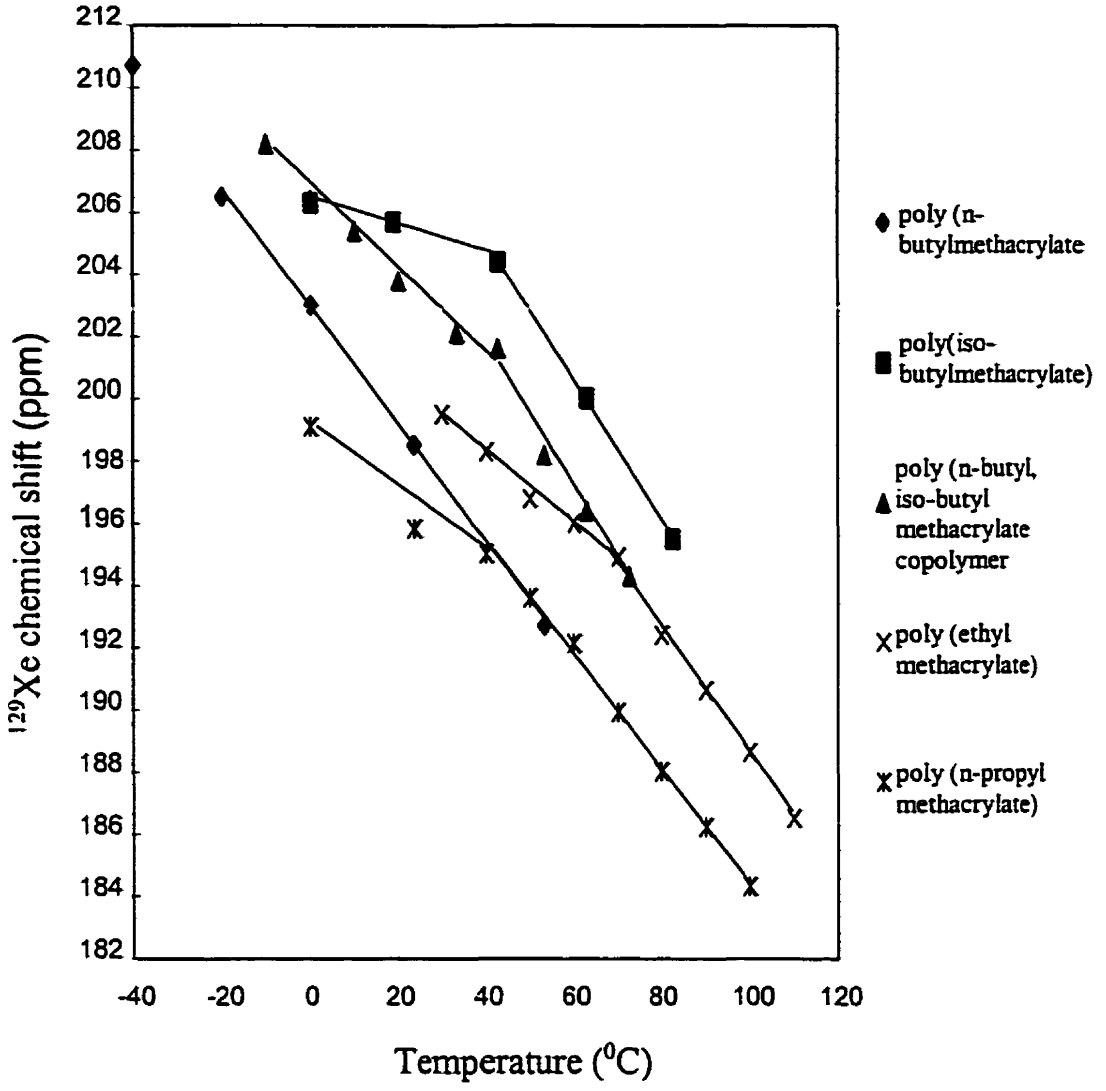

Figure 3.4 Graph of adsorbed ^{129}Xe shift against temperature for bulk poly alkyl methacrylates. Lines are to guide the eye indicating the break in the dependence of ^{129}Xe chemical shift on temperature at the glass transition temperatures. T_g values are: poly (n-butyl methacrylate); 29.9°C, poly (iso-butylmethacrylate); 56.6°C, n-butyl, iso-butyl methacrylate copolymer; 35.2°C, poly (ethyl methacrylate); 66°C and poly (n-propyl methacrylate); 35°C.

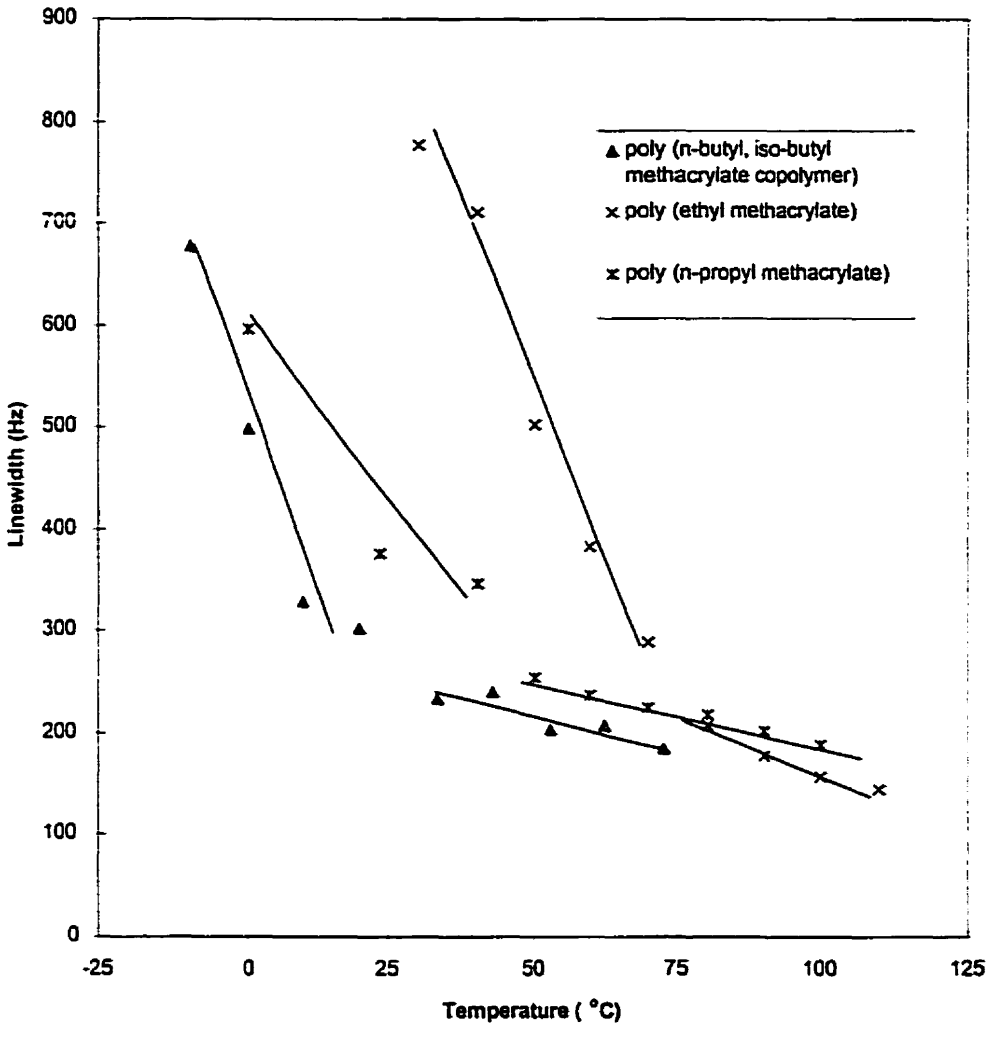

Figure 3.5 Graph of linewidth against temperature for selected poly (alkyl methacrylates). Lines are to guide the eye, indicating the discontinuities in the dependence of linewidth on temperature at the glass transition points.

The smaller linewidths above T_g are due to the higher chemical exchange rate of xenon amongst the distribution of different environments present in the amorphous phase, although the polymer chain motions may also affect xenon line shape. The linewidths above T_g for all the samples are fairly similar. Of course, above the T_g the polymer chains have significant mobility (exhibiting an almost liquid-like state) and, to the xenon atoms, may appear to provide very similar averaged environments. Below the T_g the resonances are a function of the sidechain length, the shorter the side chain, the larger the linewidth. Evidently, the shorter sidechain chain polymers create a more heterogeneous environment.

In conclusion, the optically polarized ^{129}Xe NMR studies of semicrystalline polypropylene and a range of amorphous poly (alkyl methacrylates) show that T_g can be directly detected, but is manifested differently in the two types of polymer. In semicrystalline polypropylene, the glass transition is marked by the disappearance of the adsorbed ^{129}Xe peak. This effect should be looked for in other semicrystalline polymers. In the polyalkylmethacrylates the dissolved xenon peak is still observed below the T_g, but the glass transition is marked by a break in the dependence of chemical shift and linewidth on temperature. The extent to which xenon dissolves below T_g is related to the size of the mobile sidegroups. An initial motivation was to look for a surface T_g, but the diffusion was discovered to be too rapid so that only the bulk T_g was observed. It is proposed that the observation of a surface glass transition may be possible through the study of thin polymer films. By coating a layer of polymer onto an inorganic substrate, a free surface can be created, removing the effects of bulk polymer on the ^{129}Xe spectra. Initial investigations into ^{129}Xe NMR of thin films will be explored in Chapter Four.

3.3 Exchange experiments

In order to explore the dynamic nature of the xenon adsorption process in polymers, 2D exchange spectra of a sealed sample of poly (n-butyl methacrylate) were acquired at room temperature at a range of mixing times. The principles of the experiment are identical to those of the ^{31}P tensor exchange investigation described in

Part One (n.b. the pulse sequence used does not include cross-polarization) but the resulting spectra are simplified due to the observation of isotropic shifts only. Spectra with mixing times of 10 ms and 1 s are shown in Figure 3.6.

The longer mixing time is sufficient to allow exchange of xenon between the free gas and dissolved sites, leading to the observed cross peaks. If this experiment is carried out on polymer samples consisting of monodisperse spheres of known dimensions, then the build-up of the cross peaks as a function of mixing time can be used to determine xenon diffusion constants (as shown in a study of polystyrene[9] and for two model polymer blends.[5]) Since our polymer sample was not produced in a manner which would produce controlled particle sizes, diffusion behavior can not be exactly determined. However the spectra do show that xenon diffuses into the polymer on the timescale of ~1 s, consistent with the behavior observed in polarized xenon experiments.

In comparison an exchange spectrum with a mixing time of 10 ms of xenon adsorbed on the surface of a silica monosphere sample is shown in Figure 3.7. While this sample is not directly related to the polymer sample, the experiment demonstrates that chemical exchange in the silica system is faster because the xenon merely has to travel to the surface, whereas in the polymer sample permeation into the bulk material is required. The spectrum shown above in Figure 3.7 is the 1D ^{129}Xe spectrum which displays 3 peaks, a surface peak at ~56 ppm, an interparticle peak at ~4 ppm and the free gas peak at ~0 ppm. It is interesting to note that the exchange process in this sample involves not the free gas, but rather the interparticle resonance (the 2D data is shown as a contour plot to more clearly reveal this). The nature and origins of these shifts will be discussed more fully in Chapter 4.

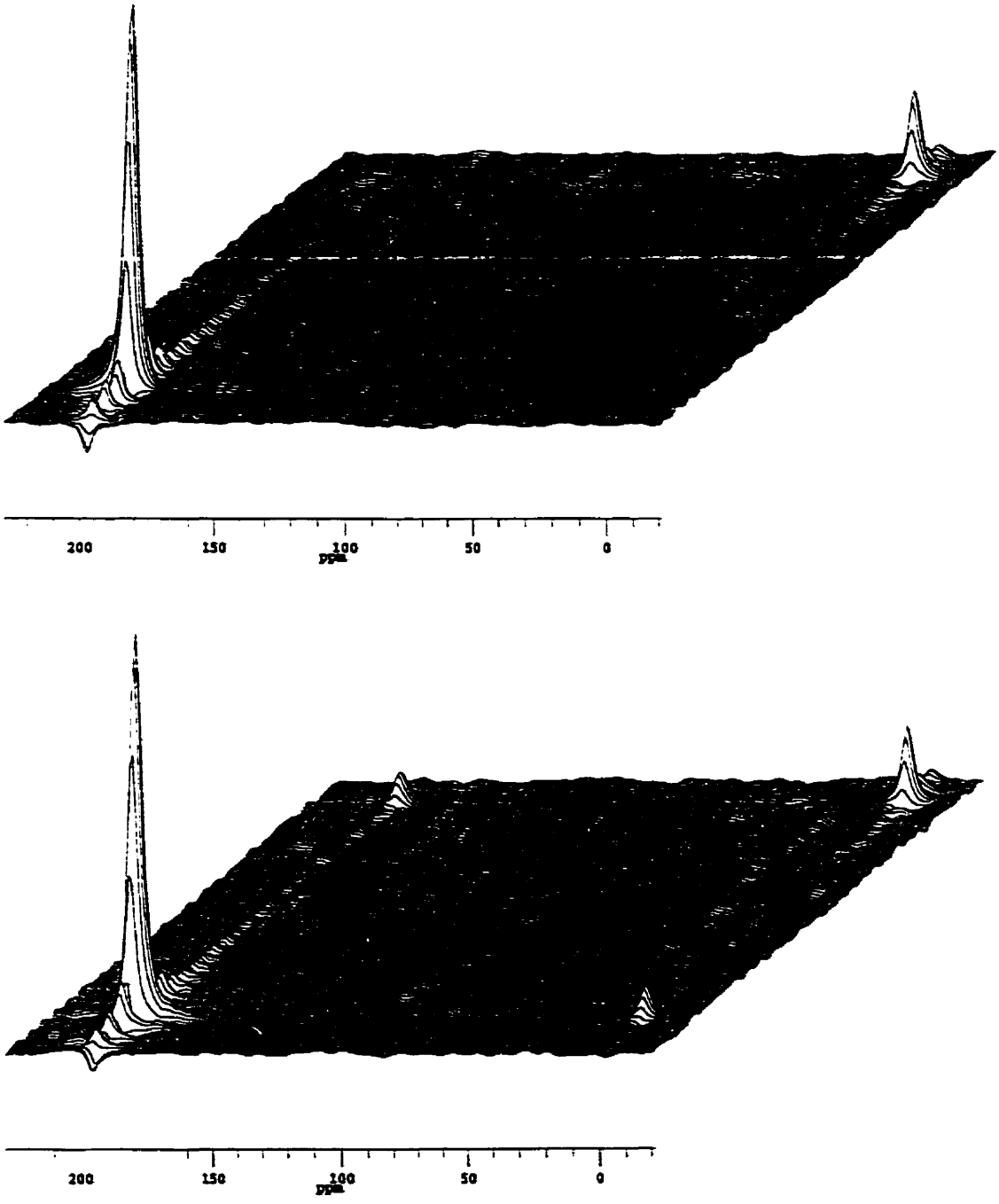

Figure 3.6 ^{129}Xe exchange spectra of a sealed sample of xenon in poly (n-butyl methacrylate) at room temperature with mixing times of: 10ms (above) and 1s (below). The baseline distortians seen in the second dimension are due to insufficient data acquisition length in the t_2 dimension. Spectra were acquired in 100 scans with a recylcle delay of 16 s. The evolution period consisted of 64 increments with a dwell of 25 μs.

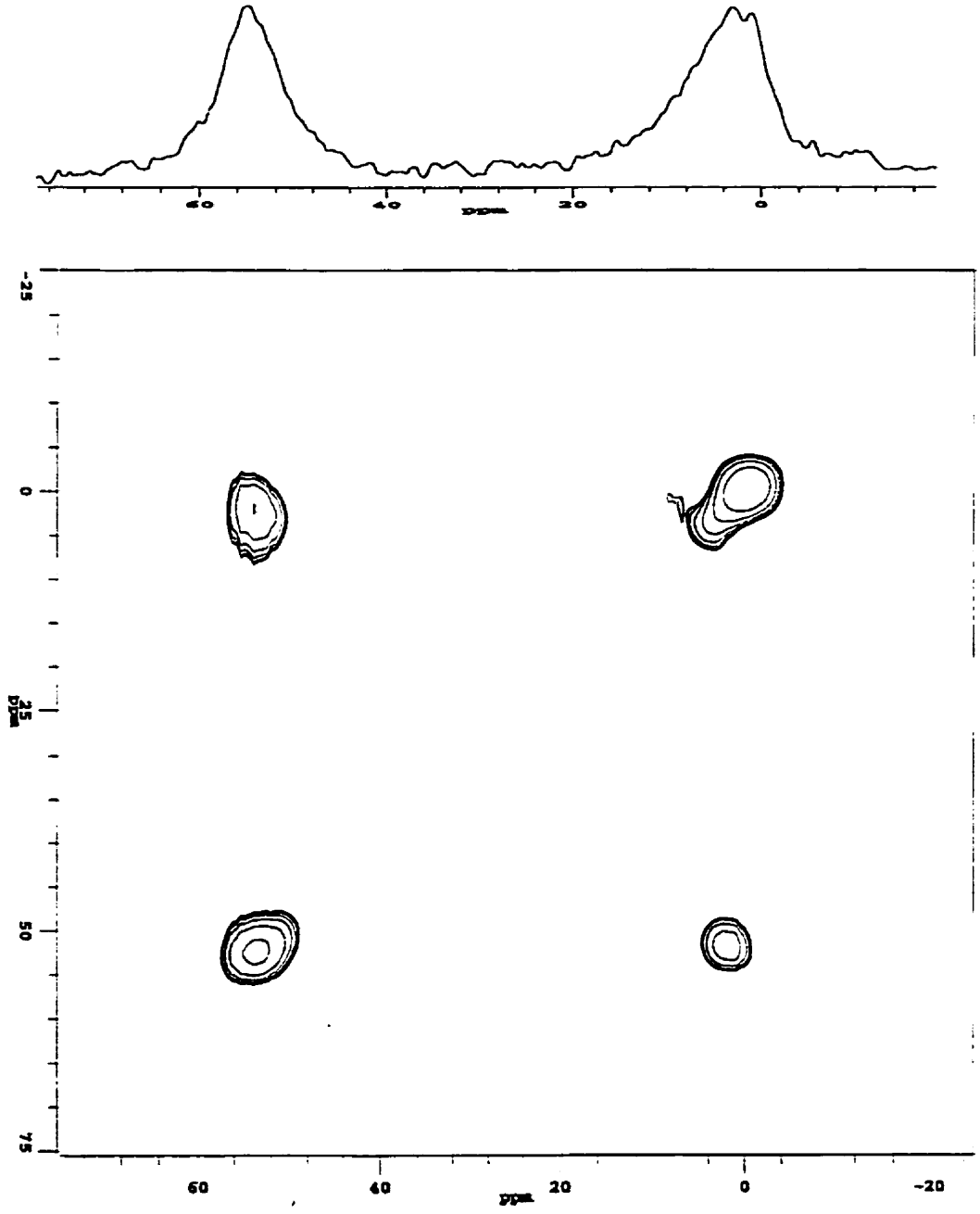

Figure 3.7 ^{129}Xe exchange spectrum of a sealed sample of xenon on silica acquired at room temperature with a mixing time of 10ms. The spectrum was acquired in 1000 scans with a recycle delay of 1 s. The evolution period consisted of 64 increments with a dwell time of 27.8 μs. The one dimensional ^{129}Xe spectrum is shown above.

3.4 Polarization transfer experiments

One of the ultimate goals of this research involves the transfer of the large optically pumped ^{129}Xe nuclear polarization to other nuclei by cross polarization. In this way the polarized ^{129}Xe experiment has the potential to enhance the sensitivity of low concentration species, for example surface sites. Cross polarization can also be used on xenon adsorbed in polymer blends to give information about the relative solubility and/or residence times of the gas in different components of the polymer system. A conventional ^{129}Xe study[10] of a xenon dissolved in a sample of a polypropylene-polyethylene copolymer dispersed in a polypropylene (PP) matrix showed adsorbed ^{129}Xe peaks for all polymer sites at -30°C. Cross polarization was successfully carried out from protons to xenon in the more rigid PP matrix, but not from protons to the more mobile copolymer fraction.

In order to ascertain the correct cross polarization parameters for the transfer of magnetization from laser pumped ^{129}Xe to protons, it was decided to first optimize the conditions for the reverse process. This is a simpler procedure, involving the conventional sealed sample approach, rather than the laser polarized experiment. Polarization transfer requires cooling of the sample to reduce chain mobility and increase xenon sticking times in order to increase the ^{129}Xe-^{1}H dipolar couplings. Poly (n-butyl methacrylate) was felt to be a good candidate for this study, since the bulky side groups on this polymer facilitate xenon adsorption at temperatures well below the glass transition.

The single pulse with proton decoupling and the cross polarized ^{1}H-^{129}Xe spectra are shown in Figure 3.8 The free gas peak is not observed in the lower spectrum, confirming that the observed peak arises from cross polarization. The use of a sealed sample allowed for straightforward optimization of the contact time, the largest transfer was achieved with a time of 5 ms. This is short compared with the contact times required for optimal polarization transfer transfer to xenon on a surface (typically ~20 ms), since in general residency times on a surface will be smaller, xenon not being trapped as it is by the polymer chains.[11]

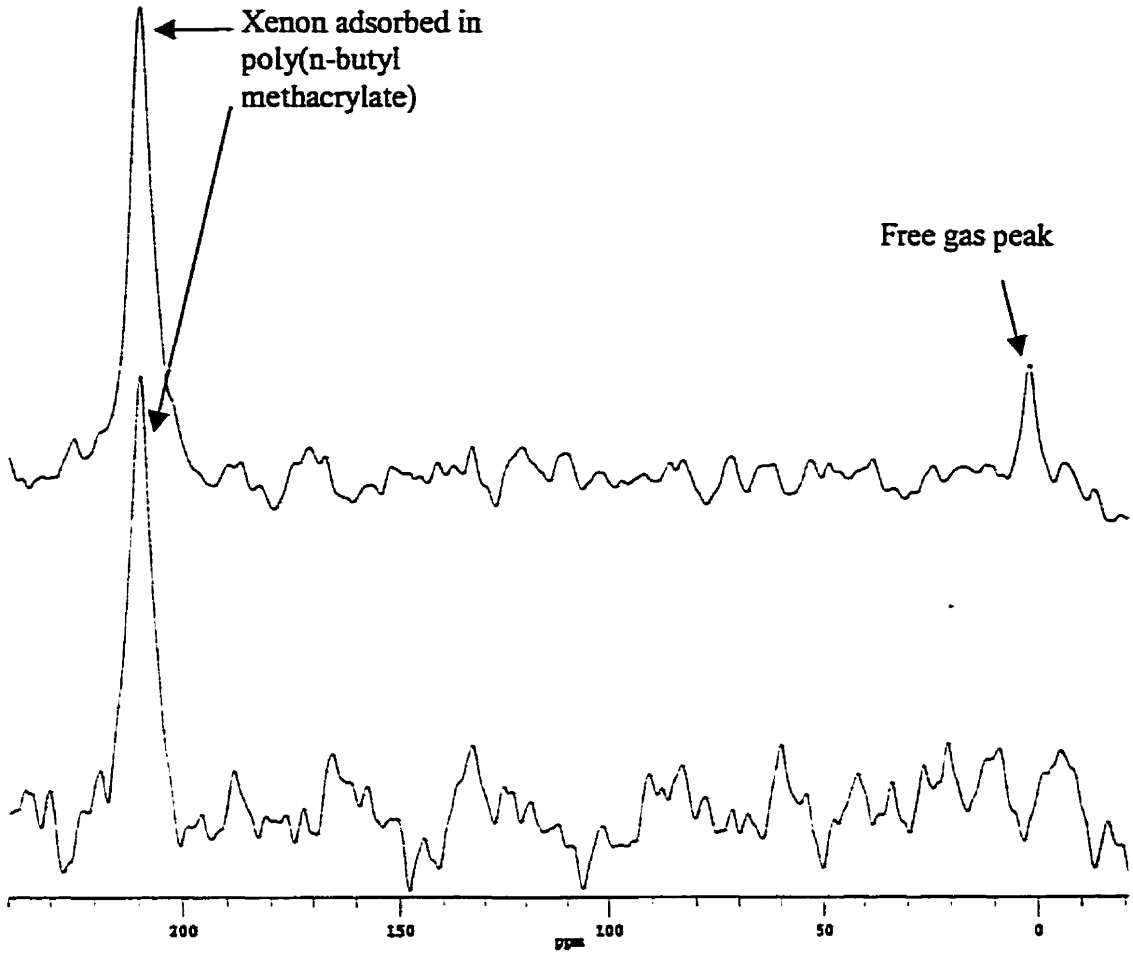

Figure 3.8 ^{129}Xe spectra of a sealed sample of xenon in poly(n-butyl methacrylate) at –30°C: The single pulse with proton decoupling spectrum (above) was acquired in 8 scans with a recycle delay of 1 minute, while the ^{1}H-^{129}Xe cross polarization spectrum (below) required 200 scans with a contact time of 5 ms and pulse delay of 0.5 s.

3.5 2D ^{1}H-^{129}Xe correlation spectroscopy

The mobility of the polymers involved in cross polarization to ^{129}Xe was further explored by the acquisition of a 2D correlation spectrum. This experiment uses the 2D WISE pulse sequence described in Part One (1.4) The spectrum at -30°C is shown in Figure 3.9. The observed proton linewidth is 38kHz, consistent with a system displaying some limited molecular mobility. As noted above, the mobile fractions which provide the free volume required for xenon permeation below T_g are the side chains, which are

expected to display linewidths narrower than those associated with rigid polymer chains. This spectrum is further proof of good Xe-H (polymer) contact. The only other example of this kind of spectrum reported in the literature is for the PP/PE copolymer dispersed in a PP matrix.[10] That study reported a very large proton linewidth (82kHz) for xenon dissolved in the rigid part of the PP matrix at -30°C. It should be noted that since the protons throughout the system will be strongly coupled, the xenon correlation experiment will yield an averaged proton linewidth, and will not give information about the precise location of the xenon atoms with respect to the different proton sites.

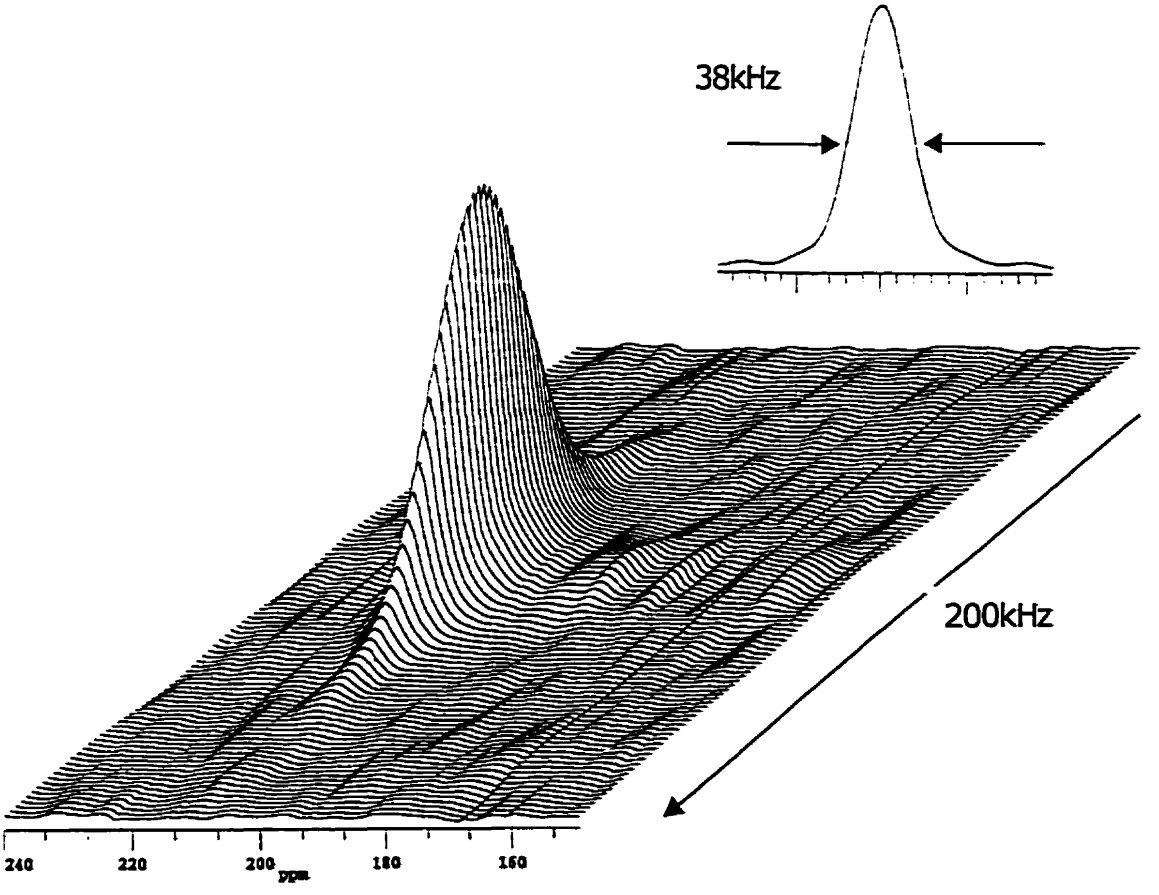

Figure 3.6 ^{129}Xe-^{1}H correlation spectrum of xenon dissolved in poly(n-butyl methacrylate) at –30°C. The spectrum was acquired in 2000 scans with a contact time of 5 ms and recycle delay of 0.5 s. The proton evolution period consisted of 16 increments with a dwell time of 2 μs.

In summary, successful cross polarization has been demonstrated between the protons of poly (n-butyl methacrylate) and ^{129}Xe dissolved in the polymer at temperatures far enough below T_g to promote long residency time of xenon at the proton sites. The optimization of CP conditions opens up the possibility of carrying out cross polarization from optically polarized ^{129}Xe to proton sites. This experiment was not implemented here due to time constraints. In order to determine whether a proton signal arose from cross polarization from the laser polarized ^{129}Xe, it would be necessary to first eliminate the proton magnetization which arises from the Boltzmann distribution. This approach has been reported in the literature,[11] where the proton signal was destroyed by use of a series of saturating pulses. Subsequently right or left circularly polarized light was used to pump the ^{129}Xe, giving spectra that differ in phase by 180°. This confirmed that the observed proton signal was due to the ^{129}Xe-^{1}H cross polarization. However since the cross polarization from ^{129}Xe to protons in the bulk polymer is much more efficient than that observed on surfaces (where much lower temperatures are necessary to increase residency time), this should be our next attempted experiment on the poly (n-butyl methacrylate) system. Since the xenon diffuses into the bulk polymer, this will ultimately be of use in the study of thin polymer films, once samples have been synthesized in which xenon adsorption is confirmed. In addition it may be possible to transfer the large ^{129}Xe polarization to other nuclei. Carbon-13 enhancement would be a desirable goal for these studies, unfortunately the construction of a ^{13}C-^{129}Xe double resonance probe is complicated by the fact that the frequencies of these two nuclei are so close (67.9 and 74.7 MHz respectively). Another possible candidate is deuterium, using labeled thin polymer films. This would be useful for obtaining further information on surface mobility.

References

[1] Miller, J.B., *Rubber Chemistry and Technology*, **1993**, *66*, 455

[2] Chung, T.T.P.; Chu, P.J.; *J.Phys.Chem.*, **1992**, *96*, 9551

[3] Stengle, T.R., Williamson, K.L., *Macromolecules*, **1987**, *20*, 1428

[4] Walton, J.H.; Roland, C.M., *J.Poly.Sci.B:Poly.Phys.*, **1992**, *30*, 527

[5] Tomaselli, M.; Meier, B.H.; Robyr, P.; Suter, U.W.; Ernst, R.R., *Chem.Phys.Lett.*, **1993**, *205*, 145

[6] Kulik, A.S.; Beckham, H.W.; Schmidt-Rohr, K.; Radloff, D.; Pawelzik, U.; Boeffel, C.; Speiss, H.W., *Macromolecules*, **1994**, *27*, 4746

[7] Mayes, A.M., *Macromolecules*, **1994**, *27*, 3114

[8] Miller, J.B.; Walton, J.H.; Roland, C.M., *Macromolecules*, **1993**, *26*, 5602

[9] Simpson, J.H.; Wen, W.; Jones, A.A.; Inglefield, P.T.; Bendler, J.T., *Macromolecules*, **1996**, *29*, 2138

[10] Mansfeld, M.; Veeman, W.S., *Chem.Phys.Lett.*, **1994**, *222*, 422

[11] Gaede, H.C.; Song, Y.-Q.; Munson, E.J.; Reimer, J.A.; Pines, A., *Appl.Mag.Res.*, **1995**, *8*, 373

Chapter Four

Polarized ^{129}Xe NMR of Polymer Coated Metal Oxides and Self Assembled Monolayers

4.1 Introduction

Polymer encapsulated inorganic particles are of interest for a variety of applications where good coupling between the polymer matrix and inorganic substrate is essential.[1] Like the SAM systems, thin polymer coatings deposited onto inorganic substrates offer a range of potential uses in surface protection and modification. Unlike the SAMs, thin polymer films are, by their nature, less conformationally ordered structures. Even where a relatively narrow molecular weight range of polymer is deposited, the possible arrangements of the polymer chain are much greater than those seen in the shorter chain monolayer systems. Polymers may be anchored to the surface by end groups (terminal attachment), or by multiple functional groups in the polymer as shown in Figure 4.1.[2] The final conformation of segmentally attached polymers can involve brush conformations with a single polymer-substrate bond for each chain, or mushroom conformations containing so-called loops, trains and tails.[3] The conformation of the film will depend on the chemical properties of the surface groups of the inorganic substrate, the deposition conditions (solvent, temperature etc.) as well as the nature of the polymer itself.

Characterization of the uniformity of polymer films on non-planar substrates is difficult. Most of the fundamental studies of adsorbed polymers have been carried out on planar substrates where film thickness and uniformity can easily be determined by ellipsometry, and structural information can be obtained through vibrational spectroscopy.

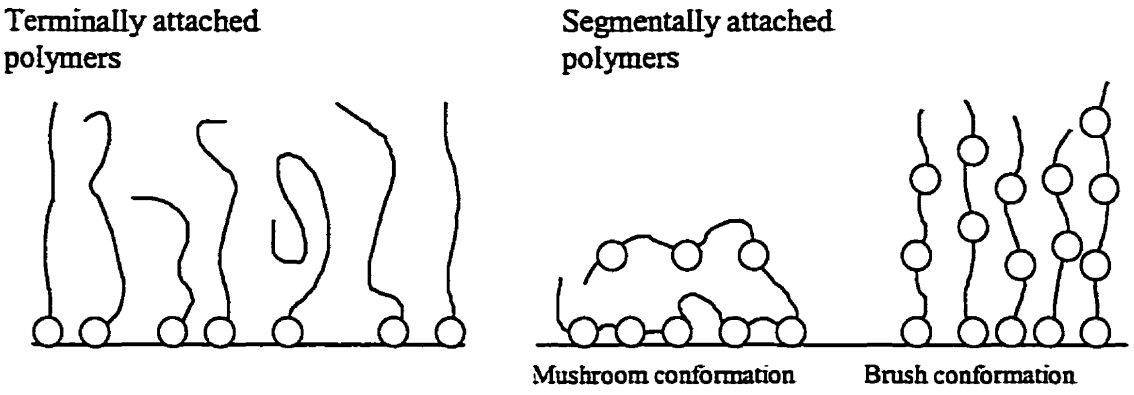

Figure 4.1 Modes of attachment for polymers on substrates. Open circles represent functional groups.

Conventional solid state NMR has been used in the characterization of non-planar polymer coated samples. CPMAS studies can be used to determine the bound fraction of some systems.[3] However one of the principle areas of interest in this field is in determining the effect of the surface on the glass transition and chain dynamics of the bound polymer. This is more difficult to study by solid state NMR because ^{13}C NMR is a relatively insensitive technique. Spin lattice relaxation time measurements probe high frequency motions, so they cannot be used to resolve questions about the slower motions involved in the glass transition. Using other techniques including ellipsometry and FTIR it has been shown that for physisorbed films T_g appears to be lowered, while for chemisorbed films it may be raised or lowered depending on whether the polymer is terminally or segmentally attached.[4] In some cases deuterium NMR has been successfully applied to this problem, but this requires labeling and more complex synthesis.[5] Our aim was to use optically polarized ^{129}Xe NMR as a probe of chain morphology and dynamics as a function of temperature. To this end we have studied the polyethylene glycol - zirconia system whose synthesis was described in Chapter Two. Polarized ^{129}Xe spectra of both the coated and bare substrate have been acquired for a range of temperatures and pressures.

The studies of self-assembled monolayers outlined in Part One have led to a high degree of characterization and a good understanding of the structure and dynamics of these systems. ^{129}Xe NMR studies of the silica-OTS and metal oxide-ODPA systems will also be presented below, and the behavior of these systems can be usefully compared with that of the thin polymer films. Since these systems are based on many of the same substrates, such studies will indicate the differences in surface coverage and protection offered by polymer coatings over shorter chain self assembled monolayer systems.

4.2 Silica substrates

In the course of this research a variety of silica powders have been used as substrates for SAMs and thin polymer films. Silica monospheres of diameter 70nm and 800nm have been investigated by ^{129}Xe NMR. Before presenting the data acquired for the coated substrates, it may be helpful to examine the effect of substrate size on the ^{129}Xe spectra. The ^{129}Xe chemical shifts for the largest and smallest particles are shown in Figure 4.2.

Although these silicas are described by the manufacturers as non-porous, and TEM does not indicate extensive particle agglomeration, all the ^{129}Xe spectra show evidence of two sites, the more shifted site becoming progressively occupied at lower temperatures. It is believed that the site which is predominantly occupied at higher temperatures is a mesoporous environment. As the temperature is decreased a second site becomes occupied, due to the onset of condensation, increasing the residency time on the surface. At low temperatures these downfield shifts tend towards a similar value, independent of particle size. The larger silica particles (diameter 800nm) have bigger interparticle void spaces, so that the ^{129}Xe chemical shift at room temperature and above is closer to that of the free gas. The smaller monospheres have smaller void spaces, resulting in higher xenon densities in the interparticle spaces shifting the peak further downfield.

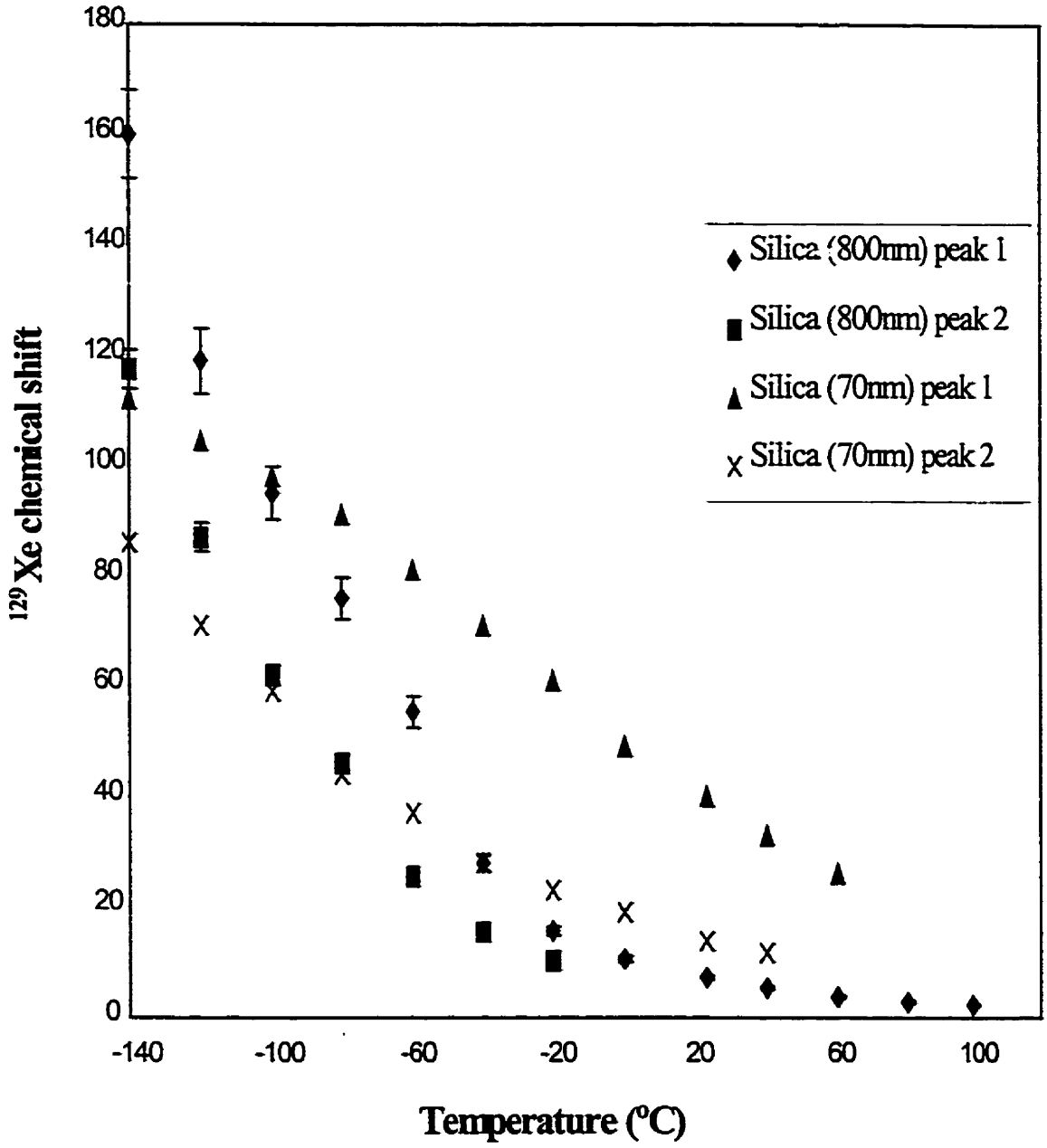

Figure 4.2 Plot of ^{129}Xe chemical shifts against temperature for silica monospheres of diameter 70nm (R100) and 800nm (M800) as indicated. Spectra were acquired using optically pumped xenon at pressures from 30 to 200 torr. The chemical shift depends on pressure for the smaller particles below –40°C. The error bars indicate the range of shifts depending on gas pressure (where higher pressures give higher shifts).

The colloidal silica has an average particle diameter of 75 nm and is described by the manufacturer to be nonporous. At 100°C, the shift of 37 ppm for the adsorbed xenon on the uncoated silica colloids is close to that measured for high surface area fumed silicas which consist of aggregates of nonporous nanometer sized spheres.[6] The lack of a pressure dependence and the large temperature dependence of the xenon shift on the colloidal silica is also observed for fumed silicas. This behavior, which greatly differs from solids with a uniform pore structure (zeolites), is attributed to rapid exchange between gaseous xenon residing in interparticle void spaces and adsorbed xenon. In the absence of strong adsorption sites, the shift of xenon adsorbed into microporous solids depends mainly on the dimensions and geometry of the void space, with larger void volumes generally leading to smaller shifts. The relatively large void spaces created by the compression of fumed silicas (15-20 nm) should lead to much smaller shifts than zeolites which have pore sizes on the order of 0.5 to 0.8 nm. The observed shifts of xenon on both powdered and compressed fumed silicas are on the order of 120- 150 ppm, much higher than expected from extrapolation of the data from zeolites.[7] The large xenon shifts on silica have been proposed to arise from adsorption of xenon into small volume void spaces created by interparticle contact points or surface roughness. The larger silica colloids (diameter 800 nm) showed a shift of 7.4 ppm at 20°C which increased to 124 ppm at -120°C as discussed previously. The smaller xenon shifts on these larger colloids are expected since the shift, the result of exchange between adsorbed and gaseous xenon, should be proportional to the surface area.

Comparison of these spectra with previous sealed sample studies of xenon adsorbed on silica only allows qualitative conclusions, since much higher gas pressures are used. One study reports optically polarized xenon spectra of a high surface area silica (aerosil 300) [8]. They report a shift of ~120 ppm at 173K, but do not carry out further analysis, since the purpose of the study was to perform CP to surface protons. One of the advantages of the optically pumped ^{129}Xe NMR experiment is that the low pressures absorbed onto the surfaces largely eliminate xenon-xenon interactions, and permit interpretation of the chemical shift data in terms of coverage. This analysis makes use of

isotherm data for xenon on the sample under investigation. A specimen isotherm of xenon adsorbed on the 70nm silica spheres at 139K is shown in Figure 4.3.

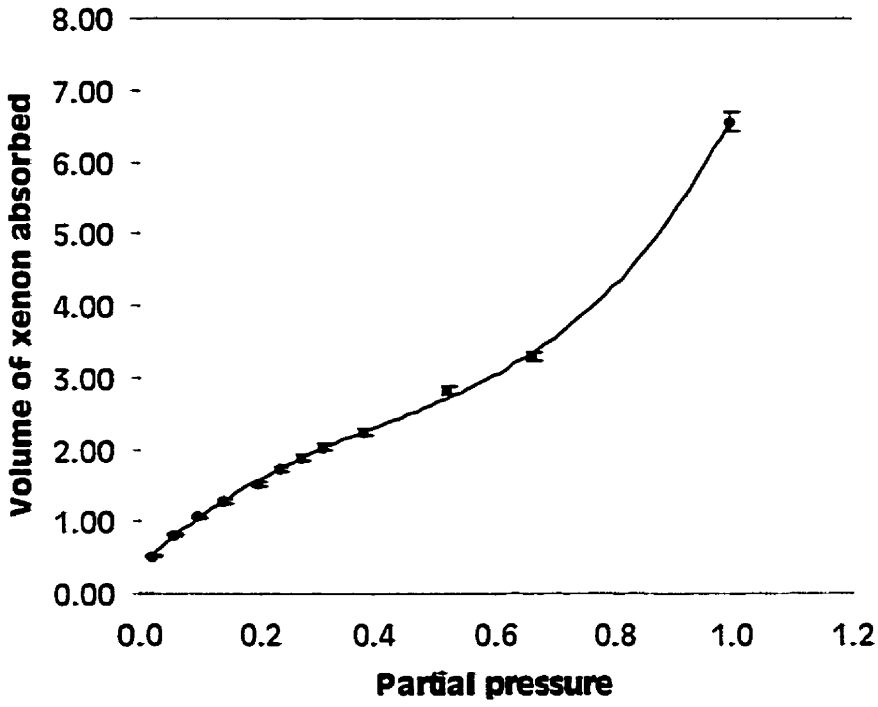

Figure 4.3 Xenon isotherm for silica particles (70nm) at 139K.

An error propagation analysis showed that the largest source of uncertainty is fluctuation in the bath temperature during the experiment. This is typically ± 2K (or ±~2% for the temperatures used here). Error bars are shown in the plot at the ± 2% level.

The derivation of the BET isotherm arises from statistical mechanics, and relies on a number of assumptions to produce an adsorption profile for an exposed surface. The original treatment was developed from Langmuir's monolayer adsorption treatment,[9] in which it is assumed that at equilibrium, the rate of condensation of gas molecules to form each adsorbed layer is equal to the rate of evaporation from the layer. By considering all adsorption sites available to the first incoming gas layer to be equal, treating the adsorbed

molecules of the first monolayer as if they were localized (i.e. confined to a particular adsorption site) and undergoing no interactions amongst themselves, and by further proposing that additional multilayers are formed by a one-to-one correspondence of molecules with those in preceding layers, and that the additional layers behave as a liquid-like structure (having no direct interaction with the surface), the BET theory produces the following statistical expression:

$$\theta = \frac{n}{S} = \frac{c\,x}{(1 - x)[1 + (c - 1)x]} \qquad \textbf{Equation 4.1}$$

where n is the number of adsorbed molecules, S is the number of sites, x is the reduced pressure and c is a dimensionless constant which is a function of temperature. The reduced pressures are calculated from saturated vapor pressure measurements.[10] θ is the coverage, which is equal to the volume of gas absorbed, v, divided by the volume required to give a full monolayer, v_m. The adsorption profile is the plot of the volume adsorbed against the partial pressure, as shown above.

Rearrangement of equation 2.1 in terms of v and v_m gives:

$$\frac{x}{v(1 - x)} = \frac{1}{v_m c} + \frac{(c - 1)x}{v_m c} \qquad \textbf{Equation 4.2}$$

Thus a plot of x / v (1-x) against x gives a straight line, with slope, s, and intercept, I, from which $v_m = 1/(s+1)$ and $c = 1 + s/I$.

In practice the assumptions made in this derivation lead to deviations from linear behavior for values of $x<0.05$ and $x>0.3$, so that the analysis is usually carried out on the reduced pressure range between these points. Having found v_m and c we can determine the surface area and adsorption energy (ΔH_{ads}) from equations 4.3 and 4.4;

$$A = \frac{N_0 v_m \sigma}{RT_0}$$ **Equation 4.3**

where N_0 is Avagadro's number, σ is the cross-sectional area of a xenon atom ($1.4793*10^{-19}$ m^2), R is the gas constant (82.05 cm^3atm) and T_0=273.2°K.

$$\Delta H_{ads} = (\ln c * RT) + \Delta H_l$$ **Equation 4.4**

where ΔH_l is the heat of liquifaction of xenon (= 3.78kcal/mol).

Isotherms are carried out at two different temperatures, and the calculated ΔH_{ads}, v_m and surface area values are shown in Table 4.1.

Temperature (K) ± 2K	ΔH_{ads} (kcal/mol) ± 4%	v_m (cc STP) ± 8%	Surface area (m^2/g) ± 10%
139	4.52	1.61	33.8
169	4.61	1.46	25.1

Table 4.1 Isotherm data of bare silica (diameter ~70nm).

From the 90% confidence limits for the slope and intercept in the linear regression using equation 4.2, the uncertainty in v_m is ± 8%. The uncertainty in ln c is ± 2%, which combined with the temperature uncertainty of ± 2% gives an uncertainty in ΔH_{ads} of ± 4%. Subsequent calculation of the surface area produces uncertainties of ± 10%. The differences in calculated surface area at the two temperatures are much larger than those calculated for the coated samples (see next section). The bare oxide powders (both silica and zirconia) pack less effectively than the coated samples, and the increase in dead volume caused by the lower amount of sample used introduces higher errors into the subsequent calculation. These errors can not be calculated.

If the ΔH_{ads} values obtained at different temperatures are in reasonable agreement, these can then be averaged and used to calculate values of c for each temperature at which ^{129}Xe spectra were obtained. The saturated vapor pressure measurements are used to determine p_0 for each experimental temperature. In general it is only at low temperatures that we observe a large pressure dependence in the ^{129}Xe chemical shift. Providing two or more pressures have been used in acquiring the optically pumped spectra, these calculated values of c can be combined with the partial pressures according to equation 4.1 to obtain the xenon coverage for each spectrum.[11] Thus the xenon chemical shift data at low temperatures can be analyzed by using the isotherm parameters, and the xenon coverages can be estimated relatively accurately without having to carry out isotherms at every experimental temperature. The chemical shift of the surface peak (the more downfield resonance, i.e. peak 1 in Figure 4.2) is then studied as a function of coverage for each experimental temperature. At each given temperature, the chemical shifts are linearly dependent on coverage and by extrapolating the data back to the intersection with the chemical shift axis, we can obtain the xenon shift at zero pressure, i.e. the surface-xenon shift in the absence of Xe-Xe interactions. At the higher temperatures (above –40°C) the surface coverage is much lower, and it is sufficient to use the chemical shift obtained with the lowest gas pressure. Finally these surface shifts are plotted against temperature, as shown in Figure 4.4.

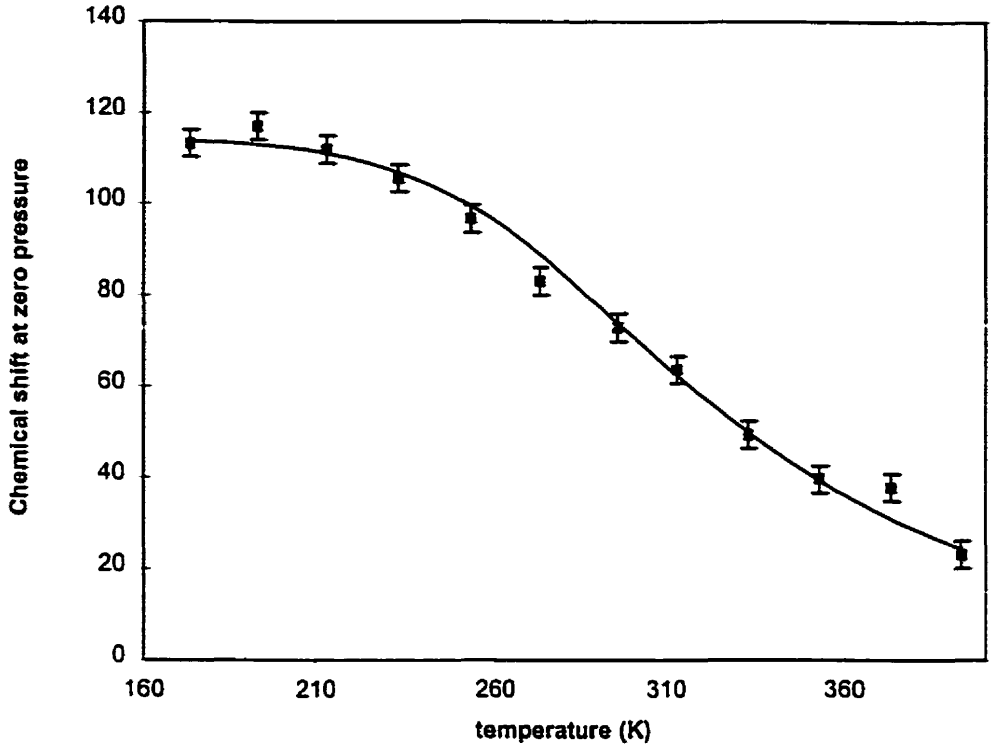

Figure 4.4 ^{129}Xe chemical shift extrapolated to zero pressure against temperature for silica (70nm). The curve is the fit of the data to equation 4.5.

Error bars in the higher temperature region arise simply from uncertainty in the measurement of the chemical shift. This is estimated to be ± 3 ppm. At the lower temperatures, the error bars represent the error limits on the intercept of the linear regressions of shift vs. coverage, which are typically ± 3%. Error bars are shown at the ± 3 ppm level.

Although silica has been studied by optically polarized ^{129}Xe NMR,[8] as stated earlier, no previous studies of silica have used this analysis. We can only compare our results with the optically polarized ^{129}Xe NMR investigations available in the literature. This method was developed during a study of polyacrylic acid,[12] where the observed surface shift was around 95 ppm. The curve shown in Figure 4.4 is generated according to the same model as that used in the polyacrylic acid study. Providing xenon-xenon interactions can be excluded (as is the case for the low pressures used in optically

pumped experiments), the chemical shift intercepts of the adsorbed xenon-surface resonances can be modeled as a chemical exchange problem. According to Raftery *et.al.* the data can be fit to a function of the form of equation 4.5;

$$\delta_{obs} = \delta_s P_s = \delta_s \left[\frac{\tau_o \exp\left(\Delta H_{ads}/kT\right)}{\tau_v + \tau_o \exp\left(\Delta H_{ads}/kT\right)} \right] \qquad \textbf{Equation 4.5}$$

where Ps is the probability of xenon being on the surface, δ_s is the surface shift, τ_v is the reciprocal of the collision rate with the surface and τ_o is the preexponential factor which is taken to be 10^{-12}s.[13] By using the adsorption energy calculated from the xenon isotherms, curves are generated by varying τ_v and δ_s. It is well-known that in fits such as these, the τ_o and τ_v variables can not be separated, however by incremental variation and minimization of the sum of the squares of the differences between the calculated and observed shifts, we were able to produce a quite reasonable fit as shown in Figure 4.4. The resulting value of δ_s=113 ppm is higher than that observed on polyacrylic acid (95 ppm). Studies of sealed samples of xenon on a variety of substrates give δ_s values at 144K and xenon loadings of less than 0.2mmole of 122 ppm on amorphous silica and 86 ppm on NaY zeolite.[14] The amorphous silica samples are described as microporous, which would account for the slightly larger shifts, however it is clear that the data for the two silica systems are quite similar. It should also be noted that this study found the dependence of shift on loading for amorphous silica to be non-linear at low pressures of adsorbed gas, indicating an exchange of gas between a broad distribution of pore sizes. Since the dependence of shift on coverage in our results is linear, it is likely that any mesoporous environment present is more homogeneous than in the amorphous samples. A study of a variety of porous silica gels found a range of ^{129}Xe shifts between 42 and 108 ppm.[15] This group used the temperature dependence of the chemical shifts to calculate the heats of adsorption which ranged from 2-5 kcal mol^{-1}, in agreement of our values of around 4.5 kcal mol^{-1}.

Unfortunately the data for the larger silica monospheres (800 nm) can not be analyzed using isotherm parameters, since isotherms of lower surface area samples can not be determined with sufficient accuracy. However the ^{129}Xe shift vs. coverage results for the bare 70nm silica particles can be compared with those observed for xenon adsorbed on the OTS coated silica particles.

4.3 Octadecyltrichlorosilane (OTS) on Colloidal Silica

Self-assembled monolayers of trichlorosilanes are commonly used to modify metal oxide surfaces. The film morphology resulting from the hydrolysis of octadecyltrichorosilane (OTS) under various conditions has been the subject of numerous studies. The principle goal in using polarized xenon NMR on these systems is in exploring its utility as a probe and a permeate in order to determine whether bulk polymer is present, and how the presence of the SAM affects the morphology of the silica spheres. There has been concern as to whether this synthetic route produces bulk polymer. It is difficult to differentiate between the formation of bulk polymer (through vertical polymerization) from the crosslinking of the siloxane backbone (via horizontal polymerization) which was proposed for this system in Part One. Neither ^{29}Si NMR nor vibrational spectroscopy can resolve this issue, for the following reasons. The silica substrate has both internal and surface silanol groups, so that detection of the consumption of surface silanols is not possible. In addition the decoupled nature of the OTS film means that very few Si-O-Si linkages are formed with the surface (see Part One: 2.4). The siloxane network which is detected by ^{29}Si NMR could arise from either a horizontal network adsorbed across the surface, or from vertical polymerization. We can only propose the former scenario on the grounds of the preparation protocol used, i.e. the use of a hydrated silica surface, dry solvent and nitrogen atmosphere. In order to determine whether ^{129}Xe NMR could be helpful in resolving the question of bulk OTS formation, ^{129}Xe NMR studies were carried out on five samples:

a) Bulk polymerized OTS: poly(octadecyl sesquisiloxane).

b) Uncoated 70 nm diameter silica colloids; preheated at 105°C under vacuum to remove physisorbed water.

c) OTS modified silica colloids with a substantial ordered component (^{13}C CPMAS spectrum indicating large peak at 33 ppm as well as one at 30 ppm as described in Part One, Chapter Three); also evacuated at 105°C. OTS coverage is around 40%. This sample is denoted silica-OTS#1

d) OTS modified silica colloids displaying only a disordered component (^{13}C CPMAS spectrum with a peak at 30ppm); also evacuated at 105°C. OTS coverage is around 25%. This sample is denoted silica-OTS#2

e) Silica colloids with several multilayers of OTS produced by repeated coating reactions at high temperature. This approach failed to produce significantly higher coverages (elemeental analysis showed 5-10% carbon), probably due to the formation of oligomers of OTS in solution which were removed during the washing steps.

Optically pumped xenon was used to study all these samples between +100 and -140°C. For the bulk OTS polymer ^{129}Xe NMR spectra are shown in Figure 4.5. Like the other bulk polymers studied, the dissolved xenon peak decreases in intensity on lowering the temperature, until at around –30°C it disappears. The ^{129}Xe shift (δ=183 ppm at 25°C) is close to the range observed for xenon dissolved in liquid alkanes (hexadecane: δ(Xe) =181 ppm)[16] rather than polyethylene (δ(Xe) ~ 200 ppm).[17] This indicates that the xenon resides principally in the alkyl chains. In simple linear alkanes, the xenon shift increases in a nonlinear fashion with the number of methylene groups, and in a linear fashion with solvent density, ranging from 150 to 180 ppm for C4 to C16.[9] Solid-state ^{13}C NMR and FTIR studies by our group,[18] and others,[19] of the polymer produced by the hydrolysis of OTS, show that the octadecyl chains are in an extended all trans conformation. While Allara and coworkers describe this polymer as crystalline, the observed shift for polymerized OTS is compatible with xenon residing in the octadecyl hydrocarbon chains. The 2D WISE spectrum of this material suggests that it is not a semicrystalline polymer containing domains of rigid and amorphous chains (like polyethylene), but rather a

sample in which the alkyl chains are undergoing sufficient motion to allow gas permeation. The disappearance of the adsorbed ^{129}Xe peak at –30°C must be related either to the freezing out of the substantial hydrocarbon sidechain motion detected in the OTS sample by the 2D WISE experiment or to a broadening in the xenon peak until it is no longer observable. This latter situation is observed for xenon dissolved in polyethylene,[20] where the linewidth increases rapidly below –20°C as the β transition is approached.

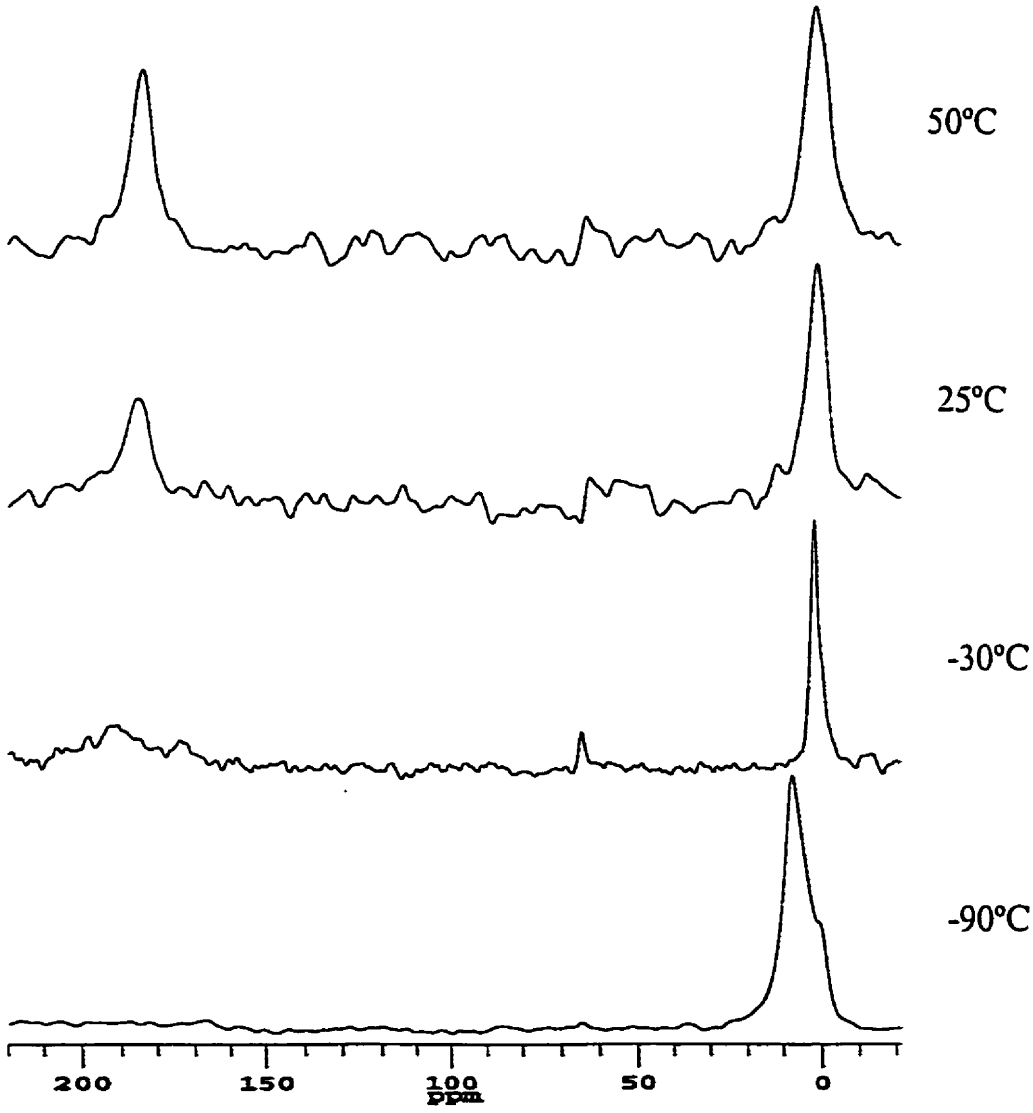

Figure 4.5 Optically polarized ^{129}Xe NMR spectra of bulk OTS polymer at the temperatures indicated.

For the two OTS monolayer samples and the uncoated silica, the spectra at 100°C are shown (Figure 4.6 a,b,c). The ^{129}Xe spectra did not display any significant pressure dependence above -100 °C. Below -100°C different ^{129}Xe chemical shifts are observed depending on the pressure (as shown in Figure 4.7; higher pressures produced higher chemical shifts).

None of the monolayer or multilayer samples studied gave any indication of the presence of xenon adsorbed in bulk polymer. In the samples in which several additions of OTS were carried out to encourage bulk polymer formation, elemental analysis indicated between 5 and 10% carbon content, which is not significantly higher than that observed in the monolayer sample. Preparation of a significant coating of multilayers by this synthetic route appears to be difficult, it is believed that most of the second layer of OTS is removed in the washing steps.

The fact that a resolved bulk polymer signal is not observed under these conditions may also be due to the inability of the xenon to detect very small domains. Literature studies of domains in copolymers investigated by ^{129}Xe NMR have established that due to the dynamic nature of the experiment, i.e. rapid exchange between free gas and dissolved xenon, there is a lower limit on the size of domains detected by ^{129}Xe NMR through the observation of separated xenon peaks.[21] Domain sizes in copolymers can be measured by 2D exchange ^{129}Xe NMR. The average distance traveled by a xenon atom during a time t is described by equation 4.6:

$$X_{RMS} = (6Dt)^{1/2} \qquad \textbf{Equation 4.6}$$

where D is the xenon diffusion coefficient. Since the diffusion constant for xenon in the OTS polymer is not known, the diffusion coefficient for polyethylene has been used (0.69×10^{-7} $cm^2 sec^{-1}$) in order to attempt an estimate of the cut-off limit. It should be noted that the actual diffusion constant is probably smaller in OTS since the chains are shorter.

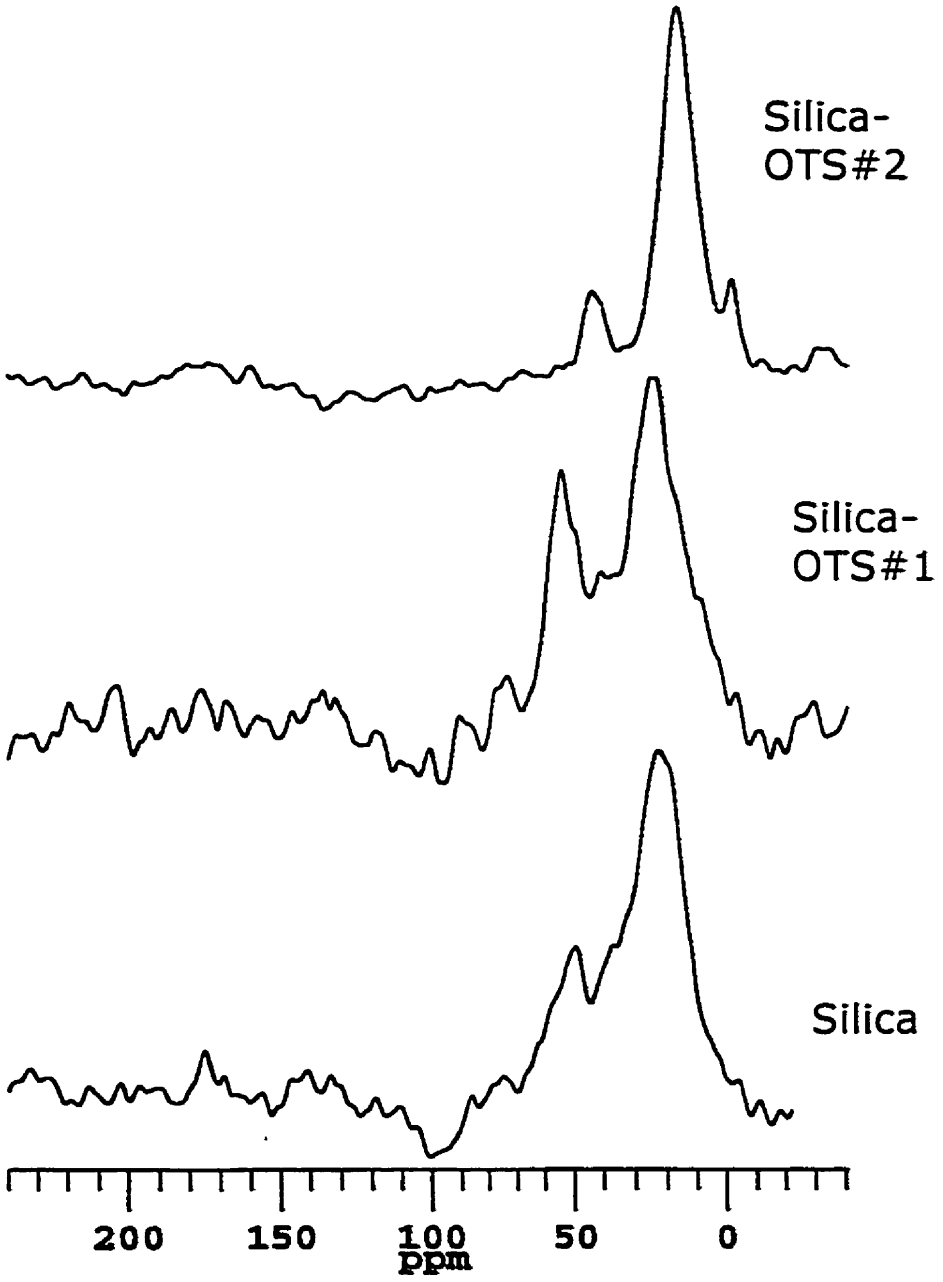

Figure 4.6 Optically pumped ^{129}Xe NMR spectra for OTS monolayers on silica (70nm) particles and bare silica substrate as indicated.

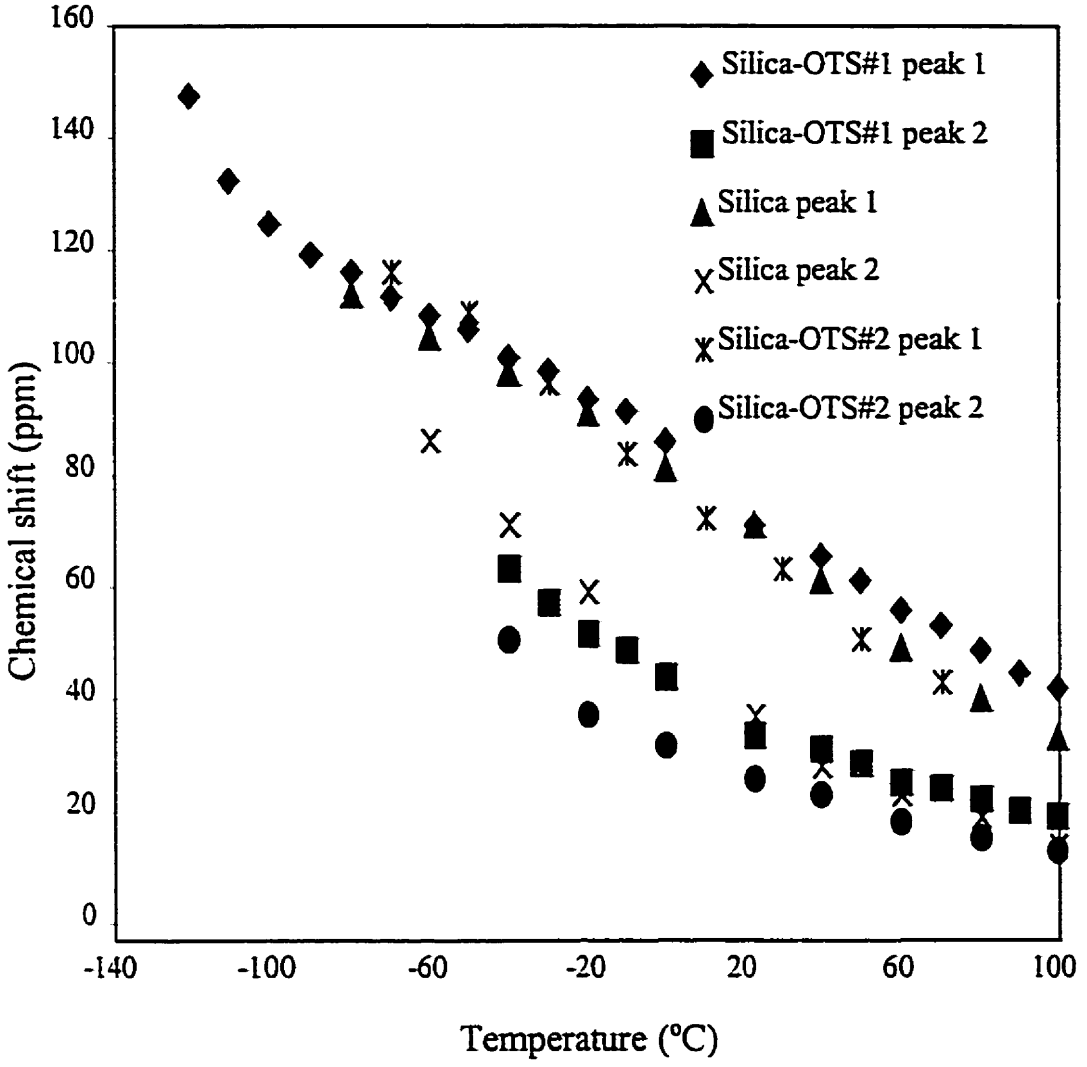

Figure 4.7 ^{129}Xe chemical shift against temperature for the coated and bare 70nm silica particles as indicated.

The condition of slow exchange is described by equation 4.7:

$$\tau\delta\omega_{\infty} >> 1 \qquad \textbf{Equation 4.7}$$

where $\delta\omega$ is the frequency difference between the sites when no exchange occurs. For a lower limit of the exchange time $\tau = 1/\delta\omega$ inserted into equation 4.6, and assuming a necessary minimum chemical shift separation of 10 ppm in order for the different domains to be observable, this gives a lower detection limit for domain sizes on our instrument of around 90nm. Assuming that the chain environment in the OTS polymer is similar to that in polyethylene, this cut-off size may account for our inability to observe a bulk polymer peak for the multilayer samples. As discussed in Chapter 2 of Part One, spin diffusion measurements indicated domain sizes for the disordered OTS regions of around 3.5 nm, clearly well below the xenon detection limit. The size of the crystalline regions is not known, and the spectra of xenon in the bulk OTS established that permeation into the crystalline regions is possible. Nevertheless it seems reasonable to propose that the absence of any bulk peak in the monolayer or multilayer samples could be due to the size of the domains. Presumably exchange between sites is rapid, and attempts to separate the peaks by cooling the sample will be prevented by the concomitant lowering of the xenon diffusion coefficient. As shown by the spectra of the bulk OTS, gas is not able to permeate the polymer below –30°C. As a test of the detection limits in the silica-OTS system, a sample containing monitored amounts of bulk polymer mixed with the silica colloids could be used.

For both the bare silica colloids and the two monolayer samples, two peaks are observed at 100°C: 37 ppm and 14 ppm for uncoated silica, 40 ppm and 20 ppm for silica-OTS#1 and 33 ppm and 12.9 ppm for silica-OTS#2. As shown in Figure 4.7, the xenon shifts of the peaks on uncoated and OTS coated silica all increase as the temperature is lowered. The intensities of the lower frequency peaks (at 20 ppm at 100°C on silica-OTS#1, 12.9 ppm on silica-OTS#2, and 14 ppm on uncoated silica at the same temperature) gradually diminish with decreasing temperature and these are no longer visible in any of the samples at - 60°C.

bare and PEG coated zirconia samples- *vide infra*). However the surface areas of both samples can be quoted as 29 ± 3m²/g. The isotherm data for the silica-OTS sample allows us to carry out the coverage analysis described for the bare silica in the previous section. The plot of surface shift against temperature is shown in Figure 4.8, along with the curve generated to fit the data obtained on the bare silica.

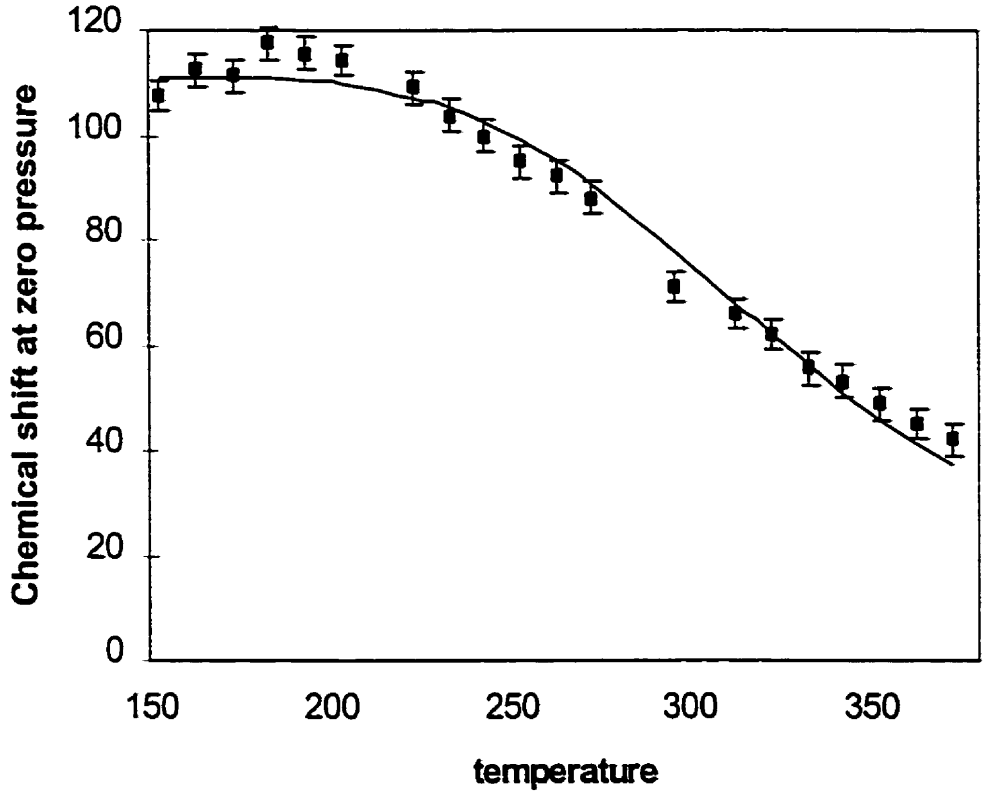

Figure 4.8 ^{129}Xe chemical shift extrapolated to zero pressure against temperature for silica-OTS#1.

The results are very similar to those observed for the uncoated silica monospheres, supporting the assertion that in this sample the xenon does not sample the thin film environment. The small changes in chemical shift are most likely due to variations in the inter-particle void spaces, and agglomeration of the silica particles.

In conclusion we propose the following to explain the observed shifts and their temperature dependence. Firstly, the peak found to lower field in all cases belongs to xenon in interparticle void spaces. As the temperature at which the experiment is carried out is lowered, the xenon tends to condense on the silica surface, and the higher field shift disappears. The downfield resonance for the bare silica and the ordered sample of silica-OTS (#1) are essentially identical because the xenon does not spend a significant time within the organic coating and resides only at the uncovered surface, of which there is a considerable amount due to the low coverage. No bulk OTS was detected, either because there was not sufficient polymer deposited, or because the domain sizes are too small to give rise to an adsorbed xenon signal.

4.4 Zirconia and titania substrates

As a further test of the ability of optically polarized ^{129}Xe NMR to act as a probe of uniformity and defects in monolayers, we went on to investigate SAM systems of higher coverage, namely the alkylphosphonate systems discussed in Part One. The behavior observed for ^{129}Xe adsorbed on these oxides can be usefully contrasted with that seen on the silica.

The use of silica in biochemical applications, in particular as a chromatographic support, is widespread and the surface chemistry has been fully characterized and is well understood.[22] Investigation of zirconia with respect to similar applications is a more recent area of research.[23] The search for stable materials for use in chromatography is important. Silica, in spite of its widespread use in this field, has many disadvantages, in particular the susceptibility of its surface to attack by extreme acidity (below pH 2) and even fairly mild basicity (above pH 8). It is also prone to dissolution at high temperatures. Zirconia offers a much more stable surface, however as noted in the first part of this thesis, the surface is considerably more complex than that of silica. In particular zirconia is noted for displaying four possible surface functionalities: basicity, acidity, reduction and oxidation. Ideally chromatographic materials should be energetically homogeneous, possess a high surface area (with no microporosity) and provide surface sites suitable for

the binding of many different chemical groups, while at the same time remaining stable under extreme conditions of pH, temperature, pressure and variation in solvents. The strengths of zirconia with respect to these latter qualities have recently increased interest in better characterizing the surface.

Zirconia is available commercially with a wide range of surface areas, pore sizes and particle sizes. As stated previously, the zirconia used in this work was provided by Degussa. The principle impurity listed is HfO_2 (up to 2%), although small quantities of Al_2O_3, Fe_2O_3, HCl, TiO_2 and SiO_2 are also present.[19] The manufacturer described the product as predominantly of the monoclinic form (in which zirconium atoms are bound to seven oxygen atoms). This structure is partially responsible for the greater chemical stability compared with silica (where a silicon atom is coordinated to only four oxygen atoms). However a recent X-ray diffraction study[24] of this material found that the sample was actually an approximately 50-50 mixture of the monoclinic and tetragonal forms (a ratio which is increased to 75-25 on treatment at 500°C). The heptacoordination of zirconia atoms in the monoclinic form is the basis of the surface acidity.[23] The structure contains planes of three coordinate and four coordinate oxygen atoms, at the surface of a particle every second oxygen atom will be coordinatively unsaturated, i.e. a Lewis base (negatively charged site: electron pair donor), while the associated zirconium atom will be a Lewis base (positively charged: electron pair acceptor). These sites are shown in Part One (Figure 3.4).

When water molecules are available, each of these Lewis acid-base pairs will dissociatively absorb a water molecule, giving an attached hydroxyl group. Since the zirconia atoms are still partially positive, it is vital to note that these hydroxyl groups will be Bronsted bases (proton acceptors) rather than Bronsted acids, as is the case for the hydroxyl groups on silica. This has important ramifications for the interaction of other chemical species with the zirconia surface. In addition a variety of hydroxyl types are present. These each have different acidities, as shown by infrared studies of the hydroxyl vibration frequency on addition of a base. In spite of the presence of these various acid groups, the surface overall exhibits slightly basic behavior. These subtle variations in the acidic/basic properties of the surface mean that special attention must be paid to the pH

used for solutions when considering adsorption chemistry. As a general rule, studies involving the adsorption of Lewis bases (e.g. pyridine) have indicated that the Lewis acid sites provided by the coordinatively unsaturated zirconium atoms are not very available to incoming species.[24]

^{129}Xe relaxation times for gas adsorbed on the uncoated oxides were very short and decreased with decreasing temperatures, so that sealed samples of these substrates were prepared. Although exact T_1 measurements were not carried out, recycle delays of 0.5 seconds were sufficient for acquisition of spectra, suggesting that the relaxation times were less than 0.5 seconds. The relaxation on the zirconia was more rapid than on any of the other bare oxides studied. Sample spectra of sealed xenon-oxide samples containing around 1 atm. of gas at -60°C are shown in Figure 4.9, along with spectra of the ODPA coated oxides. The titania exhibited a single ^{129}Xe peak, and this resonance was quite narrow at higher temperatures, indicating a fairly homogeneous environment. In addition the relaxation time at higher temperatures was longer, allowing the acquisition of optically pumped spectra for xenon on titania above 10°C. The ^{129}Xe resonances on the zirconia were much broader, consistent with the more heterogeneous nature of the zirconia surface. The relaxation behavior of ^{129}Xe on the zirconia sample will be discussed in greater detail below.

By way of comparison, samples of larger colloidal titania were synthesized by reaction of $Ti(OCH_2H_5)_4$ with water in the presence of alcohol. TEM indicated a particle size of around 600 nm. The titania colloids exhibited smaller ^{129}Xe shifts than the dispersed powder. Since the colloids are larger than the titania particles, the decrease in ^{129}Xe chemical shift is analogous to the behavior observed on the silica particles, where an increase in particle size leads to a decrease in interparticle volume causing an upfield shift. The ^{129}Xe relaxation times on this sample were longer, but on cooling the ^{129}Xe resonance became very broad. The colloids are known to exhibit a wider distribution of particle size than the smaller 30 nm particles, the broadening of the xenon resonance also suggests a more heterogeneous surface.

The differences in ^{129}Xe spin-lattice relaxation rates between the various bare oxides is interesting as it offers an additional probe of the characteristics of the surfaces.

Previous work on relaxation rates of xenon in Na-Y zeolites discussed the possible relaxation mechanisms on the zeolite surface.[25] The following T_1 dependencies were observed:

1) T_1 is independent of field strength- indicating that relaxation is not caused by modulation of the xenon CSA.
2) $1/T_1$ is inversely proportional to the gas density- indicating that the Torrey mechanism, which causes relaxation in bulk xenon gas by modulation of the electronic structure during collision producing a fluctuating magnetic field of the order of the Larmor frequency, is not active here (the Torrey mechanism is indicated by linear dependence of $1/T_1$ on gas density).
3) T_1 dependence on gas density depends on water content.
4) Relaxation is more efficient at low densities.
5) Irradiation of the proton resonance does not affect relaxation- indicating that dipolar relaxation is not involved.

In bulk solids, efficient relaxation apparently occurs by a complex mechanism involving spin diffusion to a paramagnetic center. However on a surface, this can only occur if the species being relaxed is not mobile, which xenon is. Hence we must further hypothesize rapid exchange of xenon between two sites; one where xenon sticks for a short period and is paramagnetically relaxed, and the other where physisorbed xenon is less efficiently relaxed. The impurities present in the zirconia, most likely the iron oxide would appear to be a logical source of paramagnetic relaxation. A study of ^{129}Xe in a container filled with finely powdered Fe_2O_3 found that the oxide reduced the relaxation time of the gas from 400 to 10^{-2} s.[26] Since diffusion of the gas on a surface is rapid, even a small percentage of paramagnetic impurities could be enough to cause a substantial decrease in the T_1. In all our studies of xenon on metal oxides, the relaxation rate will be decreased by the presence of any species which serves to block the surface, including water, and the organic coatings.

Although an understanding of the behavior of the bare zirconia surface is vital in determining its potential role in chromatography, most separations are actually carried out on modified supports. This is because many separations involve biological species with polar groups which are too strongly adsorbed to the sites present on bare oxides.[27] A straightforward, controllable route is therefore required for tailoring of surface activity by the presence of adsorbed species. The more ionic nature of the zirconium-oxygen bond (67%) compared to that of the silicon-oxygen linkage (50%) has been cited[23] as one reason why the coatings commonly used in silica modification, particularly silanes, are not successful for zirconia, producing unstable assemblies. Although the literature in this area remains small, some success has been achieved through grafting of both phosphate[28] and polymer[26] coatings to zirconia. The addition of polybutadiene[29] by crosslinking the butadiene monomer on the surface to create a uniform complete coating led to the formation of a highly stable reversed phase support. However this coating still allowed a degree of phosphate binding, it is thought that incomplete polymer coverage was responsible. Since the polarized xenon appears to offer a probe of the uniformity of coatings on titania and zirconia via the changes observed in the ^{129}Xe relaxation times, it was decided to use the ODPA coated samples described in Part One (Chapter 3) to investigate this approach.

4.4.1 Octadecylphosphonic acid monolayers on titania and zirconia

The properties of ODPA monolayers on these metal oxides have been investigated by conventional solid state CPMAS NMR and were discussed at length in Part One, Chapter 3. The coverage is known to be higher than that of the OTS monolayers on silica: around 60% for ODPA on TiO_2 and 70% on ZrO_2, compared with 40% for the most ordered SiO_2-OTS system. Sample spectra of xenon on the ODPA coated oxides are shown along with those of uncoated particles in Figure 4.9. In the case of the zirconia, addition of the ODPA SAM does not lengthen the relaxation time sufficiently to allow use of optically pumped xenon. Only one broad peak is observed on the ZrO_2-ODPA, the shift is not very different from that seen on the bare oxide. The ^{13}C CPMAS of this

sample indicated that the hydrocarbon chains were in an all-trans conformation, however it seems that this coating is insufficient to block access of the xenon to the surface. As discussed previously, TEM has shown zirconia to be a non-porous metal oxide in which monospheres agglomerate to produce a void structure. Due to this agglomeration, it is unlikely that the long chain phosphonic acids can access all of the surface sites whose presence is indicated by BET isotherms. These interparticle contact sites where the adsorption of xenon leads to the largest shift are likely the source of the ^{129}Xe relaxation in the ZrO_2-ODPA sample. Alternatively, if xenon does permeate the chains, the relatively loose packing indicated by the 2D WISE experiment may still allow rapid diffusion to the zirconia surface where relaxation occurs. In light of this, a thicker surface coating, in the form of poly ethyleneglycol was also deposited on zirconia in order to determine whether the relaxation of the xenon could be lengthened. This will be discussed in section 4.4.2.

The ^{129}Xe chemical shifts of the coated and uncoated titania particles and colloids are plotted against temperature in Figure 4.10. Addition of the monolayer further increases the relaxation time, so that the samples can be studied by optically pumped ^{129}Xe NMR. Presumably this is because the coating is sufficient to prevent access of the xenon atoms to the titania surface as well as due to the generally longer T_1 values on titania. Unlike the ZrO_2-ODPA and SiO_2-OTS sample, the shifts are significantly altered by the presence of the monolayer, and even at very low temperatures, the observed shifts differ appreciably from those of the xenon-titania surface shift. The ^{13}C CPMAS spectrum of the TiO_2-ODPA sample (see figure 3.7: Part One) indicates a substantial population of disordered chains, and the ^{13}C CPMAS of the ODPA on the larger colloids also indicates a similar proportion of disordered regions. The relaxation behavior of both coated samples suggests a higher degree of uniformity and total area covered by the coating, while the greater shift differences seen between the coated and uncoated titania implies that the ODPA particles are better dispersed. As noted for the silica, the largest ^{129}Xe shifts are due to the interparticle contact points, so that an improvement in dispersion which lowers the number of these contact points will tend to lower the shift.

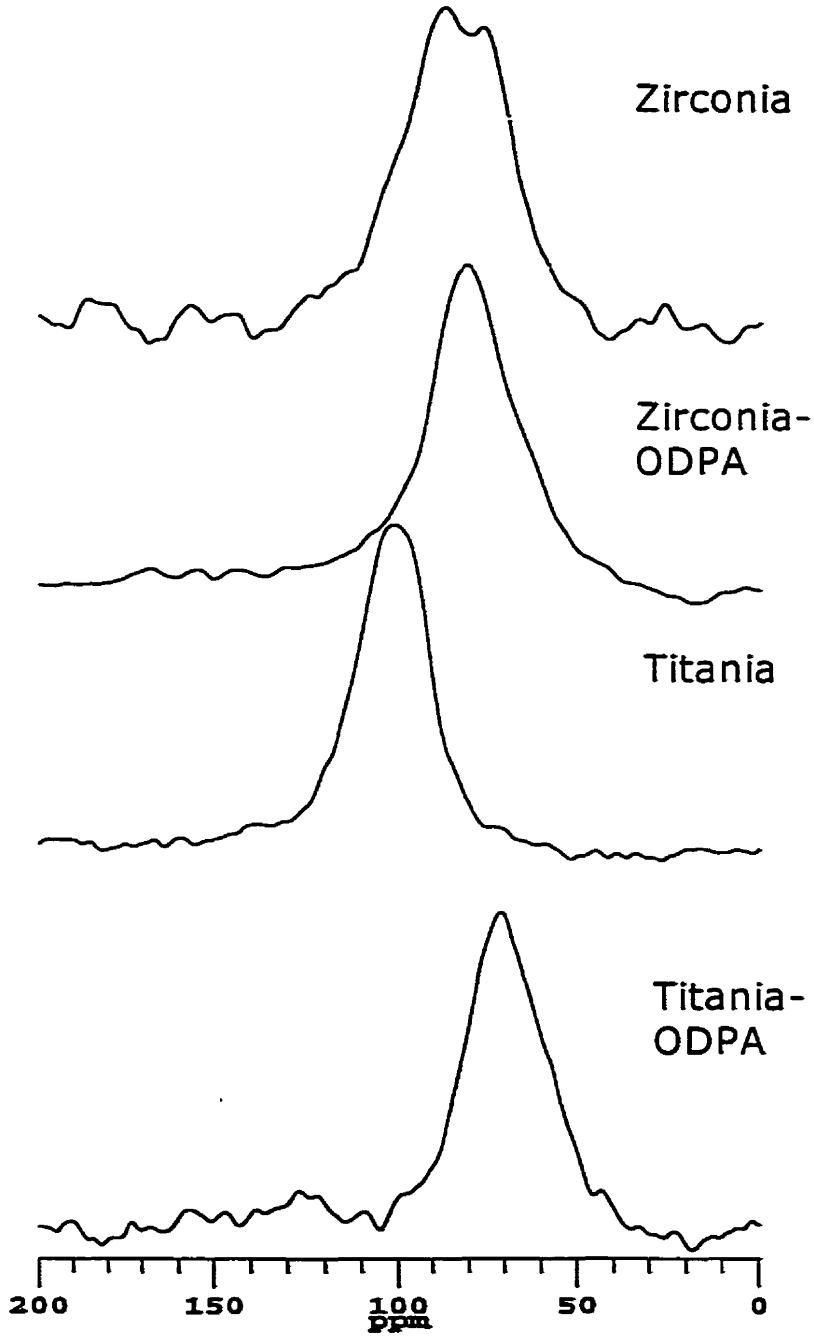

Figure 4.9 ^{129}Xe spectra at –60°C for coated and uncoated metal oxides as indicated. All spectra were acquired by preparation of sealed samples containing ~1 atm. of xenon, except for the TiO_2-OPDA where optically pumped xenon (~60 torr) was used.

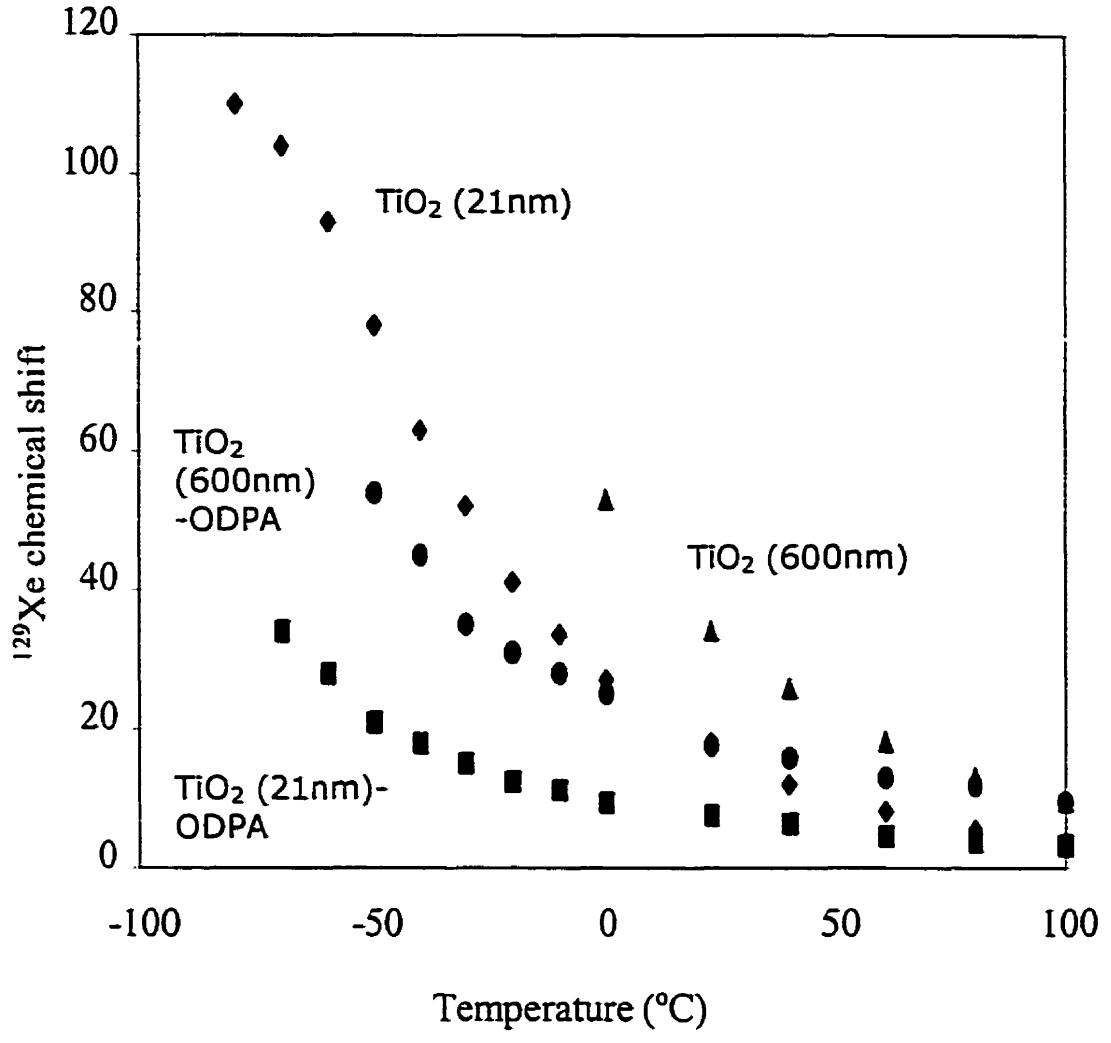

Figure 4.10 ^{129}Xe chemical shifts against temperature for ODPA coated and bare titania samples.

Unlike the tend observed for xenon on silica, the observed shifts are larger for the larger titania colloids. This may be due to a wide distribution of particle sizes, and/or the presence of a porous structure. The shift changes observed on increasing the titania particle size are mirrored in the spectra of the ODPA coated sample.

In conclusion the ODPA coating on zirconia is not uniform enough to slow down the ^{129}Xe relaxation, probably due to insufficient coverage. The titania-ODPA can be

studied by this technique, and the large differences in chamical shifts between coated and uncoated samples confirm that the surface experienced by the xenon is substantially altered by the presence of the monolayer.

4.4.2 Polyethylene glycol coatings.

Polyethylene glycol is popular in studies of adsorbed polymers, since it is commercially available in a wide range of molecular weights and with relatively low polydispersity. Its low melting point (320K for PEG1500) is useful in that a high degree of mobility can be induced at relatively low temperatures.[30] As a hydrophilic polymer, PEG creates coatings which lower the biological binding characteristics, minimizing interactions in biological environments.[31] PEG is easy to derivitize, e.g. surface groups can be added for ligand tethering such as epoxy activation[32] and is also commonly deposited as a copolymer which localizes each polymer component,[33] and allows selection of a second component which can penetrate into the surrounding medium.[34]

PEG coatings on planar silica have been widely studied; AFM has been used to confirm the self-assembly process and to study the growth of the polymer coating on silicon wafers.[27] The bulk PEG form, which consists of lamellae of crystalline helices, is preserved as alignment of the molecules on the silica at low coverages. However as the amount of deposited polymer increases, the rate of solvent evaporation is too rapid to allow crystallization and nucleation occurs, leading to branched structure. Over time these clusters rearrange to cover the entire surface. Thus although the growth process is limited by the solvent, it appears that on flat substrates relaxation of the polymer can produce a relatively even distribution of the polymer. An investigation into the use of coatings for applications involving protein adsorption[35] found that protein rejection capacity increases with increasing chain density, and that providing the molecular weight is sufficiently high, polymer loading is more important than molecular weight.

The nature and strength of the interaction of PEG with zirconia and titania has been studied in solution by Siffert et al.[36,37,38] Under the assumption that the interaction is via hydrogen bonding between the oxygen atom of the ether segment and a surface

hydroxyl on the oxide, isotherms were measured both for the bulk polymers and for a series of model ether molecules. The adsorption energy of a single segment was found to be higher for the zirconia than for the titania, and indicative of a fairly strong interaction with the surface. They also reported that the fraction of bound segments was rather higher on titania (between 5.7 and 9 %) compared with zirconia (~1.2 %) and that this fraction decreased as the molecular weight increased because the number of tails increases due to steric hindrance. This group also reported tests of four potential methods with which to determine the thickness of the adsorbed layer at the solid liquid interface. The most accurate results were given by photon correlation spectroscopy, and indicated a thickness of around 14 nm for PEG 10,000 on zirconia. The adsorbed PEG in the presence of solvent does not lie across the substrate surface, but adopts an elongated form which protrudes into the solution. In addition it is believed that some surface sites remain occupied by solvent molecules. Although no solid state studies of this system have been carried out, it seems likely that in the absence of solvent the polymer chains will lie across the oxide surface, and as discussed in the preceding section, ^{129}Xe NMR should offer a method to confirm this.

Clearly it is not possible to use elemental analysis results to calculate polymer coverage in the same manner as applied to the SAMs. Given the island structure formed by PEG adsorbed onto zirconia in solution, we deliberately used a high loading of PEG in an attempt to completely block the surface relaxation sites. Whereas we have a high loading of 84 mg/g, Siffert *et.al.* report ~3 mg of PEG per gram of zirconia. It should be noted that the surface areas of the zirconia used are rather different (they report a BET area of 12 m^2/g) and nothing more is known about the nature of the zirconia used in that study.

The studies by Siffert *et.al.*[37,38,39] were carried out using PEG polymers of MW between 400 and 20000 and at working pH values below the pH of the surface (i.e. pH 3 for the zirconia and pH 5.1 for the titania). This may explain why a study of high molecular weight PEO (MW 8000000) carried out at pH 9.5 [39] failed to observe any detectable adsorption on titania or alumina, although adsorption was seen on silica. This group concluded that the lack of Bronsted acid sites in the form of hydroxyl groups

protruding from the surface (as on silica) prevented polymer adsorption, because the ether segments of the PEO were sterically hindered from interacting with the Lewis acid sites such as the exposed Al^{3+} ions on the alumina surface. The stability and behavior of the zirconia-PEG samples produced at pH 3 in our laboratory suggest that there is some interaction with the zirconia surface, it may be that this is due to the lower MW and pH used. It has been reported,[40] that at low pH the ether linkages in PEO can be protonated to give positively charged sites. These could interact with the negative basic sites on the zirconia.

Although polymers can be grafted to higher surface area non-planar materials for NMR studies, the information available from solid state NMR is less extensive than for the SAM systems, since the polymer is a less homogeneous surfactant, and has a much larger number of nuclei within the polymer layer. Studies have been carried out by solid state NMR to estimate the bound fractions in a number of systems (e.g. PMMA on alumina etc),[41] and since NMR can detect restricted mobility rather than just those groups which are directly bound (as is the case for IR), NMR has been shown to be a useful complementary technique in some instances. However the greater thickness of the polymer layer means that in general the interface with the substrate is harder to study. An ellipsometry study of PEG films on planar substrates in aqueous solution[42] noted that characterization of particulate systems is more complex, and investigation of model systems of PEG on silica and other oxides by any technique capable of extracting information on particulate structures would be helpful in the desirable goal of optimizing such systems.

Uniform coverage is critical if a coating is to be successful for biocompatibility purposes. As shown by the study of xenon adsorbed on the ODPA coated zirconia in the previous section, the 70% coverage offered by this system is insufficient to mask the bare zirconia surface groups. The work to be presented in the final part of this chapter involves a preliminary study into PEG coated zirconia, where it is hoped that the thicker and more complete layer offered by a polymer coating may prove to be a more effective phase. The strength of ^{129}Xe NMR for this investigation is believed to lie principally in the observation of xenon relaxation behavior as a probe surface coverage.

The ^{13}C CPMAS spectra of the two zirconia-PEG samples are shown in Figure 4.17. The spectrum of the higher molecular weight coating is similar to that of the bulk polymer, while in the lower molecular weight sample resonances due to carbons near the chain ends can be seen. The elemental analysis indicates approximately 6-8% carbon in these samples.

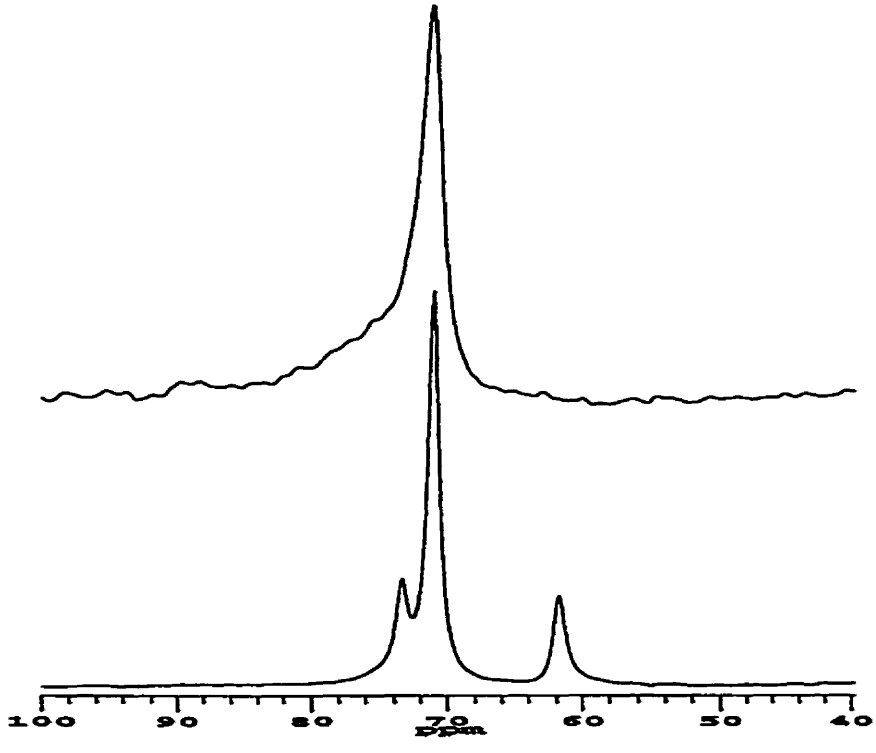

Figure 4.11 ^{13}C CPMAS spectra of PEG coated zirconia: Mw=10,000 (above) and Mw=400 (below).

The bulk PEG polymer (M_w=10,000) gave only a free gas peak at room temperature, and no evidence of xenon adsorption into the bulk polymer was observed at any temperature. Likewise investigation of a sealed sample of the polymer containing ~2 atm. of xenon did not exhibit any adsorbed peak. This sample has a melting point of 70°C. The inability to observe a ^{129}Xe peak may be due to the high crystallinity of PEG polymers with molecular weights above 1000, or a low solubility of xenon into PEG. However, no data was found in the literature on gas solubility in PEG.

Optically polarized ^{129}Xe spectra of both samples are shown for a range of temperatures in Figure 4.12. The most important observation is that the relaxation of ^{129}Xe on this sample is slowed down sufficiently to allow observation of spectra by this technique. This is evidence that the surface is completely covered by the polymer, shielding the xenon from relaxation sites on the zirconia surface.

The ^{129}Xe spectra of the zirconia-PEG samples exhibit multiple peaks. Presumably particle aggregation leads to the formation of multiple environments. With the very high polymer loading and small particle size, it is likely that some polymer chains are adsorbed to more than one particle (particularly in the higher molecular weight sample). Clearly the morphology is complex, but the ^{129}Xe spectra demonstrate the utility of carrying out studies of adsorbed polymer systems where polymer properties such as molecular weight or sidechain lengths can be varied. The next obvious experiment would be to synthesize PEG-zirconia samples with a carefully controlled range of loadings in order to determine whether a cut-off exists, below which the thickness of the polymer coating is insufficient to allow the acquisition of polarized ^{129}Xe spectra.

For completeness, xenon isotherms of the uncoated zirconia and the two polymer coated samples were carried out, giving rise to the data summarized in Table 4.3.

Sample	Temperature (K) ±2K	ΔH_{abs} (kcal/mol) ±4%	V_m (cc STP) ±8%	Surface area(m^2/g) ±10%
ZrO_2	139	4.91	0.72	33.8
	169	4.96	0.70	25.3
ZrO_2-PEG (MW 400)	139	4.23	0.90	13.1
	169	4.27	0.95	11.4
ZrO_2-PEG (MW 10000)	139	4.33	0.86	13.4
	169	4.33	0.93	11.9

Table 4.3 Isotherm data of bare and PEG coated zirconia samples.

Although the accuracy of the surface area estimated by the BET method decreases for lower surface areas, the large decrease observed in the surface area on addition of the polymer indicates that besides procing a thick coating on the zirconia surface, the PEG causes additional particle agglomeration. Clearly the polymer coating has a much more significant effect on absorption behavior of the xenon than the OTS monolayers (see data in Tables 4.1 and 4.2).

In summary, the use of a PEG coating has been shown to retard relaxation of the ^{129}Xe sufficiently to carry out optically polarized xenon spectroscopy at a range of temperatures. The technique therefore offers a way to study polymer adsorption in the solid state. Until now studies of polymer coatings on metal oxide substrates, both by NMR and other techniques have been mostly limited to the solution state.

Conclusions, contributions to knowledge and suggestions for future work

Polarized xenon is a sensitive probe of surface coverage and will be useful in the study of SAMs. The conditions for obtaining uniform coatings of surfactants on metal oxide surfaces can be monitored by this technique. Amongst the areas of interest are the thiol based monolayers on metal surfaces. Since the metal center itself would be expected to provide an extremely efficient xenon relaxation site, study of the gold nanoparticles covered by a complete alkylthiol monolayer would clarify whether thexenon relaxation is due entirely to the presence of uncoated surfaces, or if the gas can permeate the alkyl chains to access the surface. Since our conventional ^{13}C studies (in particular the 2D WISE experiments) indicated that the chain motion occuring in the alkyl thiol, phosphonate and siloxane SAMs is similar, the ability of xenon to permeate any of these chains should also be comparable.

As an extension to work presented here on the alkanesilane-silica and metal oxide-alkanephosphonate SAMs, it may be interesting to study monolayers of differing chain length and deposition of the SAMs onto dispersed metal oxides of different sizes. Using dispersed zirconia colloids rather than the fumed zirconia which is commercially available should allow the formation of a complete monolayer, since all of the surface sites would be accesible to the long chain phosphonic acids. Synthesis and characterization of a wider variety of SAMs on nanoparticles is ongoing in our group. Although the ^{129}Xe shifts themselves are not readily interpreted, the relaxation behavior of xenon on these surfaces offers a sensitive probe of monolayer quality. Use of small angle tipping pulse experiments would allow more accurate determination of the T_1 values and these could be used for comparing the various types of SAMs.

The influence of the substrate on the glass transition of supported polymer thin films is another problem which can be investigated by polarized xenon chemical shift studies. The preliminary study of PEG on zirconia described here illustrates both the strengths and weaknesses of this technique. Clearly polymer coating on non-planar substrates are difficult to characterize, and the lack of morphological information available via other techniques limits the potential for interpretation of this data. However

the possibilities for further modification of the PEG-zirconia system by more careful control of the PEG loading, and further variation of the molecular weight of the polymer should be explored. In addition other assemblies of polymers on metal oxides could be synthesized. Amongst the potential areas of interest here are coating of the poly alkylmethacrylates onto silica spheres or glass microbeads in order to determine the effects of film thickness on chain mobility and glass transition. The diameter of the spheres would need to be large enough to minimize the interparticle contacts, fortunately the lower surface area resulting from the use of larger spheres will still be observable due to the high sensitivity of the polarized xenon experiment. The synthesis of other polymer thin film samples in which xenon is known to dissolve into the bulk polymer, and the polymer contains sufficiently strong functional groups to encourage stronger polymer-oxide interactions is currently underway in our laboratory. Promising candidates include polyacrylic acid, and polypropylene-polyacrylic acid copolymer which strongly adsorb onto zirconia.

References

[1] Swalen, J.D.; Allara, D.L.; Andrade, J.D.; Chandross, E.A.; Garoff, S.; Ishraelachvili, J.; McCarthy, T.J.; Pease, R.F.; Rabolt, J.F.; Wynne, K.J.; Yu, H., *Langmuir*, 1987, *3*, 932

[2] Hofman-Caris, C.H.M., *New.J.Chem*, 1994, *18*, 1087

[3] Cosgrove, T., Griffiths, P.C., *Adv.Coll.Interface.Sci*, 1992, *42*, 175

[4] Keddie, J.L., Jones, R.A.L., Cory, R.A., *Faraday Discuss.*, 1994, *98*, 219

[5] Lin,W-Y, Blum, F.D., *Macromolecules*, 1997, *30*, 5331

[6] Conner, W.C., in *Fundamentals of Adsorption*, 1991, pp 977

[7] Conner, W.C., Weist, E.L.; Ito, T.; Fraissard, J. *J.Phys.Chem.*, 1989, *93*, 4138

[8] Brunner, E.; Seydoux, R.; Haake, M.; Pines, A.; Reimer, J.A., *J.Mag.Res.*, 1998, *130*, 145

[9] Brunauer, S.; Emmet, P.H; Teller, E., *J.Am.Chem.Soc.*, 1938, *60*, 309

[10] Freeman, M.P.; Halsy, G.D. *J.Phys.Chem.*, **1956**, *60*, 1119

[11] Long, H.W., Gaede, H.C.; Shore, J.; Reven, L.; Bowers, J.; Kritzenburger, J.; Pietrass, T.; Pines, A., *J.Am.Chem.Soc*, **1993**, *115*, 8491

[12] Raftery, D.; Reven, L.; Long, H.; Pines, A.; Tang, P.; Reimer, J.A., *J.Phys.Chem.*, **1993**, *97*, 1649

[13] Somerjai, G.A. in *Chemistry in Two Dimensions: Surfaces*. **1981**. Cornell Univ. Press

[14] Cheung, T.T.P., *J.Phys.Chem.*, **1989**, *93*, 7549

[15] Teskikh,V.V. *et.al.*, *J.Chem.Soc.Faraday.Trans.*, **1993**, *89*, 4239

[16] Luhmer, M., Bartik, K., *J.Phys.Chem*, **1997**, *101*, 5278

[17] Stengle, T.R., Williamson, K.L., *Macromolecules*, **1987**, *20*, 1428

[18] Reven. L., Dickinson, L., *Thin Films*, **1998**,

[19] Parikh, A.N., *et.al.*, *J.Am.Chem.Soc.*, **1997**, *119*, 3135

[20] Kentgens, A.P.M.; van Boxtel, H.A.; Verweel, R, J.; Veeman, W.S.; *Macromolecules*, **1991**, *24*, 3712

[21] Walton, J.H., *Polymers and Polymer. Composites*, **1994**, *2*, 35

[22] Iler, R.E., *The Chemistry of Silica*, **1979**, Wiley-Interscience

[23] Nawrocki, J.; Rigney, M.P.; McCormick, A.; Carr, P.W., *J. Chromatogr.A.*, **1993**, *657*, 229

[24] Dang, Z.; Anderson, B.G.; Amenomiya, Y.; Morrow, B.A., *J.Phys Chem.*, **1995**, *99*, 14437

[25] Smith, M.L.; Dybowski, C., *J.Phys.Chem.*, **1991**, *95*, 4942

[26] Proctor, W.G.; Yu, F.C., *Phys.Rev.*, **1951**, *81*, 20

[27] Nawrocki, J.; Dunlap, C.J.; Carr, P.W.; Blackwell, J.A.; *Biotech.Prog.*, **1994**, *10*, 561

[28] Scafer, W.S.; Carr, P.W.; Funkenbusch, E.F.; Parson, K.A., *J.Chromatogr.*, **1991**, *587*, 137

[29] Rigney, M.P.; Funkenbush, E,F.; Carr, P.W.; *J.Chromatogr.*, **1990**, *499*, 291

[30] Nettesheim, S.; Zeisel, D.; Handschuh, M.; Zenobi, R., *Langmuir*, **1998**, *14*, 3101

[31] Bearinger, J.P.; Castner, D.G.; Golledge, S.L.; Rezania, A.; Hubchak, S.; Healy, K.E., *Langmuir*, **1997**, *13*, 5175

[32] Emoto, K.; Van Alstine, J.M.; Harris, J.M., *Langmuir*, **1998**, *14*, 2722

[33] Kjellander, R., *J.Chem.Soc Faraday*, **1982**, *2*, 2025

[34] Viverat Perrin *Langmuir*, **1994**, *10*, 3635

[35] Malmsten , M.; Emoto, K.; Van Alstine, J.M., *J.Coll.Int.Sci.*, **1998**, *202*, 507

[36] Siffert, B.; Li, J.F., *Coll.and Surf.*, **1992**, *62*, 307

[37] M'Pandou., A.; Siffert, B., *Coll.and Surf.*, **1987**, *24*, 159

[38] Siffert, B.; Li, J.F., *Colloids and Surfaces*, **1989**, *40*, 207

[39] Mathur, S.; Moudgil, B.M., *J.Coll.Int.Sci.*, **1997**, *196*, 92

[40] Myers, D., *Surfactant Science and Technology*, **1988**, VCH Publishers

[41] Cosgrove, T.; Griffiths, P.C., *Adv.Coll.Int.Sci.*, **1992**, *42*, 175

[42] Van Astine, J.; Malmsten, M., *Langmuir*, **1997**, *13*, 4044

Appendix

Isotherm data

P dose	P final	deltaP	total dose	x (p/p0)	v (cc STP)	x/(v(1-x)	0.122625	: Vint*
6.8	2.6	6.8	6.8	0.0177	0.51	0.03515	0.124025	:Vint*+Vd*
10.4	7.9	7.8	14.6	0.0536	0.81	0.06995	147.3	:Po
16.2	14.1	8.3	22.9	0.0957	1.06	0.09995		
22.2	20.3	8.1	31.0	0.1378	1.28	0.12455		
30.8	28.8	10.5	41.5	0.1955	1.52	0.16025		
36.1	34.4	7.3	48.8	0.2335	1.72	0.17745		
41.7	40.3	7.3	56.1	0.2736	1.88	0.20025		
47.1	45.9	6.8	62.9	0.3116	2.02	0.22415		
58.5	56.7	12.6	75.5	0.3849	2.23	0.28125		
82.3	77.3	25.6	101.1	0.5248	2.81	0.39305		
102.2	98.1	24.9	126.0	0.6660	3.28	0.60725		
174.6	147.3	76.5	202.5	1.0000	6.56	#DIV/0!		
280	150	132.7	335.2			#DIV/0!		

SiO_2 (70 nm) isotherm data 139K

P dose	P final	delta P	total dose	x (p/p0)	v (cc STP)	x/(v(1-x))	0.123696	:Vint*
20.7	17.6	20.7	20.7	0.0186	0.36	0.05265	0.124999	:Vint*+Vd*
37.9	36.2	20.3	41.0	0.0383	0.55	0.07285	946	:Po
56.9	55.5	20.7	61.7	0.0587	0.69	0.08975		
76.4	75.2	20.9	82.6	0.0795	0.82	0.10575		
93.9	92.9	18.7	101.3	0.0982	0.92	0.11865		
115.8	114.7	22.9	124.2	0.1212	1.03	0.13455		
135.3	134.4	20.6	144.8	0.1421	1.11	0.14905		
155.5	154.5	21.1	165.9	0.1633	1.21	0.16155		
175.9	175	21.4	187.3	0.1850	1.29	0.17555		
200.5	199.4	25.5	212.8	0.2108	1.40	0.19115		
219.1	218.2	19.7	232.5	0.2307	1.48	0.20195		
240.8	240	22.6	255.1	0.2537	1.56	0.21865		
261.1	260.1	21.1	276.2	0.2749	1.65	0.22955		
278.8	277.8	18.7	294.9	0.2936	1.75	0.23712		
298.6	297.6	20.8	315.7	0.3145	1.85	0.24793		
367.6	364.9	70.0	385.7	0.3857	2.09	0.29938		
476.7	472.4	111.8	497.5	0.4993	2.48	0.40070		

SiO_2 (70 nm) isotherm data 169K

P dose	P final	delta P	total dose	x (p/p0)	v (cc STP)	X/(v(1-x))	0.1219: Vint*
7.5	4.7	7.5	7.5	0.0323	0.33	0.09995	0.1235: Vint*+Vd*
11.2	9.4	6.5	14.0	0.0646	0.55	0.12655	145.4: Po
16.5	15.1	7.1	21.1	0.1039	0.71	0.16355	
21.3	20.1	6.2	27.3	0.1382	0.85	0.18935	
26.0	24.9	5.9	33.2	0.1713	0.97	0.21215	
32.5	31.4	7.6	40.8	0.2160	1.10	0.25085	
38.0	37.3	6.6	47.4	0.2565	1.17	0.29375	
45.6	43.6	8.3	55.7	0.2999	1.41	0.30405	
53.2	51.3	9.6	65.3	0.3528	1.63	0.33475	
61.5	59.7	10.2	75.5	0.4106	1.84	0.37955	
68.7	66.8	9.0	84.5	0.4594	2.06	0.41335	
77.2	76.6	10.4	94.9	0.5268	2.11	0.52655	
87.1	83.9	10.5	105.4	0.5770	2.49	0.54715	
96.0	93.2	12.1	117.5	0.6410	2.82	0.63295	
104.3	101.2	11.1	128.6	0.6960	3.19	0.71855	
113.7	111.7	12.5	141.1	0.7682	3.41	0.97075	
127.3	121.8	15.6	156.7	0.8377	4.07	1.26815	
138.8	133.7	17.0	173.7	0.9195	4.67	2.44515	
146.7	140.8	13.0	186.7	0.9684	5.38	5.68715	
155.7	145.4	14.9	201.6	1.0000	6.63	#DIV/0!	

SiO_2-OTS (#4.2) isotherm data 139K

P dose	P final	delta P	total dose	x (p/p0)	v (cc STP)	x/(v(1-x))	0.1236 :Vint*
20.7	17.6	20.7	20.7	0.0186	0.36	0.05265	0.1249 :Vint* + Vd*
37.9	36.2	20.3	41.0	0.0383	0.55	0.07285	946 :Po
56.9	55.5	20.7	61.7	0.0587	0.69	0.08975	
76.4	75.2	20.9	82.6	0.0795	0.82	0.10575	
93.9	92.9	18.7	101.3	0.0982	0.92	0.11865	
115.8	114.7	22.9	124.2	0.1212	1.03	0.13455	
135.3	134.4	20.6	144.8	0.1421	1.11	0.14905	
155.5	154.5	21.1	165.9	0.1633	1.21	0.16155	
175.9	175	21.4	187.3	0.1850	1.29	0.17555	
200.5	199.4	25.5	212.8	0.2108	1.40	0.19115	
219.1	218.2	19.7	232.5	0.2307	1.48	0.20195	
240.8	240	22.6	255.1	0.2537	1.56	0.21865	
261.1	260.1	21.1	276.2	0.2749	1.65	0.2295	
278.8	277.8	18.7	294.9	0.2936	1.75	0.2371	
298.6	297.6	20.8	315.7	0.3145	1.85	0.2479	
367.6	364.9	70.0	385.7	0.3857	2.09	0.2993	
476.7	472.4	111.8	497.5	0.4993	2.48	0.4007	

SiO_2-OTS isotherm data 169K

P dose	P final	delta P	total dose	x (p/p0)	v (cc STP)	x/(v(1-x))	0.1218: Vint*
9.9	6	9.9	9.9	0.0394	0.47	0.08835	0.1234: Vint*+Vd*
15.9	13.9	9.9	19.8	0.0914	0.70	0.14455	152.1: Po
21.5	20.9	7.6	27.4	0.1374	0.76	0.21025	
28.9	28.1	8.0	35.4	0.1847	0.84	0.26865	
37	36.3	8.9	44.3	0.2387	0.92	0.34235	
43.7	43.2	7.4	51.7	0.2840	0.97	0.41085	
50.8	50.3	7.6	59.3	0.3307	1.02	0.48685	
57.9	57.5	7.6	66.9	0.3780	1.05	0.57765	
82.1	80	24.6	91.5	0.5260	1.27	0.87245	
96.7	95.3	16.7	108.2	0.6266	1.42	1.18355	
118.9	116.8	23.6	131.8	0.7679	1.64	2.01905	
141	138.8	24.2	156.0	0.9126	1.87	5.57675	
178.2	148.1	39.4	195.4	0.9737	5.52	6.70525	
238.1	152.1	90.0	285.4	1	15.98	#DIV/0!	

ZrO_2 isotherm data 139K

P dose	P final	delta P	total dose	x (p/p0)	v (cc STP)	x/(v(1-x))	0.1219424: Vint*
20.9	18.5	20.9	20.9	0.0196	0.26	0.0754	0.1234564: Vint*+Vd*
42.8	41.4	24.3	45.2	0.0438	0.40	0.1142	946: Po
54.1	53.3	12.7	57.9	0.0563	0.48	0.1243	
71.5	70.8	18.2	76.1	0.0748	0.54	0.1501	
88.4	87.8	17.6	93.7	0.0928	0.59	0.1744	
102.6	102	14.8	108.5	0.1078	0.64	0.1894	
120.8	120.3	18.8	127.3	0.1272	0.67	0.2170	
141	140.3	20.7	148.0	0.1483	0.73	0.2397	
154.6	154.3	14.3	162.3	0.1631	0.74	0.2627	
177	176.5	22.7	185.0	0.1866	0.77	0.2982	
196.1	195.6	19.6	204.6	0.2068	0.80	0.3253	
219	218.4	23.4	228.0	0.2309	0.84	0.3573	
240	239.5	21.6	249.6	0.2532	0.87	0.3901	
256.9	256.5	17.4	267	0.2711	0.89	0.4170	
275.7	275.4	19.2	286.2	0.2911	0.90	0.4562	
314.2	312.9	38.8	325	0.3307	1.00	0.4933	
399.1	396.9	86.2	411.2	0.4195	1.14	0.6324	
503.4	499.4	106.5	517.7	0.5279	1.47	0.7578	

ZrO_2 isotherm data 168K

P dose	P final	delta P	total dose	x (p/p0)	v (cc STP)	x/(v(1-x))	0.1213452: Vint*
6	4.9	6.0	6.0	0.0321	0.13	0.2610	0.1226284:Vint*+Vd*
11.2	10.1	6.3	12.3	0.0662	0.25	0.2792	152.5
17.1	16.1	7.0	19.3	0.1056	0.37	0.3211	
20.7	20.1	4.6	23.9	0.1318	0.44	0.3487	
25.9	25	5.8	29.7	0.1639	0.54	0.3643	
28.7	28.1	3.7	33.4	0.1843	0.61	0.3721	
32.5	32.2	4.4	37.8	0.2111	0.64	0.4194	
35.5	35	3.3	41.1	0.2295	0.70	0.4284	
37.9	37.7	2.9	44.0	0.2472	0.72	0.4586	
41.7	40.9	4.0	48.0	0.2682	0.81	0.4530	
45.4	44.9	4.5	52.5	0.2944	0.86	0.4826	
61.3	60.1	16.4	68.9	0.3941	0.99	0.6565	
70.9	70.1	10.8	79.7	0.4597	1.07	0.7914	
85.1	83	15.0	94.7	0.5442	1.31	0.9093	
98.5	97.3	15.5	110.2	0.6380	1.44	1.2236	
116.5	115	19.2	129.4	0.7540	1.59	1.9169	
129.5	128	14.5	143.9	0.8393	1.77	2.9598	
188.4	152.5	60.4	204.3	1	6.09	#DIV/0!	

ZrO_2-PEG (400) isotherm 139K

P dose	P final	delta P	total dose	x (p/p0)	v (cc STP)	x(v(1-x))	0.1204857: Vint*
18.8	18.2	18.8	18.8	0.0173	0.05	0.3392	0.1216116:Vint*+Vd*
41.1	40.2	22.9	41.7	0.0381	0.14	0.2927	1054: Po
48.2	47.9	8.0	49.7	0.0454	0.16	0.2922	
58.8	58.4	10.9	60.6	0.0554	0.20	0.2943	
70.1	69.7	11.7	72.3	0.0661	0.23	0.3016	
79.8	79.5	10.1	82.4	0.0754	0.26	0.3139	
94.9	94.4	15.4	97.8	0.0896	0.30	0.3243	
112.9	112.4	18.5	116.3	0.1066	0.34	0.3477	
129.8	129.3	17.4	133.7	0.1227	0.38	0.3636	
136.8	136.4	7.5	141.2	0.1294	0.42	0.3500	
151.1	150.7	14.7	155.9	0.1430	0.46	0.3652	
168.2	167.7	17.5	173.4	0.1591	0.50	0.3800	
180.9	180.5	13.2	186.6	0.1713	0.53	0.3886	
201.7	200.9	21.2	207.8	0.1906	0.60	0.3891	
208.4	208.2	7.5	215.3	0.1975	0.62	0.3963	
228.2	227.6	20.0	235.3	0.2159	0.67	0.4101	
256.6	255.8	29.0	264.3	0.2426	0.73	0.4353	
269.1	268.8	13.3	277.6	0.2550	0.75	0.4518	
282.4	282.1	13.6	291.2	0.2676	0.77	0.4692	
301.6	301.1	19.5	310.7	0.2856	0.81	0.4891	
313	312.7	11.9	322.6	0.2966	0.84	0.5017	

ZrO2-PEG(400) isotherm data 169K

P dose	P final	delta P	total dose	x (p/p0)	v (cc STP)	x(v(1-x))	0.1206223: Vint*
10.4	8.1	10.4	10.4	0.0553	0.27	0.2209	0.1221367: Vint*+ Vd*
15.6	14.3	7.5	17.9	0.0977	0.41	0.2624	146.4: Po
21.7	20.5	7.4	25.3	0.1400	0.55	0.2972	
26.4	25.7	5.9	31.2	0.1755	0.62	0.3410	
31.5	30.6	5.8	37.0	0.2090	0.73	0.3642	
35.8	35.2	5.2	42.2	0.2404	0.79	0.4002	
41.8	41.1	6.6	48.8	0.2807	0.87	0.4504	
48.7	47.8	7.6	56.4	0.3265	0.96	0.5024	
59.1	58	11.3	67.7	0.3962	1.08	0.6063	
69.8	68.8	11.8	79.5	0.4699	1.19	0.7473	
80.2	79.2	11.4	90.9	0.5410	1.29	0.9127	
90.4	88.8	11.2	102.1	0.6066	1.47	1.0489	
101	100	12.2	114.3	0.6831	1.57	1.3697	
119.9	117.2	19.9	134.2	0.8005	1.87	2.1428	
136	132.4	18.8	153	0.9043	2.28	4.1400	
152.4	146.4	20.0	173	1	2.98	#DIV/0!	
180	146.4	33.6	206.6	1	7.03	#DIV/0!	

ZrO_2-PEG (10000) isotherm 139K

P dose	P final	delta P	total dose	x (p/p0)	v (cc STP)	x/(v(1-x))	0.120061: Vint*
26.6	25.4	26.6	26.6	0.0241	0.11	0.2252	0.121416: Vint*+Vd*
40.3	39.7	14.9	41.5	0.0377	0.16	0.2412	1054: Po
54.9	54.3	15.2	56.7	0.0515	0.21	0.2532	
72.5	71.9	18.2	74.9	0.0682	0.26	0.2787	
88.4	87.8	16.5	91.4	0.0833	0.31	0.2901	
104.9	104.3	17.1	108.5	0.0990	0.36	0.3026	
125	124.3	20.7	129.2	0.1179	0.42	0.3185	
139.9	139.3	15.6	144.8	0.1322	0.47	0.3230	
167.3	166.4	28.0	172.8	0.1579	0.54	0.3454	
183.3	182.7	16.9	189.7	0.1733	0.59	0.3537	
202.3	201.7	19.6	209.3	0.1914	0.64	0.3703	
219.7	219.2	18.0	227.3	0.2080	0.68	0.3888	
244.9	244.2	25.7	253.0	0.2317	0.73	0.4156	
259.2	258.7	15.0	268	0.2454	0.76	0.4247	
270.5	270.2	11.8	279.8	0.2563	0.78	0.4384	
294.5	293.8	24.3	304.1	0.2787	0.83	0.4609	
328.8	327.8	35.0	339.1	0.3110	0.91	0.4947	

ZrO_2-PEG 10000 isotherm 169K